NEUTRON DOSE EQUIVALENT AND SPECTRA DETERMINATION FOR A MEDICAL LINEAR ACCELERATOR USING DOSIMETRIC AND MONTE CARLO METHODS.

JOSEPH BARTON AWOTWI-PRATT

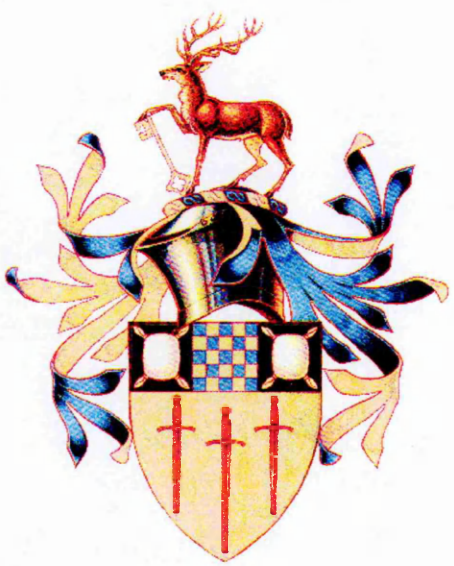

A thesis submitted to the University of Surrey for the degree of

Doctor of Philosophy.

September 2003

Department of Physics, University of Surrey, Guildford, GU2 7XH, UK.

ProQuest LLC.
789 East Eisenhower Parkway
P.O. Box 1346
Ann Arbor, MI 48106 – 1346

Abstract.

Medical linear accelerators (linacs) operated above 8 MV photon energy have their output contaminated with neutrons resulting from the photon interactions with the materials of the linac head components. Photoneutron contamination in the photon output was investigated on the Varian Clinac 2100C linear accelerator operating at 15 MV photon beam energy and a dose rate of 4 Gy/min using experimental and Monte Carlo (MCNP) simulations.

In order to ensure that the output of the MCNP code was valid, an ^{241}Am-Be isotopic irradiation facility was simulated to study the scattered and transmitted neutron fluxes emanating from a rectangular phantom placed in 'short' and 'long' width orientations. The results of the scattered and transmitted neutron fluxes were compared with those obtained by measurements using the Microspect-2 Neutron Probe (N-Probe) and a new neutron detector, the LGB detector, based on a scintillator containing Li, Gd, and B. Results show a reasonable agreement between measurements and MCNP calculations for both transmitted and scattered neutron flux.

Good and accurate knowledge of all the relevant nuclear parameters involved and reliable as well as reproducible experimental conditions are required in neutron flux measurements using foils. A Monte Carlo based Fortran 90 program, COLDET, was developed to calculate the solid angle subtended by both 'bare' and collimated γ-ray detector to point, disc and cylindrical sources. Results show good agreement with theory and those obtained by others, however, some differences arise when the finite dimensions of the source and detector are taken into account.

Superheated drop detectors (SDDs) were employed in the photoneutron dose measurements due to their insensitivity to high energy and intensity photons in contrast to activation foils. The high and low neutron sensitivity SDDs (Apfel Enterprises Inc., U.S.A), recommended for out of beam and in-beam measurements were used, respectively. Measurements were carried out for both in air and in a water phantom in the patient plane at 100 cm source-to-surface (detector) distance (SSD) in order to investigate the variation of neutron dose equivalent with field size in and

outside the irradiation beam and also in the maze of the linac bunker and the control room.

The neutron dose equivalent on the beam axis increased gradually as field size was varied from 5x5 cm^2 to 40x40 cm^2 for in-air measurements and was independent of field size outside the irradiated field at distances greater than 20 cm. The neutron dose equivalent for 10x10 cm^2 and 40x40 cm^2 field sizes was found to be 1.57 ± 0.10 $mSvGy^{-1}$and 1.74 ± 0.09 $mSvGy^{-1}$, respectively. The neutron dose equivalent in the maze for all the field sizes was much higher at gantry angles 0° and 180°. The neutron dose equivalent on the beam axis for the 10x10 cm^2 field size at a depth of 1 cm in water was 1.42 ± 0.09 $mSvGy^{-1}$ for the in-phantom measurements and 1.81 ± 0.08 $mSvGy^{-1}$ for the 5x5 cm^2 field size for the same depth but was independent of field size at depth ≥5 cm in water.

MCNP simulation of the 15 MV photon energy Varian Clinac 2100C head was carried out to investigate the photoneutron contamination in its output for the purpose of comparison with experiment. Though the precise linac information about the treatment head was not made available to us due to manufacturer's proprietary rights and commercial secrecy, there was good agreement between simulation and experiment for both in-air and in-phantom to within 15% and 20%, respectively. The fractional neutron dose equivalent to radiosensitive organs of the patient during high-energy photon treatment was determined using the tissue equivalent phantom BOMAB compatible with MCNP.

In a design study, MCNP simulation of a linac bunker was undertaken to determine the effect on the total neutron flux and dose at the exit of the maze in terms of treatment room modification and in cladding the maze with neutron absorbing materials. The neutron spectrum of an isotropic ^{252}Cf source was used for the purposes of simulation to represent the unfiltered neutron component of the linear accelerator beam and was placed at the SSD. The modification of the treatment room reduced the total neutron flux and dose by approximately 40 and 45%, respectively, whereas the addition of neutron absorbing materials resulted in further reduction of approximately 90%.

THIS THESIS IS DEDICATED TO THE MEMORY OF MY GRANDFATHER,

Rt. Rev. Charles Awotwi-Pratt (1907 – 93)

and also

Jacklyn, Andrew, Stephanie and Regina

Acknowledgements.

Whatever goes up must come down. I thank God for a fruitful conclusion to this work. It has been a long winding road but 'You' have been my rock of ages.

I am most grateful and indebted to Prof. Nicholas Marcus Spyrou for his untiring efforts and contribution to this work. Many thanks for your kindness and encouragement.

I wish to express my sincere gratitude to Drs Olufunso Akanle and Waleed Altaf for their invaluable pieces of advice and also delighted to mention ever-helpful Mrs Sue Jenner.

It is a privilege to be a Commonwealth Scholar. I thank all those at the Commonwealth Secretariat, UK and Ghana for this opportunity.

I am extremely grateful to Elizabeth McCauley for making available the linac at the Physics Department, St Bartholmew's Hospital, London, for the experiments and sitting through in spite of her state of health. I am also thankful to Mr Dennis Libaert and John-William Brown for lending me their eve ready helping hands for the experiments in the University. Also worthy to mention is Mr Roger Warren for his expertise in constructing the water phantom used in the experiments at the hospital.

Many thanks to those I shared office with during the course of my studies, especially Andy Ma with whom I had useful discussions on MCNP and Ali G for the experience at St. Bartholomew's Hospital, London. I am also delighted to mention Dr Darren Cutts, the PET brain of room 2AC05 (never again!!), Dr Charlotte Ridge (Terminator), Dr Sabar Baur (silent monk), Imane, Nadia, Carol, Rabbi Mark, Eleanor, Abdul Rahman, Daniel, LL Admans, 'Irish-Mos' Carol, Mohammed and El-Fatih et al.

List of Contents.

List of figures

Chapter 1

Chapter 2

Chapter 3

Chapter 4

Chapter 5

Chapter 6

Chapter 7

Chapter 8

List of tables

Chapter 2

Chapter 3

Chapter 4

Chapter 5

Chapter 6

Chapter 7

Chapter 8

1. Introduction

Cancer is a major cause of morbidity in the United Kingdom (UK) and the rest of the developed world with more than 262,000 new cases diagnosed in the UK alone according to a report published by Cancer Research UK in 2002 [Can02]. About 65% of the people diagnosed are over the age of 65 years. There are more than 200 different types of cancer, but four of them – lung, breast, large bowel (colorectal) and prostate – account for over half of all new cases. Breast cancer emerged as the most common cancer in the UK with 39,250 cases. This may be attributed to, in part to more painstaking and much better diagnostic procedures in screening women for breast cancer. It accounts for more than 1 in 4 of all female cancers followed by colorectal and lung cancers with 16,800 and 14,790 new cases respectively. Lung cancer is the most common cancer for men with 24,000 cases diagnosed followed closely by prostate cancer with about 22,900 cases. Lung cancer incidence rates in men have been on the decline in the UK since the 1960s while prostate cancer incidence continues to rise [Can02].

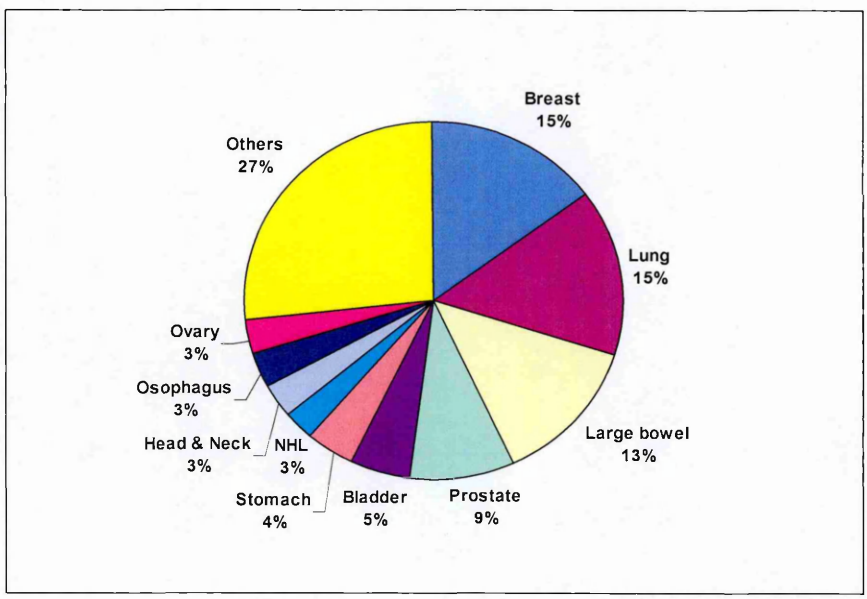

Fig. 1.1.The ten most common cancers diagnosed in UK persons, 1998, excluding non-melanoma skin cancer [Can02]. (NHL – Non-Hodgkins lymphoma.)

The treatment of cancer is achieved with the use of radiotherapy alone or in combination with chemotherapy or surgery. External beam therapy and brachytherapy are the two types of radiotherapy commonly used in cancer treatment with either one playing a complementary role depending on the type of treatment adopted. External beam therapy involves the use of machines to direct radiation, bremsstrahlung photons produced from medical electron linear accelerators (linacs) or gamma rays produced as a result of the decay of radionuclides' notably cobalt 60, on the tumour. The primary aim of a treatment is to destroy the tumour cells in the treated area while sparing as much as possible normal surrounding tissue such that cell repair can occur. Depending on the energy, the photon beam can be used to destroy cancer cells on the surface of or deeper in the body. The higher the energy of the beam the greater the penetration in the body and therefore the better the treatment of deep-seated tumours.

Cobalt 60 units are still used for radiotherapy in a large fraction of the developing world and a good proportion of developed countries. It is only relatively recently that these are being replaced by medical linear accelerators. The invention of the microwave generator magnetron and amplifier klystron during the Second World War facilitated the long-term development of medical electron linear accelerators (linacs), which have become increasingly more sophisticated due to continuous research and development. The number of linacs installed all over the world is growing apace and linacs of energies up to 25 MV photon energies are relatively common place, an indication of the efficacy of radiation in cancer treatment. However, linacs operating at photon energies greater than 8 MeV have their output contaminated with neutrons that contribute extra, unaccounted dose to the patient undergoing treatment. The neutrons originate mainly from the prompt photodisintegration interaction of the high-energy photons with the materials constituting components of the linac head. The average binding energy per nucleon for these materials is generally over 8 MeV, a threshold energy. A much smaller fraction of less than one tenth is produced directly from electron interactions.

One of the main objectives of the present work was to determine the neutron dose contribution in the output of 15 MV Varian Clinac 2100C or any other linac using experimental and MCNP calculations. The use of experiment and simulation serve as a comparison of both methods and gives added confidence in the determination of

some parameters such as neutrons produced in the target and collimators that cannot be directly found using experimental methods. It is known [Ong00, NCR84, Kha94] that neutron dose is about 1% or less of the photon output of linacs, however, the relative biological effectiveness (RBE) of neutrons is not only higher than that of photons and electrons but also energy dependent and not confined to the x-ray field. This is due to the linear energy transfer (LET) resulting from the secondary charged particles that neutrons produce on interaction with a target material. In spite of the relatively small percentage of neutrons produced in linacs, neutrons have been measured [NCR84, Ong00, Tho02] at greater distances from the reference 100 cm source-to-surface distance, including the accelerator bunker maze and the shielding door, due to the isotropic nature of photoneutron production. Besides, neutrons undergo capture reactions with the materials of the bunker to induce radionuclides that contribute to the radiation dose received by radiation workers in the treatment room. Transmitted neutrons will also deliver dose to staff and the general public in the vicinity of the treatment room.

In order to authenticate the MCNP simulation output, an ^{241}Am-Be irradiation facility with a rectangular water phantom placed in two different orientations was simulated for the purpose of comparing calculated data with that of experiment. The scattered and transmitted neutron fluxes from the 'short' and 'long' widths of the phantom were calculated. In chapter 3, the simulation results are compared with experimental data obtained using the Microspect-2 Neutron Probe (N-Probe) and a new neutron-sensitive inorganic scintillator containing lithium gadolinium borate, LGB [Mas83, Czi02]. Based on the outcome of the comparison, the neutron flux distribution with depth in the bulk sample for both phantom orientations was also investigated. This is difficult to determine using experimental techniques.

Neutron flux measurement by activation analysis involves counting the induced activity in the activation foils using a γ-ray detector. Good and accurate knowledge of all the relevant nuclear parameters involved as well as reliable and reproducible experimental conditions are required. The geometrical factor or the solid angle subtended by the detector onto the irradiated source is discussed in chapter 4. A Monte Carlo based Fortran 90 program, COLDET, has been written to calculate the solid angle subtended by a bare and collimated detector for point, disc and cylindrical

source shapes. A random number generator has been added to the program and therefore does not require an external random number generator. The program takes into account the actual size of both the source and detector, a feature ignored by most programs for this purpose. The solid angle calculated using this program has been compared with those using the well-known formula for a point source and the program written by Carrillo [Car96].

The measurement of photoneutrons from linacs has been an area of research interest spanning many years [Axt72, Nat84, Ash90, D'Er98a, Ong00, Tho02]. Several methods and measurement procedures have been used, notably activation analysis [Axt72, Ash90] by measuring induced activity in activation metal foils exposed to intense photons from the linac directly or by moderation of the neutrons using Bonner spheres [Tho02]. The drawback of either method is that neutrons can be generated by the interaction of the intense photons within the foils directly and induced activity. In the case of the moderating material neutrons can be generated in the moderating material or the photoneutron is absorbed in the moderating material itself. Therefore photoneutron measurements using the activation technique can be over or under estimated. Ideally, a detector which does not respond to the intense and pulsed photon beam background, will be suitable for measuring photoneutrons. Superheated Drop Detectors (SDDs), based on bubble technology have been found, to some degree, to be insensitive to photons [Apf79, Ing85] under certain conditions and therefore suitable for measurements in intense photon fields. The SDD is a tissue equivalent material made up of a superheated emulsion in the form of droplets suspended in the matrix of a holding gel such that the metastable state of the droplets is maintained until nucleation is initiated by the interaction of a neutron. The growth of the bubble into a visible measurable size gives an indication of a neutron interaction. Though there are active detectors based on this principle the ones used in this work [Apf79], as discussed in chapters 5 and 6, are passive ones due to the nature of the measurement and also because the bubbles formed can be converted easily to the dose equivalent value using calibration and temperature correction factors. The detectors have been calibrated such that the resulting neutron interaction is a measure of the dose equivalent, which takes into consideration the quality factor of the neutron in contrast to neutron dose. The superheated drop detector (SDD) manufactured by Apfel Enterprises Inc. in the USA, has been used to determine the variation of the

photoneutron dose equivalent with field size and gantry rotation in the patient plane and in the maze of a linac bunker for both in-air and water phantom scenarios.

In chapter 7, a general Monte Carlo N-Particle Transport Code, MCNP4C2 [Bri01], has been used to estimate the photoneutron content in the output beam of 15 MV photon energy of a Varian Clinac 2100C, the same linac on which experimental determination of photoneutrons was carried out discussed in chapter 6. This MCNP version, MCNP4C2, unlike preceding versions has photoneutron production libraries for most of the isotopes that make up the components of the linac head. In order to authenticate the simulation, all the parameters that were measured have been compared with simulation. Further, due to the agreement between measurement and calculation, the neutron dose equivalent in the various regions of a tissue equivalent (human) phantom, BOMAB, [Sat89] during photon treatment has been investigated. BOMAB is a MCNP compatible file of a tissue equivalent (human) phantom without detailed anatomical structures.

The efficacy of radiation therapy increases with photon energy since the photons are more penetrating and efficient in treating deep-seated tumours. Shielding against photons is achieved relatively easily and this is well established, however the neutrons produced by photoneutron reactions require extra shielding due to the fact that neutrons can scatter several times before attaining thermal equilibrium and subsequent capture. The practice in most hospitals is the use of shielding doors composed of neutron moderating material in addition to gamma-ray attenuating materials to reduce to the barest minimum dose due to neutrons and capture gamma rays. In some hospitals, linacs operated at photon energies above 10 MV have been avoided entirely by appropriate design in order to dispense with the expense of shielding doors. One of the measures to encourage the use of high-energy linacs is to have a neutron attenuating oriented bunker to drastically cut down the neutron and photon component before reaching the exit of the maze. In the final chapter of this work, the MCNP code has been used to design a linac bunker capable of attenuating both neutrons and photons. This is of the same general design as those found in most hospitals but without a shielding door. The bunker designed for high-energy photon shielding, was modified to include concrete baffles in the treatment room and the maze and also neutron absorbing materials were employed in the maze, cladding at

the appropriate points, walls and ceiling, in order to study the effect of these modifications on the neutron component at the exit of the maze. A ^{252}Cf source spectrum which resembles the unfiltered neutron spectrum from linacs [NCR84, McC79] was used as the simulation source.

2. Neutron contamination in the output of Medical Linear Accelerators

2.1 Introduction

In spite of recent developments in medicine such as the decoding of the human gene, most cancer tumours will undoubtedly continue to be treated in the foreseeable future using radiotherapy, with external beam therapy, employing high-energy photons and electrons being preferred. There has been a significant upsurge in the use of medical linear accelerators (linacs) in the last decade and the number installed around the world is growing apace.

Medical linacs are designed to operate at high energies up to 25 MV for more efficient and effective treatment of deep rooted tumours since high energy photons are more penetrating. However, the main problem associated with high energy linacs is that their output is contaminated with a non-negligible neutron field. The neutrons are produced by the interaction of the high-energy photons (bremsstrahlung) and electrons with the various materials of the target, flattening filter, collimators and other shielding components that make-up the treatment head and also with the patient and the couch. The treatment head is made of high atomic number (Z) materials notably lead, tungsten and iron. The binding energy per nucleon of these nuclei range between 7 and 9 MeV, therefore, production of neutrons occurs at energies above this threshold.

Measurements and Monte Carlo calculations have shown the existence of a small but significant neutron dose in linacs [Ong00]. It has been shown that in the 16 to 25 MV photon therapy mode the neutron dose equivalent along the central axis is approximately 0.5% of the photon dose and falls off to about 0.1% outside the field [Axt72, Soh79 Pri78]. Ongaro et al [Ong00] used calculations, employing the Monte Carlo code MCNP-GN (and also carried out measurements) found that there is a quick zeroing of the photon absorbed dose equivalent in positions outside the treatment field in contrast to the neutron dose equivalent which has values which cannot be ignored even in positions far from the photon field. The neutrons thus produced expose the patient to an unaccounted neutron dose as well as secondary radiation generated by neutron capture reactions occurring in the patient, the accelerator and the concrete material of the treatment room [Toc79]. Healthy tissues receive a neutron contribution that can represent a non-negligible neutron dose to radiosensitive organs, due to the high neutron quality factor and radiobiological effectiveness (RBE) [ICR91]. Therefore,

an accurate knowledge of the neutron dose is very pertinent in view of optimisation of the radiotherapy treatment and the protection of radiation workers.

ICRP Publication 60 [ICR91] prescribes reduction in the mean annual effective dose limit from 50 mSv to 20 mSv. The recording level set according to ICRP 26 [ICR71] is a tenth of the annual dose equivalent limit. The importance of this concept has been confirmed in ICRP 60 but the value of the corresponding level has neither been confirmed nor rejected [Por92]. Thus the annual recording level could be lowered from 5 mSv to 2 mSv. A neutron dosimetry system should be capable of detecting annual doses at or below the recording level when the neutron fraction of the total effective dose is taken into account. In the case where the neutron radiation contribution is 50% of the total recording level, a neutron dosimetry system should be capable of measuring the minimum detectable neutron dose of 1 mSv per year or 0.08 mSv per month. Superheated drop detectors can achieve a sufficiently low-level detection threshold, which should meet this requirement. Since they can also be made relatively insensitive to photons the neutron contribution can be measured more accurately in an intense photon field such as the output of a medical electron linear accelerator.

2.2 Photoneutron production

It is well-known that electromagnetic radiation and electrons produced by medical linear accelerators operating above 8 MeV have their output contaminated with unwanted neutrons. Following the pioneering work of Laughlin [Lau51] the neutron emission from these high-energy x-ray radiotherapy machines has been of great concern to radiological physicists. The source of neutrons is through photonuclear (γ, n), (γ, 2n) and electronuclear (e, e'n) reactions. The cross-section for the (e,e'n) reactions are much smaller at least by a factor of about 10 or more than those of the (γ,n) reactions [Kha94, McG76]. Consequently, neutron production during electron beam therapy mode is quite small compared with that during x-ray mode and therefore considered negligible except at energies above 20 MeV. Photoneutrons are principally produced through the giant dipole resonance (GDR) in the photo-disintegration reaction between photons and target nuclei. In the region of the GDR, the (γ,n) cross section for high Z elements is a factor of ten higher than that for low Z ones. The GDR is related to the mass number A by the following [San89, Boh75]:

$$E = 79A^{-1/3} \tag{2.1}$$

where E is the peak GDR energy in MeV.

Resonance peaks of some of the isotopes of materials constituting the various parts of the accelerator head and beam collimation system are as shown in figure 2.1.

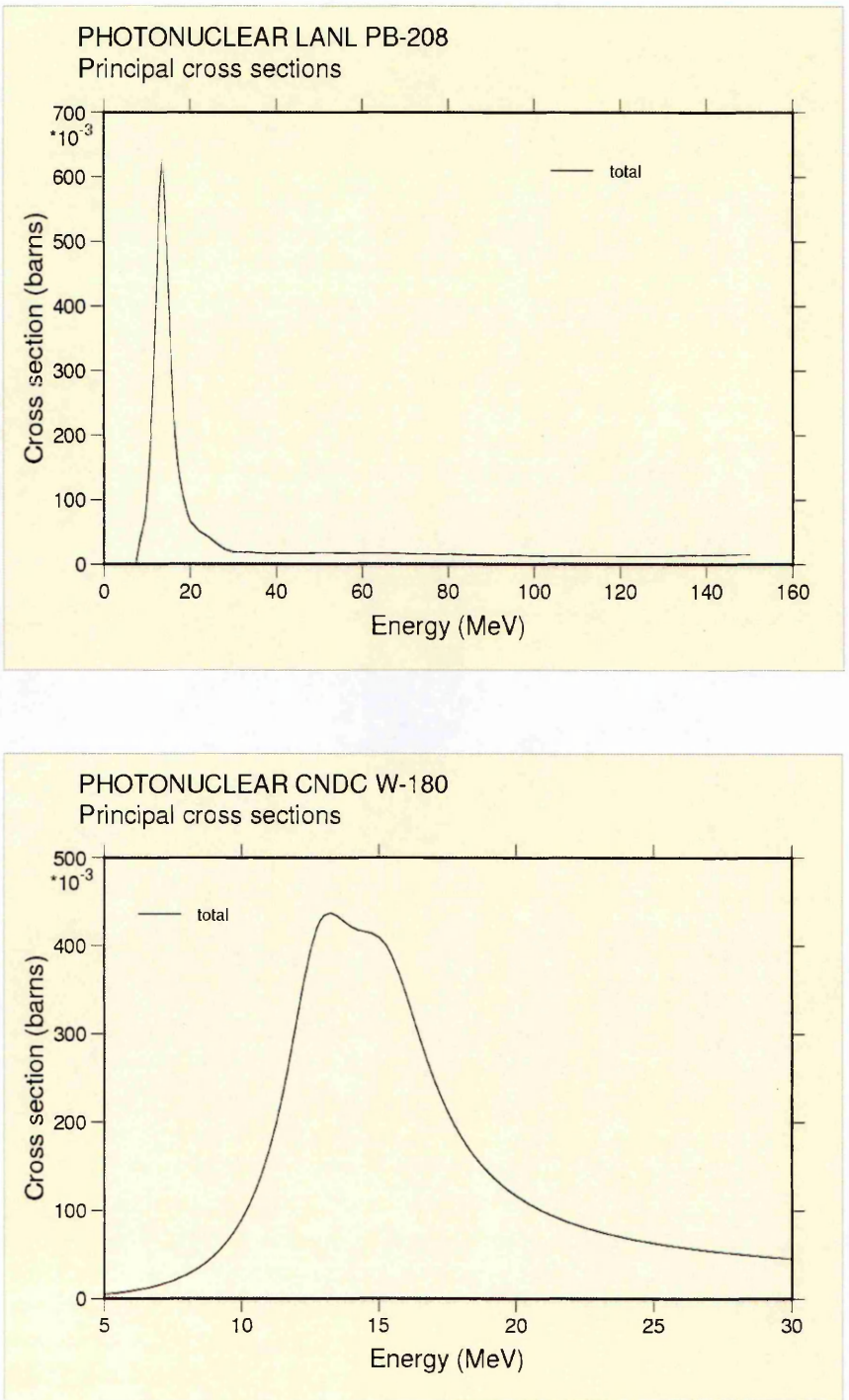

Fig. 2.1a: Photoneutron resonance peaks of the isotopes lead (^{208}Pb) and tungsten (^{180}W)

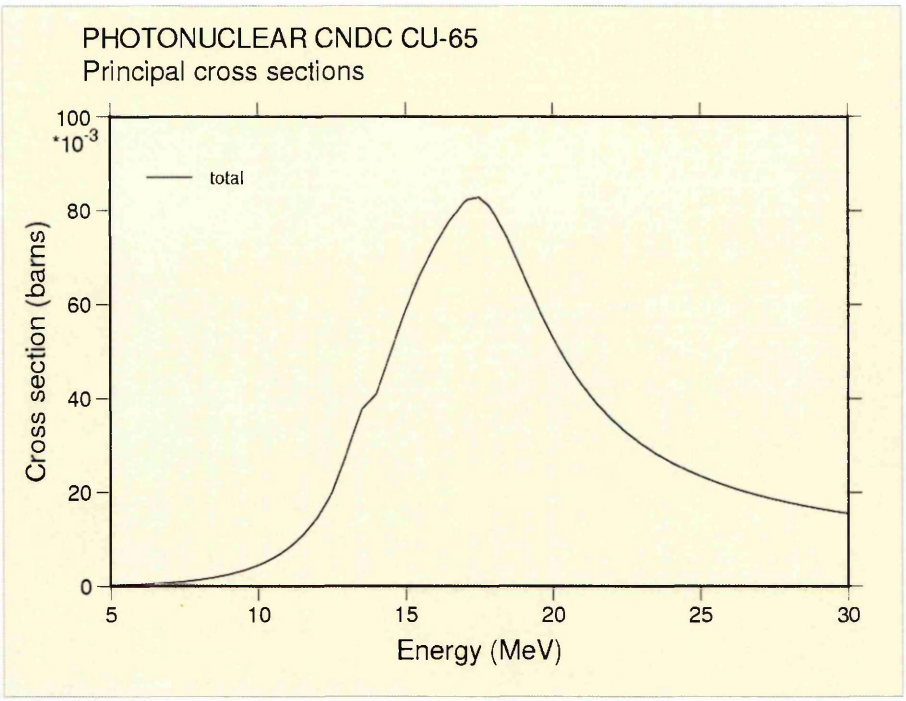

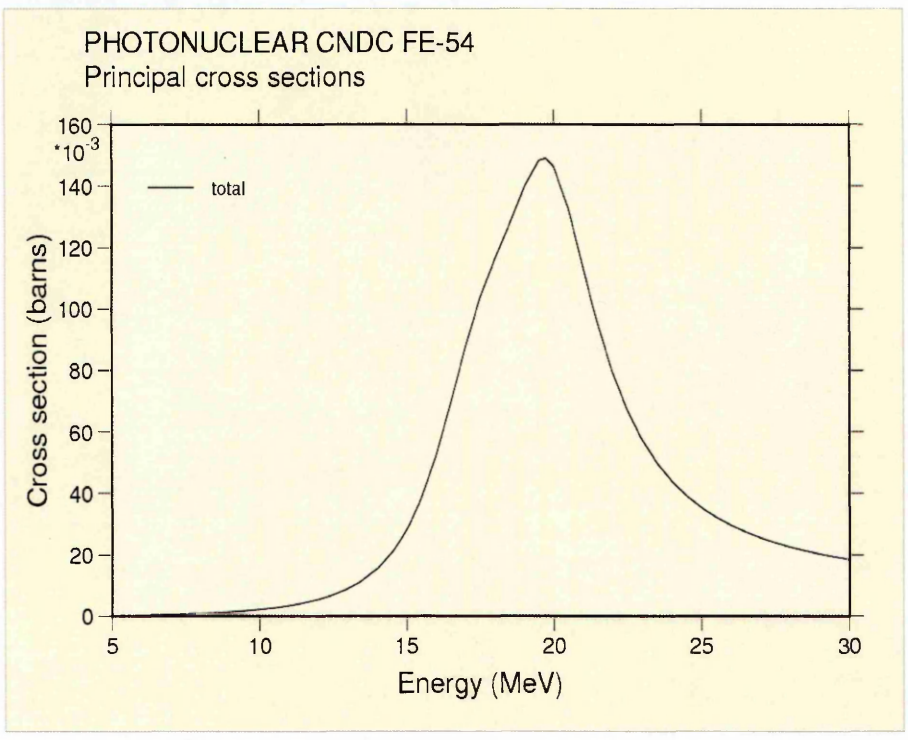

Fig. 2.1b: Photoneutron resonance peaks of the isotopes of Copper Cu (^{65}Cu) and iron Fe (^{54}Fe).

2.3 Photoneutron spectrum

The energy distribution of neutrons emitted by photonuclear disintegration is characterised by two components [Ong00]: a peak around 1 MeV, due to nucleon evaporation, and a bump in the higher energy region due to the direct reaction. The mean energy of the neutron spectrum generated by the (γ,n) reaction is around a few MeV, however, in the patient plane, neutrons have a more complex distribution due to transmission through the accelerator head and a reduced mean energy. There is also the neutron component that has scattered several times on the walls of the treatment room that irradiates the patient plane uniformly. Hitherto, it was frequently stated that the photoneutron spectrum from linacs resembles the fission spectrum of ^{252}Cf. This is only true for the primary neutron spectra [NCR84] because the spectrum is filtered by the accelerator head and scattering in the bunker therefore the spectrum is degraded with respect to that of ^{252}Cf. The neutron angular distribution is usually assumed to be isotropic, since direct neutrons, characterised by a $\sin^2\theta$ angular distribution (θ is the angle between photon and neutron direction) represents only a small percentage of the entire spectrum, whilst neutrons generated by the evaporative process are isotropically emitted. Figures 2.2 and 2.3 show the photonneutron spectra of tantalum and tungsten. The modified spectrum of 10 cm thick tungsten in a concrete room are also shown in comparison with ^{252}Cf spectrum.

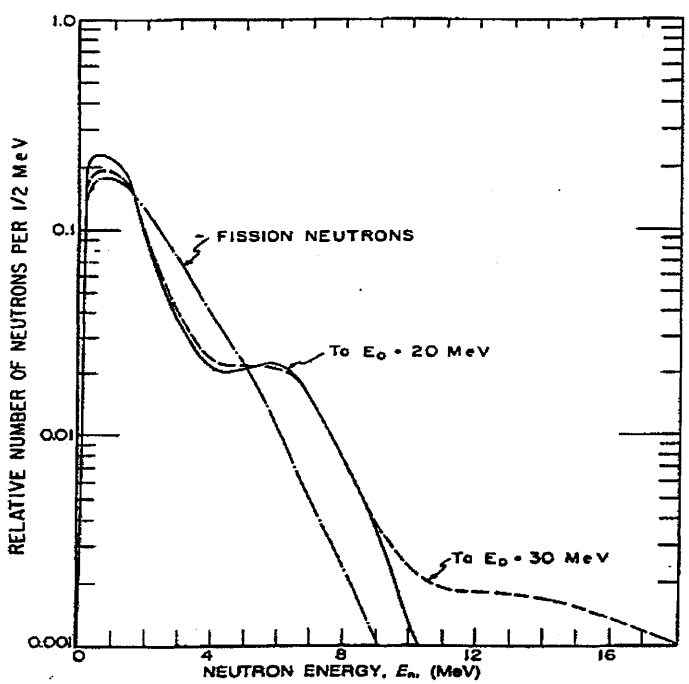

Fig.2.2: Photoneutron spectra for tantalum with peak bremsstrahlung energies of 20 and 30 MeV. The fission spectrum is shown for comparison [NCR64].

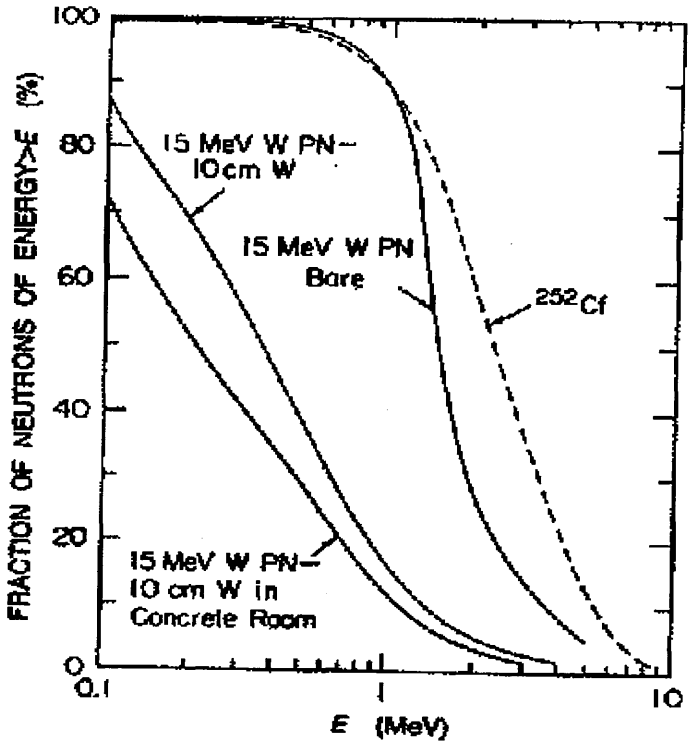

Fig.2.3: Integral photoneutron spectrum for 15 MeV electrons striking tungsten target. A fission spectrum ^{252}Cf is shown for comparison [McC79]. PN stands for photoneutrons

2.4 Mechanism of neutron interactions

Neutrons interact with the nuclei of target materials through scattering and absorption. Neutron absorption reactions result in the increase in the mass number of the target atoms leading to the formation of an excited compound nucleus. For the system to be stable the de-excitation of the compound nucleus ensues to return the compound nucleus to the ground state. The type of compound nucleus formed and the energy of the incident neutron have an effect on the decay or de-excitation process that follows.

The absorption of a neutron can result in the formation of a compound nucleus which always de-excites by the emission of charged particles. This process is generally referred to as transmutation of the target nuclei. The charged particles are released through reactions such as (n, p), (n,d), (n,α) and (n, ^{3}He). These reactions are generally threshold reactions suggesting that the incident neutron should possess a minimum energy required for this to take place. However, reactions such as $^{10}B(n, \alpha)$ and $^{6}Li(n, \alpha)$ have high thermal neutron cross-sections and are exceptions. The threshold energy for absorption reactions is given by

$$E_{thld} = -Q\left(\frac{M + m_n}{M}\right) \tag{2.2}$$

where the negative sign denotes the endothermic nature of the reaction, m_n is the neutron mass, M is the mass of the target nucleus and Q is the mass difference in energy units. The charge particle produced should possess enough energy to overcome the Coulomb barrier before being ejected.

Neutron scattering reactions, unlike absorption, do not alter the identity of the target material but rather affect the energy and momentum of the neutron on interaction. The neutron transfers some of its energy to the nucleus in the scattering process which is responsible for slowing down the neutron. The neutron is said to scatter elastically when the total kinetic energy of the neutron and the target nucleus is unchanged and momentum is conserved. The transfer of energy between the neutron and the nuclei of the medium continues until the neutron comes into thermal equilibrium with the medium. When this occurs the average total kinetic energy transferred to the nuclei of the medium by the neutrons is equal to the average total kinetic energy received by the neutrons of the medium.

Inelastic collisions result in conservation of momentum but not in kinetic energy. The collision results in the transfer of energy to the target nuclei by the neutrons creating an excited state of the target nuclei. The excited nuclei de-excite by the emission of prompt gamma rays in order to restore stability. Inelastic scattering can be written as (n,n'γ) with the incident neutron energy exceeding the threshold energy for the reaction with the target nuclei. Therefore the higher the incident neutron energy the greater the probability of an interaction occurring taking into consideration the cross-section for the particular reaction. Inelastic scattering is generally dominant at neutron energies above 1 MeV for elements of moderate to high mass number, however, for elements of low mass number the threshold energy for inelastic scattering is higher.

Neutrons in thermal equilibrium with the target nuclei tend to undergo radiative capture (n,γ) with the nuclei. Prompt gamma rays are emitted within about 10^{-14} s on the capture of the thermal neutron. The compound nucleus formed if unstable will in general decay preferentially by emitting β negative particles. If the emission of the β particle does not take the nucleus to the ground state then de-excitation takes place with the emission of delayed gamma rays to the ground state of the nucleus. A competing process to delayed gamma ray emission is the emission of conversion electrons. A sketch of the radiative capture process is given below:

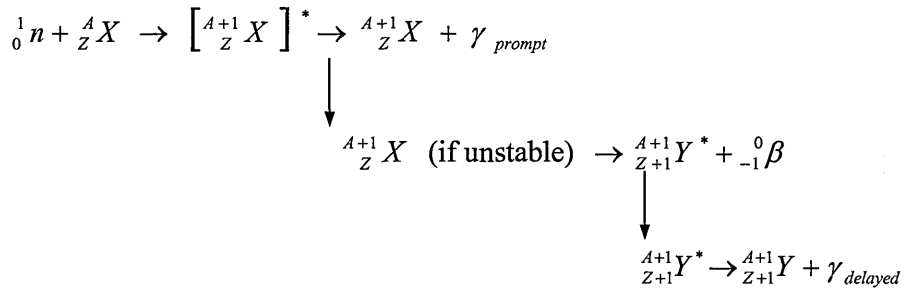

Fig. 2.4: Schematic representation of radiative capture process

2.5 Neutron dose to tissue

Neutrons constitute the most important radiation for which protection considerations must take into account not only radiation quantity but also radiation quality. Gamma-rays, x-rays and electrons of energies in common use produce substantially equal biological effects for equal doses. However, the relative biological effectiveness and the quality factor of neutrons are much higher and energy dependent. The differences in biological effects of radiation are related to differences in the linear energy transfer (LET) of charged particles produced in neutron interactions that deliver the dose. In Table 2.1 the quality factors (Q) for several types of radiation are shown where the dependence of the quality factor on neutron energy is evident.

Table 2.1: Quality factors for several types of radiation

Radiation type	**Quality factor (Q)**	**Neutrons energy**	**Quality factor (Q)**
Gamma-rays	1	<10 keV	5
X-rays	1	10keV to 100 keV	10
Beta particles:	1	100 keV to 2 MeV	20
Electrons	1	2 MeV to 20 MeV	10
Positrons	1	> 20 MeV	5
Protons	5	-	-
α-particle	20	-	-
Recoil nuclei	20	-	-

Neutrons interact with the human body and deliver energy to it through elastic and inelastic collisions with the nuclei, and through secondary radiation emitted by the radionuclides produced after neutron capture. If an individual is exposed to fast neutrons, most of the energy transfer takes place through elastic collisions with hydrogen (approximately 90%) and to a lesser extent through collisions with oxygen and carbon nuclei. The average energy of the loss per collision with hydrogen, a proton, is approximately 50% of the incident neutron energy; the corresponding fractions for carbon and oxygen are 14% and 11% [Tso95]. These recoil nuclei are charged particles which lose energy as they move and slow down in tissue. This is true for neutron energies down to 20 keV [Tso95]. At neutron energies much lower than 20 keV, the importance of elastic collisions decreases and the reaction $^{14}N(n, p)^{14}C$ produces more significant effect. This exothermic reaction produces protons with kinetic energy of 584 keV and also radioactive ^{14}C is produced emitting betas with a maximum energy of 156 keV. Therefore the biological damage is mainly due to the protons and not the β-particles of ^{14}C. Thermal neutrons are absorbed in the body mainly through the reaction $^{1}H(n,\gamma)^{2}H$ with the emission of prompt gamma-rays of energy 2.223 MeV. Of some importance is the reaction $^{23}Na(n,\gamma)^{24}Na$. The ^{24}Na isotope produced has a half-life of 15 hours and on β minus decay emits two energetic gamma rays with energy 1.37 and 2.75 MeV. Thus when thermal neutrons are absorbed, damage is caused by the gamma rays that are emitted as a result of neutron capture.

2.6 Materials in neutron detectors

Most active neutron detectors have either of the following as the target material for the in-coming neutron to interact with: boron, lithium, or helium (all 1/v absorbers) and most recently a combination of lithium, boron and gadolinium. Lithium and boron give off alpha particles and ions on capture of slow neutrons that can be detected directly. The thermal neutron cross of these elements is very large, 3840 and 940 barns for ^{10}B and ^{6}Li respectively. However, like ^{3}He the cross-section value drops rapidly with increasing neutron energy and is proportional to 1/v, where v is the neutron velocity. The thermal neutron cross-section for ^{3}He reaction is 5330 barns but the physical state of the material and the high cost are major drawbacks in some applications. Gadolinium has one of the largest known thermal neutron cross sections of 255,000 barns in the ^{157}Gd isotope. This isotope forms about 15.7% of the natural gadolinium and neutron absorption results in prompt reaction products that include gamma rays and conversion electrons. It is the direct emission of the fast conversion electrons that is made use of in neutron detection. The most significant of the conversion electrons (72 keV) are emitted in 39% of the neutron capture reactions. They have a range of about 20 μm

so typically gadolinium containing layers of about this thickness is employed as a converter of incident neutrons into fast electrons that can then be recorded. The conversion efficiency can be as high as 30%, much higher than 1% and 3-4% of ^{6}Li and ^{10}B layers respectively. A new neutron detector based on a combination of lithium, gadolinium and boron is in the developmental stages [Cza02] and has great potential in neutron detection. Section 3.2 of chapter 3 gives some more information on this type of neutron detector which was investigated for this work.

2.6.1 Neutron detection by scattering

The most common method of fast neutron detection is based on the elastic scattering of neutrons by light nuclei. Since protons and neutrons have about the same mass, a neutron may in one collision transfer on average half its energy or most of its kinetic energy to the proton. The most popular target is hydrogen since the cross section of neutron elastic scattering for hydrogen is quite large and its energy dependence is well known. Recoil protons are relatively easy to detect and serve as the basis for a wide variety of fast neutron detection.

Organic scintillators have proven to be excellent fast-neutron detectors because they have high and known efficiency of detection, good energy resolution and low sensitivity to gammas [Kno00]. The high efficiency is due to their high hydrogen content (1.1 hydrogen atoms per carbon atom, density about 10^3 kg/m^3) and the relative high hydrogen cross section, 2.5 barns for 2.5 MeV neutrons. Organic scintillators are the main detectors used for neutron spectroscopy from approximately 10 keV to 200 MeV [Bro79]. The NE series in particular NE 213 has been extensively used to detect fast neutrons [Bro79, Nor84]. The scintillator commonly used consists of xylene, activators, the organic compound POPOP (wavelength shifter) and naphthalene which improves light emission. The density of NE 213 is about 870 kg/m^3 and composed of carbon and hydrogen with a formulation $CH_{1.21}$. The NE 213 is the fast neutron detector component of the Neutron Probe discussed in section 3.2 of chapter 3.

2.6.2 Neutron detection by moderation

The detection of fast neutrons is also achieved by 'slowing down' or moderation before detection. The incident fast neutron can then lose a fraction of its initial kinetic energy before reaching the detector as a low energy neutron for which the detector efficiency is generally high. For an optimal thickness of the moderator detection efficiency is high. A neutron may

be absorbed within the moderator before it has the chance of reaching the detector. The moderator of choice is made of hydrogenous material such as polyethylene or paraffin wax, with the optimum thickness ranging from a few centimetres for keV energy, up to several tens of centimetres for neutrons in the MeV energy range. Bonner Spheres with a small lithium iodide scintillator or activation foil placed at the centre of polyethylene moderating spheres of different diameter is an example of a moderating detector. By measuring the count rate with each sphere individually, an unfolding process can in principle provide some information about the energy distribution of the incident neutron [Kno00].

By moderating a neutron before detection, eliminates almost all information about the original energy of the fast incident neutron. Also the detection process through moderation is relatively slow. Such detectors cannot provide a fast detection signal in many neutron detection applications. If the neutron energy is not far less than or not a significant fraction of the Q-value of the reaction, measurement of the reaction product energies will give the neutron energy by subtraction of the Q-value. The detection process can be fast because the in coming fast neutron will typically spend no more than a few nanoseconds in the active volume of the detector, and only a single reaction needs to occur to provide a signal for detection.

2.7 Neutron detection by activation

Neutron measurement can be carried out indirectly through the radioactivity that is induced in some materials by neutron interaction. The material is exposed to a flux of neutrons for a period of time and removed so that the induced activity can be counted. The induced radioactivity can then be used to deduce information about the flux and or energy distribution of neutrons in the original field. To achieve a high degree of sensitivity, materials are chosen which have a large cross-section for a neutron-induced reaction, which leads to a measurable form of radioactivity. Because the mean free path of neutrons in materials of high cross-section is quite small, the thickness of material is kept small to avoid perturbation of the neutron flux under measurement. The half-life of the induced activity should be neither too short, nor too long. For many applications, a value of a few hours is near the optimum because of the convenience to irradiate and count induced activity in a reasonable time. Long half-lived radionuclides require a relatively longer period of irradiation in order to achieve measurable activity and the specific activity becomes smaller with increasing half-lives. The radiative capture reaction, (n,γ), typically has the largest cross-sections at thermal energies and therefore materials in which this reaction predominates are preferred for slow neutrons.

Very high purity materials are used for neutron detection to avoid interference from other neutron-induced reactions.

2.7.1 The activation equation

The schematic process of neutron radiative capture has been given in section 2.4 and will be referred to in the derivation of the general neutron activation equation. Neutron activation analysis can be used to determine the elemental composition of materials or to measure the neutron flux if it is unknown. Consider mono-energetic neutrons in a neutron beam of density n and velocity v incident on a material of atomic weight A_w. The number of neutrons falling per unit area per unit time on the target $nv = \phi$ the neutron flux.

The reaction rate per unit area of target is given by

$$\varphi\sigma N_v dx \tag{2.3}$$

where, dx is the thickness of the material and N_V is the number of nuclei per unit volume of target element given by $N_v = \frac{\rho N_{AV}}{A_w}$, N_{AV} is Avogadro's number equal to 6.022169E+23 atoms/mole. In reality not all the neutrons incident on the target material will interact with the material since the reaction depends on the interaction cross-section σ of the target. The total reaction rate of element X is thus equal to

$$\frac{\varphi\sigma\rho V N_{AV}}{A_w} \tag{2.4}$$

From fig. 2.4, the total reaction rate for isotope ${}^{A}_{Z}X = \frac{\varphi\sigma m N_{AV} f}{A_w}$, where f is the isotopic abundance of the isotope of interest, ${}^{A}_{Z}X$.

If a radionuclide is produced in the process, it will start to decay just as it is formed. The activity of the radionuclide formed is λN_{A+1}, where λ is the decay constant of radioisotope ${}^{A+1}_{Z}X$. The rate of production of ${}^{A+1}_{Z}X$ is equal to the difference in the production and decay of the radioisotope. This also represents the growth in activity in the isotope for the element of atomic weight A_w. Therefore the reaction rate in conventional activation analysis is given by

$$\frac{dN_{A+1}}{dt} = \varphi\sigma N_{AV} - \lambda N_{A+1} \tag{2.5}$$

For an irradiation time t_i the induced activity of the isotope can be calculated by integrating the expression above to give,

$$N_{A+1} = \frac{\varphi\sigma N_{AV}}{\lambda}(1-e^{-\lambda t_i}) \tag{2.6}$$

In terms of activity at the end of the irradiation;

$$A_i = \lambda N_{A+1} = \varphi\sigma N_{AV}(1-e^{-\lambda t_i}) \tag{2.7}$$

After irradiation, the foil or sample is transferred for counting after a waiting time t_w and so the activity of the isotope after this period is $A_w = A_i e^{-\lambda t_w}$ and the activity at the end of counting is given by

$$A_c = A_i e^{-\lambda(t_w+t_c)} \tag{2.8}$$

The total number of particles produced in conventional activation analysis is the combination of A_i, A_w and A_c that is:

$$N_{A+1} = \frac{A_i}{\lambda}(A_w - A_c) \tag{2.9}$$

Hence

$$N_{A+1} = \frac{\varphi\sigma N_{AV}}{\lambda}(1-e^{-\lambda t_i})e^{-\lambda t_w}(1-e^{-\lambda t_c}) \tag{2.10}$$

The gamma-ray detector response (the number of photons detected for the gamma-ray energy of interest) is thus given by

$$D_d = \frac{\varepsilon_\gamma I_\gamma \varphi\sigma N_{AV} mf}{\lambda A_w}(1-e^{-\lambda t_i})e^{-\lambda t_w}(1-e^{-\lambda t_c}) \tag{2.11}$$

where ϵ_γ is the absolute efficiency of the gamma-ray detector for the gamma-ray energy of interest and I_γ is the branching ratio of this delayed gamma ray of interest. Knowing the detector response enables the determination of the neutron flux, if all other factors are known.

2.7.2 Correction factors

For accurate application of the activation technique in quantitative measurements of neutron fluxes, correction factors have to be applied. The resulting count of an irradiated foil should be corrected in order to obtain the counts proportional to the unperturbed flux. Correction is required for neutron self-shielding, flux depression and foil edge effect. In a diffusing medium, the neutron flux in the immediate vicinity of the foil will be depressed due to the fact that some neutrons have been removed in their passage through the foil. This is applicable in a phantom or enclosure but generally, not in air. Also, the effective neutron flux at the centre of the foil will be less than that at its surface due to attenuation or self-shielding. These effects are minimised by keeping the foil very thin, however, the induced activity may be so low as to create measurement difficulties.

2.8 Photoneutron measurement

In order to protect patients, radiation therapy workers and the public in the vicinity of a linac treatment room from leakage radiation generated by medical electron linear accelerators, various national and international bodies such as the US NCRP (National Council on Radiation Protection and Measurements) and IEC (International Electrochemical Commission) recommend dose limits for radiation leakage. Therefore, it is absolutely necessary to measure doses due to photoneutrons in (γ, n), (γ, 2n) etc reactions with the materials of the linac head as previously discussed. Such measurements are difficult to perform due to the extremely intense electron and photon fields and also because detectors largely insensitive to these types of radiation are required. It is highly improbable to use active detectors such as the N-Probe as the readings would be perturbed by primary radiation and also the inconvenience in reading the dose even if a closed circuit television (CCTV) camera is focused on the dial of the meter. Consequently, such measurements are usually performed using passive detectors or dosemeters, for example, with activation pellets, which may or may not be placed inside a moderator or with thermoluminescence dosemeters placed inside moderators. The shortcomings of these types of dosemeters are their large size and more importantly the photon-induced reactions within them. Phosphorus pentaoxide, which has been used by a number of researchers also generates neutrons through photonuclear reactions but to a much lesser extent. NCRP Report 79 [NCR84] outlines various different methods for measuring photoneutrons mostly using neutron activation analysis and gives a summary of results obtained by some workers.

2.8.1 Activation detectors

Activation detectors have been widely used to measure photoneutrons generated in medical linacs. Several workers have used this method including Axton and Barbell [Axt79] who used gold foils placed in the centres of 20 and 25 cm diameter polythene moderator spheres and calibrated at two different energies to determine the neutron dose equivalent of a 35 MeV betatron. Fenn and McGinley [Fen95] used a 15.2 cm diameter paraffin wax moderator and 25.4 cm Bonner sphere both with an indium foil located at its centre to estimate the neutron fluence within and outside, respectively of a GE Saturne acccelerator operated at 12, 18, 15, and 25 MV photon energies. The in-beam paraffin moderator was housed in a cadmium thermal neutron shield to eliminate any response produced by slow neutrons. The points of measurement were in the patient plane at 100 cm source-to-skin distance (SSD) and a field size of 20x20 cm^2 for in-beam and also with the collimators (X and Y jaws) closed for all cases outside the beam. A similar procedure was used by McGinley et al [McG93] to estimate the neutron dose of Philips SL-25 and SL 20 accelerators with nominal end point electron energy of 25 MeV and photon energy of 20 MV, respectively.

These detectors are based on the principle of detector material becoming radioactive when bombarded with neutrons as discussed in section 2.7. This radioactivity is the consequence of absorption reactions; (n,p), (n,α), (n,γ) or (n,2n) type reaction, fission reactions or spallation reaction. Neutron dose equivalents are deduced from the fluence rates determined from specific activity measurements of the bombarded material. NCRP Report 79 [NCR84] and that by Palta et al [Pal84] elaborate further on the use of activation foils in photoneutron detection in medical linacs. Some of the disadvantages associated with activation detectors emanate from the reactivity produced by the intense gamma field with the activation foils to produce neutrons through (γ,n), (γ,2n), (γ,p), (γ,np) reactions. This can lead to errors in the neutron dose determination and has been quantified by Allen and Chaudhri [All91]. It was concluded that the error due to photonuclear reactions is of the order of 30 to 60% for aluminium pellets at 23 MV photon energy and of the order of 2 to 4% for P_2O_5 powder at 25 MV photon energy. They also evaluated an error of 39% for indium in a paraffin moderator sphere at 33 MV photon energy and 17 % for gold in a polyethylene cylinder. Some of the activation products may have relatively short radioactive half-lives for example aluminium ($^{27}Al(n,p)^{27}Mg$, half-life of 9.46 min), requiring very rapid sample counting on site [Ash90].

2.8.2 Phosphorus penta-oxide (P_2O_5)

Phosphorus is used in activation analysis in the form of P_2O_5 powder placed into a small vial. The vial 1.2 cm diameter by 3.5 cm high usually contains on the average 2.5 g of P_2O_5. The irradiated powder is later dissolved in water, then mixed with a scintillation cocktail and counted in a liquid scintillation spectrometer because the activation products ^{31}S and ^{31}P are essentially pure beta (β) emitters. This technique leads to counting efficiencies of 95% for ^{31}Si and 97% ^{32}P [Pri78] through the reactions $^{31}P(n,p)^{31}Si$ ($T_{1/2}$ = 2.62h) and $^{31}P(n, \gamma)^{32}P$ ($T_{1/2}$ = 14.28d), respectively. The former reaction is sensitive to fast neutrons above 0.7 MeV and the latter is significant for thermal neutrons only. These detectors are to some degree sensitive to photons as reported on Sagittaire 25 MV x-ray linac [Pri78] and in the Saturne 43F linac beam [Bou97]. Loye et al [Loy99] and Bading et al [Bad83] used this detector to determine neutron component in the output of 18 MV photon linacs and in addition, Loye et al compared this detector with bubble detectors. There are no direct photonuclear interactions which will produce these isotopes, however, photon contamination is possible due to a two step process: [γ,(n,pn or 2n)] in the phosphorus or oxygen followed by $^{31}P(n,p \text{ or } \gamma)$ reaction [Pri78]. Notable sources of error of this method are the preparation of the cocktail and the fact that intermediate energy neutrons are not accounted for.

2.8.3 Thermoluminescence detectors (TLD)

A pair of lithium fluoride detectors, the first ^{6}Li enriched and a second made of ^{7}Li enriched has been used by a few workers including Anderson and Hwang [And83] and Veinot et al [Vei98] to determine photoneutrons from linacs. These detectors are placed inside an appropriate dimensioned hydrogenated moderator. The variation in the fluence response of the detector as a function of neutron energy is similar to the variation in the conversion factors giving the dose equivalent per unit fluence [And83]. Some disadvantages associated with this form of neutron detection is the determination of neutron dose by subtraction which imposes limits on the photon doses recorded by the detector, and also measurements in the primary beam cannot be made with this sort of detector. The detector is voluminous, that is, it is housed inside its moderator such that radiation homogeneity must be accounted for. There is also the possibility of a (γ,n) reaction taking place in the moderator.

2.8.4 Etched track detectors

Etched track detectors are based on the microscopic radiation damage tracks formed in solids, which have been irradiated with heavy particles. When the solids are etched, the tracks are etched much faster than the undamaged portions and become visible under a microscope

[You58]. Tracks can be made visible in a variety of dielectric materials including minerals, natural and artificial inorganic glasses, and especially organic polymers, which have proven to be considerably more sensitive than the inorganic detector. Etched track detectors have been used to measure fast neutron dose around medical linear accelerators by several workers including Kerkim and Robinson [Ker72] and Sohrabi and Morgan [Soh79]. They have also been used in combination with other neutron detectors to measure photoneutrons around medical linacs using the multi-elemental nuclear track detector based on the CR-39 polymer [D'Er01, She88]. A drawback associated with this type of detector is that defects such as cracks or scratches will be amplified and counted as neutron tracks. Also their sensitivity to photon radiation increases with increasing photon dose, which is a disadvantage in a very intense photon field such as the output of linacs.

2.8.5 Superheated drop detectors (SDDs)

First described by Apfel in 1979 [Apf79] the bubble or superheated drop detectors have become prominent in neutron dose measurements. The bubble detector consists of a plastic vial or tube in which thousands of superheated liquid drops are dispersed in a holding polymer or gel medium. The droplets vaporise when exposed to high LET recoils from neutron interactions and the number of bubbles is proportional to the neutron dose equivalent received by the detector. Unique for this dosemeter is the high sensitivity up to a few bubbles per μSv. The detector is read directly by the naked eye; costly measurement equipment is therefore not required. The detector is insensitivity to electrons and γ-radiation as electrons and photoelectrons have stopping powers insufficient to induce phase transitions [Che95]. They are relatively small and therefore homogeneously irradiated and are also insensitive to intense electric fields and can thus be used in pulsed fields.

The results of measurements made with bubble dosemeters do not require any interpretation: doses can be determined by counting the number of bubbles generated and multiplying by a dose equivalent number of bubbles conversion factor. On the contrary, other measurement techniques often lead to results which can be difficult to interpret mainly because of the unknown neutron spectra and difficulties encountered in deciding the quality factors that should be applied to spurious photonuclear reactions [Bou97]. Nath et al [Nat93] performed an inter comparison for which a Monte Carlo code was used to interpret measurements made at the isocentre for 25 MV photons. Bourgois et al [Bou97] deduced that for photon energies higher than 15 MV from the same linac, bubble detector measurements systematically give values lower than those determined by other methods. This was attributed

to the fact that as other methods employ moderators, significant over estimations may be due to photoneutrons generated in the moderators. Such an over estimation demonstrates that (γ,n) reactions in voluminous detectors lead to systematic errors, which increase with increasing photon energy.

The demerits of bubble dosemeters are very few and can be controlled. It is only reasonable to count less than about hundred bubbles with the naked eye. This has been overcome by the use of a calibrated pipette by Apfel Enterprises as corresponding displacement to record the volume created by the bubbles. The dosemeter is temperature sensitive, implying a stable ambient temperature is required to function well. This is achieved by performing measurements in temperature-controlled rooms such as the air-conditioned or air-controlled rooms where most linacs are operated. The dosemeters are relatively expensive even if they can be reused several times. These are the dosemeters with which the majority of the present work was carried out.

3. Bulk sample neutron activation analysis and Monte Carlo simulation.

3.1 Introduction

The general theme of this work has been to determine the neutron contamination in the output of medical linear accelerators using Monte Carlo calculations (MCNP code) [Bri01] and experiments. In order to ensure that the output of the MCNP simulation was valid, a simulation of an isotopic (^{241}Am-Be) irradiation facility was carried out for the purpose of comparison of the output with experimental measurements using the Neutron Probe and a new neutron-sensitive inorganic scintillator, lithium gadolinium borate, the LGB detector [Mas83, Czi02]. This procedure was also used: to test the possibility of using neutron dosimeters and detectors in measuring photoneutrons to correlate computational and theoretical values and to gain some experience in neutron activation analysis.

The ^{241}Am-Be irradiation facility has been in use for over 20 years in the Physics Department mainly to determine elemental concentrations of bulk biological and environmental samples that cannot be irradiated in a reactor. This system has the capability of undertaking prompt, conventional and cyclic activation analysis and has been used by various workers including Matthews [Mat79], Nicolaou [Nic83], Ashrafi [Ash90] and Alamin [Ala95]. The latter two improved the system by incorporating computer control systems for precise and accurate irradiation and acquisition timing parameters.

In this work, the Monte Carlo Code has been used to model the irradiation facility and experimental set up. A rectangular water phantom placed in two orientations was considered in the simulation with emphasis on scattered and transmitted neutrons from the phantom. The results are compared with experimental data obtained using the Neutron Probe and LGB detector. The one problem associated with determination of elemental composition of bulk samples is the distribution and energy of neutron flux in the bulk and comparator samples. Based on the outcome of the comparison

between simulation and experiments, the variation of neutron energy spectrum and neutron dose with depth into the sample was estimated.

3.2 Irradiation facility

The irradiation facility incorporates a 1.85E11 Bq (5Ci) ^{241}Am-Be neutron source designed and built to be used for prompt, conventional and cyclic activation analysis by Spyrou and collaborators [Spy81, Mat80, Nic83] and subsequently modified by Ashrafi [Ash90] and Alamin [Ala95] by incorporating computer control of the source movement. The system consists of two domestic water tanks assembled as shown in figure 3.1 to provide biological shielding. A Perspex tube of length 1.07 m with an inner diameter of about 50mm runs through the central long axis of the larger tank. The source can be moved between the irradiation and shielding positions with the aid of compressed air. Additional small water tanks placed two on each side of the large water tank to provide extra shielding from neutrons. The source stops at the irradiation end which consists of an iron plate with a circular hole the diameter of which is 10 mm less than that of the Perspex tube. Covering the iron plate is boron clay to absorb neutrons. Powdered Li_2C0_3 in a Perspex box acts as a neutron shield and is placed in front of the neutron source. The gamma-ray detector is encased in a Li_2C0_3 shield to protect it from damage due to neutrons and has a lead collimation. Detailed description of the facility is outlined in Spyrou and Matthews [Spy80].

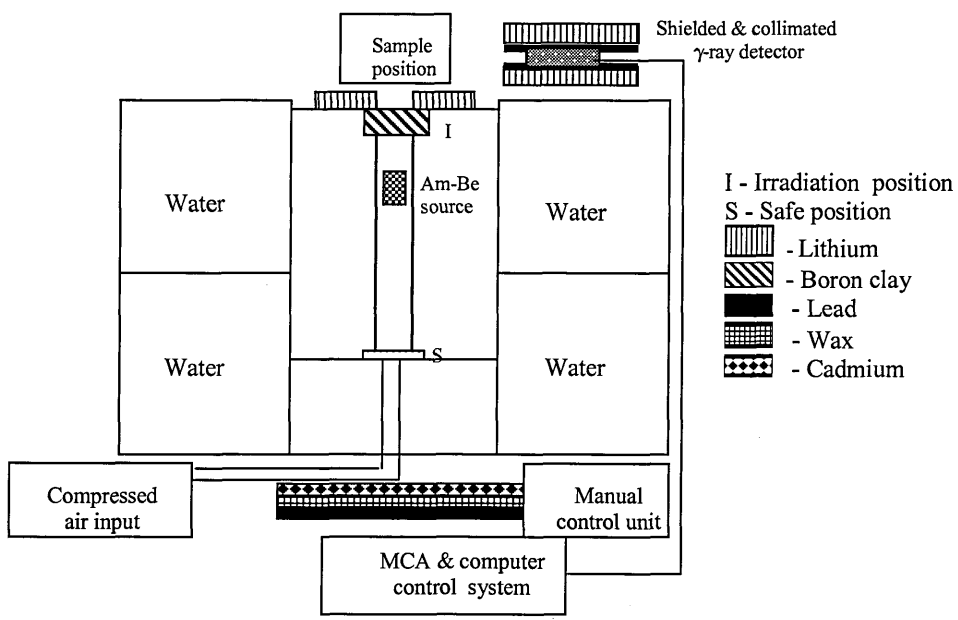

Fig.3.1 A block diagram of the irradiation facility

3.3 Operation of irradiation facility

3.3.1 Computer control of source movement

The system can be operated in two modes, manual and computer programmed. Prompt and conventional irradiations may not necessarily require for long irradiations and acquisition times extremely accurate and reproducible timing of the movement of the source to and from the irradiation and 'safe' positions. In contrast, cyclic activation requires accurate timing parameters and fast response. This has been achieved with the aid of micro switches and an input/output card in a computer (PC) which controls the source movement. During cyclic activation analysis, the sample is irradiated for a relatively short period governed by the half-life of the element of interest, followed by a much shorter time of measurement and then followed by another irradiation. The source is moved to the safe position during measurements after which another cycle of irradiation begins. A complete cycle includes irradiation, waiting and measurement times and has been investigated by Nicolaou [Nic83] to be of the order of 10 seconds for half-lives of 15 – 20 seconds and even as short as 1 – 2 seconds for half-lives of fast decaying isotopes. It is clear that such times can only be achieved with a computer system and reproduced to within ± 1ms.

3.3.2 Manual control of source movement

In the absence of suitable computer software and hardware to ensure more accurate source movement, the system can also be operated manually. A manually controlled panel is incorporated in the overall system that has the facility to move the source to and from the irradiation position. On this panel is a timing device that can be set to control the source during cyclic activation but is obviously not suitable for very short cyclic times. Delayed activation analysis is basically suitable for elements with relatively long half-lives such that after irradiating the sample there is a considerable waiting time period between irradiation and measurement. The sample does not necessarily need to be in the irradiation position for measurements to be carried out with the source in the safe position. For our tests, comprising long irradiations (30min–90min), prompt gamma activation analysis (PGNAA) required the source to be in the irradiation position during the entire process of irradiation and data acquisition. Therefore, in this work the source was manually controlled between the irradiation and safe positions.

The source movement is achieved with the aid of compressed air connected to the source through a flexible tube. The optimum operating pressure required to move the source to and from the irradiation position was observed to be 2 bars (kg/m^2). Below this pressure the possibility of the source getting stuck in the Perspex tube is very high. To prevent any radiation mishap, the pressure gauge was constantly monitored and adjusted when necessary. During prompt activation analysis data acquisition is on-line as such the gamma detection system is placed at a position such that the field of view of the detector can intercept the resulting gamma produced by the de-excitation of the elements of interest. The on-line gamma ray detector position is as shown in figure 1 and is adequately shielded with the lithium containing material as described above. The devastating effect of neutron on germanium is well known and documented by several workers including Chao [Cha93], Chung and Chen [Chu92], Llacer and Kraner [Lla72], and Chasman et al [Cha65].

3.3.3 ^{241}Am-Be neutron source

Table 3.1: Physical properties of ^{241}Am-Be neutron source

Parameter	Value
Half-life	433 years
Mode of decay	A (100%)
Activity	1.85E11 Bq
Neutron emission rate	1.1E7 ns^{-1}
Mean low neutron energy	400 keV
Mean high neutron energy	4.4 MeV
Fraction of neutrons below 1.5 MeV	23%
Photon emissions per neutron	0.7 at 443 MeV from ^{12}C de-excitation 6.0E3 at 60 keV from ^{241}Am
Neutron dose rate at 1 m	110 μSv/hr
Photon dose rate at 1 m	125 μSv/hr

Some of the physical properties of the ^{241}Am-Be source are as shown in Table 3.1. The fraction of neutrons having much higher energies is relatively high compared to ^{252}Cf implying a much greater penetration in bulk samples. With mean neutron energy of 4.4 MeV, the source is ideally suitable for threshold neutron activation analysis of elements above 2 MeV, for example, ^{64}Zn(n,p)^{64}Cu (reaction threshold energy, $E_{th,}$ of 2.8 MeV and half-life of 12.8 h). A disadvantage of this source is the copious amount of gamma rays that accompanies the de-excitation of ^{12}C (4.43 MeV) from the ^{9}Be(α,n)^{12}C and the de-excitation of ^{237}Np (60 and 103 keV) following the

decay of ^{241}Am. One of the advantages of neutron sources such as ^{252}Cf over ^{241}Am-Be is the much lower photon dose rate (about 10 times less). The external dimensions of the cylindrical source are 30 mm diameter and 60 mm long.

3.4 Biological shielding

The shielding of neutrons is achieved with the aid of water in domestic tanks arranged to provide effective neutron shielding. Water has high hydrogen content and neutron having the same mass number interacts about 18 times with a molecule of water compared with carbon or other neutron moderating material. Besides, water is not a hazardous material, it is cheap and readily available. However, prompt gamma rays of energy 2.223 MeV are emitted on the capture of a thermal neutron $^{1}H(n,\gamma)^{2}H$ and thus interfere with gamma ray measurement from elements of interest. This is a prominent peak in all the gamma spectra acquired.

3.5 Prompt γ-ray elemental activation analysis

PGNAA is a rapid non-destructive, instrumental, nuclear technique used for trace and major component analysis of various elements. It is based on the detection of capture gamma rays emitted by a target material while it is being irradiated with neutrons. Nuclei formed in capture have excitation energies equal to the binding energy of the added neutron. The excitation energy is released by emission of gamma rays in the range of 100 keV to 10 MeV. Nearly every neutron capture yields gamma rays that are potentially usable for analysis of the capturing element. However, the energy spectrum of capture gamma rays of most nuclides is fairly complex. The capture gamma rays emitted by shielding material, etc., also complicates the analysis. Therefore, the relative merit of this technique for analysis of a particular element must be reviewed on the basis of each case. The technique is generally capable of performing trace analysis for elements with large neutron capture cross sections, such as H, B, Cd, Sm, and Gd. The technique is also used for elements, which on neutron capture become stable nuclides or nuclides having long half lives. Other elements, for example, S and P, which after thermal neutron irradiation produce radionuclides which are in the main pure beta-emitters, can be detected by using this technique.

3.5.1 Detector response for PGNAA

PGNAA involves on-line measurements of the gamma rays as a result of the de-excitation of isotopes of elements on neutron capture. The detector response obtained by measuring the resulting prompt gamma rays of a nuclide is given by

$$D_p = \varepsilon_\gamma I_{\gamma p} \varphi \sigma_A N_A t_i \qquad (3.1)$$

where N_A is the number of target nuclei of interest in the elemental mass, that is, $N_A = \frac{N_{AV} m f}{A_w}$ and as before, N_{AV} the Avogadro's number {6.02257E23 (g-mole)$^{-1}$}, f is the isotopic abundance of the isotope of interest, m is the elemental mass within the detection volume (related to the photo peak counting rate of the radioisotope) and the atomic weight A_w of the element of interest.

σ_A - neutron reaction cross-section of the isotope of interest in barns

ϕ - neutron flux of the reactor or isotopic source in this case (most nuclear reactors have neutron fluxes up to 10^{12} cm^{-2}s^{-1} compared to 10^6 cm^{-2}s^{-1} for isotopic neutron sources);

$I_{\gamma p}$- the number of prompt γ-rays of interest emitted per neutron captured in the nucleus;

ϵ_γ- absolute detection efficiency of the detector at the γ-ray energy measured and

t_i - irradiation time which is equal to the counting time in this case.

Corrections for photon attenuation within the sample and non-uniformity of neutron flux in the sample should be included in the formula for bulk samples.

3.6 Conventional or delayed activation analysis

Activation analysis is routinely carried out to determine the elemental composition of samples. The sample is irradiated for a selected period of time and then either transferred to another place for counting as with experiments using nuclear reactors or the source retracted to the safe position in the case of our irradiation

facility. The duration of the experiment depends on the radionuclides of interest. The detector response in this case for detection of delayed gamma-rays is given by

$$D_d = \frac{N_{AV} m f \sigma \varphi I_\gamma \varepsilon_\gamma}{\lambda A_w}(1-e^{-\lambda t_i})e^{-\lambda t_w}(1-e^{-\lambda t_c}) \quad (3.2)$$

where all the symbols have been defined in chapter 2 section 2.7.1

3.7 Cyclic activation analysis

As discussed above, cyclic activation is more suitable for short-lived isotopes. These isotopes require successive irradiation and counting sequences in order to accumulate a statistical peak (good signal-to-noise ratio) for the isotope of interest. This is carried out by repeating the irradiation cycle for 'n' times and counting for each period (T) and is given by [Spy80, Spy81]

$$T = t_i + t_w + t_c + t_{w'} \quad (3.3)$$

where $t_{w'}$ is the time taken to transfer the sample back to the irradiation position after counting or the source returned to the irradiation position in the case of our irradiation facility. Therefore, the detector response for the first cycle is the same as that for the conventional activation analysis. For the second cycle, the detector response is the summation of that of the cycle and the residual activity from the first cycle, that is,

$$D_n = D_d(1+e^{-\lambda T}) \quad (3.4)$$

where $e^{-\lambda T}$ is the decayed (residual) activity.

For the n^{th} cycle, the detector response is given by

$$D_n = D_d(1+e^{-\lambda T}+e^{-2\lambda T}+...+e^{-(n-1)\lambda T}) \quad (3.5)$$

or

$$D_n = D_d\left[\frac{1-e^{-n\lambda T}}{1-e^{-\lambda T}}\right] \tag{3.6}$$

The cumulative detector response for n cycles is thus given by [Spy81]

$$D_c = \sum_{i=1}^{n} D_i \tag{3.7}$$

therefore

$$D_c = D_d\left[\frac{1}{1-e^{-\lambda T}}\right]\left[n - e^{-\lambda T}\left(\frac{(1-e^{-n\lambda T})}{(1-e^{-\lambda T})}\right)\right] \tag{3.8}$$

The maximum cumulative detector response for an experimental time, nT, occurs when $t_i = t_c$ and $t_w = 0$. Though these conditions are not feasible in practice, conditions close to these can be attained to maximise the detector response.

Ideally the total experimental time ($T_{tot} = nT$) can be expressed as a multiple of half-life of the isotope of interest, and also the cycle period as a multiple of half-life, that is, $T_{tot} = m\,\tau_{1/2}$ and $T = L\,\tau_{1/2}$ where m and L are integers.

3.8 Experimental work

3.8.1 Objective of experiment

The main objective of this work was to determine the transmitted and scattered neutrons from a water phantom (bulk sample) on irradiation with the ^{241}Am-Be source so that a comparison could be made between experiment and Monte Carlo simulation. The outcome of the comparison would then substantiate the estimation of the neutron flux distribution in the bulk sample. The knowledge of the neutron flux distribution in the bulk sample gives an indication of the attenuation and the extent of interaction of the neutron beam in the sample. Also information about the possible interaction sites and gamma attenuation from the interaction can be predicted.

3.8.2 Water phantom

Ordinary tap water was used for this study forming a homogeneous phantom even though most bulk samples are heterogeneous in nature. A Perspex phantom measuring 15x32.5x15 cm^3 with the top end open was filled with water and placed at the sample position as shown in figure 3.1. Two orientations of the phantom, the 'long' and 'short' width with respect to the gamma ray detector were adopted as shown in figures 3.2a and 3.2b with the simplified irradiation facility.

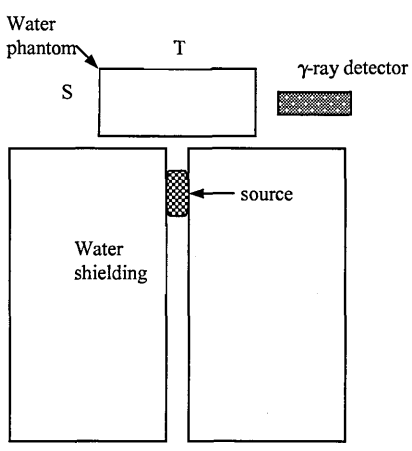

Fig. 3.2a: 'Short' width phantom orientation

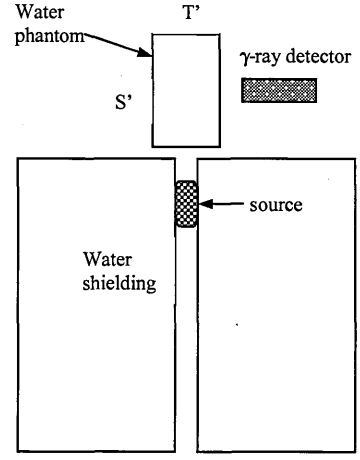

Fig. 3.2b: 'Long' width phantom orientation

3.9 Measurement procedure

3.9.1 Calibration of detectors

The N-Probe and the LGB used for the measurement were borrowed from the Nuclear Department of HMS Sultan, in Gosport. They form part of the collaboration in neutron detection and dosimetry research between the Royal Navy (Prof. P.A. Beeley) and the Department of Physics, University of Surrey (Prof. N.M. Spyrou). These were calibrated at the National Physical Laboratory, Teddington, England, using neutrons in the energy range from thermal to 14.7 MeV produced by a Van der Graaff accelerator irradiation facility. The neutron energies are as shown in Table 3.2 and also included are their targets and reactions. Table 3.3 lists some of the neutron energies used and the corresponding fluence obtained from calibrating the N-Probe and the LGB.

Table 3.2: Neutron energies used to calibrate the detectors and production reaction.

Energy / MeV	Reaction
Thermal	$^{9}Be(d,n)^{10}B$ + graphite moderetion
0.001 – 0.05	$^{45}Sc(p,n)^{45}Ti$
0.05 – 0.63	$^{7}Li(p,n)^{7}Be$
0.63 – 2.8	$T(p,n)^{3}He$
2.8 – 6.0	$D(d,n)^{3}He$
13.5 – 14.7	$T(d,n)^{4}He$

Table 3.3: Some of the neutron energies used and the neutron fluence obtained by NPL for calibrating the N-Probe and LGB.

Device	Energy / MeV	Fluence/ cm^{-2}
LGB (^{6}Li)	0.144	5.84E+5
N-Probe	0.144	1.32E+6
LGB (^{6}Li)	0.565	1.55E+6
N-Probe	0.565	1.11E+6
LGB (^{6}Li)	1.2	2.51E+5
N-Probe	1.2	4.02E+5
LGB (^{6}Li)	2.5	4.39E+5
N-Probe	2.5	4.72E+5
LGB (^{6}Li)	5.0	9.74E+5
N-Probe	5.0	1.35E+6

3.9.2 Microspec-2 N-Probe

The Microspec-2 N-probe is manufactured by Bubble Technology Industries (BTI) as part of its Microspec range of portable instruments. The N-Probe is designed around two standard detector types, an NE213 organic liquid scintillator and a helium-3 detector fitted with a 'boron shield'. They are housed one above the other in a conveniently portable unit, together with their high voltage supply circuits and rechargeable battery. This probe unit connects to the Microspec analyser unit, consisting of an amplifier and 256-channel MCA coupled to an Atari Portfolio palm-top computer with a LCD screen. The operating software is stored together with the acquired data on a 1.0 Mb memory card specific to the Atari Portfolio. Data can be transferred to a PC or printer via a parallel port connection on the analyser unit. The NE213 scintillator covers the energy range 800 keV to 20 MeV according to the BTI literature, while the ^{3}He detector covers energies from thermal to 800 keV. Together the two detectors report the neutron energy spectrum from thermal to 20 MeV in 18 energy groups. Figure 3.3 shows the N-Probe and the palm-top computer. Following the principle of spectral dosimetry, the dosimetric quantities are calculated from the spectrum using the desired fluence-to-dose conversion factors. These are read from a simple text file, and so can be updated as necessary.

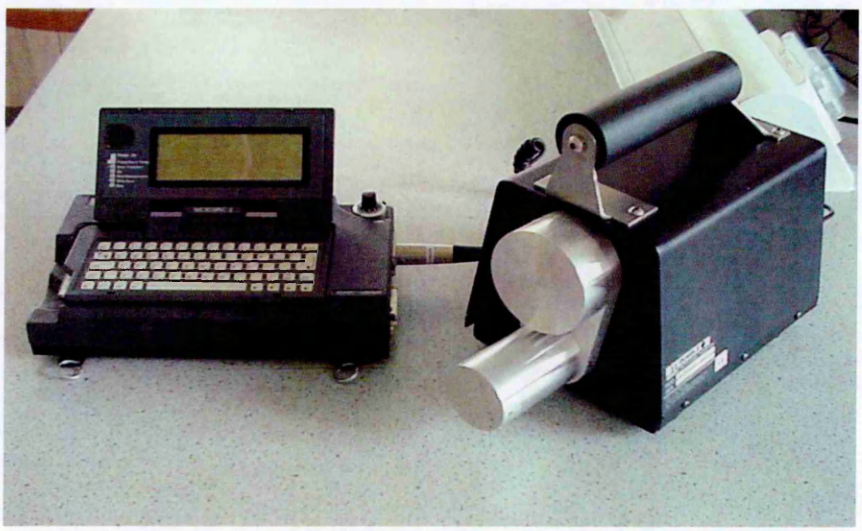

Fig. 3.3: The neutron probe (N-Probe) and Atari Portfolio palm-top computer with a LCD screen. (By kind courtesy of the Nuclear Department, HMS Sultan, Gosport, UK)

3.9.3 Lithium Gadolinium Borate (LGB)

This is a new neutron-sensitive inorganic scintillator that is utilised for neutron detection in capture-gated spectrometers. Lithium, gadolinium and boron all have isotopes with very large neutron absorption cross-section at different energies. The lithium gadolinium borate spectrometer is capable of distinguishing between thermal, epithermal and MeV and also provides the dose rate to a high accuracy [Czi02] with the possibility of high efficiency neutron detection. The crystalline material has an isotopic composition of $^{6}Li_{6}{}^{nat}Gd(^{11}BO_3)_3$:Ce and is incorporated in approximately $100cm^3$ of plastic scintillator, at a concentration of 10% by weight [Czi02]. This is possible because the refractive index of the crystal is 1.66, which is close to that of organic polymers (1.6).

The dosimeter is sensitive to incident thermal neutrons through capture in Gd and to incident epithermal neutrons through capture in ^{6}Li. Gadolinium capture yields approximately 8 MeV of gamma-ray energy, which produces a large, fast signal in the plastic scintillator matrix (5ns decay time). Capture of epithermal neutrons in ^{6}Li produces a mono-energetic slow signal (270ns decay) that is easily distinguished from the Gd-capture signals. An incident MeV neutron interacts first with the plastic scintillator where there are multiple neutron and proton elastic collisions and subsequently by capture at low energy in ^{6}Li. Fast neutrons scatter elastically from hydrogen in the plastic scintillator producing recoil protons. Therefore, fast neutron detection and discrimination against other events occurs on the basis of this "double pulse" signal, a proton recoil pulse followed by a ^{6}Li capture pulse. This is often referred to as "capture gating", since the proton recoil signals are being gated to the output on the condition that, a capture pulse follows. The dual signal from a single incident neutron discriminates against simple gamma background events and yields the neutron energy by summing the multiple signals from the proton collisions. A total of 12 energy bins will be employed when fully implemented, that is, thermal, epithermal, and 10 high-energy bins, to provide the detailed spectral information required for high-precision dosimetry to conform to ICRP recommendations.

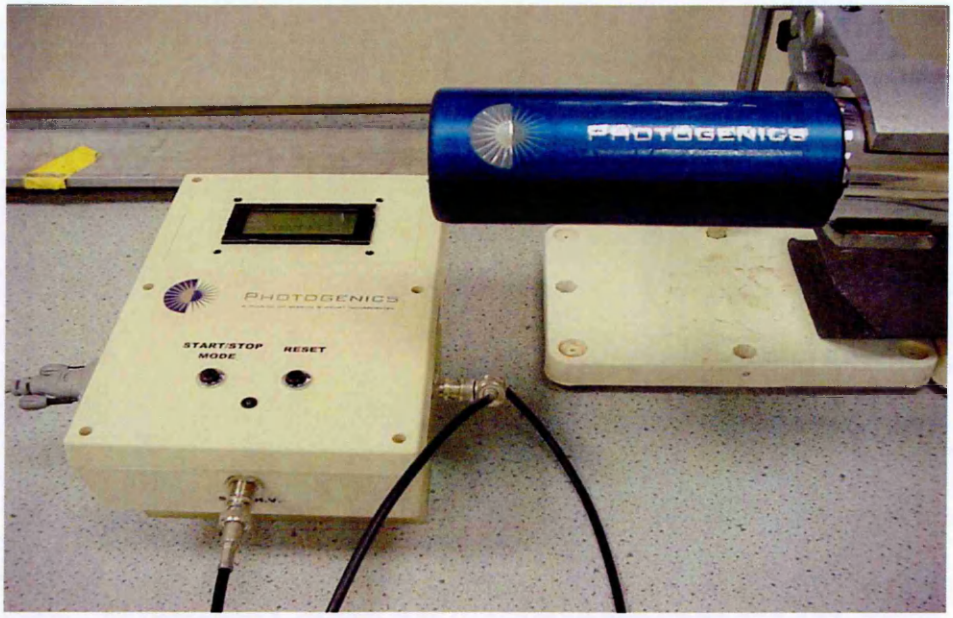

Fig. 3.4: Lithium gadolinium borate (LGB) detector and the Photogenics© digitiser box (By kind courtesy of the Nuclear Department, HMS Sultan, Gosport, UK)

Signals from the detector are fed into a purpose built Photogenics© digitiser box which consists of a fast 8-bit analogue-to-digital converter, ADC, (30MHz, 100MS/s) and logic control on printed circuit board. The pulse area and pulse shape are recorded for each detected particle and sorted into the appropriate classification for processing into the overall dose. Varying the isotopic composition of the capturing nuclei in fabricating this scintillator yields great versatility for various applications. For ~~high~~ low efficiency and ~~low~~ high resolution ^{10}B and ^{7}Li are used due to the high capture cross-section of ^{10}B and its 1/v dependence, and, therefore, an isotopic composition of $^{7}Li_6Gd(^{10}BO_3)_3$:Ce is used. The version used in this work was $^{6}Li_6Gd(^{11}BO_3)_3$:Ce which has a high efficiency and low resolution. Figure 3.4 shows the detector crystal (blue) and the associated Photogenics© digitiser box, display and electronics.

3.10 Experimental procedure

Each detector, the N-probe and the high efficiency type of LGB detector, was placed in front of the water phantom pointing in the direction and along the central axis of the source to determine the incident neutron flux. The detectors were then

placed in turn in direct contact with the sides and the rear of the phantom at the mid-level of the water column. For transmitted neutrons each detector was placed at positions T and T' and positions S and S' for scattered neutrons for the two orientations of the phantom as shown in figures 3.2a and 3.2b. Measurements were taken for the same irradiation time for each detector to ensure consistency and also no simultaneous measurements using the two detectors was carried out due to the complexity of such a set-up for data acquisition and analysis if interference from scattering etc from one detector on another was to be avoided.

3.11 MCNP Simulation

A near replica of the irradiation facility was simulated in order to concentrate on the activities enclosing the sample and the source and also to minimise simulation time and computer space. Dimensions of the irradiation facility were taken and replicated in the simulation. Two water tanks of volume equivalent to the combined volume of the actual water tanks were simulated in order to simplify the geometry. This did not affect the overall outcome of the results but rather reduced the time for simulation using MCNP4C2. It excluded the shielding at the control desk and the parts not directly involved with activities at the irradiation position. Two orientations of the phantom were considered as discussed above and neutron flux (F4) tallies spheres were set at points in front of, the back and on the sides of the phantom at similar positions as in the experiment. These points represented the incident, transmitted and scattered neutron flux, respectively. The variation of the neutron flux with depth in the phantom was simulated by setting F4 tallies in the phantom and also the neutron flux at the gamma ray detector position and shielding.

The Monte Carlo code MCNP4C2 [Bri01] was used to simulate the irradiation facility and was run using a Pentium IV processor at 1.9 GHz and an average of 160 to 200 million particles were simulated. Figures 3.5a and 3.5b are plots (for pz = 0 ie. the x and y plane) of the geometries of the irradiation facility showing the 'short' and 'long' widths of the phantom, respectively. Also shown are the shielding of the source with the boron clay (yellow), lithium powder, and the gamma ray detector shielding and collimation. The rings or circles shown within and outside the phantom are the tally sites and are spherical in shape.

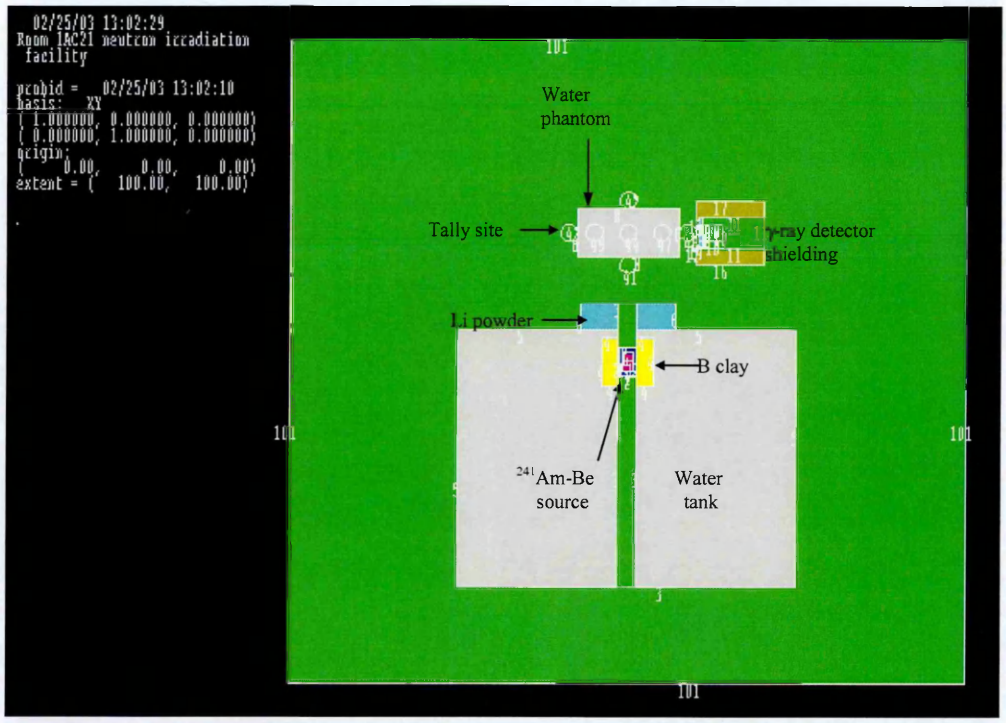

Figure 3.5a: MCNP geometry plot of irradiation facility for the 'short' width phantom orientation.

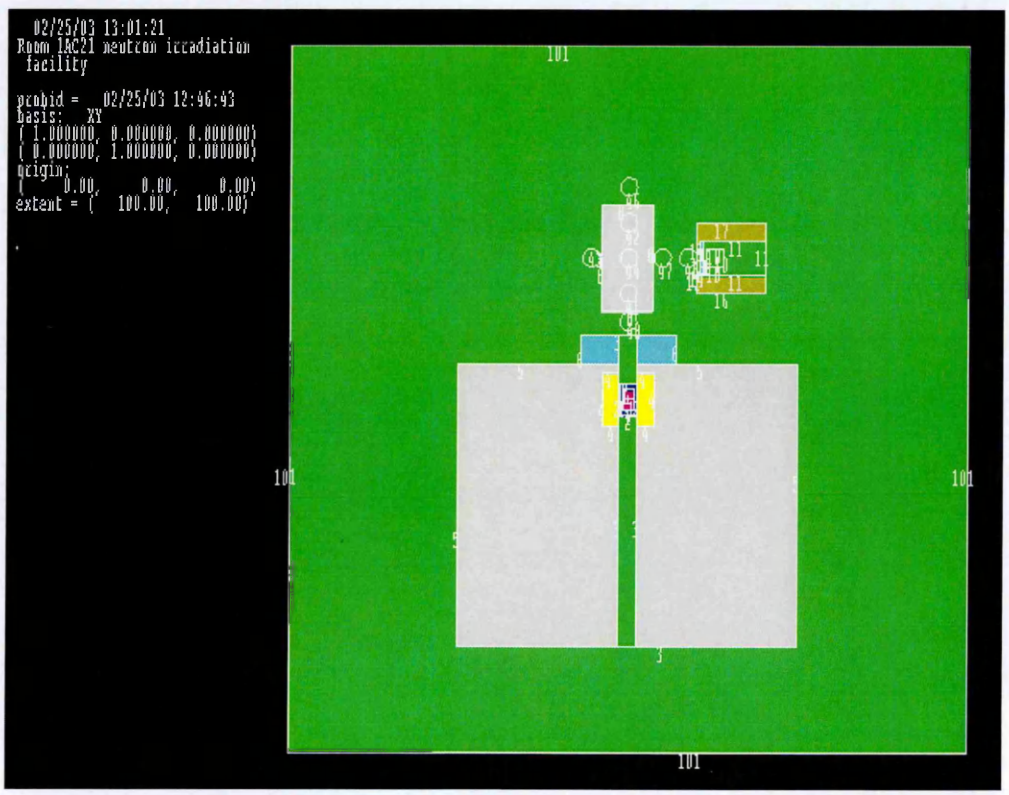

Figure 3.5b: MCNP geometry plot of irradiation facility for the 'long' width phantom orientation.

3.12 Results and discussion

Tally spheres of volume much smaller than the actual size of the N-Probe and the LGB detectors were set for the MCNP simulation to avoid the complex geometry of these detectors. Table 3.4 shows the total neutron flux and the ratios of the transmitted and scattered neutron flux for N-Probe, LGB and those obtained from MCNP tally calculations. Ratios of the total neutron fluxes of the transmitted to scattered neutrons were calculated in order to compare measurement with calculations. The high values of the neutron fluxes for the N-Probe are attributed to the following: these detectors respond to scattered neutrons in the room, from the detector itself and instrumentation and also neutrons reaching the detectors direct from the ^{241}AmBe source. These form a good proportion of the number of neutrons detected and hence the neutron flux. It is also known that the N-Probe is also used to measure photons and therefore the high response could be due in part to the inability of the detector to completely discriminate between photons and neutrons in an environment where there are copious amounts of prompt gamma rays of energy 2.223 MeV from hydrogen, through the reaction $^{1}H(n,\gamma)^{2}H$ in the water shielding on capture of thermal neutrons. In contrast, the MCNP simulation excluded the walls of the room restricting the geometry to a simplified version of the irradiation facility concentrating on the parts directly involved with the irradiation process and also configured a much smaller tally volume sphere than the physical size of the two detectors. This was necessitated by the hard disc space available on the computer for the simulation and also to avoid very long simulation times running into months.

Table 3.4. Neutron flux through the 'short' and 'long' width orientations of the water phantom

Detector	Transmitted (T) Flux /cm^{-2}s^{-1}		Scattered (S) Flux /cm^{-2}s^{-1}		Ratio T/S	Ratio T/S
	Short	Long	Short	Long	Short	Long
N-Probe	1.2E3±25%	1.3E2±20%	3.1E3±30%	2.0E3±30%	0.40	0.06
LGB	5.1E2±20%	1.2E2±15%	1.3E3±20%	1.4E3±20%	0.40	0.08
MCNP	1.79 ± 4%	1.27 ± 3%	23.4± 1.2%	28.7±0.6%	0.10	0.05

The N-Probe and the LGB show approximately the same ratio of transmitted to scattered neutron flux of 0.4±0.02 and 0.4±0.08, respectively for the short width

orientation of the water phantom in contrast to 0.1±0.02 using MCNP simulation. However, the ratios are much closer for the N-Probe, LGB and MCNP in the case of the long width phantom orientation with values of 0.06±0.007, 0.08±0.004 and 0.05±0.001, respectively. There is a much greater agreement between the N-Probe and MCNP which is an indication of some degree of convergence between measurement and calculation in the total neutron flux for the scattered and transmitted neutrons for the long width orientation of the water phantom. In spite of this observation, a further improvement of the MCNP simulation to include the walls of the room and the actual size and structure of the detectors is a necessity for further work. On the other hand, the MCNP simulation without the walls of the room gives an indication of the transmitted and scattered neutron fluxes due mainly to neutrons that emerge from the water phantom.

MCNP calculation for the transmitted neutrons is down by approximately 30% from the 'short' to the 'long' width of the phantom. The neutrons are attenuated to a greater effect due to the fact that the neutrons traverse almost twice the distance compared with the short width and therefore a much greater interaction with the water. There is a relatively much smaller difference approximately 20% between the scattered neutron fluxes using MCNP for both phantom orientations. This is expected since the contribution of the scattered neutrons are mainly from the phantom, a larger surface area will have more scattered neutrons and vice versa. The distribution of neutrons in the water phantom, that is, the neutron spectrum of the transmitted neutrons for the 'long' and 'short' width orientations of the phantom are as shown in figures 3.6a and 3.6b. Measurements using the N-Probe are compared with those obtained by MCNP simulation with each normalised to their respective total neutron flux. The long width phantom orientation shows a much higher estimation using MCNP except for energies less than 10 keV. MCNP simulation accounts for all the neutrons that arrive in the tally sphere. However, there is the possibility that not all the transmitted neutrons interacting with the N-Probe detector material will result in a measurable signal especially in the higher energy range as some neutrons will bounce off the detector. In the lower energy range, the N-Probe response includes scattered neutrons of lower energy in the room and therefore the observed peak value of neutron flux for energies from thermal to 10 keV. There is a much greater agreement

between the transmitted neutron spectra using the N-Probe and MCNP simulation for the short width phantom orientation than the long width.

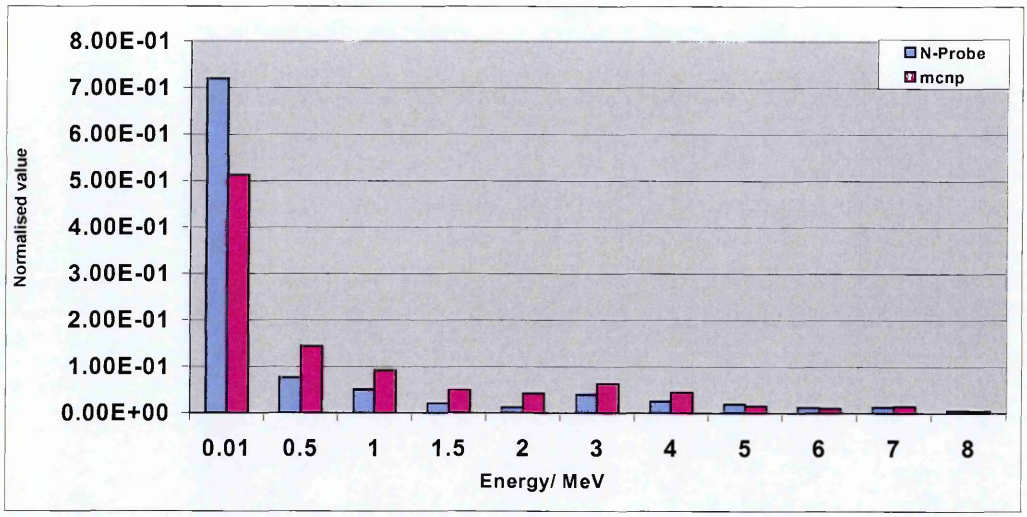

Fig. 3.6a: Comparison of measurement and simulation for the transmitted neutron flux in the 'long' width orientation of the water phantom. These have been normalised to their total neutron flux.

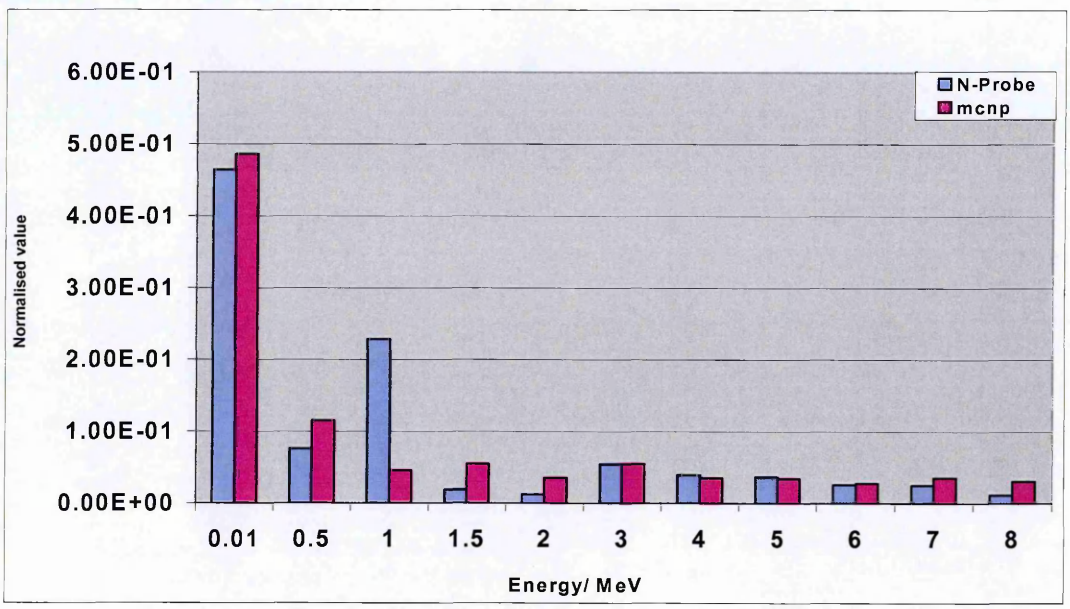

Fig. 3.6b: Comparison of measurement and simulation for the transmitted neutron flux in the 'short' width orientation of the water phantom. These have been normalised to their total neutron flux.

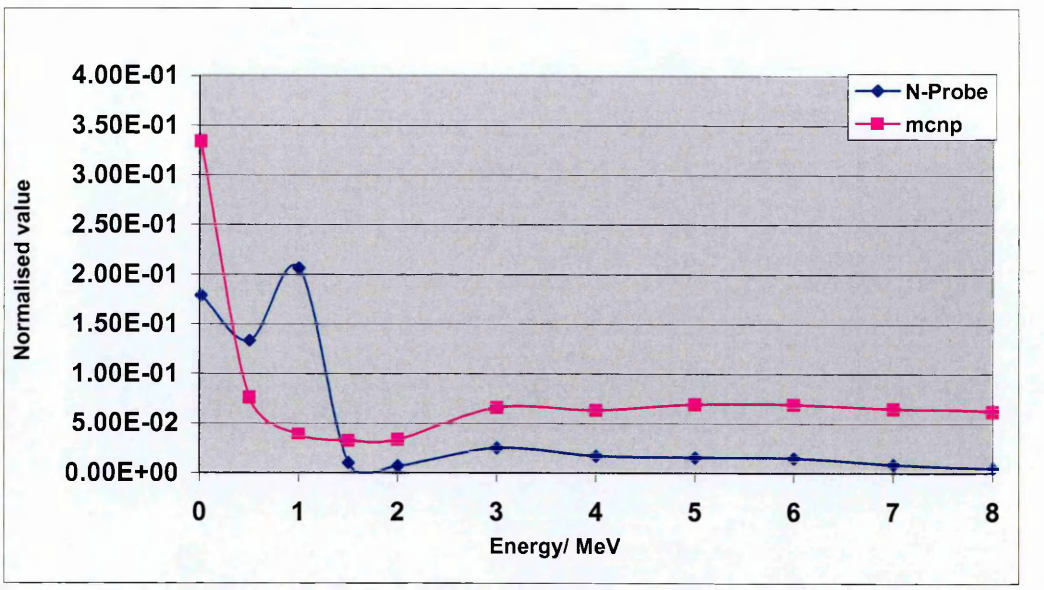

Fig. 3.7a: Comparison of measurement and simulation for the scattered neutron flux in the 'long' width orientation of the water phantom. These have been normalised to their total neutron flux.

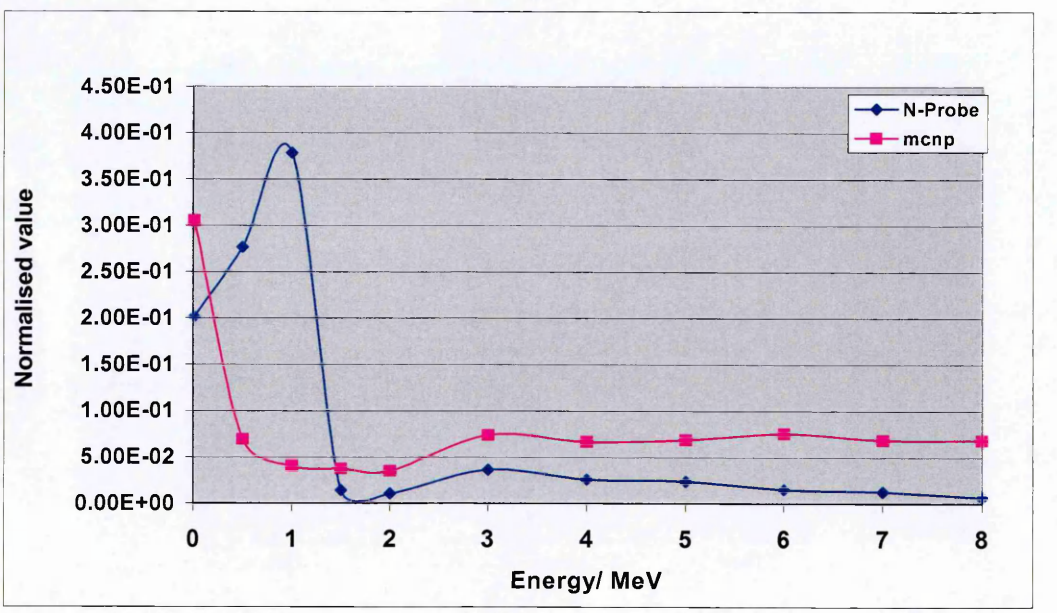

Fig. 3.7b: Comparison of measurement and simulation for the scattered neutron flux in the 'short' width orientation of the water phantom. These have been normalised to their total neutron flux.

There is at best a modest agreement between MCNP and measurement for the scattered neutrons as shown in figures 3.7a and 3.7b. MCNP over estimates the neutron flux at high energies compared to measurement with the N-Probe as observed with the transmitted neutrons. At lower energies the disparity between the two methods grows due to the peak between 0.7 and 1.0 MeV measured with the N-Probe. Most of the scattered neutrons will have energies lower than the mean ^{241}Am-Be source energy of 4.4 MeV. At energies lower than 2.0 MeV the effect of room-scattered neutrons becomes evident hence the resulting peak.

Figures 3.8a and 3.8b show the neutron spectrum in the water phantom in the 'long' width orientation. Three tallies were set and designated front, mid and rear for the front part of the phantom directly facing the source, the middle and the rear part, respectively, as shown in the MCNP geometry plot of figure 3.5b. The neutrons are attenuated to a greater extent by traversing through the phantom as shown by the difference in the peaks for the front, mid and rear profiles in the energy range 1 to 10 keV in figure 3.8a. Figure 3.8b shows the spectrum at each section of the phantom normalised to their total neutron flux, respectively. The neutron spectrum remains virtually unchanged, however, due to the extent of attenuation the neutron beam intensity is much lower on exiting the phantom. The attenuation results from the scattering of high-energy neutrons to lower energies and the subsequent neutron capture with the emission of 2.223 MeV gamma rays in the water phantom.

In the case of the 'short' width the neutron flux distribution is highest in the central part of the phantom as shown in figures 3.9 and 3.10. The abbreviations TD, MD and AD refer to the side of the phantom towards the gamma detector, central section and the section of the phantom further most from the detector, respectively, as shown in the MCNP plot of figure 3.5a. It is quite obvious that a greater proportion the neutrons are concentrated in the central part of the phantom and almost evenly distributed on either side. Also the profile of the neutron spectrum remains virtually the same irrespective of the tally point as shown in figure 3.9b.

The neutron distribution in the 'short' width phantom orientation shows a high concentration of neutrons in the central section of the phantom as shown in figure 3.10. The neutron fall off on both sides of the central section, that is, TD and AD is

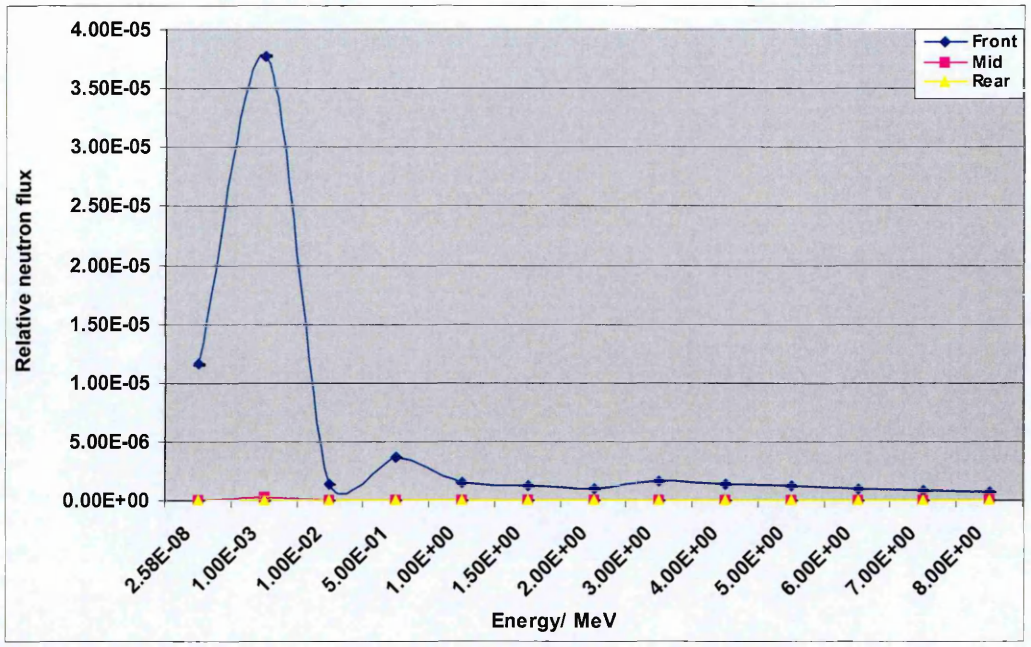

Fig. 3.8a: Neutron spectra in the water phantom at the sections towards the source (Front), central section (Mid), and the rear section (Rear) with the phantom in the 'long' width orientation and calculated using MCNP.

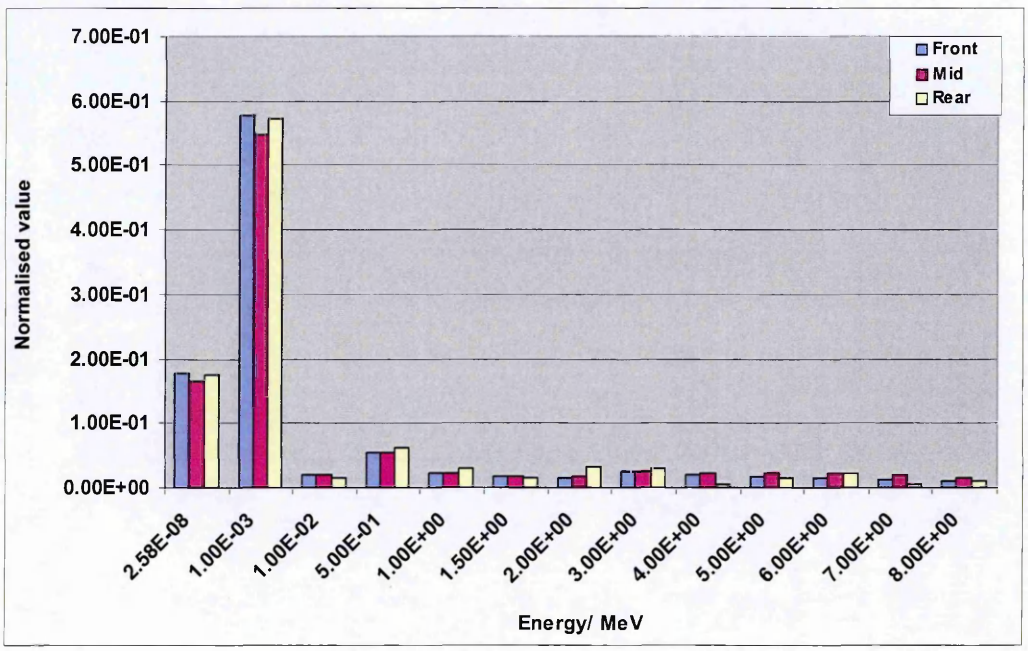

Fig. 3.8b: Normalised neutron spectra in the sections of the phantom towards the source (Front), central section (Mid), and at the rear section (Rear) with phantom in the 'long' width orientation. The values have been normalised to their respective total neutron flux.

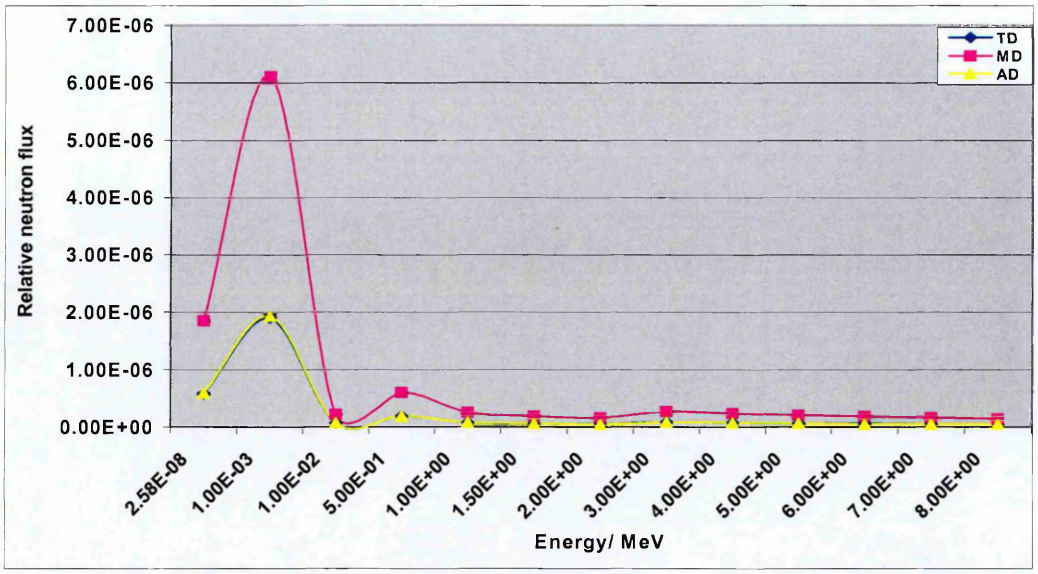

Fig. 3.9a: Neutron spectra in the water phantom at the sections towards the gamma ray detector (TD), central part (MD), and further most from the gamma ray detector (AD) with phantom in the 'short' width orientation and calculated using MCNP.

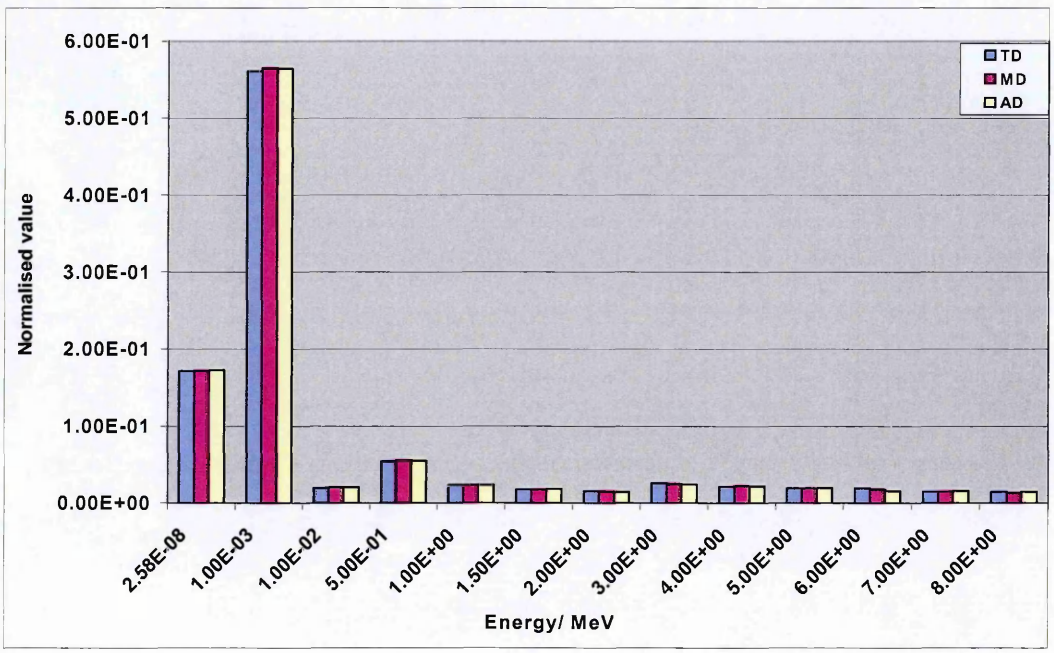

Fig. 3.9b: Normalised neutron spectra in the sections of the phantom towards the gamma ray detector (TD), central part (MD), and away from the gamma ray detector (AD) with phantom in the 'short' width orientation. The values have been normalised to their respective total neutron flux.

almost the same and approximately 70% down on the central section. This distribution is expected of homogeneous bulk samples such as the phantom used in this work, however, environmental and other bulk samples such as sawdust or the human abdomen are heterogeneous in nature and therefore the neutron distribution will depend on the matrix and composition of the bulk sample.

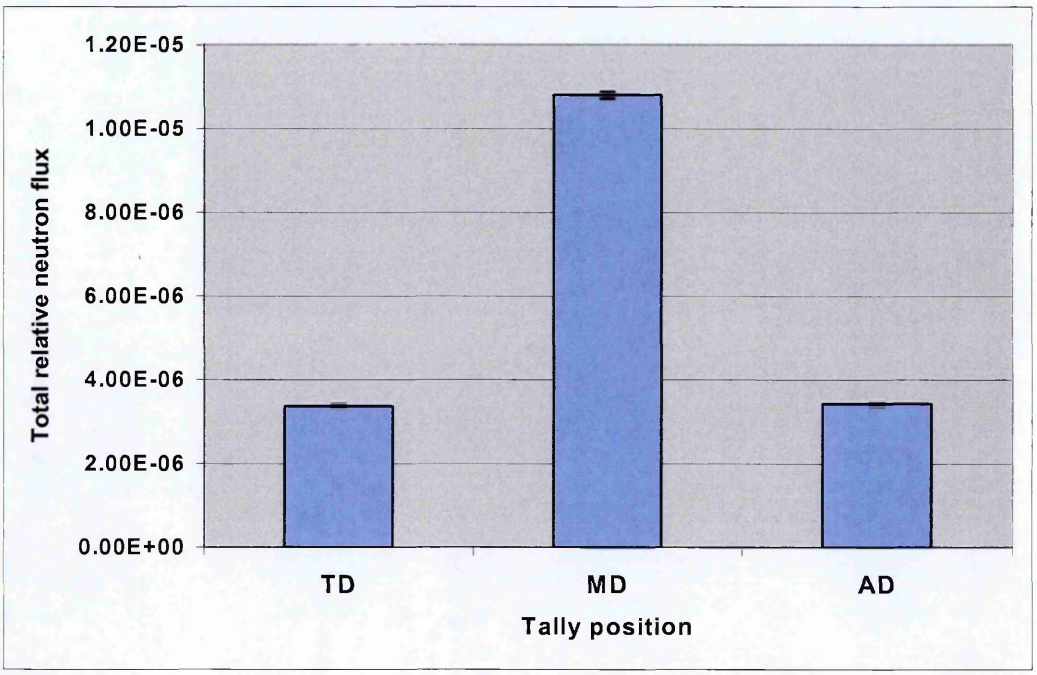

Fig.3.10: Neutron distribution in the water phantom for the 'short' width orientation calculated using MCNP.

Figures 3.11 shows the neutron spectra at the gamma ray detector position for both phantom orientations. Also shown are the neutron spectra on the opposite side of the phantom, that is, scattered neutrons for the 'long' and 'short' phantom orientations. The higher neutron flux at the gamma-ray detector position can be attributed to the number of direct neutrons from the ^{241}AmBe source and scattered neutrons from the water phantom and those from the vicinity of the detector shielding. In contrast, the scattered neutrons on the opposite side of the phantom are composed of mostly scattered neutrons reaching the tally sphere from the phantom and are therefore much fewer than those at the gamma-ray detector position. The presence of neutrons at the gamma ray detector position despite the shielding shows the vulnerability of such detectors for neutron-induced experiments. Neutron reaching the

detector cause considerable damage, especially semiconductor detectors such as germanium. On the other hand, this can be used to develop appropriate shielding for such detectors acknowledging the fact that complete insulation against neutrons is not feasible. The peaks at 1 keV and 0.5 MeV are due to scattered neutrons reaching the gamma ray detector area from the water phantom and its vicinity including the neutron shielding.

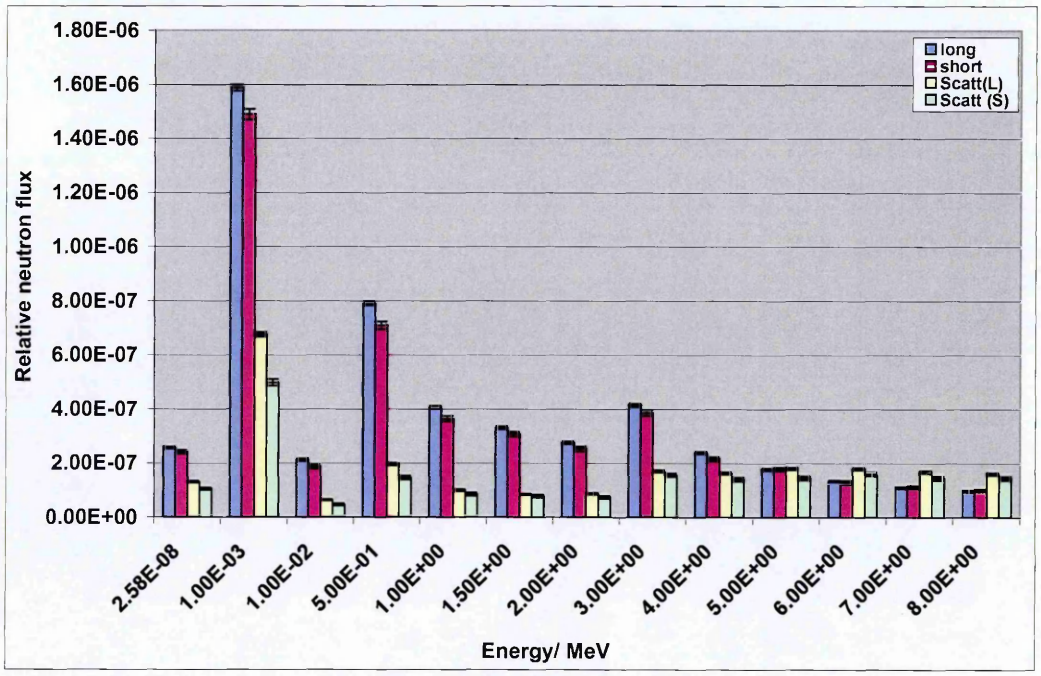

Fig.3.11: Relative neutron spectra at the gamma ray detector position for both phantom orientations.

3.13 Conclusions

The MCNP code (MCNP4C2) has been used to simulate the irradiation facility for prompt gamma neutron activation analysis for bulk samples. A slightly simplified version of the irradiation facility was simulated to reduce simulation time and also avoid structures that are not directly involved with irradiation of samples. The results of the simulation were compared with that obtained from measurement using the N-Probe and lithium gadolinium borate (LGB) detectors for the 'short' and 'long' width phantom orientations.

The total neutron flux for both phantom orientations for the transmitted and scattered neutrons obtained by MCNP calculations were about two orders of magnitude lower than that of measurement. This is attributed to the simplification of the simulation which does not include the walls of the room and the actual size of the detectors. The measured neutron flux includes scattered neutrons in the room as well as those scattered from the detector itself and associated instrumentation. The ratio of the transmitted to scattered neutrons for the 'long' width phantom orientation shows some degree of convergence between simulation and measurement. Ratios of 0.06 ± 0.007, 0.08 ± 0.004 and 0.05 ± 0.001 were obtained for the N-Probe, LGB and MCNP calculations, respectively.

The transmitted neutron spectra measured with the N-Probe for the 'short' and 'long' width phantom orientations compare well with calculations except at energies less than 1.0 MeV where the disparity between the two methods becomes obvious due to the effect of room scattered neutrons. This effect is much higher for measurements and calculations of scattered neutrons for both phantom orientations where a peak was measured between 0.7 and 1.0 MeV.

The neutron flux distribution in the water phantom for the 'long' width orientation falls off exponentially with distance along the width of the phantom, however, the neutron profile remained unchanged. In the case of the 'short' width phantom orientation, the neutron distribution in the phantom was highest in the central section but fell to approximately 70% on both sides of the central section. The near symmetric distribution of neutrons with respect to the central section is mainly

due to the homogeneity of water, however, the neutron distribution will be much different for heterogeneous bulk samples.

The neutron distribution at the gamma-ray detector position is approximately the same for both phantom orientations and therefore independent of phantom orientation. This implies that a greater percentage of the neutrons reaching the gamma-ray detector are scattered neutrons from the water phantom and also direct neutrons from the source. Neutrons reaching the gamma-ray detector are approximately a factor of 2 more than the scattered neutrons calculated on the other side of the phantom. This necessitates an improvement of the neutron shielding around the gamma-ray detector and this can be investigated using MCNP calculations which also take into consideration room-scattered neutrons.

4. The geometrical factor

4.1 Introduction

Neutron flux measurements in and outside the photon beam of medical linear accelerators employing foil activation has been used by many researchers. The induced activity in the foils will vary depending on their positions in and out of the photon beam. The foils are irradiated either bare or placed in moderators depending on the type of study being undertaken.

Measurement of the induced activity in the foils requires good and accurate knowledge of all the relevant nuclear parameters involved and reliable as well as reproducible experimental conditions are required. It is obvious that the size, shape and orientation of the foils and that of the detector have an effect on the absolute full-energy-photo peak efficiency of the detector. In practice, active foils are placed much further from the detector face to obtain low dead time and less active ones much closer for improved counting statistics. These two sources thus represent different geometrical configurations that must be accounted for. Also the efficiency of the detector determines the fraction of the particles that are recorded by the detector. The geometry can affect the measurement in several ways including the possibility of absorption and scattering of particles by the medium between the source and detector.

The aim of this study was to investigate that the effect of the shape of the foils and their position on and off the central axis of the detector have on the geometrical factor or the solid angle. The initial proposition was to use activation foils for the photoneutron measurements in the photon irradiation field and in the treatment room as well as the maze. Both collimated and uncollimated detectors were considered in the study and calculation of the geometrical factor was based on the Monte Carlo method proposed by Wielopolski [Wie77] and adopted by Nicolaou et al [Nic86] and Hosseini-Ashrafi and Spyrou (Hos92). The Monte Carlo program, written for the present work by the author in Fortran 90, makes use of the total variance reduction technique to simulate the isotropic emission of photons uniformly distributed in the sample. A random number generator is used to generate points of disintegration and the random direction of the emitted photons. The random number generator is an

integral part of the program and therefore does not require an external random number generator such as RANDU [Wie77] to run the program. The program calculates the solid angle substended by bare or collimated detector at the photon emitting source. It takes into consideration the finite size and shape of both the source and detector and also the attenuation of the photon in the sample and the detector as well as that of the medium between them. For a point source the results obtained are compared with those calculated using equation 4.5 and those computed using the the program by Carrillo [Car96]. For disc and cylindrical sources, the solid angles computed are compared with those by Carrillo [Car96].

4.2 Definition of solid angle

The solid angle or the geometrical factor is an important parameter to consider in radiation measurements. Isotropic sources emit radiation with equal probability in every direction. If a detector is placed in front of the source, only some of the particles have the chance to enter the domain of the detector. This portion can be equated to the solid angle subtended by the detector at the location of the source. The solid angle is thus defined as the ratio of the number of particles per unit time (seconds) emitted from inside the space defined by the source and the detector to the number of particles per unit time (seconds) emitted by the source. In the case of the collimated detctor, the total solid angle and the effective solid angle subtended by the detector are also defined since some of the photons are lost due to penetration in the collimator. The total solid angle is defined as the average solid angle containing up to a minimum set penetration fraction of about 1% through the collimator edges. The effective solid angle is the average solid angle which contains the primary beam and any contribution from the penetrating photons through the collimator normalised with respect to the primary beam [Hos92].

4.2.1 General expression of solid angle

The general expression for the solid angle can be derived from the definition given above as follows: consider a plane isotropic source, figure 4.1a, of area A_s emitting S_o particles per unit area and time, located at a distance d from the surface of a detector of area A_d. By considering two differential areas dA_s and dA_d and integrating [Tso95] the solid angle is given by:

$$\Omega = \frac{\int_{A_s}\int_{A_d}(S_o dA_s)/(4\pi r^2)dA_d(\frac{\hat{n}\cdot r}{r})}{S_o A_s} \tag{4.1}$$

where $\hat{n}$ is a unit vector normal to the surface of the detector aperture. From figure 4.1a

$$\frac{\hat{n}\cdot r}{r} = \cos\omega \tag{4.2}$$

Therefore, the solid angle is given by the following:

$$\Omega = \frac{1}{4\pi A_s}\int_{A_s} dA_s \int_{A_d} dA_d \frac{\cos\omega}{r^2} \tag{4.3}$$

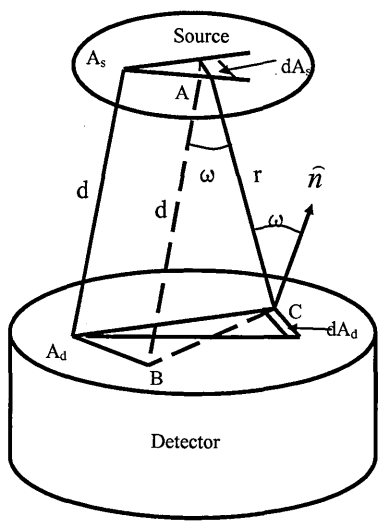

Fig. 4.1a: The solid angle for a plane source and a plane detector parallel to the source [Tso95].

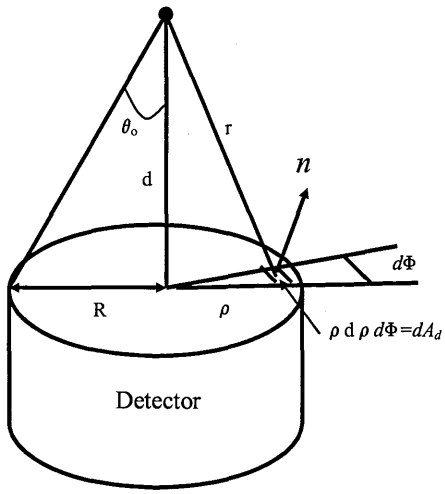

Fig. 4.1b: The solid angle between a point isotropic source and a detector with a circular aperture [Tso95].

It can be shown from figure 4.1b [Tso95] that for a full 4π geomety around a point source the solid angle subtended by the detector is given by

$$\Omega = 2\pi(1-\cos\theta_o) \tag{4.4}$$

or

$$\Omega = 2\pi\left(1-\frac{d}{\sqrt{d^2+R^2}}\right) \tag{4.5}$$

Where R is the radius of the detector face.

From Equation 4.5 and for the case where R<<d, the solid angle approximates to the following, after expanding the square root series using the Binomial theorem and taking the first two terms, Ω approximates to;

$$\Omega = \frac{\pi R^2}{4\pi d^2} \tag{4.6}$$

It is implied in Equation 4.6 that for a large source to detector distance, the solid angle is independent of the detector size.

4.2.2 Review of work done by others

The evaluation of the solid angle has been carried out by several workers for different geometries using analytical and or Monte Carlo methods. For point sources the use of the analytical method is quite straightfoward, the difficulty arises when complicated geometries are considered which require complex processes involving Monte Carlo calculations. Masket et al [Mas56], Verghese et al [Ver71] and Gardner and Verghese [Gar70], used analytical methods to determine the solid angle. As source-to-detector geometries become complicated the analytical method becomes less accurate. The Monte Carlo technique has been employed to determine the solid angle for complicated geometries employing the variance reduction technique to optimise the computational time. Gardner and Verghese [Gar70] developed a Fortran program for calculating the solid angle subtended by a regular polygon with n (even) sides with area equal to that of a circle of radius R and concluded that the accuracy for approximating a circle improves monotonically with an increasing number of polygon sides. Ruby [Rub93] developed a promising algebraic approximation based on the Bessel function to calculate the geometrical efficiency of a parallel disc source and detector system. However this formula has defects which are clearly pointed out by Carrillo [Car96] who used a more appropriate formula and confirmed it using the Monte Carlo method and numerical integration utilising Mathematica. Wielopolski [Wie77] employed the Monte Carlo method utilising total variance reduction to calculate the average solid angle subtended by a right circular cylindrical bare detector from a point of arbitrary position of a distributed source of unusual shape. The calculated values for various cases of interest compared well with values given in the literature thus validating the method. Meons et al [Moe81] used a semi-empirical method which calculates the effective solid angle for a reference experimental configuration and corresponding absolute full energy photopeak efficiency and then for any required source to detector distance and source geometry and the corresponding absolute full energy photopeak efficiency. In this way the absolute full energy photopeak efficiency for any corresponding configuration (solid angle) is computed using the expression;

$$P_x = P_{ref} \frac{\overline{\Omega}_x}{\overline{\Omega}_{ref}} \tag{4.7}$$

where $\overline{\Omega}_x$ is the effective solid angle subtended at the source by the detector and P_x is the absolute efficiency. The method takes into cosideration the attenuation of gamma rays from the point of disintegration in the source through the material between source and detector and in the detector including the aluminium can.

4.3 The solid angle subtended by a collimated detector to a cylindrical source

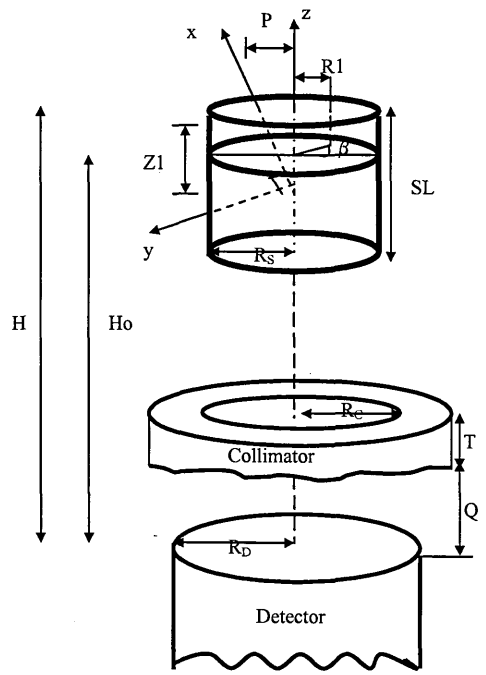

Fig.4.2: Geometrical configuration of a collimated detector and a cylindrical target (source) with its axis coinciding with the central axis of detector and collimator.

The solid angle subtended by a cylindrical target (source) on the detector axis is as shown in figure 4.2. The variable position of the generated points is given by the following:

$$Z1 = SL(X1 - 0.5), \quad R1 = R_S\sqrt{X2} \quad \text{and} \quad \beta = 2 \cdot \pi \cdot X3$$

where X1, X2 and X3 are three independent random numbers equi-distributed in [0,1] [Wie77], R_S is the radius of the cylindrical source at a given distance from the centre of the source and SL is the length of the source. The variable position [P,H] of the selected point in relation to the detector axis and with reference to the base of the detector is given by

$$P = R1 \cdot \cos(\beta) \qquad (4.8)$$

and

$$H = H_0 + R1 \cdot \sin(\beta) \tag{4.9}$$

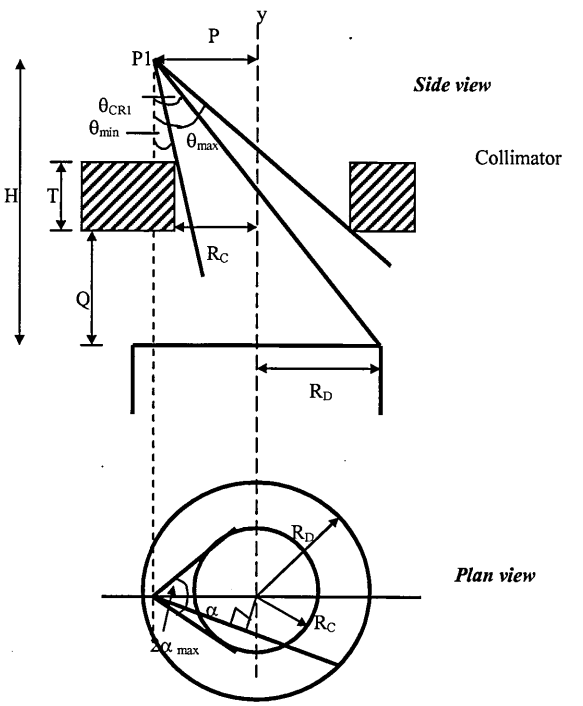

Fig. 4.3. Geometrical configuration of a point source above the collimator at a distance greater than the radius of the collimator.

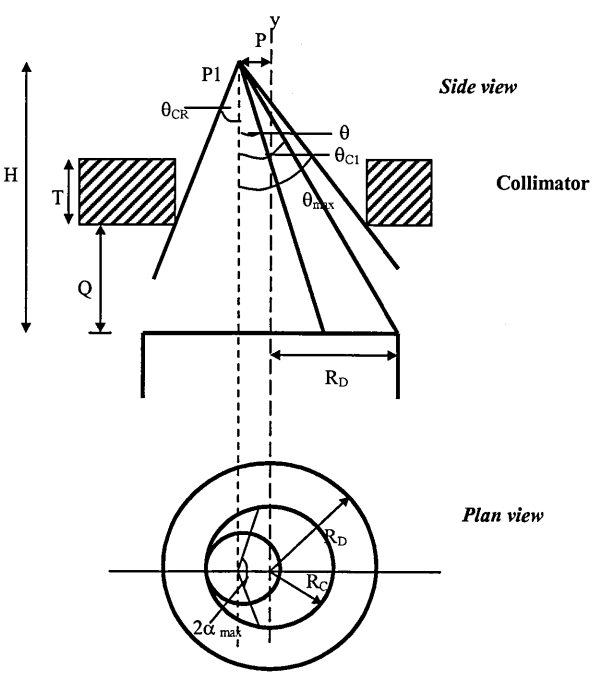

Fig. 4.4: Geometrical configuration of a point source above the aperture of the collimator.

Using spherical co-ordinates for the isotropic emission of the source into a sphere of unit radius, the solid angle dΩ is given by :

$$d\Omega = \sin\theta d\theta d\alpha \tag{4.10}$$

where θ and α are the longitudinal and horizontal angles respectively, $p(\theta, \alpha)$ is the joint probability density distribution for isotropic emission (Wie77). The fraction of radiation emitted in dΩ described by $p(\theta, \alpha)$ is given by:

$$p(\theta,\alpha)d\theta d\alpha = \frac{d\Omega}{4\pi} \tag{4.11}$$

$$p(\theta)d\theta = \int_0^{2\pi} d\alpha \frac{\sin\theta}{4\pi} \tag{4.12}$$

yielding

$$p(\theta) = \frac{\sin\theta}{2} \quad , \quad \text{for} \quad 0 \le \theta \le \pi \tag{4.13}$$

and

$$p(\alpha)d\alpha = \int_0^{\pi} \sin\theta d\theta \frac{d\alpha}{4\pi} \tag{4.14}$$

$$p(\alpha) = \frac{1}{2\pi} \quad , \quad \text{for} \quad 0 \le \alpha \le 2\pi \tag{4.15}$$

To ensure that the selection of θ and α result in the interception of a photon by the detector, weighting factors W1 and W2 are chosen such that $Wi = W1 \cdot W2$ where Wi represents the solid angle subtended by the detector for that particular selection of θ and α. The solid angle Ω(P) for the configuration is given by:

$$\Omega(P) = \frac{1}{N} \cdot \sum_{i=1}^{N} Wi \tag{4.16}$$

and the associatd standard deviation $\sigma_{\Omega(p)}$ is computed using the following

$$\sigma_{\Omega(P)} = \left[\frac{1}{N(N-1)}\left(\sum_{i=1}^{N} Wi^2 - N\Omega(P)^2\right)\right]^{\frac{1}{2}} \quad (4.17)$$

In the case where the attenuation of the photon within the source and the media between the source and detector crystal is considered, the effective solid angle is given by:

$$\overline{\Omega}(p) = \frac{1}{N}\sum_{i=1}^{N} Ei \quad (4.18)$$

where

$$Ei = Wi\cdot\left[1-e^{-\mu_d x_d}\right]\cdot e^{-\mu_{Al} x_{Al}}\cdot e^{-\mu_s x_s} \quad (4.19)$$

and μ_d is the photon absorption coefficient of the detector material (Ge) for a given photon energy and μ_{Al} and μ_S are the linear attenuation coefficient of aluminium (window material of the detector) and source material, respectively for a given photon energy. x_d, x_{Al} and x_S are the track lengths in the detector, aluminium and source material in the particular simulation path.

4.4 The solid angle subtended by a collimated detector

In the following cases, the assumption is that collimator penetration is negligible and that photons reaching the detector do not interact with the collimator.

4.4.1Case 1 – Point P1 located outside detector aperture

Point P1, is located outside the collimator aperture as shown in figure 4.3 where $P \geq R_C$. α_{max} remains constant for any selection of θ for which a photon intercepts the detector. X, is defined as a uniformly distributed random number between zero and one [0,1] [Wie77, Nic86] and the angle α is determined from the following:

$$X = \frac{\int_{-\alpha_{max}}^{\alpha} \frac{d\alpha}{2\pi}}{\int_{-\alpha_{max}}^{\alpha_{max}} \frac{d\alpha}{2\pi}} \Rightarrow \alpha = \alpha_{max}(2X-1) \quad (4.20)$$

and $$-\alpha_{\max} \le \alpha \le \alpha_{\max}$$

where

$$\alpha_{\max} = \tan^{-1}\left(\frac{R_C}{(P^2 - R_C{}^2)^{\frac{1}{2}}}\right) \tag{4.21}$$

The weighting factor associated with this selection of α is $W2$ [Wie77, Nic86]

$$W2 = \frac{\int_{-\alpha_{\max}}^{\alpha_{\max}} \frac{d\alpha}{2\pi}}{\int_0^{2\pi} \frac{d\alpha}{2\pi}} \tag{4.22}$$

Therefore

$$W2 = \frac{\alpha_{\max}}{\pi} \tag{4.23}$$

From figure 4.3, θ_{min} and θ_{max} can be computed from the following once α has been determined

$$\theta_{\min} = \tan^{-1}\left\{\frac{P\cos\alpha - (R_C{}^2 - P^2\sin^2\alpha)^{\frac{1}{2}}}{H - (Q+T)}\right\} \tag{4.24}$$

$$\theta_{\max} = \tan^{-1}\left\{\frac{P\cos\alpha + (R_D{}^2 - P^2\sin^2\alpha)^{\frac{1}{2}}}{H - Q}\right\} \tag{4.25}$$

A critical angle θ_{CR1} exists which is an indicator of whether the randomly selected direction intercepts the detector, this is given by

$$\theta_{CR1} = \tan^{-1}\left\{\frac{P\cos\alpha + (R_D{}^2 - P^2\sin^2\alpha)^{\frac{1}{2}}}{H}\right\} \tag{4.26}$$

The weighting factor W1 associated with the selection of θ is given by [Wie77, Nic86]

$$W1 = \frac{\int_{\theta_{min}}^{\theta_{max}} \frac{\sin\theta}{2} d\theta}{\int_{0}^{\pi} \frac{\sin\theta}{2} d\theta} \tag{4.27}$$

for $\theta_{max} < \theta_{CR1}$, $W1 = \frac{\cos\theta_{min} - \cos\theta_{max}}{2}$

and $\theta_{max} \geq \theta_{CR1}$, $W1 = \frac{\cos\theta_{min} - \cos\theta_{CR1}}{2}$

as $\alpha \rightarrow \alpha_{max}$ then $W1 \rightarrow 0$

4.4.2 Case 2 – Point P1 located within collimator aperture

The point P1 is located inside (within) the collimator aperture as shown in figure 4.4, that is, P<R_C. In this case θ_{max} remains constant and is given by

$$\theta_{max} = \tan^{-1}\left(\frac{R_C + P}{H - Q}\right) \tag{4.28}$$

Also the critical angle θ_{CR2} below which α may vary over 2π and above which the variation of α is limited to $2\alpha_{max}$ [Wie77, Nic86] is given by

$$\theta_{CR2} = \tan^{-1}\left(\frac{R_C + P}{H - Q}\right) \tag{4.29}$$

A particular selection of θ will allow the the determination of α_{max}. θ is computed from the definition of random number X given by

$$X = \frac{\int_{0}^{2\pi} \frac{\sin\theta}{2} d\theta}{\int_{0}^{\theta_{max}} \frac{\sin\theta}{2} d\theta} \tag{4.30}$$

$$\therefore \theta = \cos^{-1}[1 - X \cdot (1 - \cos\theta_{max})]$$

The weighting factor associated with this selection of θ is computed by

$$W1 = \frac{\int_0^{\theta_{max}} \frac{\sin\theta}{2} d\theta}{\int_0^{\pi} \frac{\sin\theta}{2} d\theta} \tag{4.31}$$

and

$$W1 = \frac{1-\cos\theta_{max}}{2}, \qquad \text{for } \theta_{max} \le \theta_{C2} \text{ and}$$

$$W1 = \frac{1-\cos\theta_{C2}}{2}, \qquad \text{for } \theta_{max} > \theta_{C2}$$

where

$\theta_{C2} = \tan^{-1}\left(\frac{R_D + P}{H}\right)$; if for a particular selection of θ, $\theta > \theta_{C2}$ then W1=0

Once θ has been chosen, the weighting factor associated with the selection of α is also determined from the following conditions,

if $\theta \le \theta_{CR2}$, α: [0, 2π] and W2=1

if $\theta > \theta_{CR2}$, $\alpha \le 2\alpha_{max}$ and $W2 = \frac{\alpha_{max}}{\pi}$

4.5 Uncollimated (bare) detector

There are three distinctive cases for a bare detector [Wie77] and these can be described as follows. Case one is where the source is above the detector and at a distance greater than the radius of the detector, that is, P>RD and H>0 where the top of the detector is the zero mark. The source in this case is in the field of view of the top of the detector as well as its side. In the second case the source is on the side of the detector corresponding to P>RD and H<0. The final and obvious case is where the source is above the detector and at a distance such that P<RD and H>0. The solid angle has been computed for only the cases where H>0 for use in this work.

4.6 Monte Carlo based program COLDET

The Monte Carlo based Fortran 90 program developed by the author, COLDET, has its own random number generator and computes the solid angle for both bare and collimated detector for the cases discussed above by supplying the appropriate input data. For the collimated detector, the program assumes no septa penetration and

disregards photons degraded following their interaction with the collimator. However, it does take into consideration the attenuation of the photon due to the medium between the source and detector, the material covering the detector and that within the source itself. A collimated detector is clearly distinguished from a bare detector from the input options available to the user. The solid angles have been computed for points on and off the central axis of the detector and at points 50, 75, 100, 150, 200 and 250mm from the detector surface. The solid angle computed using this program is compared with those calculated using equation 4.5 and also that by Carrillia [Car96] for point sources. For a disc and cylindrical sources, only that of Carrillia [Car96] is compared. The geometrical dimensions of the sources are the same as those used in the experimental verification as shown in Table 4.1.

4.7 Experimental work

4.7.1 Verification of solid angle

In neutron activation analysis, samples of variable shapes and sizes are irradiated, the resulting radiation, usually photons produced through the (n,γ) reaction, is recorded using a calibrated detector. Depending on the procedure adopted and the half-life of the elements of interest, prompt, delayed or cyclic activation analysis is carried out. The samples are placed such that the field of view of the collimated or bare detector can intercept the resulting radiation emitted by the samples. The position of the sample can vary marginally on or off the central axis of the detector. Also samples are moved closer or away from the detector, to achieve an acceptable deadtime. The investigation conducted was to varify the relationship between the solid angle and the number of counts recorded by experiment. In order to do this three different geometrical shapes of sources, that is, cylindrical, disk and point were considered. A rig was designed and fabricated for the experiment which can only fit onto the bare detector and therefore only the bare detector was used in the experiment. The rig permits sources to be moved on the central axis towards and away from the detector as well as lateral movement normal to the central axis.

4.7.2 Solid angle and efficiency

A detector with an intrinsic full energy photopeak efficiency, ϵ_{ip}, records N counts under the full energy peak in a spectrum using an isotropic source of activity S. The solid angle relates to the counts in the full energy peak as follows

$$\Omega = \frac{4\pi N}{\varepsilon_{ip} S} \tag{4.32}$$

Deductions from Equation 4.32 and assuming a constant source activity throughout the experiment, the solid angle is proportional to the counts in the full energy photopeak, that is,

$$\Omega = AN \tag{4.33}$$

where A is a proportionality constant. The intrinsic efficiency of a detector depends primarily on the detector material, radiation energy, the physical thickness of the detector in the direction of the incident radiation. Its dependence on the distance between the detector and the source is almost negligible but, not entirely so because the average path length of the radiation through the detector will change somewhat with the spacing between the detector and source [Kno00].

To acertain the practicality of this relationship, the net counts in the photopeak was recorded for uniformly distributed cylindrical, disk and point sources of ^{137}Cs of dimensions as given in table 4.1. These sources were placed at 50, 75, 100, 150, 200, 250 and 300 mm from a Ge(Li) detector with the aid of the rig described in section 3.7.1. The characteristics of the Ge(Li) detector are as shown in Table 4.2 below.

Table 4.1: Geometry and dimensions of ^{137}Cs point, disc and cylindrical sources used for the experiment.

Source geometry	Diameter /mm	Thickness/Length /mm
Point	1.0	1.0
Disc	25.0	3.0
Cylindrical	6.4	12.0

Data obtained from Radiation Teaching Laboratory, Physics Department, University of Surrey.

Table 4.2: Characteristics of HPGe and Ge(Li) detectors

Detector	HPGe	Ge(Li)
Operating voltage	-2500 V	+4800 V
Crystal diameter	55.0 mm	47.5 mm
Length	51.0 mm	43.0 mm
Window material	Beryllium	Aluminium
Thichness	0.5 mm	0.5 mm
Distance between material and endcup	3.0 mm	5.0 mm
Relative efficiency* at 1332 keV (%)	25.8	10.8 ± 0.2
Resolution (FWHM) at 1332 keV	1.9 keV	2.0 ± 0.04 keV
Active volume	121.16 cm^3	76.2 cm^3
Peak-to-Compton ratio	57.1	30 ± 2

*The relative efficiency was quoted or measured relative to a NaI(Tl) detector (76.2 mm X 72.6 mm) at a source-to-detector distance of 250 mm.

4.7.3 Efficiency of a semi-conductor HPGe detector

The adherence to careful and accurate gamma-ray spectrometry calibration practice is a way forward in solving some of the counting problems. This is so because even in relative measurements it is often impracticable to count both the standard and sample under the same geometrical conditions. This can be influenced by the maintenance of a reasonable dead time for low and high activity sources. Semiconductor detectors are preferred to scintillator due to their better resolution which enhances the identification of gamma-rays very close in energy. It is important to determine the absolute full energy photopeak efficiency in order to calculate the concentrations of elements under investigation. The absolute full energy photo peak efficiency is the fraction of gamma-rays of a particular energy emitted by a radioactive source that gives rise to full-energy peak events in the pulse height spectrum. The intrinsic efficiency, on the other hand, is the number of detected events expressed as a fraction of the number of photons incident on the detector. The variation of efficiency with energy and source distance from the detector window need to be well understood in order to correctly interpret results. Also for most detectors there is a gap between the crystal and the detector window which effectively increases the actual distance between the source and the detector crystal. This needs to be determined in order to accurately calculate the geometrical factor the sample makes with the detector. The absolute full energy photopeak efficiency and its

variation with energy and distance from detector window have been investigated for a HPGe detector and also the gap between the crystal and the detector window has been determined.

4.7.4 Experimental procedure

In performing the experiments it was ensured that during counting a dead time of approximately 5% or less was recorded and also good statistics were obtained. The detector used in this work is an EG&G ORTEC high purity germanium detector, HPGe, with a crystal diameter of 55mm and a length of 51mm (volume of approximately 121.16cm^3). The manufacturer's information about the detector is summarised in Table 4.2. A set of standard point sources including ^{137}Cs, ^{60}Co, ^{57}Co and ^{152}Eu from the Radiation Teaching Laboratory, Physics Department, were used for the experiment which provided an energy range from 121 keV to 1408 keV. The same rig used in section 4.7.1 was used to maintain spatial reproducibility. The source can be moved from very close to the detector to 300 mm away from it reproducibly with an accuracy to the nearest millimetre on the rig. The standard counting electronics comprising of spectroscopic amplifier, analog-to-digital converter (ADC) and PC based multi-channel analyser (MCA) were used. Gamma-ray spectra of the standard sources were obtained for the detector at source to detector distances of 50, 75, 100, 150, 200 and 250 mm. Counting was carried out over 300 seconds and two replicate spectra were collected for each standard source and for each source-to detector distance. The net peak areas of the full-energy peaks recorded were averages of these replicates.

4.8 Results and discussion

Table 4.3 shows the comparison of of the calculated solid angle subtended by the Ge(Li) detector to the point source using equation 4.5, the Monte Carlo program by Carrillo [Car96] and that calculated in this work. These are in good agreement despite some minor differences. The differences can be attributed to the fact that both Equation 4.5 and Carrillo [Car96] ignore the actual dimensions of the source and the detector. These consider only the distance between the detector and source and the diameter of the cylindrical covering of the detector crystal. The actual size of the source and detector are critical in determinig the solid angle and these factors have been accounted for in the program developed for this work. As shown in Table 4.1. a

point source has definite dimensions so however minor should be taken into consideration. The size of the detector is vital since it determines the number of particles that the detector will intercept and have the chance of being counted. A difference of between 0.5% to 0.8% exists between the solid angles calculated in this work and the other two methods.

As the source size departs from being negligible, significant differences are observed in the solid angle. Table 4.4 is a comparison of the solid angle subtended by the detector to a disk source calculated using the program by Carrillo [Car96] and this work. A difference of 13% exists between the solid angles at 50 mm and falls to 5% at 250 mm from the face of the detector. For the cylindical source the difference between the two methods is approximately 7%, irrespective of distance from the detector as deduced from Table 4.5. These are quite significant compared to those of the point source. The differences confirm the effect that the finite size of the source and detector have on the solid angle and one that this is more pronounced at distances close to the detector. As expected, the solid angle diminishes as the distance between the source and detector face increases. The percentage differences reported here indicate good agreement between the program developed for this work and that developed by other workers and what has been established in theory. The finite size of the source and the detector have an important bearing on the solid angle. The same detector dimensions (detector radius, RD = 3.25 cm, detector length, LD = 13.0 cm) were used to compute the solid angles (in steradians) for all three sources.

Table 4.3: Table of results showing the comparison of the solid angle calculated using analytical and Monte Carlo methods for the point source.

Distance from detector, H/ mm	Equation 3.5 / steradians	Carrillo [Car96] / steradians	This work / steradians
50	1.015088 ± 0.008425	1.015230 ± 0.000279	1.023914 ± 0.000276
100	0.307662 ± 0.005928	0.307763 ± 0.000085	0.310013 ± 0.000057
150	0.142483 ± 0.003318	0.142534 ± 0.000039	0.143477 ± 0.000018
200	0.081350 ± 0.002056	0.081381 ± 0.000022	0.081886 ± 0.000006
250	0.052429 ± 0.001386	0.052448 ± 0.000014	0.052761 ± 0.000001

Table 4.4: Table of results showing the comparison of the solid angle calculated using analytical and Monte Carlo methods for the disc source.

Distance from detector, H/ mm	Carrillo [Car96] /steridians	This work /steridians
50	1.000000 ± 0.000255	1.159138 ± 0.001058
100	0.304760 ± 0.000063	0.335991 ± 0.000108
150	0.141897 ± 0.000048	0.152323 ± 0.000079
200	0.081157 ± 0.000028	0.085964 ± 0.000060
250	0.052355 ± 0.000011	0.055005 ± 0.000044

Table 4.5: Table of results showing the comparison of the solid angle calculated using analytical and Monte Carlo methods for the cylindrical source

Distance from detector, H/ mm	Carrillo [Car95] /steradians	This work /steradians
50	1.013157 ±0.000248	1.095533 ± 0.000909
100	0.307454 ± 0.000085	0.331440 ± 0.000228
150	0.142454 ± 0.000040	0.153033 ± 0.000093
200	0.081347 ± 0.000027	0.087194 ± 0.000048
250	0.052432 ± 0.000020	0.056117 ± 0.000029

Table 4.6: Table of results showing the variation of solid angle (calculated) with source geometry along the axis of a collimated Ge(Li) detector of collimator radius, 2.0 cm and the gap between the detector and collimator 0.5 cm

Distance from detector H/ mm	Point /steradians	Disc /steradians	Cylindrical /steradians
50	0.035231	0.035371	0.035086
100	0.012928	0.012813	0.012865
150	0.006269	0.006433	0.00648
200	0.003801	0.003758	0.003778
250	0.002422	0.002416	0.002419

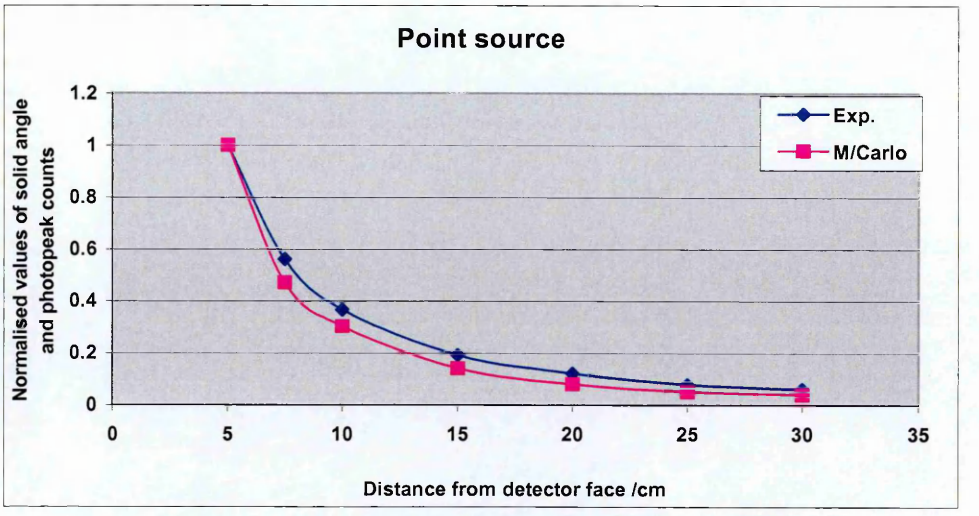

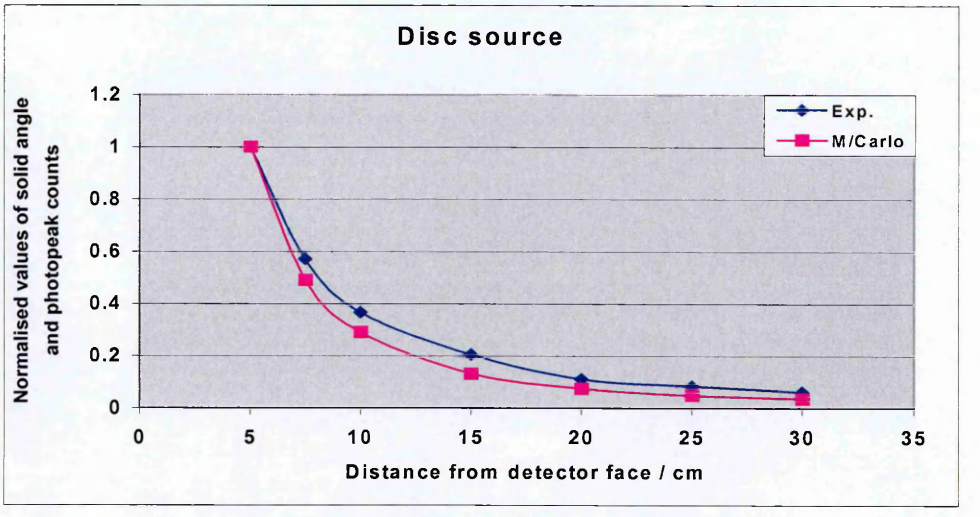

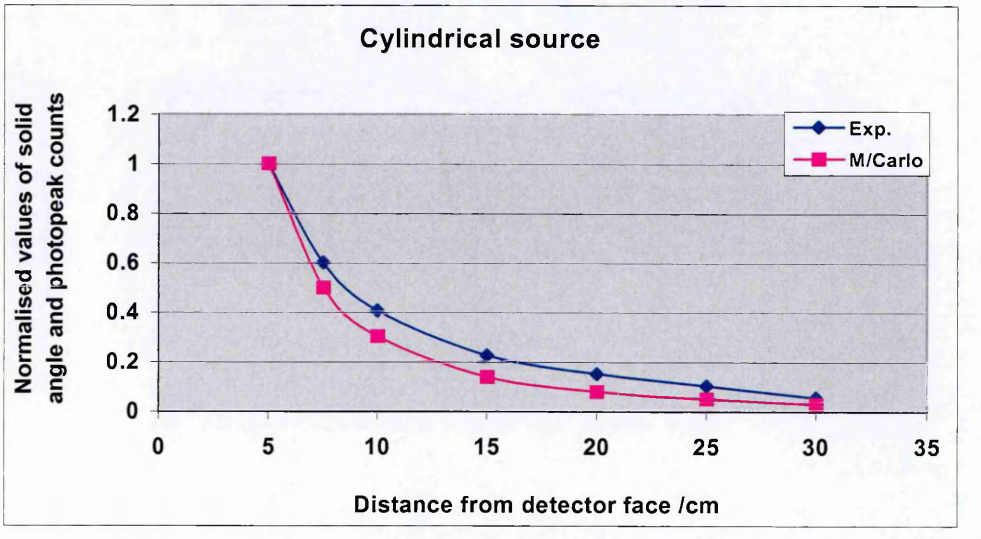

Fig. 4.5: Comparison of experiment and calculation for point, disc and cylindrical ^{137}Cs sources using the HPGe. The solid angle Ω (calculated) are compared with the number of counts in the full energy photopeak for sources.

The variation of solid angle with source geometry for collimated (Ge(Li)) detector is as shown in Table 4.6. The collimator was 0.5 cm above the detector with a circular opening of radius 2.0 cm. For a detector face of radius (3.25 cm) greater than the collimator opening only part of the detector surface was in full view of the source. It can be deduced that the the solid angle changes only marginally with source geometry for this detector and collimator arrangement. Most collimated detectors used in experiments have this sort of arrangement.

Figure 4.5 shows the comparison between measurement and calculation for the relationship between the solid angle for uncollimated detector (Ge(Li)) and the number of particles that the detector intercepts and are counted for the point, disc and cylindrical source of dimensions given in Table 4.1, respectively. There is a reasonable agreement between measurement and calculation for all three sources. The agreement is greater for a point source than the others and as with all three sources, the longer the distance between the source and detector the greater the agreement between experiment and calculation. In spite of these differences due to factors relating to experiment and calculation, this gives an indication of the cone of particles that are able to reach the detector and have the chance of being counted.

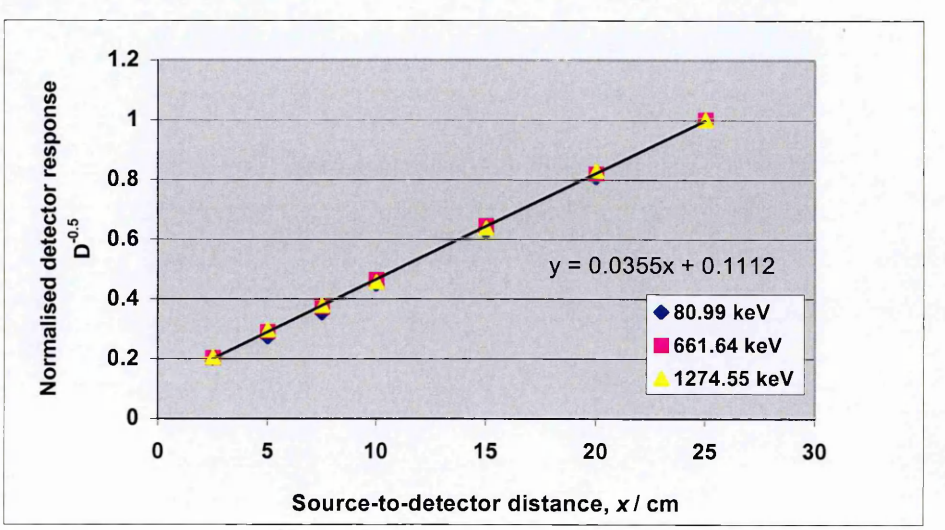

Fig. 4.6: Variation of normalised inverse square root of the uncollimated HPGe detector response with the source-to-detector surface distance. A fitting line to the experimentally determined data and equation are as shown.

Figure 4.6 shows the gamma-ray peak energies of 80.99, 661.64 and 1274.55 keV of standard reference point sources ^{133}Ba, ^{137}Cs and ^{22}Na, respectively, the normalised values of the inverse of the root of the uncollimated HPGe detector's response ($D^{-0.5}$) are plotted against the source-to-detector distance x. A linear graph with a common intercept on the x-axis at approximately -3.10 ± 0.05 cm is obtained from the equation fitting the common line. The negative sign is attributed to the fact that the surface of the detector is the zero mark and therefore any distance beyond is negative. This is the virtual length by which the source-to-detector distance must be increased to achieve the effective distance between the detector (HPGe) crystal and the face of the aluminium can covering and beryllium window. It is common knowledge that the detector is not in direct contact with the detector window. Therefore the effective source-to-detector distance is approximately x + 3.10 ± 0.05cm compares well with that qouted by the manufacturers, 3.0 cm, in Table 4.2. This distance is energy dependent at photon energies below 60 keV but is however constant at higher energies [Ade01]. At lower energies there is increased contribution from the photoelectric effect in the aluminium covering of the detector which is predominant. At much higher energies such as those used in this work, the window is virtually transparent to the gamma-rays, hence the common intercept extrapolated in figure 4.6.

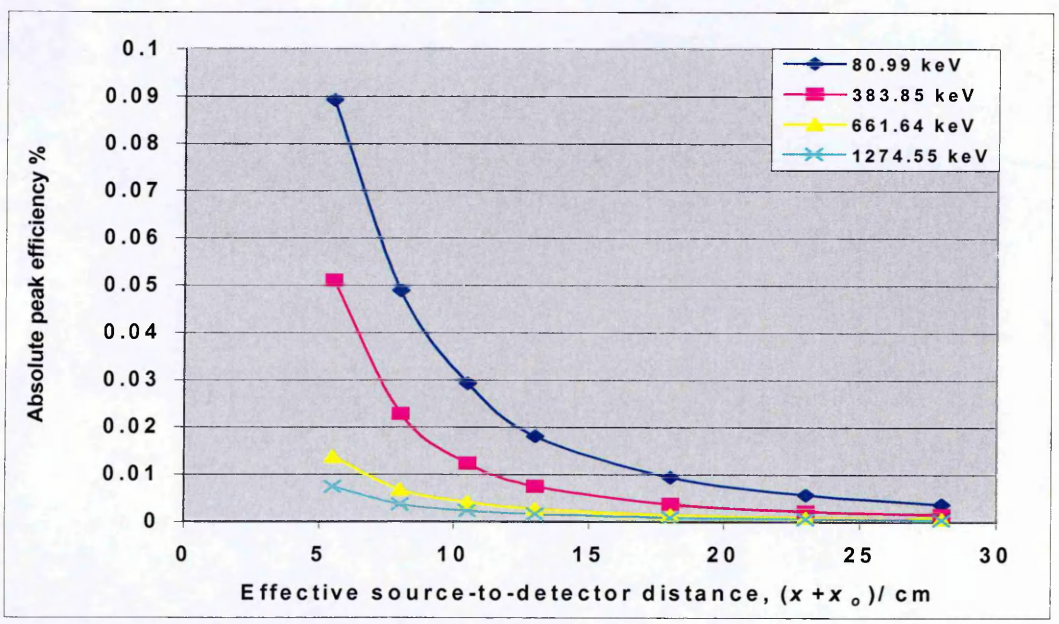

Fig. 4.7: Variation of absolute peak efficiency with the effective source-to-detector surface distance for 80.99, 383.85, 661.64 and 1274.55 keV gamma-ray energies.

The variation of the absolute full energy photopeak efficiency with effective source-to-detector distance and gamma-ray energy are as shown in figures 4.7 and 4.8, respectively. Figure 4.7 shows the variation of the absolute efficiency with effective source-to-detector distance at 80.99, 383.85, 661.64, and 1274.55 keV gamma-ray energies. It is clear that the absolute full energy photopeak efficiency depends on both the gamma-ray energy and the effective source-to-detector distance ($x + x_o$). The value of x_o is taken as 3.0 cm. Figure 4.8 shows the variation of the absolute efficiency with energy at effective source-to-detector distances of 8, 13, and 23 cm. The solid lines are exponential fits to the experimental data.

Adesanmi et al [Ade01] derived a semi-empirical formula (using the SAMPO program) that expresses the absolute efficiency as a function of distance of source from the detector and the gamma-ray energy as follows:

$$\varepsilon_{ab}(x,E_\gamma)=\left[\frac{x_n+x_0}{x+x_0}\right]^2\left(1-e^{-k(x+x_0)}\right)\varepsilon(x_n,E_\gamma) \qquad (4.34)$$

where $\varepsilon(x,E_\gamma)$ is the absolute efficiency at the source to detector distance x, k is a fitting constant (i.e. k = 1, 2, 3 ...) and $\varepsilon(x_n,E_\gamma)$ is the absolute efficiency determined experimentally at a known source-to-detector distance x_n. In this case all that is required is to experimentally determine the efficiency at a known source-to-detector distance and also the distance between the detector crystal and window, x_0, the absolute full energy photopeak efficiency, $\varepsilon_{ab}(x,E_\gamma)$, of a detector can be calculated for a given source-to-detector distance using equation 4.34 given above.

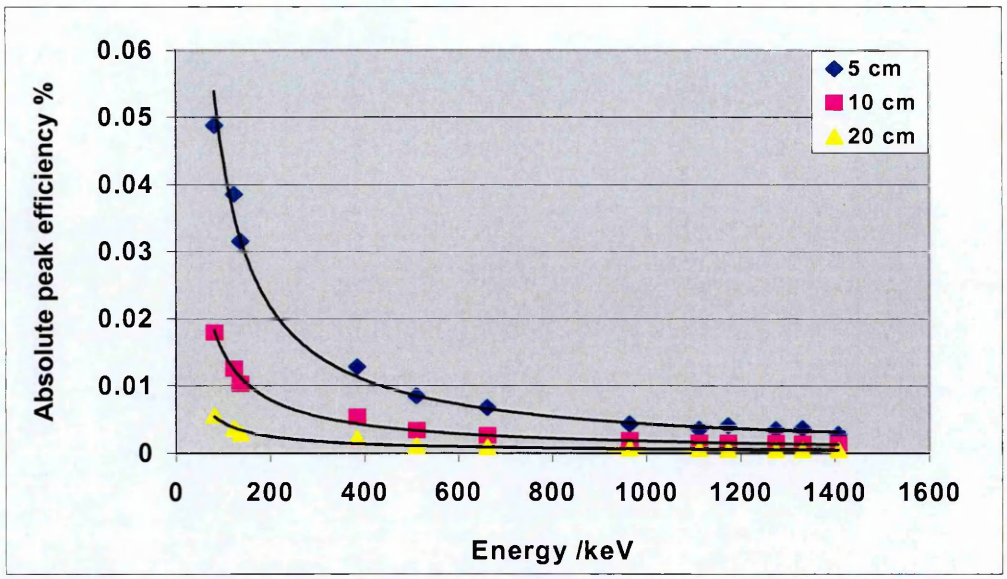

Fig. 4.8: Variation of absolute full energy photopeak efficiency with gamma-ray energy at effective source-to-detector distance of approximately 8, 13 and 23 cm. The solid lines are fits to the experimental data.

4.9 Conclusions

A Monte Carlo-based program, COLDET, which utilises variance reduction methods has been developed and satisfactorily calculates the solid angle subtended by both collimated and uncollimated detector to a source. Incorporated in this program is a random number generator and therefore does not require an external source of random number generator contrary to what pertains in other known programs developed for such purposes. The solid angles subtended by an uncollimated detector calculated for point, disc and cylindrical sources compare well with that of theory and work done by other workers. However, it was observed that some differences arise when the actual size of the source and detector are taken into account. It has been demonstrated that the solid angle subtended by an uncollimated detector is directly proportional to the number of particles the detector intercepts and have the chance of being counted. The solid angle subtended by a collimated detector of aperture much wider than the collimator opening and at a fixed distance apart is nearly independent on the source geometry.

5. Neutron dosimetry using Bubble Detectors (BD).

5.1 Superheated state of a liquid

Thermodynamically, the temperature of a liquid can be raised to a temperature higher than its boiling point without vaporising. This metastable state of the liquid is known as the superheated state of the liquid. Figure 5.1 illustrates the phase diagram of a substance of various ranges of temperature and pressure. Liquid and vapour can co-exist in equilibrium along the portion of the curve called the (co-existence) line or liquid-vapour equilibrium line. Under special conditions it is possible to have a substance in a pressure-temperature region associated with one state while maintaining the form of another state. As shown in figure 5.1, state ***B*** is normally a vapour, however, if the pressure from state ***A***, (liquid) is slowly reduced to reach state ***B*** crossing the equilibrium line, state ***B*** remains liquid. Also state ***B*** can be arrived at by gradually increasing the temperature from state ***C*** without vaporising. Irrespective of the path taken to reach state ***B***, so long as the substance at ***B*** is a liquid, then it is in a metastable state often referred to as superheated state of the liquid. ***T*** is the triple point where all phases of the substance co-exist at the same time.

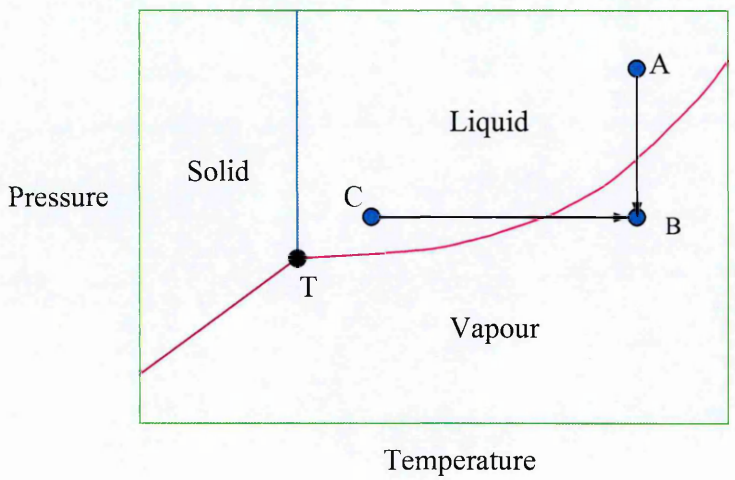

Fig. 5.1. Phase diagram of a substance in solid, liquid and vapour phase.

In general, the metastable state is observed to be fragile and short-lived owing to the presence of any of the following: (i) abundance of heterogeneous nucleation sites such as microscopic air bobbles, gas pockets, and solid impurities and (ii) radiation interaction or homogeneous nucleation caused by large scale density fluctuations at the molecular level.

The bubble chamber discovered by Glaser [Gla57] utilises the initiation of boiling of superheated liquid by nuclear radiation. The liquid is first superheated by suddenly dropping the pressure below the liquid's vapour pressure. The nuclear event is then recorded by a trail of bubbles nucleated by the elementary particles. The chamber is then rendered stable again by re-pressurisation. The Superheated Drop Detector (SDD), invented by Apfel [Apf79] works on the same principle, however, there is a collection of drops of superheated liquid suspended in a holding medium, such as a gel or polymer. By dividing the whole liquid into small drops, it has been assured that one nucleation will not consume the whole sample and the re-pressurisation procedure is avoided.

5.2 Introduction of superheated liquid in gel

There are two ways drops of superheated liquid can be introduced into the holding gel with reference to figure 5.1. The drops can be introduced at a temperature below the liquid's boiling point, and then the temperature gradually increased to the required superheat; alternatively, the drops introduced at a pressure greater than the liquids vapour pressure and the desired superheat attained by lowering the pressure. In effect each drop in the SDD is a continuous sensitive, miniature bubble chamber and therefore a point detector. Each drop represents stored mechanical energy that is released when triggered by radiation. The total amount of vapour evolved from the radiation-induced nucleation of drops can serve as a convenient measure of the integral exposure of the detector to a particular type of radiation above a threshold energy in the case of the threshold type. The neutron response function of the superheated drop detector is defined in terms of the number of bubbles per unit fluence of the SDD. It is a function of neutron energy and thermophysical properties of the superheated liquid and not that of the detector size or geometry. The response function, therefore, corresponds to that of a point source.

5.3 Bubble nucleation

The theory of neutron-induced nucleation of superheated drops involves the following physical processes: neutron-nucleus interaction, interaction of ion with matter and the dynamic process resulting in a microscopic vapour bubble. The bubble nucleation, referred to as an "event", can only be partially accounted for in theory. This is attributed to the fact that there are different physical processes occurring over a length scale covering twelve orders of magnitude [Roy87]. Although there has been some controversy about the mechanism of vapour bubble nucleation, it is generally agreed that Seitz's "thermal spike" model [Sei58] is the best approach [Pey67]. The "theory" hypothesis is that ions deposit energy locally, which is equivalent to a hot spot that literally explodes, creating vapour nuclei of critical size. The energy deposited along the path of the ion's range corresponding to approximately twice the critical radius of the liquid, will contribute significantly to bubble formation. It has been observed that only a fraction about 4-6% [Apf85] of that energy is effective in producing a bubble of critical size. The maximum energy that a nucleus of atomic mass A can receive from a neutron of energy E_n when the two interact through the head-on elastic collision is given by:

$$E_{\max} = \frac{4AE_n}{(A+1)^2} \tag{5.1}$$

The nucleus is ejected from the atom and shuttles through the liquid depositing its energy through linear energy transfer (LET) until it comes to rest. Nuclei of carbon, chlorine and fluorine that are common constituents of SDDs have different LETs, therefore, in a drop containing these the one with the highest LET will play a major role in the vapour nucleation. Also, knowledge of the stopping power (dE/dx) of relevant ions in relevant liquids plays a primary role in predicting the threshold energy to trigger a vapour nucleation in a given liquid.

5.4 Bubble vaporisation

The interaction rate (ψ) for a given liquid and a given flux of neutrons of certain energy depends on the effective nuclear cross-section at that neutron energy and the volume of the liquid. It does not depend on the uniformity of drop size provided there are sufficiently large numbers of drops present. For neutrons of energy E_n and flux ϕ

($cm^{-2}s^{-1}$) incident on superheated drops of total volume V, liquid density ρ, and molecular weight M, the vaporisation interaction rate is given by [Apf79, Apf85]:

$$\psi = \frac{\varphi V \sigma(E) N_{AV} \rho}{M} \tag{5.2}$$

Where N_{AV} is Avogradro's number and σ is the effective neutron-nucleus cross-section provided the total number of drop vaporisation events is small compared to the total number of superheated drops.

Apfel and Roy [Apf83] deduced, using elastic scattering theory by Fermi [Fer50], that the effective nuclear cross section can be estimated to be the product of the conventional nuclear cross section and a factor $(1\text{-}E_T/E_n)$ where E_T is the threshold neutron energy below which no events are observed and E_n is the incident neutron energy. An event does not only depend on the neutron-nucleus interaction but also on whether the interaction leads to a macroscopic bubble; thus σ depends on both the neutron energy and the degree of superheat. In the case of Freon-12 (CCl_2F_2) the reactivity of the chloride ion enables it to be sensitive [Apf83] to thermal neutrons even though the threshold for bubble formation is approximately 1.2 keV. The sensitivity of Freon-12 to thermal neutrons is due to the following nuclear reaction:

$$^{35}_{17}Cl + ^{1}_{0}n \rightarrow ^{35}_{16}S + ^{1}_{1}H(598keV) \tag{5.3}$$

The sulphur ion deposits its entire 17 keV in a range that is typically less than a critical radius r_c. The proton deposits only a small fraction of its energy in the critical bubble.

Bubble nucleation only occurs when sufficient energy is deposited within a superheated drop. The higher the superheat of the liquid, the lower the minimum energy that must be imparted to the drops in order to nucleate their evaporation. Charged particles generate trails of sub-microscopic vapour cavities inside the droplet but only embryos exceeding a minimum critical size can develop into bubbles as shown in figure 5.2. When this critical size is reached, the expansion becomes

irreversible and the whole droplet evaporates. The amount of energy deposited and the critical size are necessary for bubble nucleation and depend on the composition of the emulsion and on its degree of superheat. There are a number of emulsions available each specific for the detection of different directly and indirectly ionising radiations. These emulsions have different physical and chemical properties therefore they are selected according to the purpose it is intended for. From Table 5.1, dichlorotetrafluoroethane (R-114) and octafluorocyclobutane (C-318) are threshold detectors in contrast to dichlorofluoromethane (R-12) which is sensitive to thermal and epithermal neutrons. C-318, Isobutane and R-114 are only nucleated by high-energy heavy ions, such as the recoils generated by fast neutrons inside or next to the superheated drops [D'Er98c] and are also completely insensitive to photons. Emulsions of R-12, C-318, and R-114 are most suitable for neutron dosimetry applications as their response matches the fluence to dose-equivalent conversion factors [D'Er94a, D'Er96]. Emulsions of monochloropentafluoroethane (R-115) are sensitive to electrons and thus detect photons through their secondaries and also charged low-LET ions through Coulomb interactions [D'Er94b].

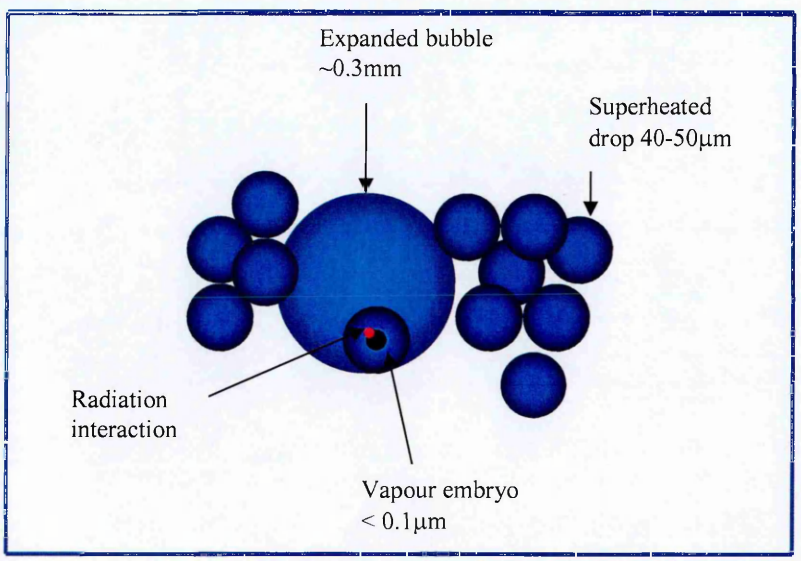

Fig. 5.2: Bubble formation steps in a superheated emulsion [D'Er98]

Table 5.1: Thermo-physical properties of various superheated emulsions [D'Er98c].

Halocarbon	Chemical formula	Boiling point at 1 atm (°C)	Density (g cm^{-3})	Vapour tension (pressure) at 22°C (atm)	Radiation sensitivity at 22°C
R-114	$C_2Cl_2F_4$	+3.5	1.5	2.0	Heavy ions, n ≥8 MeV
R-12	CCl_2F_2	-30.0	1.3	6.1	Heavy ions, n ≥thermal
R-142B	$C_2H_3ClF_2$	-9.3	1.1	3.0	Heavy ions, n ≥3 MeV
R-115	C_2ClF_5	-39.0	-	8.6	Light ions, n & photons
C-318	C_4H_8	-6.0	-	2.9	Heavy ions, n ≥2 MeV
Isobutane	C_4H_{10}	-11.7	0.6	3.1	Heavy ions, n ≥2 MeV

Table 5.2: Chemical data for superheated emulsion chamber versus data for reference soft tissue [D'Er98c]. TE – tissue equivalent, SEC – Superheated emulsion chamber Elemental composition.

Material	H	C	O	N	F, Cl	Density (g /cm^3)
SEC	8.8	28.2	62.5	-	0.5	1.2
TE	10.1	11.1	76.2	2.6	-	1.0

5.5 Types of bubble detectors or dosemeters

Superheated-drop (bubble) neutron detectors (SDD) or bubble damage detectors (BD) are suspensions of over-expanded halocarbon and/or hydrocarbon droplets which vaporise upon exposure to the high LET recoils from neutron interactions. A variety of devices based on this technology are commercially available. Some are active monitors detecting drop vaporisations acoustically by means of two piezo-electric transducers and recording the exposure time-history (Apfel Enterprises Inc., New Haven, Connecticut, USA). The problem with such detectors, using emulsion R-12, is when ambient levels of noise and temperature exceed 100 dB and 40°C [D'Er97], respectively. Others are passive, integrating, pen-size dosemeters (PNDs) relying either on the optical – manual or automated – counting of the bubbles (Bubble Technology Industries, Chalk River, Ontario, Canada and Apfel Enterprises, USA). This type of detector, BD-PND, has adopted a mechanical pressurisation of the detector at the end of its use to virtually reset the device. Another passive detector by

Apfel Enterprises, relies on the measurement of the total volume of gel displacement in a graduated capillary tube to determine the neutron dose equivalent.

5.6 Suitability for area monitoring

Owing to the progressive depletion of superheated drops, the integrated response of the detectors as a function of dose, that is, the number of counts (bubbles) exponentially approaches an asymptote corresponding to the initial number of drops. For this reason SDDs are always used up to a maximum of about 3000 [D'Er94] (bubbles) counts so that their response would still be close to linear and only minor corrections necessary such as for temperature. The SDD is virtually a zero-background detector therefore one bubble determines its detection threshold. Using a high sensitivity R-12 detector, D'Errico and Alberts [D'Er94] found that at 30°C the minimum detectable dose falls below 0.5 μSv. This is the value recommended in area monitoring [Leu92, Hol94] and in addition to this the SDDs have isotropic response.

5.7 Response function of SDDs

The SDD known to respond to neutrons from thermal to fast at room temperature consists of a collection of superheated halocarbons-12 (R-12) dispersed in an aqueous gel. It is virtually insensitive to photons, isotropic and can be used in small volumes to yield measurements with good spatial resolution. The sensitive material is so close in both formulation and density to tissue equivalent compositions that it neither interferes with the particle equilibrium inside a phantom nor requires a displacement correction factor [D'Er90]. At high neutron energies the free-in-air detector's response [Apf84, Apf85, Lo87] is in good agreement with the fluence to dose equivalent conversion factor d(E) recommended by [NCR71], however, the SDD underestimates the effect of low energy neutrons as shown in Figure 6.3 (chapter 6). The comparison would be better [Roy87] if higher neutron quality factors had been adopted. Also that d(E) represents the maximum dose equivalent delivered to a tissue equivalent phantom and because it takes into account both neutrons and secondary gamma components of the dose equivalent, the SDD on the contrary, is not sensitive to photons at room temperature [D'Er90]. The ideal response function for an in-

phantom dosemeter is the kerma equivalent factor q(E) [D'Er90], that is, the tissue kerma per unit fluence weighted by the appropriate quality factors to give dose equivalent. It should be noted as shown in figure 6.4 (chapter 6) that in the epithermal to intermediate energy range, where monoenergetic neutron beams are not available, Monte Carlo radiation transport techniques have been used to simulate the detector response [D'Er96, Gua97].

5.8 Reduced superheat factor

The fluence responses of SDD emulsions have been determined to be a combined function of neutron energy and operating temperature. The higher the operating temperature, the lower the minimum neutron detection threshold, in other words, the minimum energy that neutron secondaries must transfer to the superheated droplets to cause their nucleation. The threshold energies are not simply correlated to the degree of superheat $S=T-T_b$ (T_b – boiling point) and the reduced temperature factor $T_R=T/T_c$ (Tc- critical temperature of droplets). In view of this D'Errico [D'Er99] introduced a new parameter 'reduced superheat' defined as [$s = (T-T_b)/(T_c-T_b)$] which represents the normalised operating point of an emulsion within the temperature range corresponding to the metastable superheated state. The boiling point represents the

Table 5.3: Thermodynamic parameters corresponding to the thermal neutron sensitisation of dichlorofluoromethane (R-12), monochlorodifluoroethane (R-142B) and dichlorotetrafluoroethane (R-114). T – temperature, s – reduced superheat, W_{tot} – vaporisation energy and R_c – critical radius [D'Er99].

Halocarbon	T (°C)	s	W_{tot}(keV)	R_c(μm)
R-12	17.0	0.330	17.0	0.047
	17.5	0.334	16.1	0.046
	18.0	0.337	15.2	0.044
R-142	41.0	0.343	17.8	0.044
	41.5	0.346	16.9	0.043
	42.0	0.350	16.0	0.042
R114	50.5	0.330	17.8	0.047
	51.0	0.333	16.8	0.046
	51.5	0.337	15.9	0.045

lower limit of superheat of an emulsion while the critical temperature is the upper limit of superheated state representing the irreversible transformation from the liquid to vapour state. This correlation applies to only pure halocarbons but not those

modified with lithium or bismuth for increased sensitivity to thermal [Ing97] and high-energy neutrons respectively. From Table 5.3 it is clear that all the three halocarbons are sensitive to thermal neutrons some at sufficiently high temperatures corresponding to a reduced superheat of $s > 0.33$. Among the similar properties of halocarbons are their reduced temperatures $T_R > 0.64$ and homogeneous nucleation points corresponding to reduced temperatures $T_R > 0.88$. Homogeneous nucleation is analogous to leakage current in p-n diodes, that is, it occurs when a superheated liquid becomes intrinsically unstable and vaporises without irradiation or heterogeneous agents. The density fluctuations at the molecular level are sufficient to create cavities that can expand spontaneously and vaporise the entire bubble.

5.9 Mechanism of bubble formation

The introduction of neutron sensitive and photon discrimination superheated drop detectors has provided solutions to mixed field dosimetry needs. Hans and Peacock [Hah63] first observed neutron-induced cavitation in superheated liquids. Glaser's [Gla52] electrostatic theory and Seitz's [Sei57] 'temperature spike' model have unsuccessfully been complemented with the explanation of this complex process. The latter theory suggests that when a heavy particle slows down moving through a liquid, its kinetic energy is transformed as thermal energy to extremely small regions (temperature spikes) through the intermediaries of delta (δ) rays. The intense heating induces localised boiling, creating trails of microscopic vapour cavities that develop into macroscopic bubbles when the density of energy deposition is high enough. The shortcoming of Seitz's approach is that the aspects of atomic and nuclear physics as well as fluid thermodynamics have been avoided in the bubble formation. It assumed that a spherical vapour cavity of radius r embedded in a liquid of surface tension σ and vapour tension P_v expands indefinitely when

$$P_v - P_e > \frac{2\sigma}{r} \tag{5.4}$$

where P_e is the external pressure and a critical radius, r_c, given by

$$r_c = \frac{2\sigma}{\Delta P} \tag{5.5}$$

defines the discriminant between growing bubbles and those collapsing under the action of external forces. Bell et al [Bel74] derived various semi-empirical expressions of the formation energy for such critical bubbles, however, these do not reflect the physics of bubble formation according to D'Errico et al as discussed below [D'Er97a].

5.9.1 Semiemperical approach to bubble formation

The actual phenomenon according to D'Errico et al [D'Er97a] involves a first phase with the generation of a strong shock wave resulting from the heating of a small region to temperatures and pressures far beyond their critical values. When the hot, high-pressure region has expanded sufficiently, the critical parameters are achieved at a certain radius. Then an interface separating liquid and vapour can be defined and demarcated by a temperature-dependent surface tension. The vapour bubble continues to expand and reaches a radius of critical size if the initial neutron-nucleus interaction had been sufficiently energetic for the given degree of superheat. The complete temporal and spatial history of the energy deposition process by a charged particle in a superheated liquid was determined through computational fluid dynamics techniques [Sun92]. The assumption here was that the behaviour of the medium can be described by the usual macroscopic fluid equations (continuum mechanics approximation) and that the energy is deposited instantly and uniformly along an infinite line in the immediate vicinity of a heavy charged particle. The flow fields, as a function of time t and radial distance r of a viscous, heat-conducting and compressible fluid subject to the singular initial condition of a sudden energy deposition and then governed by five fluid dynamic equations: three conservation equations (mass, momentum and energy), one equation of state and its associated specific internal energy equation (treating the medium as a Horvath-Lin fluid) [Hor77, D'Er97a]. However, the required amount of calculations does not permit the general use of this approach even with hybrid computational methods [D'Er99], therefore,

semi-empirical methods based on the thermodynamics of the isothermal spontaneous nucleation modified according to the thermal spike theory. The critical radius is given by [D'Er99]:

$$R_c = \frac{2\sigma}{p'' - p'} \approx \frac{2\sigma}{\left[(p_s - p')(1 - \frac{v'}{v''})\right]} \tag{5.6}$$

where σ is the surface tension, p is the pressure (P_s is the saturation value), v is the specific volume, and $'$ and $''$ denote the liquid and vapour states, respectively. The energy, W_o required in the radiation-induced nucleation in the bubble chamber is given by [D'Er99]:

$$W_o = \frac{16\pi\sigma^3}{3(p_s - p')^2(1 - \frac{v'}{v''})^2}\left(1 + \frac{2\Delta H}{(p_s - p')(v'' - v')}3\frac{T}{\sigma}\frac{d\sigma}{dT}\right) \tag{5.7}$$

Where, all symbols have been previously defined and ΔH (enthalpy) the latent heat of vaporisation of the fluid and T – the ambient temperature.

The first term is the Gibbs free energy W_G needed for the isothermal process of spontaneous nucleation of the critical bubble in equilibrium with the surrounding medium. It amounts to the difference between the surface free energy of the bubble and the work done in the expansion against the pressure of the liquid and this difference is a maximum for a critical radius R_c. The second factor, in brackets, accounts for the heterogeneously initiated nucleation by ionising radiation. The assumptions here are that the energy be initially available in the form of heat and also that the evaporating process be adiabatic represented by dσ/dT. The process of bubble formation involves the contrasting action of viscous forces to the transfer of kinetic energy to the liquid by the motion of the vapour wall and to the emission of sound waves that are irreversible energy losses. The total formation energy was first proposed by Bell et al [Bel74] and echoed by Roy [Roy01] and is given by:

$$W = W_{gibbs} + H + E_{wall} + F \tag{5.8}$$

Where, H is the vaporisation energy, E_{wall} is the kinetic energy imparted to the liquid by the motion of the vapour wall and F is the energy imparted to the liquid during the growth of the bubble by the viscous forces. It has been found that the last two terms are negligible and can thus be neglected [Gib57, Bel74]. However, D'Errico et al [D'Er99], adopted an expression representing an upper limit for the kinetic energy and viscous force losses, that is,

$$W_{irr} = 2\pi\rho' R_c^3 \dot{R}^2 \tag{5.9}$$

where $\dot{R}$ is the vapour-wall velocity given by:

$$\dot{R} = 4D\left(\frac{p''}{p'}\right)^{1/3} R_c^{-1} \tag{5.10}$$

and $D = \frac{k}{p'c_p}$ is the thermal diffusivity of the liquid, k is thermal conductivity and c_p is the specific heat capacity. The total vaporisation energy W_{tot} is given by $W_{tot} = W_o + W_{irr}$ and values of W_{tot} and R_c of emulsions dichlorotetrafluoroethane (R-114) and octafluorocyclobutane (C-318) have been calculated [D'Er99].

5.10 Work done by others using bubble detectors

A few workers have reported using bubble dosemeters to determine photoneutrons in the output of photons from medical linear accelerators. Table 5.4 gives a summary of the linac, type of bubble detector used and neutron dose equivalent measured by some research groups.

D'Errico et al [D'Er98a] used three superheated drop detectors with different neutron energy responses to evaluate dose-equivalent and energy distributions of photoneutrons in a tissue equivalent phantom irradiated by an 18 MV x-ray beam. At 30°C R-12 emulsions respond from thermal to fast neutrons, while R-114 and C-318 present effective energy thresholds of 1.0 and 5.5 MeV, respectively. A maximum

dose equivalent of 4.5 $mSvGy^{-1}$ of photon dose was observed at a depth of 1 cm for a 10x10 cm^2 field size and doses were also relatively higher at 10 and 20 cm off-axis. On the other hand, at depths of 5, 10 and 15 cm the neutron dose equivalent appeared to be effectively shielded by the neutron attenuation in tissue which is largely due to the moderation action of hydrogen nuclei. Similar work was done by D'Errico et al [D'Er01], but coupled with Monte Carlo calculations for a Varian Clinac and Siemens KD 2 accelerators operating in the 6 – 18 MV range. Bourgois et al [Bou97] used BDT and BD-PND to measure the neutron component in the primary beam and outside the radiation field for 8, 15, 18 and 25 MV photons from a Saturne 43F linac. The dose equivalent per Gy of photons for a 10x10 cm^2 field size ranged from 0.25 to 7.52 mSv. Ongaro et al [Ong00] used a BDS spectrometer and Monte Carlo (MCNP-GN) calculations to estimate the neutron dose-equivalent and the neutron spectra in terms of fluence as a function of neutron energy in the output of medical linear accelerators SL 20I ELECKTA and Siemens Mevatron operated at 18 and 15 MV, respectively. The former is fitted with a multileaf collimator and the latter is a traditional linac. The in beam neutron dose-equivalent for the 15 and 18 MV were 1.67 and 4.8 $mSvGy^{-1}$ respectively at 100 cm source-to-surface distance (SSD). It was concluded that while the photon field tends to zero outside the treatment field, the neutron field is prominent well beyond the field with a value of 2.30 $mSvGy^{-1}$ for 18 MV and 0.89 $mSvGy^{-1}$ for 15 MV at 20 cm away from the field. This can represent a risk for healthy radiosensitive tissues and can contribute to secondary malignancy insurgence.

D'Errico et al [D'Er98b] used SDDs (Neutrometer-HD, Apfel Enterprises Inc.) to determine neutron dose equivalent in patients undergoing high-energy x-ray and electron therapy. In-vivo studies were conducted on patients to determine potential foetus dose by using a probe specifically designed for the vaginal cavity containing an SDD vial and a photon-sensitive diode. Neutron and photon measurements were carried out on patients undergoing pelvic treatment and on a tissue-equivalent (TE) pelvic box phantom using 18 MV x-rays beam of a CGR-MeV Saturne 20 linear accelerator. For a complete treatment course of 46.5 Gy for a pelvic field, the photon dose to the cervix added up to about 0.28 Gy and additional neutron dose-equivalent contribution of 0.02 Sv together exceeding the 0.05 Gy threshold indicated by the AAPM Task Group (1995) [Sto95] for the risk of malformation. A similar study was

carried out by Roy and Sandison [Roy00] but in this study neutron shielding material, borated polyethylene, was used to block neutrons from reaching the foetus during a thoraxic treatment on an anthropomorphic Rando phantom. Following on from this, Ding et al [Din02] used varying thicknesses of 5% borated polyethylene slabs from 5 cm to 10 cm in the field of the beam and close to the surface of a 48x48x48 cm^3 water phantom to investigate the effect of the size of the borated plastic slabs on the neutron dose at 1 cm depth in water. The results showed that the slabs reduced the neutron dose by a factor of 2 and that the neutron dose-equivalent at a depth of 0.75 cm on the central axis for a 10x10 cm^2 field was 4.8 $mSvGy^{-1}$ for an 18 MV Varian Clinac-2100EX accelerator. The BD-PND bubble detectors of various sensitivities were used by Lin et al [Lin01] to measure the neutron dose equivalent in the treatment room where a Siemens Primus medical accelerator has been installed. This accelerator is designed to execute intensity modulated radiation therapy (IMRT) achieved by coupling dynamic wedge and multileaf collimator and operates at 6 and 15 MV photon mode and 6 to 21 MeV electron mode. It was concluded that for the field sizes of 40x40 cm^2 and approaching 0x0 cm^2 the neutron dose equivalent for the 15 MV were respectively1.84 ± 0.09 $mSvGy^{-1}$ and 0.17 ± 0.06 $mSvGy^{-1}$.

Table 5.4: Summary of neutron dose equivalent measured with bubble detectors by other researchers.

Type of linac	Photon energy/ MV	Field size/ cm^2	Depth/ cm	Type of BD	Neutron dose equivalent/ $mSvGy^{-1}$	Medium	Reference
Varian	18	10x10	1	SDD	4.5	TEP	[D'Er98a]
Siemens KD2	10, 15, 18	10x10	1	"	1.4, 1.9, 5.5	Water phantom	[D'Er01a]
Saturne 43F	8, 15, 18, 25	10x10	100 SSD	BD-PND	0.246±0.03 2.36±0.60 2.98±0.30 7.52±0.67	Air	[Bou97]
SL20I – ELECTA	18	10x10	100 SSD	BD-PND	4.7	Air	[Ong00]
Mevatron Siemens	15	10x10	100 SSD	BD-PND	1.67	Air	"
Saturne 20	18	28x31 10x10 "	9.5 8 (5cm off axis) 10 (5cm off axis	SDD " "	0.43 1.6 1.5	Patient (Pelvis region) " (Vagina cavity)	[D'Er98b] " "
Siemens Primus (IMRT)	15	40x40 0x0 (closed jaws)	100 SSD "	BD-PND "	1.84±0.09 0.17±0.06	Air "	[Lin01] "
Varian Clinac 2100EX	18	10x10	0.75	SDD	4.8±20%	Water phantom	[Din02]
Varian 2100C/D	18	30x30	15	SDD	0.18±20%	Foetus	[Roy00]

6. Neutron dose equivalent measurement with Superheated Drop Detectors (SDDs).

Photoneutron contamination in the output of the 15 MV photon energy beam of a Varian Clinac 2100C is discussed in the following section. Bubble detectors were used for this purpose and for consistency all measurements were carried out in the same horizontal plane at 100 cm source-to-detector distance. Measurements were conducted in the patient plane and also in the maze of the bunker for both in-air and water phantom scenarios. The variation of neutron dose equivalent with field size and gantry angle rotation was also studied. The bubble detectors used in this work were the Neutrometer™–HD and Neutrometer™-S detectors manufactured by Apfel Enterprises Inc., 25 Science Park, New Haven, CT 06511, USA.

6.1 Neutrometer™-HD

The Neutrometer™–HD consists of a package of passive integrating neutron detectors configured for the measurement of high dose bursts of neutrons. It is intended for in-beam calibration of medical linear accelerators and other high-rate neutron measurements, particularly useful when electronic instruments cannot be used. Each superheated drop vial contains 4 mL of sensitive material in proprietary aqueous gel and calibrated plastic pipette (calibration in units of 0.01 ml). Neutron dose equivalent ranging from 0.5 to 50 mSv can be measured using this detector with a maximum dose rate limitation of 4 $Gy(min)^{-1}$ in a high-energy photon beam. This commercial neutron dosemetor is calibrated to measure the neutron dose equivalent, but not neutron dose (D). There is a beam quality factor, Q, involved in the conversion from dose to dose equivalent $H=QD$ which is a radiation protection parameter of units Sieverts, Sv. The recommended values of quality factor, Q, for neutrons range from 5 to 20 depending on neutron energy ICRP report 60 [ICR91]. The detector's response to different neutron energies is not constant and it is less sensitive at epithermal energies [D'Er98a, Nat93].

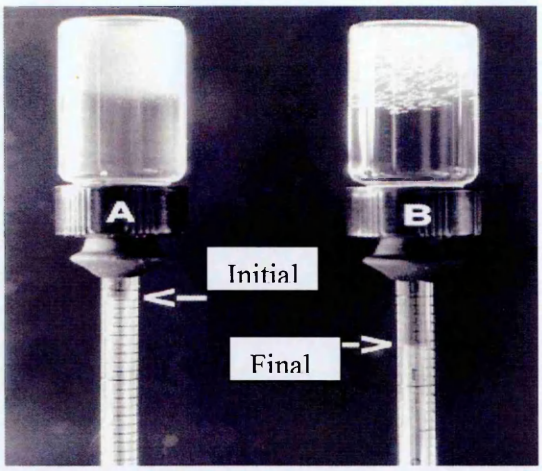

Fig 6.1: Neutrometer™-HD showing the vial containing the SDD and the graduated pipette and also the initial and final gel displacement before and after irradiation respectively.

6.2 Neutrometer™–S

The Neutrometer™–S is a versatile, pen-shaped high sensitivity passive dosemeter specially designed for out of beam neutron measurements: low-level neutron exposures. Unlike Neutrometer™–HD, this dosemeter produces bubbles which are counted directly to determine the neutron dose equivalent. It is reusable and can provide information on dose equivalent neutron exposure over a wide energy range: thermal to fast 66 MeV. The dosimeter is encased in a transparent protective plastic material to prevent it from breaking and clear enough for the bubbles to be counted. In the bottom of the inner tube is a quantity of gel containing a large number of micro drops of the superheated liquid. The drops are too small to be seen individually but cause the gel to have a cloudy appearance. Above the gel is a clear piston which is impervious to the gel and gas and which can move up the tube. The dosemeter is stored in the upright position so that large bubbles can migrate to the piston where they are annihilated but used in the horizontal orientation. In a way, Neutrometer™-S operates in the same manner as the BD-PND but does not require the application of pressure to clear the bubbles in to order reset for future use.

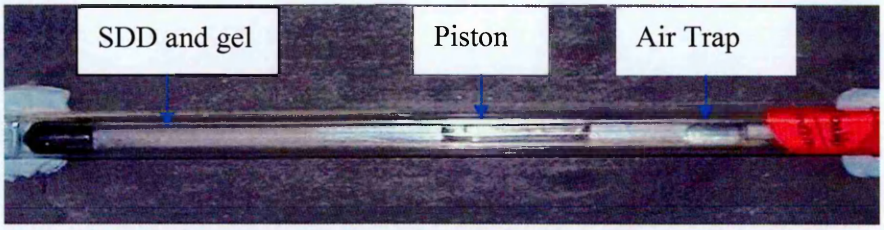

Fig 6.2: Neutrometer™ S in the irradiation position (horizontal).

6.3 Percentage composition of R-12

The superheated drop material employed here is a halocarbon: (CCl_2F_2) commercially known as Freon 12 or R-12. The elemental composition by weight is 9.6% hydrogen, 23.4% carbon, 66.3% oxygen, 0.24% fluorine, and 0.46% chlorine and its physical density is 1.14 g/cm^3 [Nat93] and boiling point –29.8°C. The sensitivity of SDDs depends on their chemical composition and their degree of superheat, that is, their operating temperature. These detect high linear energy transfer (LET) particles only – neutron recoils in this case – and completely discriminate against photons [D'Er98b]. The neutron detection efficiency, or fluence response, that is, number of bubbles per incident neutron per square centimetre of the R-12 emulsions as a function of operating temperature and neutron energy is shown in figure 6.3. The response curves indicate that R-12 emulsions are sensitive to fast neutrons – through the recoils they generate inside or next to the superheated drops, but also to thermal and intermediate neutrons. The thermal response occurs as the droplets contain chlorine and are sufficiently superheated to be vaporised by the exothermic capture reaction $^{35}Cl(n,p)^{35}S$. This reaction releases energy of 615 keV and creates densely ionising 17 keV sulphur ions.

Due to the lack of monoenergetic beams in the intermediate energy range, the response has been determined using MCNP simulations. Figure 6.4 shows the combined experimental and simulation response for R-12 emulsions at 30°C [D'Er98b] against the kerma-equivalent-factor $k_\Phi Q_n$ [Gua97, Sie82]. This is the average tissue kerma of neutron recoils from first collisions with a small element of soft tissue, weighted by the quality factor of the recoils.

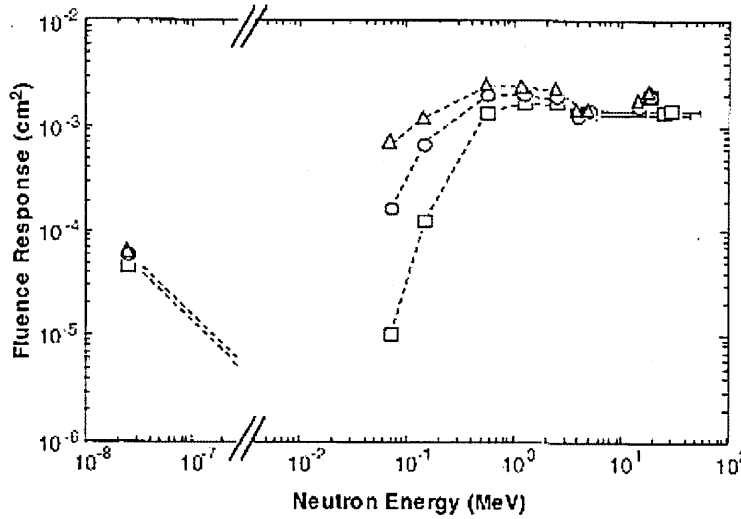

Fig. 6.3: Fluence response of a dichlorofluoromethane emulsion as a function of neutron energy, measured at 25 (□), 30 (○) and 35 (Δ) degrees Celsius [D'Er98b, D'Er94].

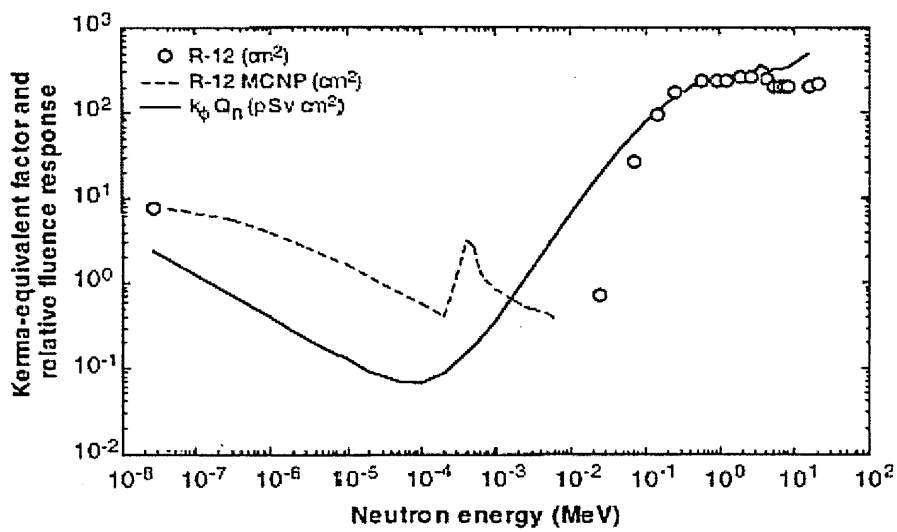

Fig. 6.4: Fluence response of superheated drop detectors verses fluence-to-kerma factor $k_\Phi Q_n$, plotted as a function of neutron energy [D'Er90, D'Er98b].

It is the ideal response function for the measurement of dose equivalent at depth in tissue, provided charged particle equilibrium is attained at the point of measurement. Figure 6.4 seems to imply that R-12 emulsions can be used to measure dose equivalent values at depth in tissue irrespective of the neutron energy. It is worth mentioning that this detector's response to different neutron energies is not constant and it is less sensitive at epithermal energies [D'Er98b, Nat93]. The accuracy

associated with the use of R-12 emulsions is estimated at 20% [Din02, D'Er98] taking into account calibration uncertainties, temperature fluctuations, discrepancies between detector response and kerma factor, and also during the read-out.

Table 6.1: Chemo-physical data for SDD emulsions, ICRU recommended TE composition, TE liquid [D'Er98] and water. Elemental composition by weight in percent

Material	H	C	O	N	F,Cl	Density ($g\ cm^{-3}$)
SDD	8.8	28.2	62.5	-	0.5	1.2
ICRU TE	10.1	11.1	76.2	2.6	-	1.0
TE liquid	10.2	11.1	76.1	2.6	-	1.1
Water	33.3	-	66.7	-	-	1.0

Based on the above-mentioned properties of the R-12 emulsions, a batch of Neutrometer™ -HD consisting of 20 units of approximately 4.5 mL vials and 10 graduated pipettes and 10 units of Neutrometer™-S were acquired from Apfel Enterprises (New Haven, CT, USA).

6.4. Neutron dose equivalent calculation

6.4.1 Neutrometer™-HD

The bottom part of the Neutrometer™ -HD is radiation sensitive, containing millions of droplets suspended in a thick gel which prevents the drops from migrating. These detectors are of the volumetric type and the vial cups are connected to the graduated pipettes by adding drops of "top-off" gel supplied with the detectors to indicate the initial position or mark in the pipette before irradiation. When the vial is irradiated, an amount of gel equivalent to the total volume of the expanded bubbles is displaced into the pipette as shown in figure 6.1. This allows for an immediate reading of the response while the detector is entirely passive and also the ambient temperature is recorded in order to apply a temperature correction factor since the detectors were calibrated at 20°C, according to the manufacturer. The correct displacement is obtained by multiplying the pipette displacement by the corresponding factor as in Table 6.2.

The correlation between neutron ambient dose equivalent and the mean gel displacement for the batch of dosemeter used in this work is not linear as shown in figure 6.4. Therefore, the doses for the initial and final displacements were calculated and the difference represented the dose due to the irradiation.

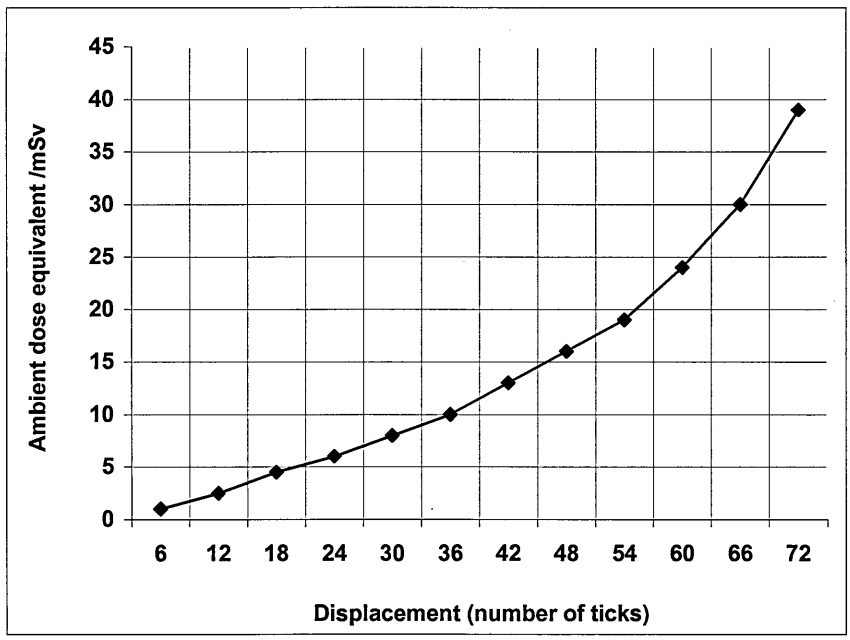

Fig. 6.4: The correlation between neutron dose equivalent and mean gel displacement for the dosemeter batch used for the measurement. Copied from Neutrometer-HD instruction manual.

To convert from displacement to dose, the following formula provided by Apfel Enterprises was used, that is, the neutron ambient dose equivalent D is given by:

$$D = - A \ln (1 - BV) \qquad (6.1)$$

where A = 17 and B = 1.25 are constants for in-air measurements and V the volume of gel displaced. For in phantom measurements, a kerma equivalent value was used to compute dose equivalent values corresponding to A = 14.5. This formula yields ambient dose equivalent values based on the fluence to dose conversion factors from ICRP report number 74 and ICRU report number 57 and is valid up to a maximum displacement of 0.80 mL on the graduated pipette. It should be noted here that the

constants A and B are specific for this batch of SDDs used in this work and therefore cannot be used for other SDDs.

Table 6.2: Temperature sensitivity correction factors for the volume displacement in the graduated pipette for the Neutrometer-HD. Taken from Neutrometer-HD instruction manual.

Temperature/ °C	Correction Factor	Temperature/ °C	Correction Factor
16	1.24	24	0.81
17	1.17	25	0.77
18	1.11	26	0.73
19	1.05	27	0.69
20	1.00	28	0.65
21	0.95	29	0.62
22	0.90	30	0.59
23	0.85	31	0.55

6.4.2. Neutrometer™-S

Each tiny bubble in the emulsion of the Neutrometer™-S acts as a point detector. In a radiation field the bubbles grow on interaction and can be seen by the naked eye and thus counted. In this work, it was more convenient to count bubbles not exceeding 50, consequently, the accumulated number of bubbles did not exceed this number even though in our trial irradiations as many as 100 bubbles were counted. The dosemeters were calibrated in air and water phantom at 20°C and the calibration factors were bubble per 1.02 and 0.91 μSv, respectively. Temperature correcting factors provided for ambient dose equivalent calculations are provided in Table 6.

Table 6.3: Temperature sensitivity correction factors (multiply) for Neutrometer™–S. Taken from Neutrometer™–S instruction manual.

Temperature /°C	Correction Factor
18	1.02
19	1.01
20	1.00
21	0.99
22	0.98
23	0.97
24	0.95
25	0.94

6.5 Transportation of dosemeters

Both dosemeters, Neutrometer™-S and Neutrometer™-HD, were shipped to the University of Surrey, UK from Apfel Enterprises Inc. USA in refrigerated containers that kept them cold for the period due to their temperature sensitivity. They were stored in a refrigerator (not frozen) when not in use and only taken out for the experiments. The detectors were transported in an ice chest containing ice cubes from the University of Surrey, Guildford to St Bartholomew's Hospital, London, where the experiments were conducted. The treatment room in the hospital is air-conditioned so the ambient temperature was fairly constant at 21°C. The elapse time for the dosemeters to attain room temperature on removal from the ice chest was approximately 20 minutes. Prior to their use in the hospital, the neutron dose equivalent or detector response as a function of energy, was cross-checked at the National Physical Laboratory (NPL) Teddington, UK, and were found to compare reasonably well with manufacturer's data. Three monoenergetic (256keV, 469keV and 5.5MeV) neutrons produced from the Van de Graaff accelerator were used.

6.6 Neutron dose equivalent measurements

6.6.1 Photon sensitivity

The neutron dose equivalent due to photoneutrons produced in the output of the Varian Clinac 2100C operated at 15 MV was determined in air and in a water phantom. To confirm that the dosemeters are insensitive to photons at room temperature, one of each type was exposed to ^{137}Cs (661.64 keV, 185 kBq), ^{60}Co (1.17 MeV and 1.33MeV, 130 kBq) in the University of Surrey for several hours and also 6 MV photons from the linear accelerator in the hospital. In all these cases no visible bubbles were observed.

6.6.2 In-air measurements

6.6.2.1 Measurements using Neutrometer™-HD

In all the in air measurements, seven (7) Neutrometer™-HD dosemeters were arranged on the couch, along the patient plane and in upright positions as shown in the schematic diagram as shown in figure 6.5 with the aid of foam blocks and also spirit level to ensure that the detectors were of the same height and upright. Since most of the superheated emulsions in the vials are deposited at the bottom of the vial (when connected to the graduated pipette and erected it becomes the top part of the dosemeter) the source-to-detector surface distance was maintained at 100 cm (standard source-to-surface distance, SSD) all through the measurements. The central detector was positioned on the beam central axis and tagged the zero mark in terms of distance measurement. Detectors positioned towards the gantry (**G**) were in the "negative" distance while those away (**T**) in the "positive" distance as shown in figure 6.5. The distance from the edge of each selected field size to the first, second and third detector, on each side of the central detector, were 10, 20 and 50 cm respectively. The field sizes considered in this experiment were 5x5 cm^2, 10x10 cm^2, 20x20 cm^2 and 40x40 cm^2. In effect, the distances of the first two detectors on both sides of the central detector were 12.5 cm, 15 cm, 20 cm and 30 cm for 5x5 cm^2, 10x10 cm^2, 20x20 cm^2 and 40x40 cm^2 fields respectively. By varying the field size it was possible to relate the effect of the field size on the neutron dose equivalent in the patient plane and the maze. Also investigated was the relationship of the gantry rotation with the neutron dose equivalent in the patient plane and the maze. In this case the gantry was rotated through 90°, 180° and 270° for all the above-mentioned field sizes and irradiation carried out in each case.

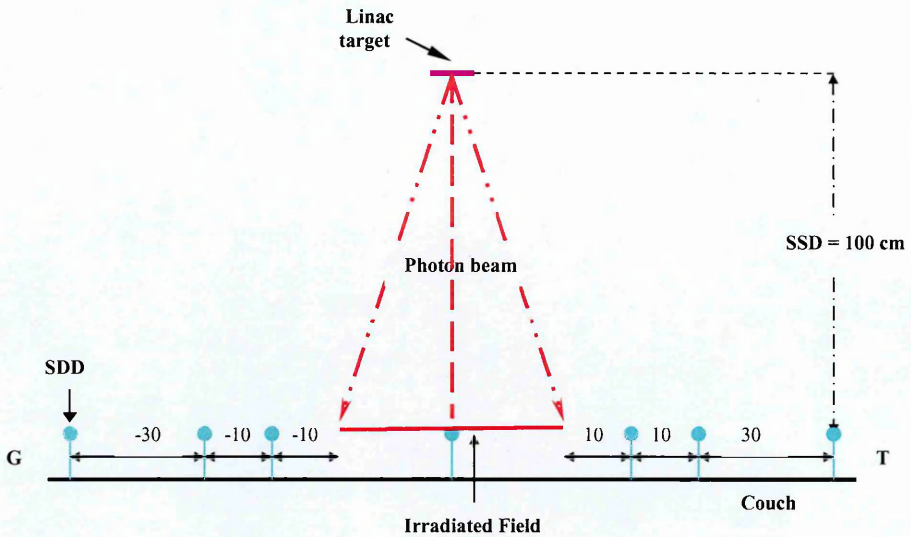

Figure 6.5a: Schematic diagram of experimental set-up for in-air measurements using Neutrometer™-HD dosemeters at 0° gantry angle.

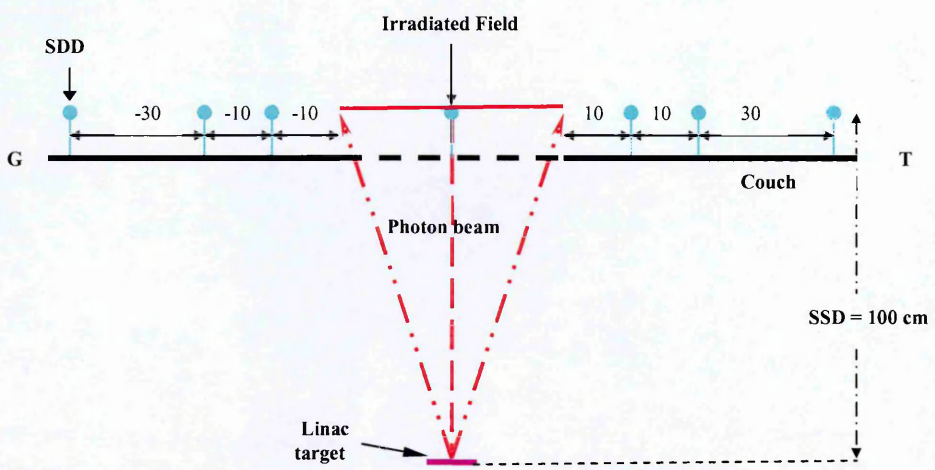

Figure 6.5b: Schematic diagram of experimental set-up for in-air measurements using Neutrometer™-HD dosemeters at 180° gantry angle. The beam goes through the racket in the couch.

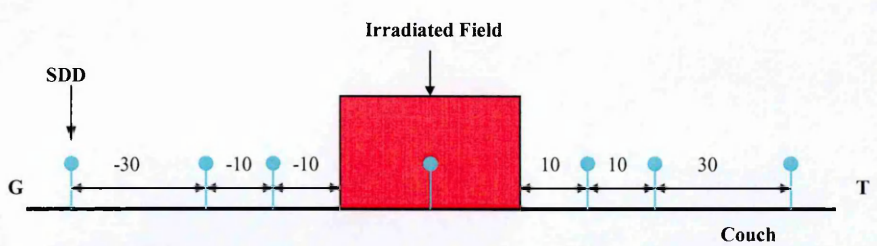

Figure 6.5c: Schematic diagram of experimental set-up for in-air measurements using Neutrometer™-HD dosemeters at 90° and 270° gantry angle.

6.6.2.2 Measurements using Neutrometer™-S

The neutron dose equivalent in the maze and the control panel were measured using the Neutrometer™-S since these points are further away from the isocentre. With reference to figure 6.6 two of these were placed at points ***A*** and ***B*** in the maze entrance from the treatment room, one at the inner surface facing the maze of the shielding door point ***D*** and another one at the 'duct' entrance, point ***C*** in the control panel area. The 'duct' is a narrow tunnel from the treatment room to the control panel through which connecting cables are passed from the treatment room to the control panel area. With the exception of the detector placed at the entrance of the 'duct', all others were positioned at the same height as the SSD to ensure uniformity. The spirit level was used to position the detectors horizontally.

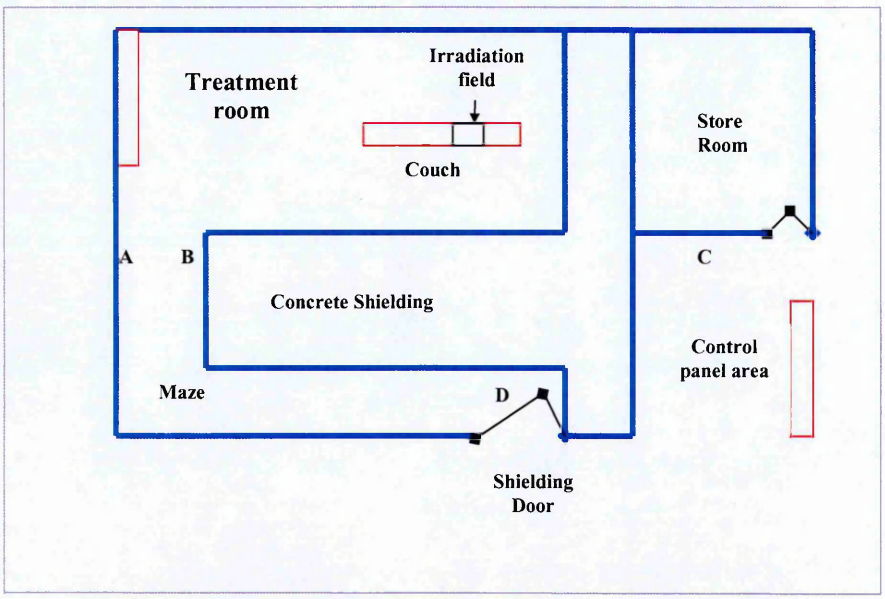

Fig.6.6: Plan view of linac bunker for Varian Clinac 2100C at St Bartholomew's Hospital (not drawn to scale).

6.6.3 In-phantom measurement

A 25x60x45 cm^3 (internal dimensions) Perspex water phantom was designed and constructed at the Physics Department workshop, University of Surrey for the purpose of investigating the variation of neutron dose equivalent with depth in water within and outside the photon beam. This particular size of the phantom was chosen due to the maximum permissible weight the couch can support and also to study the neutron

dose distribution up to a depth of 20 cm. The gantry was maintained at the 0^{o} angle all through the measurements and field sizes 5x5 cm^2, 10x10 cm^2 and 20x20 cm^2 in turn were investigated. Four Neutrometer™-HD dosemeters were used in this work due to the space available and also to ensure maximum scatter contribution from the 20x20 cm^2 field size. One detector was placed on the beam axis and the others at a distance of 10, 20 and 30 cm as shown in figure 6.7 from the field edge of each chosen field size to investigate the neutron dose equivalent outside the field. The top of the water was maintained at 100 cm SSD all through the experiments. The second parameter investigated simultaneously with the first was the variation of the neutron dose equivalent with depth. For every chosen field size, the neutron dose equivalent was measured at depths of 1, 5, 10 and 20 cm in the water phantom. Prior to filling the phantom with water, the detectors were irradiated in the 'empty' phantom to determine the neutron dose equivalent contribution, if any, from the Perspex used to construct the phantom. The estimation of the neutron dose equivalent in the maze and at the control panel was also done simultaneously with the phantom measurement. In contrast to the in-air measurement, the dose equivalent in the maze were measured with varying water level above the detectors in the phantom.

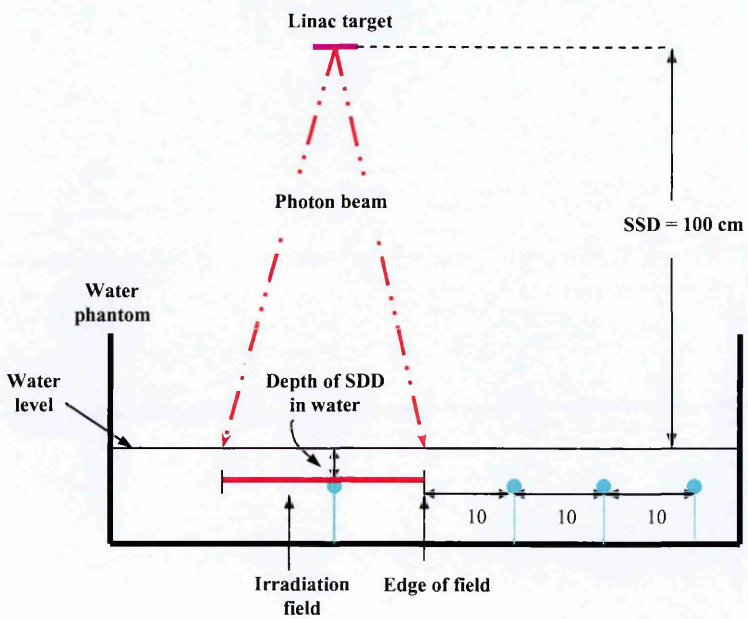

Fig. 6.7: Schematic diagram of experimental set-up for in-phantom measurements using Neutrometer™-HD dosemeters. The distance between adjacent detectors is 10 cm.

Fig. 6.8: A 25x60x45 cm^3 (internal dimensions) Perspex water phantom used for the in phantom measurements. The SDDs are as shown in the erect (irradiation) position.

6.7 Results and discussion

The neutron dose equivalent per unit photon dose measured in-air and water phantom using superheated drop dosemeter are discussed herein. The detecters first proved to be insensitive to photons when no visible bubbles were observed after irradiation with 6 MV photons. It also confirmed the non-existence of background radiation during measurement which was very significant since any bubble formation was absolutely due to photoneutrons. The dosimetry of neutrons for radiation protection is a very complex discipline and the measuring and characterisation of mixed neutron-photon fields is an uphill task. It is generally acknowledged that the total uncertainty associated with SDDs' measurement including that of calibration carried out by the manufacturers is approximately 20% [Din02, D'Er98c, D'Er01]. Detailed results of all measurements are available in the Appendix.

6.7.1 In-air measurement

Gantry angle 0^o

Figure 6.9a shows the variation of neutron dose equivalent per unit photon dose on the beam central axis as a function to field size. There is a gradual increase in neutron dose equivalent from 1.41 ± 0.11 $mSvGy^{-1}$ to 1.74 ± 0.09 $mSvGy^{-1}$ for 5x5 cm^2 and 40x40cm^2 fields respectively. The neutron dose equivalent recorded for the

10x10cm^2 was 1.57 ± 0.10 mSvGy^{-1} whilst that for the 20x20cm^2 was 1.54 ± 0.10 mSvGy^{-1}. The neutron dose equivalent per unit photon dose for the 10x10 cm^2 is consistent, with that measured from 15 MV Siemens Mevatron by Ongaro et al [Ong00], that is, 1.67 mSvGy^{-1} at 100 cm SSD using bubble detectors. The neutron dose equivalent measured by Lin et al [Lin01] using BD-PND bubble detectors for a 15 MV Siemens Primus medical linac for a 40x40 cm^2 field at the isocentre was 1.84 ± 0.09 mSvGy^{-1} as against 1.74 ± 0.09 mSvGy^{-1} obtained in this work. From 5x5 cm^2 to 40x40 cm^2 field size the neutron dose equivalent increased by a factor of 1.2. This seems to suggest that the neutron dose equivalent per unit photon dose is apparently independent of field size and primarily produced in the target, flattening filter and the primary and secondary collimators. These form the fixed part of the linac head. The discrepancy in the apparent decrease in neutron dose equivalent with field size at 20x20 cm^2 field is interesting since the same trend was observed when the measurements were repeated. A school of thought by Zhu and Bjarngard [Zhu95] suggests that maximum scatter of radiation in the treatment head occurs with this size of collimator opening and therefore less neutrons getting to the detector. This requires further investigation in order to confirm or otherwise this observation.

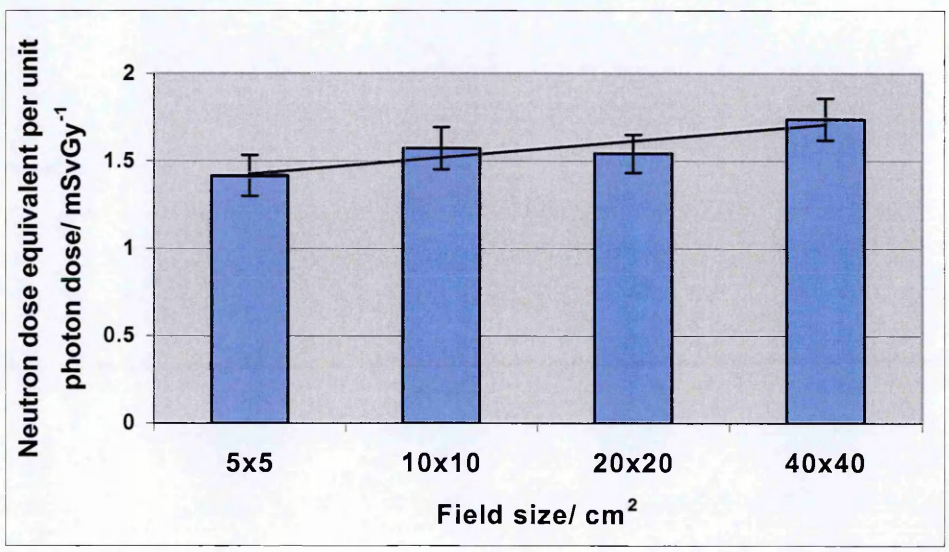

Fig.6.9a: Variation of neutron dose equivalent per unit photon dose at 100 cm SSD on the beam axis as a function of field size.

Figure 6.9b shows the variation of the neutron dose equivalent per unit photon dose with distance on and off the central beam axis at distances 10, 20 and 50 cm from the field edge of 5x5 cm^2, 10x10 cm^2, 20x20 cm^2, and 40x40 cm^2 field sizes. The measurements were taken outside the irradiation field to assess the trend of the neutron dose equivalent outside the treatment field. With the exception of the dose equivalent for the 20x20 cm^2 field which shows a distinctly higher dose at 10 cm on both sides of the field, the rest show very little variation. It is apparent that the neutron dose equivalent per unit photon dose outside a given field size at distances greater than 10 cm from the field edge is virtually constant and independent of field size. This is consistent with findings by D'Errico et al [D'Er98b].

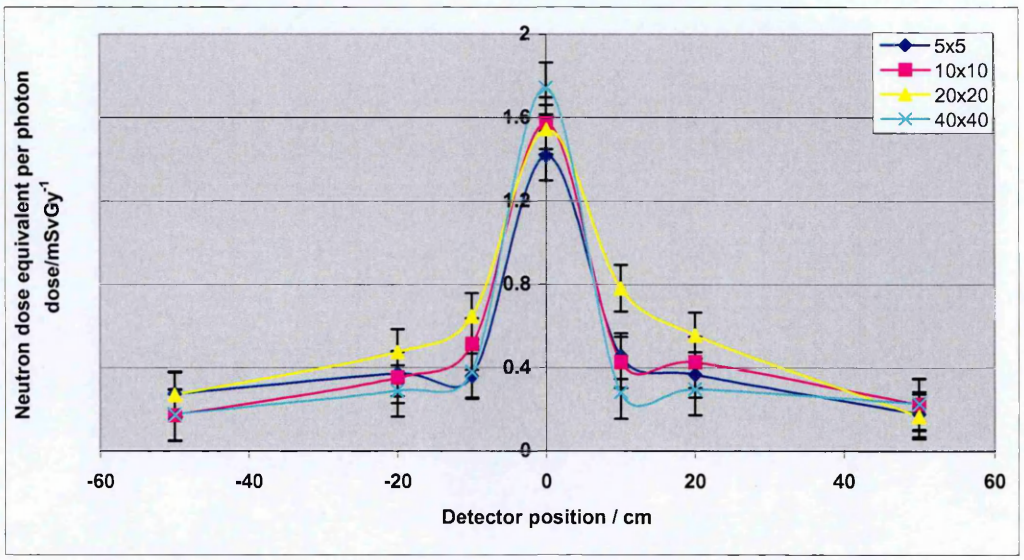

Figure 6.9b: Variation of the neutron dose equivalent per unit photon dose with distance on and off the central beam axis.

Other gantry angles

The angular distribution of neutron dose equivalent per unit photon dose on the beam axis is shown in figure 6.10 and Table 6.4. Figure 6.10 shows graphical representation with the corresponding data in Table 6.4 of the angular spread of neutron dose equivalent on the central beam axis as a function of field size. For the 5x5 cm^2 field, the highest dose equivalent of 1.61 ± 0.11 $mSvGy^{-1}$ occurs at 180° whilst the lowest dose equivalent for the 10x10 cm^2 field was recorded at 270° gantry angle. Neutron dose equivalent of 1.82 ± 0.10 $mSvGy^{-1}$ and 1.79 ± 0.10 $mSvGy^{-1}$

were recorded for 90° and 180° respectively for the 10x10 cm^2 field and also 1.43 ± 0.10 $mSvGy^{-1}$ for 270°. Determination of neutron dose equivalent with the 20x20 cm^2 field size is much different, the highest dose occurs at 0° whiles the lowest at 180°. Neutron dose equivalent of 1.27 ± 0.10 $mSvGy^{-1}$, 1.04 ± 0.10 $mSvGy^{-1}$, and 1.37 ± 0.10 $mSvGy^{-1}$ for 90°, 180°, and 270°, respectively.

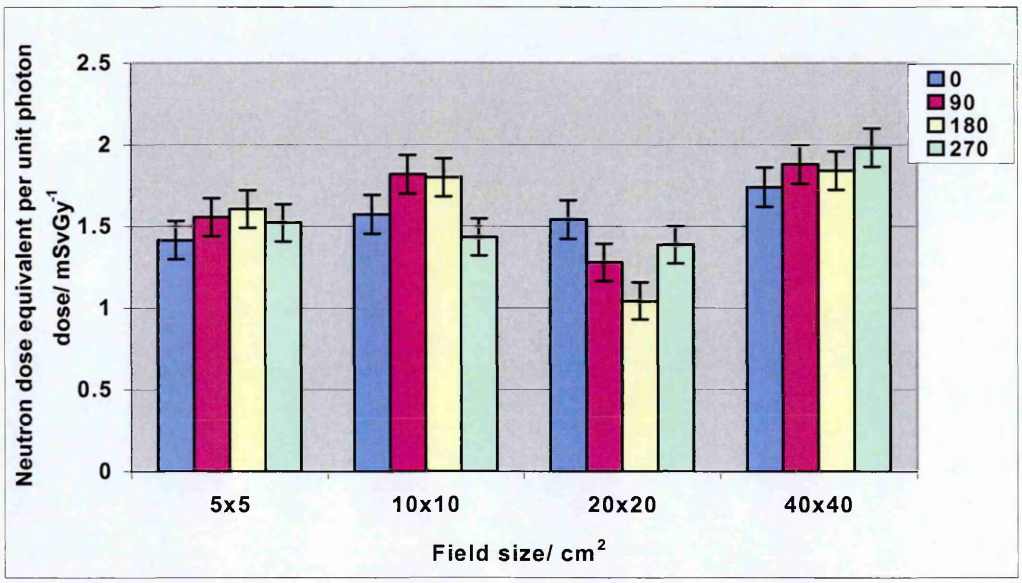

Fig. 6.10: Angular spread of neutron dose equivalent per unit photon dose on the beam axis as a function of field size.

Table 6.4: Table of results showing the variation of the neutron dose equivalent ($mSvGy^{-1}$) on the beam axis with field size and gantry angles.

Field size/ cm^2	Gantry angle			
	0°	90°	180°	270°
5x5	1.41±0.11	1.55±0.11	1.61±0.11	1.52±0.11
10x10	1.57±0.10	1.82±0.10	1.79±0.10	1.43±0.10
20x20	1.54±0.10	1.27±0.10	1.04±0.10	1.37±0.10
40x40	1.74±0.09	1.88±0.09	1.84±0.09	1.98±0.09

The neutron dose equivalent for the 20x20 cm^2 on the beam axis showed the lowest amongst the field sizes investigated. This measurement was repeated with fresh detectors but the same observations were made. As expected the 40x40 cm^2 field

gives the highest neutron dose equivalent per unit photon dose with the highest occurring at 270°. The neutron dose equivalent of 1.88 ± 0.09 $mSvGy^{-1}$, 1.84 ± 0.09 $mSvGy^{-1}$, and 1.98 ± 0.09$mSvGy^{-1}$ was recorded for 90°, 180°, and 270°, respectively. These results confirm the complexity and the random non-isotropic nature of the neutron field around the medical linear accelerator after attenuation in the head and multiple scattering off the concrete walls of the treatment room.

The variation of angular spread with detector position from the edge of the field as a function of the field size is given in the Appendix. The neutron dose equivalent outside the 10x10 cm^2 field show higher values than the other field sizes for 0°, 90°, 180°, and 270° gantry rotations. At distances greater than 20 cm outside the irradiation field, the neutron dose equivalent is nearly independent of field size and this can be attributed to the effect of scattered neutrons from the walls of the treatment room which uniformly irradiate the detectors.

6.7.2 Phantom measurement

Figure 6.11 shows the variation of the central axis neutron dose equivalent per unit photon dose with depth in a water phantom for 5x5 cm^2, 10x10 cm^2 and 20x20 cm^2 field size. The highest dose equivalent was observed at 1 cm depth for the 5x5 cm^2 field and the lowest at 20x20 cm^2. The measured values at 1 cm depth were 1.805±0.087$mSvGy^{-1}$, 1.415±0.091$mSvGy^{-1}$ and 1.348±0.088$mSvGy^{-1}$ for 5x5 cm^2, 10x10 cm^2 and 20x20 cm^2, respectively. The value obtained for the 10x10 cm^2 compares reasonably well with ~1.45 $mSvGy^{-1}$ measured by D'Errico et al [D'Er01]. From the depth of 1 cm to 5 cm, the dose equivalent falls off more sharply from 1.805±0.087 to 0.796±0.086 $mSvGy^{-1}$ (55.5%) for the 5x5 cm^2 field compared with 1.415±0.091 to 0.825±0.085 $mSvGy^{-1}$ (42%) and 1.348±0.088 to 0.695±0.088$mSvGy^{-1}$ (48%) for 10x10cm^2 and 20x20cm^2, respectively. The central axis depth of 50% maximum neutron dose equivalent, d_{H50}, measured in this work was less than 5 cm for 5x5 cm^2 but greater than 5 cm for 10x10 cm^2 20x20 cm^2. 50% maximum neutron dose equivalent, d_{H50} for a 10x10 cm^2 field size of between 7.5cm and 8.5cm for photoneutrons produced by photon energies between 10 and 18 MV have been reported by D'Errico et al [D'Er01].

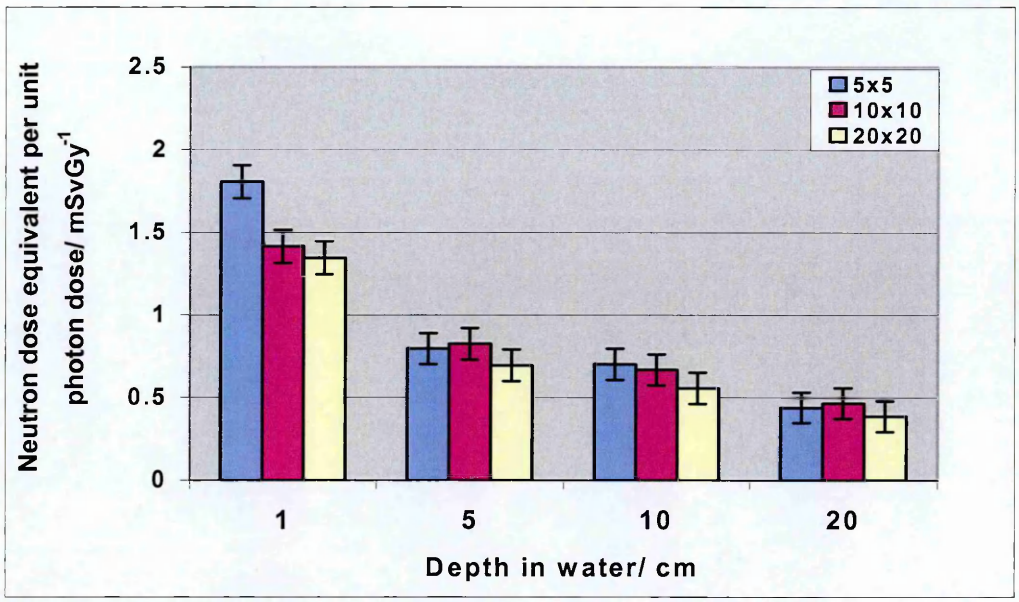

Fig. 6.11: Variation of neutron dose equivalent per unit photon dose on the beam central with field size as a function of depth in water.

For smaller fields, there are more energetic or high-energy neutrons but much less in quantity due to the small collimator opening at depths closer to the surface but this effect diminishes at greater depth. The most energetic neutrons are found at and close to the beam central axis since the most energetic photons that produce neutrons in the forward direction are thought to be on the beam axis. For a smaller field size the mean photoneutron energy is much higher compared to larger fields due to a smaller low energy photoneutron component. From 5cm to 20cm depths the dose fall off is independent of field size, that is, 45% for all field sizes. This is computed from 0.796 ± 0.086 mSvGy^{-1} to 0.439 ± 0.083 mSvGy^{-1} for 5x5 cm^2, 0.825 ± 0.085 mSvGy^{-1} to 0.466 ± 0.084 mSvGy^{-1} for 10x10cm^2 and 0.695 ± 0.088 mSvGy^{-1} to 0.386 ± 0.087 mSvGy^{-1} for 20x20 cm^2. More energetic neutrons travel longer radiation distances before attaining thermal equilibrium in water before being captured. At greater depth the neutron component on the central axis is virtually the same for all fields since the less energetic neutrons attain thermal equilibrium in the water and undergo radiative capture reaction $^1H(n,\gamma)^2H$ producing gamma-rays of energy 2.223 MeV. Hence, the almost constant neutron equivalent dose irrespective of field size observed on the central beam axis at greater depth in water.

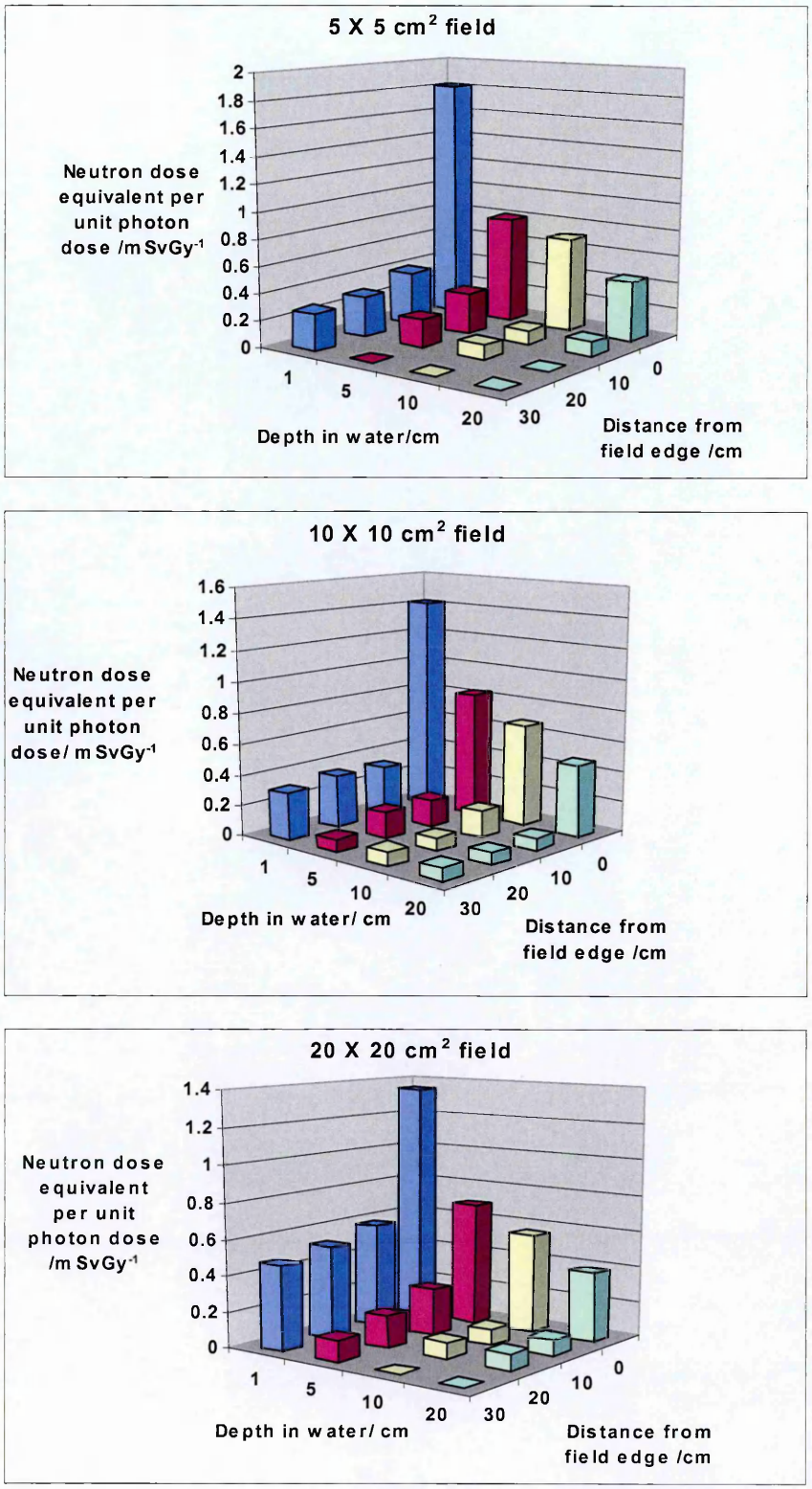

Fig. 6.12: Variation of neutron dose equivalent per unit photon dose with respect to depth and distance from field edge for 5x5 cm^2, 10x10 cm^2 and 20x20 cm^2 field sizes.

Figure 6.12 shows the distribution of neutron dose equivalent per photon dose as a function of depth and distance from field edge for field sizes 5x5 cm^2, 10x10 cm^2 and 20x20 cm^2. At a depth of 1 cm the dose equivalent at 10, 20, and 30 cm from the edge of each field is virtually constant with the exception of the 20x20 cm^2 field which shows a marginally higher dose equivalent. The least dose for each field size is observed at the greater depth, 10 and 20 cm and further from the field edge at 20 cm and 30 cm. This effect is more predominant in the 5x5 cm^2 field in contrast to the 10x10 cm^2 and 20x20 cm^2 fields. The neutron dose equivalent determined for the 10x10 cm^2 field is consistent with work done D'Errico et al [D'Er01, D'Er98b]. The data for figure 6.12 are available in the Appendix.

6.7.3 Neutron dose equivalent in maze

In-air (without water phantom)

Table 6.5 shows the variation of neutron dose equivalent in the maze and control panel area with gantry rotation for in-air measurement for the 5x5 cm^2, 10x10 cm^2, 20x20 cm^2, and 40x40 cm^2 fields. Positions A, B, C and D are locations as defined in figure 6.6 (pp-99) the schematic diagram of the linac bunker. It is quite obvious that position A, the outer surface wall at the maze entrance from the treatment room side, received the highest neutron dose equivalent irrespective of gantry angle and field size. The highest dose equivalent is observed with the 5x5 cm^2 and 10x10 cm^2 fields with the greatest, 16.35 ± 3.86 $\mu SvGy^{-1}$, at 180° for the 10x10cm^2 field. The inner surface wall B, received a much smaller neutron dose compared to position A. With the exception of a neutron dose equivalent per unit photon dose of 0.86± 0.80$\mu SvGy^{-1}$ measured at the shielding door (D) for the 10x10cm^2 at 0° gantry angle, it is apparent that there is adequate neutron shielding in place. Neutron dose equivalent as low as 1.02 μSv, corresponding to one bubble can be recorded with this detector. The neutron dose equivalent was measured in the same (horizontal) plane as the source-to-detector distance. The neutron dose equivalent outside of this plane, such as, on the floor and ceiling is not known and should be a subject of further investigation. Also unknown is whether the maze is lined with neutron-absorbing materials as there is no documentation at the hospital on this in the shielding of the bunker.

At gantry angles 90° and 270° energetic neutrons are incident on opposite side of two parallel primary shielding surfaces of the treatment room. The neutrons are most likely to undergo multiple scattering off the walls assuming they follow a straight path until the neutrons attain thermal equilibrium in the treatment room and inevitably some neutrons enter the maze. At 180° the field of view of the photon beam is towards the ceiling as such neutron scattering occurs with the couch and in the ceiling and may result in a more wide spread of neutrons compared to 90° and 270° gantry angles. The assumption is that much more neutrons enter the maze at 180° and 0° gantry angle rotation compared to 90° and 270° hence the observed neutron dose equivalent in the maze with respect to gantry angle. As shown in Table 6.5, with the exception of the neutron dose equivalent for 20x20 cm^2 field size which shows a marginally lower value of 3.29±1.68 $\mu SvGy^{-1}$ at 180° and 15.49±3.75 $\mu SvGy^{-1}$for 10x10 cm^2 at 270°, the neutron dose equivalent for the 180° and 0° gantry angles are much higher than those of 270° and 90°.

Table 6.5: Table of results showing the variation of neutron dose equivalent per photon dose ($\mu SvGy^{-1}$) in the maze at detector position A (Figure 6.6) with field size and gantry angle.

	Gantry angle			
Field size/ cm^2	0°	90°	180°	270°
5x5	*10.10±3.22*	8.25±2.90	*10.08±3.22*	9.16±3.10
10x10	*13.77±3.5*	10.33±3.10	*16.35±3.86*	15.49±3.75
20x20	*8.19±2.66*	3.28±1.68	*3.29±1.68*	3.28±1.68
40x40	*8.60±1.97*	3.91±1.80	*6.26±2.27*	0.78±0.70

Water phantom on couch

Neutron dose equivalent per unit photon dose was investigated for only the 0° gantry angle since other gantry orientations discussed in the in-air measurement in the previous section will result in the beams penetrating the Perspex before reaching the detectors. Table 6.6 shows the neutron dose equivalent recorded at the respective

detector positions in the maze for field sizes 5x5cm^2, 10x10 cm^2 and 20x20 cm^2 and the water level in the phantom. The 10x10 cm^2 field shows a drop in neutron dose equivalent from 8.45±2.80μSvGy^{-1} and 3.38±1.77 μSvGy^{-1} for 17cm column of water in the phantom, to 2.53±1.53 μSvGy^{-1} for 36cm column of water for both detector positions A and position B at the maze entrance as in figure 6.6. In contrast, the dose equivalent for the 20x20 cm^2 field shows an increase from 6.44±2.38 μSvGy^{-1} for 17cm column of water to 17.7±3.96 μSvGy^{-1} for 36cm column of water for detector position A but no measurable dose equivalent was recorded at detector position B. In the case of the 5x5 cm^2 field size, a mixed trend was observed, the neutron dose equivalent increased with increasing water level in the phantom up to 26cm but fell at level 36cm. The highest neutron dose equivalent of 10.8±3.35 μSvGy^{-1} was measured for this field at detector position A for the water column of 26cm. As expected no measurable neutron dose equivalent was recorded at the control panel (C) and the inner surface of the shielding door (D). Since the measurements with the phantom in a way replicate that of a patient, by considering the densities of human tissue, tissue equivalent material and water there is a measurable neutron dose equivalent in the maze during patient treatment.

Table 6.6: Table of results showing the variation of neutron dose equivalent per photon dose (μSvGy^{-1}) at detector position A in the maze (Figure 6.6) with water level in phantom.

	Water level in phantom/ cm			
Field size/ cm^2	17	21	26	36
5x5	3.60±1.94	6.30±2.46	10.80±3.35	7.20±2.74
10x10	8.45±2.80	6.76±2.50	5.07±2.17	2.53±1.53
20x20	6.44±2.38	8.04±2.66	12.10±3.26	17.7±3.96

The neutron dose equivalent in the maze was measured in the same plane (horizontal) as the source-to-surface distance of 100 cm of the linac with the exception of the detector at position C the point of exit of the duct. There is the possibility of neutrons in other planes such as the ceiling and the floor due to the multiple scattering and the non-isotropic nature of photoneutrons in the treatment

room. Investigation of neutron dose equivalent in the other planes such as the ceiling and floor will enhance the understanding and throw more light on the nature of photoneutrons in the treatment room and maze.

6.8 Conclusions

The neutron dose equivalent arising from the neutron contamination produced mainly from the (γ,n) reaction as a result of photon interaction produced by a medical linear accelerator with energy above 10 MeV may not be negligible when considering the patient and the staff who operate it. The neutron dose equivalent per unit photon dose of a 15 MV Varian Clinac 2100C for various configurations of field size and gantry orientations have been measured in the patient plane at 100 cm source to detector distance (SSD) for in-air and in phantom scenarios using bubble detectors.

The superheated drop detectors (SDD) were used to measure and estimate the neutron dose equivalent per unit photon dose on the beam central axis and at stipulated distances outside the chosen field size in the patient plane. Measurements were also made at positions in the maze and control panel. The measured neutron dose equivalent per unit photon dose in and outside the 10x10 cm^2 field size at 0^o gantry angle compares well with that measured by other workers using similar detector technology, 1.67 $mSvGy^{-1}$ for in air measured by Ongaro et al [Ong00] and 1.45 $mSvGy^{-1}$for phantom measurement at 1 cm depth by d'Errico et al [D'er98] for a 15 MV photon energy linac. The measured values, found in this work, were 1.57 ± 0.10 $mSvGy^{-1}$ and 1.42 ± 0.091 $mSvGy^{-1}$ for in-air and phantom, respectively. Also the neutron dose equivalent for a field size of 40x40 cm^2 found to be 1.74±0.09 $mSvGy^{-1}$ is approximately 0.1 $mSvGy^{-1}$ less than that reported by Lin et al [Lin01]. The neutron dose equivalent per unit photon dose on the central beam axis increased gradually with field size with very little to choose between the 10x10 cm^2 and 20x20 cm^2, however, outside the irradiated field at distances greater than 20 cm and up to 50cm, as measured in this work, it is independent of field size and about 10 to 20% of the central axis dose.

The angular spread of neutron dose equivalent per unit photon dose in the patient plane was investigated for in-air measurement. There was no clear-cut relation of

angular distribution with field size, however, much lower values were recorded for the 20x20 cm^2 field size for all the gantry angles. This trend remained unchanged after a repeat of the measurements. At the maze entrance, the highest value 16±0.84 $\mu SvGy^{-1}$ was observed at 180° for the 10x10 field size. Results show that at 0° and 180° gantry rotation the neutron dose equivalent per photon dose is much higher than those of the 90° and 270° for all field size. This may be due to scattering of neutrons in the ceiling and floor and also the couch resulting in a wider spread of scattered neutrons in the treatment room and the maze. At 90° and 270° the neutrons are assumed to undergo multiple reflection off the two parallel surfaces of the treatment room in direct view of the neutron beam. The neutrons attain thermal equilibrium and are subsequently captured in the concrete wall, as such much less neutrons enter the maze compared to 0° and 180° gantry angles.

For the in phantom measurements, the highest neutron dose equivalent of 1.805±0.087 $mSvGy^{-1}$ was measured at 1 cm depth on the beam central axis for the 5x5 cm^2 field size. On the beam axis, the neutron dose equivalent is independent of field size at depth greater than 5 cm because of the increased probability of neutron thermalisation and capture at greater depth. The depth of 50% maximum neutron dose equivalent is less than 5 cm for 5x5 cm^2 but much greater for 10x10 cm^2 and 20x20 cm^2 field sizes.

The neutron dose equivalent per unit photon dose falls off rapidly to <1 $\mu SvGy^{-1}$ at the shielding door and control panel for both in-air and phantom measurements. The effect is more obvious with the water phantom and the dose equivalent does not vary consistently as a function of field size and gantry angle. The highest neutron dose equivalent per unit photon dose of 17.7±3.96 $\mu SvGy^{-1}$ was recorded on the outer wall of the maze entrance from the treatment room (position A) for the 20x20 cm^2 field size for the in phantom measurements when the water column in the phantom was 36cm, the maximum level investigated. This observation can be due to increased neutron scattering with the phantom.

The neutron dose equivalent per unit photon dose obtained in this work in the patient plane forms less than 0.1% of the photon dose and may be considered negligible. On the contrary, this can represent a risk for healthy tissues and contribute

to secondary malignancy insurgence in a patient receiving treatment. From the measurements in the maze, the effect due to neutrons is nullified in the maze and control panel due to the adequate shielding provided, but from the radiation protection perspective, the situation may be entirely different because of the radionuclides created (not studied here) by the activation of the different materials in the treatment room and the maze through radiative capture reactions. For example, $^{23}Na(n,\gamma)^{24}Na$ in the concrete with a half-life of 15 hrs and gamma energies of 1.369 MeV and 2.754 MeV which can produce additional dose to the radiation workers who enter and leave the treatment facility during the course of the working day. This problem has been investigated by Spyrou and collaborators [Spy91] in and around the bunker of 18MV Varian medical linear accelerator.

7. Monte Carlo simulation of a Medical Linear Accelerator head.

7.1 Introduction and historical sketch

The treatment of deep-seated tumours requires high-energy radiation notably x-rays with penetrating characteristics. The medical linear accelerator is currently the most preferred device for this application though a rekindled interest in cobalt 60 machines for radiotherapy has arisen in recent times due to recent developments such as a dose rate of 2 Gy/min at 100cm SSD [Gla96]. Since 1945, the development of high voltage machines and isotope teletherapy units has produced a dramatic change in the practice of radiotherapy. As technical developments continued to take place, machines that were popular over a period became less popular because new and improved units became available for example linear accelerators, linacs replacing cobalt 60 units in most hospitals.

The development of linear accelerators, linacs, dates back to World War II when the radar was developed from the production of microwave generators in the form of magnetron and the klystrons [Met02]. These devices have the capability of producing intense electromagnetic fields in the microwave cavities and thus enable the acceleration of electrons to near relativistic velocities when incorporated with suitable waveguide structures. By 1960, linacs were in use in nuclear physics, radiotherapy and radiochemistry. Linacs are currently the modality of choice for the production of high-energy x-rays in radiotherapy applications over cobalt 60 units (1.17 and 1.332 MeV γ-rays) of mean energy 1.25 MeV because they have the possibility of producing multiple electron and photon energies up to 25 MeV which permit treatment to a required depth. Also a much higher dose rate is achieved with linacs in the range of 1 to 10 Gy/min which implies shorter treatment times. Another advantage is that linac beams have sharper dose fall-off at the beam edge than cobalt 60 γ-ray

beams in that linacs have a smaller virtual source size of about 2 mm in diameter [Mun88].

The betatron preceded the introduction of the linacs by a few years. Although these can provide x-ray and electron beam therapy over a wide range of energies just as the linac, they are inherently low electron-beam current devices. The x-ray dose rates are low and field sizes are small compared to linacs and even modern cobalt 60 units, however, the electron beam current is adequate to provide high electron dose rates. Protons are currently used to treat cancer patients in very few centres in the USA and in Europe and the UK due to expense [Met02]. One very favourable property is their well-defined Bragg peak that enables the beam to reach a peak of dose deposition at significant depth and a rapid fall off beyond this depth. Proton beams of energy up to 250 MeV are used to treat deep-seated tumours [Hal88, Mul96].

Linacs have become more sophisticated and complex due to the continuous research and development as demand increases. Improvement in applications has been achieved with the use of multileaf collimators and more recently the introduction of intensity modulated radiotherapy (IMRT). The average binding energy per nucleon of the elements that make up the components of the linac head, range between 7 and 9 MeV, therefore, neutron production becomes significant beyond this energy threshold. This is a matter of concern due to the possibility of a significant whole body dose to a patient undergoing treatment, radiation workers involved in the treatment and the general public in the vicinity of the treatment room. In this work, the simulation of the linac head of Varian Clinac 2100C is carried out to estimate the neutron dose equivalent and spectra in the patient plane during photon treatment. These will be compared to experimentally determined values. A major hindrance to this approach is the lack of precise information on the design, construction, and materials of the linac, especially the head given out by the manufacturers due to confidentiality.

7.2 The Linear Accelerator

7.2.1 External features

The common features of all linacs are the couch and gantry. The couch is capable of vertical, horizontal and rotational movements and on which the patient is positioned for treatment. The gantry houses the beam production devices and treatment head and is capable of a complete rotation around the couch or patient enabling different beam angles to be directed at the patient. The treatment head consists of the beam shaping devices internally mounted at the end of the gantry and capable of rotational movement. A dial on the gantry indicates the angular position of the gantry and beam shaping settings while the couch position is observed on a monitor. A typical linac is shown in figure 7.1:

MATERIAL REDACTED AT REQUEST OF UNIVERSITY

Fig. 7.1: External features of a Varian Medical Linear Accelerator, Linac. Taken from Varian Associates website.

7.2.2 Principles of Operation

The linac accelerates electrons linearly to nearly relativistic velocity and high energy using high-power microwaves. The main feature of the linac is the accelerating waveguide, where the electrons are accelerated. Linacs used in radiotherapy accelerate electons either by standing or travelling electromagnetic waves of frequency approximately 3 GHz. The difference between these types of accelerators is in the design of the accelerating waveguide structure. Functionally, the travelling wave structures require a terminating load in order to absorb the residual power at the end of the structure thus preventing a backward reflected wave. In contrast, the standing wave structure provides a maximum reflection of the waves at both ends of the structure so that the combination of forward and reflected waves will give rise to stationary or standing wave. In the standing wave design, the microwave power is coupled into the structure via side coupling cavities rather than through the beam aperture. Such a design tends to be more efficient than the travelling wave designs since the axial, beam transport cavities, and the side cavities can be independently optimized. However, it is more expensive and requires the installation of an isolator between the power source and the structure to prevent reflections from reaching the power source.

The microwave energy required to accelerate electrons is delivered to the accelerating structure in the form of short duration pulses, 5 microseconds in duration, from the klystron or magnetron via a rectangular transmission microwave waveguide. An electron gun injects low-energy electrons at one end of the accelerating waveguide. The timing of the electron injections into the guide is controlled by a gun driven system. The electrons are accelerated along the guide to speeds approaching the speed of light and the electrons then enter the bending magnet assembly whereby they are redirected towards the centre of beam's gantry axis of rotation, the isocentre. The electrons are then bent through a suitable angle, usually about 90^{o} or 270^{o} between the accelerator structure and the target. The precision bending of the electron beam is accomplished by the beam transport system consisting of the bending magnets and focusing foils. When a linac is operated in the x-ray mode, the electron beam hits a target and photons are produced predominantly by bremsstrahlung production process, however, in the electron mode, the electrons generally strike a scattering foil prior to being collimated. Detailed description and functions of parts of

the linac including the auxiliary systems are given elsewhere including Metcalfe et al [Met02], Johns et al [Joh83] and Karzmark [Kar83].

7.2.3 Treatment head

The treatment head consists of a thick shell of high-density and high atomic number (Z) shielding material such as lead, tungstein, or lead-tungstein alloy. The components of the head include the following: x-ray target, scattering foil for electrons, the primary and secondary collimators, flattening filter, ion chamber, the jaws for defining field size, and light localiser system. Some linacs have multileaf collimators for defining treatment outline and more recently intensity modulated radiotherapy (IMRT). There are also dynamic and static wedges available on some conventional linacs. Figure 7.2 reveals some internal features of Varian 2100C and 2300C linacs.

MATERIAL REDACTED AT REQUEST OF UNIVERSITY

Fig. 7.2: Standing wave design for Varian 2100C and 2300C linacs including the head components, taken from Metcalfe et al [Met02] and Varian Associates, Inc.

7.2.4 Target and flattening filter

The narrow electron beam emerging from the bending magnet is converted to a broad x-ray beam by mainly bremsstrahlung production and characteristic x-rays in a target usually made of tungstein with copper backing. Since linear accelerators produce electrons in the megavoltage range, the x-ray intensity is peaked in the forward direction. To make the beam intensity uniform across the field, a cone shaped flattening filter is inserted in the beam with the point of the cone facing the target and is usually made of lead or copper although tungstein, uranium, steel, aluminum, or a combination of these has been suggested [Kha94].

In the electron mode, the target and flattening filters are generally replaced by thin metallic, usually made of lead, electron scattering foil. This spreads the beam as well as creating uniform electron fluence across the treatment field and the thickness is such that electrons are scattered instead of producing bremsstrahlung. The scattering foils are usually mounted on a circular tray at the same level as the flattening filter. During a change of mode from x-rays to electrons, the target is retracted, the flattening filter is driven out of the beam and the foil is placed in the beam path. The flattening filter and the electron foils generally sit below the target on a circular mechanism, the carousel. Some machines use an electron raster scan for electron mode instead of a scattering foil; these employ magnetic steering similar to that employed on electron cathode ray tube [Met02, Kha94].

7.2.4.1 Bremsstrahlung

Otherwise known as white radiation or braking radiation, occurs as a result of radioactive 'collision' (interaction) between a high-speed electron and the field of nuclei of an atom. When an electron passes close to the nucleus of an atom of the target, it experiences an electromagnetic force that results in an energy loss and change of direction. Radiation is emitted by conservation of energy predicted by Maxwell's general theory of electromagnetic radiation. The probability of such an interaction increases as the distance of the electron from the nucleus decreases. Since an electron may have one or more bremsstrahlung interactions in a material and an interaction may result in partial or complete loss of electron energy, the maximum

energy of the bremsstrahlung photon can be no more than the incident electron energy. A spectrum of photon energies below this value is produced. There is also bremsstrahlung production due to electron-electron interaction in which the Coulomb field of an orbital electron decelerates the secondary electron. The direction of emission of bremsstrahlung photons depends on the energy of the incident electrons [Kha94]. At energies below about 100 keV, x-rays are emitted in almost equally in all directions. As the kinetic energy of the electron increases, the direction of x-ray emission becomes increasingly forward. Consequently, transmission-type targets are used in linear accelerators, in which the electrons bombard the target from one side and the x-ray beam is obtained on the other.

7.2.4.2 Characteristic x-rays

An electron with kinetic energy E_o, may interact with the atoms of the target by ejecting an orbital electron, such as a K, L, or M electron, leaving the atom ionized. The original electron will recede from the collision with energy $E_o - \Delta E$, where ΔE is the energy given to the orbital electron. A part of ΔE is used to overcome the binding energy of the electron and the remainder carried by the ejected electron. With a vacancy created, an outer orbital electron will move to occupy this vacancy and in so doing the energy is radiated in the form of electromagnetic radiation characteristic of the atom in the target and of the shells between which transitions occurred. With higher atomic number targets, such as tungsten, the characteristic radiation emitted is of high enough energy to be considered in the x-ray part of the electromagnetic spectrum. Unlike bremsstrahlung, characteristic radiation or x-rays are emitted at discrete energies. If the transition involved an electron descending from the L shell to the K shell, the photon emitted will have energy equivalent to the difference between the electron binding energies of the K shell and L shell. The incident electron must possess critical absorption energy in order to eject an electron from the atom.

7.2.5 Monitor (Ionisation) chambers

The electron beam or the flattened x-ray beam is incident on the dose monitoring chambers. The monitoring system consists of several ion chambers or a single chamber with multiple plates made of kapton or mica. Although the chambers are usually transmission type, that is, flat plate chambers to cover the entire beam, cylindrical thimble chambers have also been used in some linacs. The mica chambers are usually filled with nitrogen, whereas the kapton chambers are filled with oxygen-enriched air. Both these types are sealed to avoid correcting for changes of gas density within the volume due to ambient pressure and temperature variation. In some linacs, the chambers are not sealed; these generally have an accurate electronic temperature pressure compensation device. The chamber plates are mounted so that one is rotated 90^{o} on the beam axis from the other. This enables the monitoring of beam symmetry and flatness in the beam's radial and transverse planes, respectively. Since the chambers are in a high-intensity radiation field and the beam is pulsed, the ion collection efficiency is maintained with changes in dose rate by the application of bias voltages in the range of 0.3 to 1kV across the chamber electrodes, depending on the design. The function of the ion chamber is to monitor dose rate, integral dose, and field symmetry. It ensures the reproducibility of dose prescribed for each patient.

7.2.6 Collimation

Various devices are used to collimate and modify the intensity of the x-ray beam. These are the primary and secondary collimators, the X and Y jaws, multileaf collimators (mlc) that have replaced shielding blocks in recent times and are very useful in conformal therapy including intensity modulation radiation therapy (IMRT) and dynamic and static wedges.

7.2.6.1 Primary collimation

A primary fixed collimator, generally made of tungsten, is mounted just below the target and above the flattening filter. Shaped like a slightly diverging cone open at both ends, this device allows only forward scattering x-rays and electrons to exit the linac. It also helps to prevent head leakage such as scattered photons escaping from the treatment head. The dimensions of this collimator are such that a maximum field size not exceeding 40x40 cm^2 at 100 cm source-to-surface distance (SSD) is achieved in combination with the secondary collimators.

7.2.6.2 Secondary collimation

A secondary collimation system consists of a fixed collimator, and two pairs of moveable metal blocks (X and Y jaws) usually made of tungsten or lead alloy. The fixed collimator provides a further divergence of the beam from the primary collimator while the jaws can be adjusted to produce different rectangular field definitions from nearly 1x1 cm^2 to 40x40 cm^2. The jaws are designed such that they drive at an angle to the beam that closely matches the angle of divergence at different field sizes. This ensures that the full jaw face is parallel to the edge of the x-ray beam and thus reduces the beam penumbra due to partial jaw transmission. The collimators are mounted at a source collimator distance (SCD) of about 40 cm. In the electron mode, the jaws are usually opened wider than the required field, and final collimation is provided by an electron applicator. This is a demountable device that attaches to an accessory mount and provides collimation at about 5cm from the patient surface. This is required because electron scattering in air produces a wide beam penumbra if the collimators are further away. A visible light field defines the geometric centre and edges of the radiation field. In most modern linacs the light field is produced by a light source reflected from a thin nonretracting myla mirror set in the head of the machine just above the secondary collimators. The centre of the field is defined by a crosshair etched onto thin myla window mounted above the jaws that define the field edge.

7.2.7 Beam modifying devices

Devices such as blocks, wedges and multileaf collimators are used to create irregular field shapes to prevent radiation reaching radiosensitive organs of the human body such as the heart, lung, or spine and may be shielded from the direct treatment beam.

7.2.7.1 Shielding Blocks

Lead blocks are commonly used to modify the x-ray treatment field dose distribution. These are mounted on block trays that slide into a removable accessory mount just below the jaws and at a distance of about 65 cm from the source. Each linac has a set of lead blocks in standard shapes and of thickness generally sufficient to provide at least five half–value layers (HVL) of shielding. A low melting point

alloy such as Lipowitz or Cerrobead (50% Bi, 26.5% Pb, 13.3% Sn and 10% Cd) of melting point 70 °C [Kha94] is also used to shape blocks for irregular field treatment and is more convenient to mould than lead. The HVL is not quite as good as that of lead because they are less dense and a slightly greater thickness of the material is required.

7.2.7.2 Multileaf collimators (mlcs)

Multileaf collimators have become available in the last decade and have replaced shielding blocks in most machines to shape photon beams. They are usually made of tungsten and consist of a set of interleaved collimators that are affixed to the machine just beyond the X and Y jaws and in front of the accessory holder. In some machines the leaves have replaced a pair of jaws while it is an add-on component in others. The mlc consist of two carriages that move independently and in the same direction as one set of jaws. Each leaf is driven independently by a dedicated motor and adjacent mlc leaves have a tongue and groove interlocking mechanism in order to reduce leakage radiation between them. The mlc can create most geometrical shapes but can also be used in conjunction with a block tray on rare occasions such as lung blocks for Hodgkin's mantle fields [Cil87]. A set of leaves is about 40 on the average and each leaf specification is manufacturer dependent which produces a jagged shaped dose distribution at the field edge. The leaves produce discrete steps at the edge of the treatment field however patient field shapes can be attained satisfactorily. The leaves can be driven 10 cm beyond the geometric centre of the field, that is, the beam central axis. The clearance from the bottom of the leaves to the isocentre is approximately 42 cm. There are dynamic mlcs that provide field shape changes when multiple fields are employed and during intensity modulated radiation therapy (IMRT) and also micro mlcs are used for very small field sizes. Figure 7.3 is a Varian type mlc made up of 80 leaves, that is, 40 pairs of leaves.

MATERIAL REDACTED AT REQUEST OF UNIVERSITY

Fig. 7.3: Varian multi-leaf collimators made up of 40 pairs of leaves

7.3 Principles in radiotherapy

The choice of external radiotherapy as a treatment modality is based on adequate clinical work-up including confirmation of the histological diagnosis and staging. Prescription of the radiation treatment includes the aim of therapy, the definition of treatment volumes and dose prescription as well as other treatment parameters such as fractionation. The prescribed dose also depends on the aim of the treatment, however, the tolerance of surrounding normal tissues is taken into account. The kind of radiation to be used, either electron or photon and more recently protons, for the treatment as well as their energies are chosen depending on the location and extent of the tumour.

7.3.1 Radical and palliative radiation treatment

The two main options in radiation treatment are radical and palliative. The aim of radical treatment is to decrease the number of tumour cells to the level that achieves permanent local tumour control. The volumes to be irradiated have to include any demonstrated tumour and also volumes in which sub-clinical spread is expected in

nearby tissues or associated lymph nodes. These different volumes will often have to be irradiated to different dose levels. When the tumour has been previously removed, for example, mastectomy or hysterectomy the remaining tissue may contain subclinical disease, the limits of which cannot be demonstrated clinically. In constrast to radical, palliative treatment is to decrease symptoms of the malignant disease due to its spread and late stage. The treatment may include all or part of the demonstrated tumour and also secondaries due to the spread to other parts of the body with painful effect. It is generally carried out to alleviate the pain the patient may be suffering from.

7.3.2 Treatment volume

The determination of treatment volumes involves several distinct steps irrespective of the type of treatment. Considerations are also given to patient movement and inaccuracies in the treatment set up. The volumes considered are as follows: gross tumour, clinical target, planning target, treated and irradiated. A schematic diagram is given below in figure 7.4:

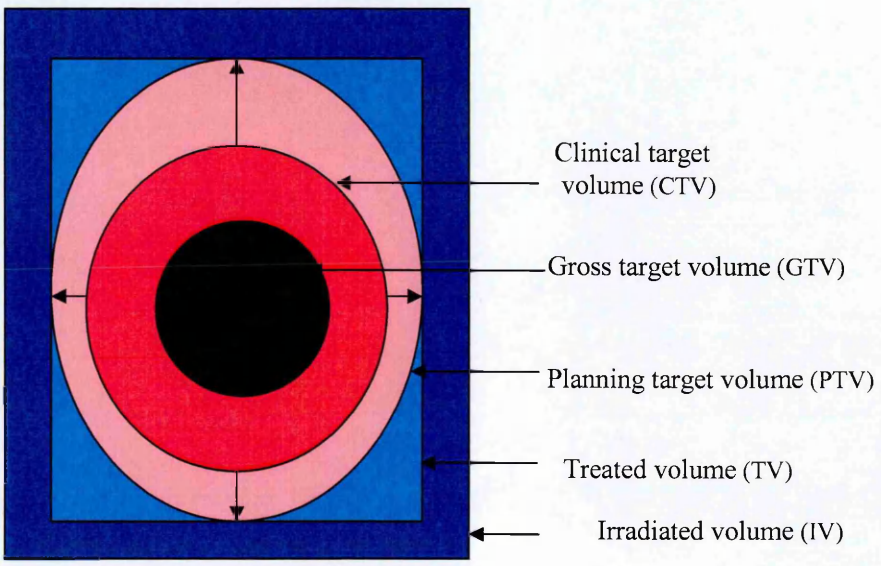

Fig. 7.4: Schematic illustration of the different treatment volumes, taken from ICRU report 50 [ICR93]

The gross tumour volume (GTV) is the palpable or visible extent and location of malignant growth. It consists of the primary tumour and other metastases including that of the lymph nodes. The shape, size and location of the tumour may be determined by inspection. Also various imaging techniques such as computed tomography (CT), isotope imaging and MRI are employed. The clinical target volume (CTV) is an expansion of the GTV to include the subclinical microscopic malignant (disease) cells that have to be eliminated. This volume thus has to be treated adequately in order to achieve the aim of the therapy. To ensure that all tissues included in the CTV receive the prescribed dose, tumour irradiation is planned in principle to include a much larger volume than the CTV. The planned target volume (PTV) therefore takes into consideration the net effect of all the possible geometrical variations in order to ensure that the prescribed dose is actually absorbed in the CTV. Ideally, the treatment dose should cover the PTV, however, due to limitations in radiation treatment technique, this is unrealistic. Therefore the treated volume (TV) which is enclosed by a given isodose surface or contour (usually 95% isodose) is selected as being appropriate to achieve the purpose of the treatment. In some cases the PTV and TV are closely matched. The irradiated volume (IV) is that tissue volume which receives a dose that is considered significant in relation to normal tissue tolerance and depends on the treatment technique used. The choice of radiation type and energy depends on the location of the primary tumour assuming an early stage tumour. Deep-seated tumours require more penetrating and therefore high-energy radiation and vice versa.

7.3.3 Dose delivery

In a typical treatment, a number of beams are arranged from different angles and centred on the tumour such that a maximum dose is delivered to the tumour volume and relatively little to the healthy normal tissues surrounding the tumour to achieve a high therapeutic ratio. In cases where radiosensitive and critically vulnerable organs are within the volume under consideration, various shielding techniques are employed to ensure a better treatment. According to the International Commission of Radiation Units and Measurement (ICRU) report 50 [ICR93], the PTV should receive no less than 95% of the prescribed dose and that 'hot spots' greater than 107% should be avoided. To achieve these, beam modifiers such as wedges and 'beam weighting' are used. The prescription of radiation treatment includes a definition of the aim of

therapy and volumes to be considered and also a prescription of dose and fractionation. For radical treatment with the sole aim of eradicating the primary tumours, the absorbed dose delivered should be kept within +7% and -5% of prescribed dose [ICR93].

7.3.4 Sources of error in dose delivery

There are random and systematic errors associated with radiotherapy treatment delivery. The main sources of error include the following: calibration of the secondary standard of ionisation chambers and electrometers to the primary standard, the calibration and consistency of the treatment machine. Also the transformation of phantom dose to patient dose, errors in treatment planning system used, patient in-homogeneity and movement and reproducibility during simulation and treatment amongst many others.

7.4 Neutron production in medical linacs

Recent medical LINACs are designed to operate at high energies up to 25 MV for more efficient and effective treatment of deep rooted tumours since high energy photons are more penetrating. However, the main problem associated with high energy LINACs is that, the photon beam is contaminated with a non-negligible neutron field. The neutrons are produced by the interaction of the high-energy photons (bremsstrahlung) and electrons with the various materials of the target, flattening filter, collimators and other shielding components that make up the treatment head and also to some extent with the patient and the couch as discussed in previous chapters. The underlining fact is that the average binding energy per nucleon of these nuclei is about 8 MeV and above, therefore, the production of neutrons tends to be higher at energies above this threshold. When the photon energy exceeds approximately 7 MeV, the radiation beams are contaminated with neutrons. Above 10 MV, the level of photoneutron contamination of the x-ray beams becomes significant and it is important to evaluate the neutron dose (D) or dose equivalent (HD, H – quality factor) received by the patient, radiation workers involved with treatment and the general public in the vicinity of the therapy room so that appropriate radiation protection consideration can be given [McG93, Ncr84]. Researchers have used either

experiments or calculations or both methods to determine the neutron contamination in medical linear accelerators. In the following sections calculations have been used to determine the neutron component in the output of Varian Clinac 2100C linac operated in the photon mode at 15 MV energy using Monte Carlo codes MCNP4C2 [Bri01]. The choice of this linac is to compare parameters experimentally determined from the same linac at St. Bartholomew Hospital, London with calculation.

7.5 Monte Carlo calculations of photoneutron production

7.5.1 Work done by others

Mao et al [Mao97] estimated the neutron yields in various head components by using the EGS4 code together with the MORSE-CG Combinatorial Geometry scheme to model the actual accelerator head. With jaws closed, a 20 MeV Varian Clinac 2100C/2300C yielded 2.2E-3 neutrons per incident electron and concluded that the total neutron yield decreased dramatically when the electron energy was reduced to 10 MeV. Using the same linac and running at 20, 18, 15 and 10 MeV, the relative neutron yield when the jaws are closed were 1:0.55:0.21:0.006 respectively. It was also observed that the total neutron yield varied inversely as the field size. Kase et al [Kas98] also simulated the Varian Clinac 2100C/2300C and demonstrated the agreement between the use of complex geometry of linac for calculations and measurements of the neutron flux as opposed to a simplified geometry. The measurements and calculations were done at positions 1 m from the target and in all directions with adjacent positions at right angles to each other. Agosteo et al [Ago92] evaluated the influence of the materials constituting the target and the gantry shield on the angular and the spatial distributions of the direct component of the neutron flux by using the MCNP code to simulate a 25 MeV beam delivered by the GE-CGR Saturne 43 electron linear accelerator. In their work a point source placed at the centre of a hollow spherical shield was used as a simplification of the linac head. Agosteo et al [Ago93a, Ago94] discussed calculations for evaluating the leakage neutron fluence aimed at developing an analytical method that compares well with Monte Carlo calculations using a point source surrounded by a tungsten spherical shield. Sanchez et al [San89] used Monte Carlo transport to calculate the neutron spectrum through a modelled accelerator head. A Monte Carlo code MCNP-GN was developed by

Ongaro et al [Ong00] to simulate photoneutron production. The photoneutron generation routines of the Monte Carlo code GAMMAN [Ong99, Man97] were inserted in the transport code MCNP4B [Bri97]. The new code was then used to simulate photoneutrons in the output of the linear accelerator SL201-ELECTA 18 MeV photon energy and equipped with a multileaf collimator system (mlc) and also that of a traditional Mevatron Siemens 15 MeV photon energy. In comparing experiments with simulation, it was concluded that the neutron dose equivalent for a 10x10 cm^2 ranged between 1 and 4.8 mSv/Gy of photon dose depending on the accelerator characteristics and the distance from the isocentre in the patient plane. Several other workers have used analytical and or Monte Carlo methods to determine the photoneutrons in the output of high-energy medical linacs including Uwamino et al [Uwa86], Agosteo et al [Ago93b] and Ongaro et al [Ong99].

7.5.2 Monte Carlo simulation of Varian Clinac 2100C

In this work the Monte Carlo code MCNP-4C2 [Bri01] has been used to evaluate the photoneutron component of the output of a Varian 2100C medical linear accelerator, fitted with multileaf collimator system, operated at 6 and 15 MV photon energies. Even though the ultimate aim of the project is to predict the neutron dose equivalent and compare that to measurements, the neutron dose contribution from different parts of the linac head such as the target, flattening filter and the collimators can be estimated using this model. The neutron doses in air and in a water phantom at 100 cm, source-to-surface (detector) distance, have been calculated for both within and outside the field of treatment in much the same way as that discussed in the experimental determination of photoneutrons (chapter 6). In practice, it is not feasible to determine the neutron dose received by other parts of the patient during the course of treatment. This has been achieved in this work with the aide of a human tissue equivalent phanton, BOMAB [Sat89], by calculating the fractional neutron dose in some parts of the phantom relative to the neutron dose in the pelvis.

7.5.3 The Varian Clinac 2100C linear accelerator

The linear accelerator simulated in this work is a Varian Clinac 2100C, manufactured by Varian Associates Inc. It operates in two x-ray energy modes, 6 and 15MV and five electron energy modes, 6, 9, 12, 16, and 20 MeV. The linac is fitted with a multileaf collimator (mlc) underneath the main collimators and has a portal image vision which provides real time imaging of the treatment field. The field shape is determined by the mlc and the jaws (X and Y) are used in as close as possible around the irregular shape outlined by the mlc. The components that constitute the head are the target, primary collimators, flattening filter, ionisation chamber, secondary collimator, field light mirror, X and Y jaws, mlc, light field reticule and wedge which is used in some treatment modes. The mlcs are used mainly for shaping fields treated by x-rays though Blomquist et al [Blo02] have used mlcs to shape electron fields. It should be noted that the precise dimensions and material of the various components will not be divulged here since this is exclusively Varian property and can thus be obtained directly from Varian Associates Inc. In spite of this, an attempt has been made to give a description of the various components.

7.5.4 Linac head

A schematic diagram of the Varian Clinac 2100C head geometry is as shown in figure 7.5. The linac head is made up of two sections, the fixed and the moveable sections during any mode of operation. The primary and secondary collimators define the spread of the beam from the target in a cone shape and their positions cannot be adjusted. On the other hand the X and Y jaws and the mlcs have variable positions and can thus be adjusted to conform to a chosen field size and tumour outline. The electron beam emerging from the 270° bending magnet was assumed to be monochromatic and to have a diameter of approximately 2 mm, similar in size to the aperture positioned at the exit of the bending magnet. The aperture has been designed such that it cuts out any electrons to include only those within ±3% of the mean beam energy. The initial position of the beam was chosen to be just above the target and striking it at the origin (x_o, y_o, z_o). The direction (u_o, v_o, w_o) of the emerging photon produced was in the (0, 0, –1) direction. The initial kinetic energy E_o of the electron beam was assumed to be 15 MeV although the correct energy may be either a little higher or lower according to AAPM TG21 [Aap93].

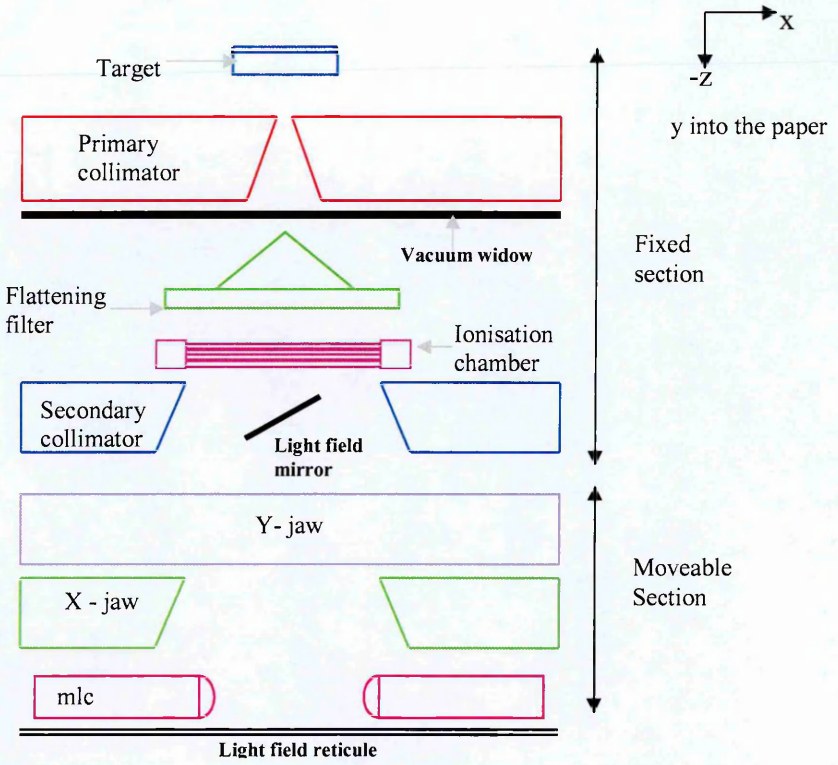

Figure 7.5: A block diagram of the Varian Clinac 2100C treatment head.

The threshold energy for the production of neutrons range between 7 and 9 MeV therefore a cut-off energy of 7.143 MeV, the neutron production threshold energy of iron, was set such that photons below this energy were not traced to save simulation time and obtain much better statistics since these will not produce neutrons.

Ideally, the simulation could be divided into two or more parts such that a run could be executed to accumulate neutrons from the fixed part in a plane just below the secondary collimator. The accumulated neutrons would then form the input source for the moveable parts comprising jaws and mlc. However, this was not feasible in this work due to lack of adequate computer memory and CPU storage. The 'runtpe' file was so huge that the simulation terminated automatically at some point. The simulation was done using a PC with Intel Pentium IV processor, 256 RAM and 45Gb. CPU storage. Ideally, a cluster of computers is most suitable for this purpose since it has much larger storage and runs faster since more computers are involved.

As a result of this, the entire head geometry was considered as one unit in each input file for the simulation and therefore the number of neutrons produced by the various components of the linac head could not be determined as initially planned.

7.6 Head geometry

As discussed above the head consists of the target, primary collimator, vacuum window, flattening filter, ionisation chamber, secondary collimator, X and Y jaws and the mlcs. The exact dimensions and positions of these parts as found in the Clinac 2100C head will not be stated since this is the property of Varian Associates Inc.

7.6.1 The target

The target is a disc-shaped composite material of two layers in vacuum. The top layer made of high Z material produces the x-rays and bremsstrahlung radiation in the photon mode and the bottom layer is a backing for the top layer and also acts as a cooling device. There are different dimensions for 6 MV and 15 MV photons. Varian Clinac 2100C has a standing wave accelerating guide and a 270^{o} bending magnet. An electron beam of approximately 2mm in diameter strikes the target after exiting the bending magnet in the –z direction (0,0,-1) from this geometry as shown in figure 7.6.

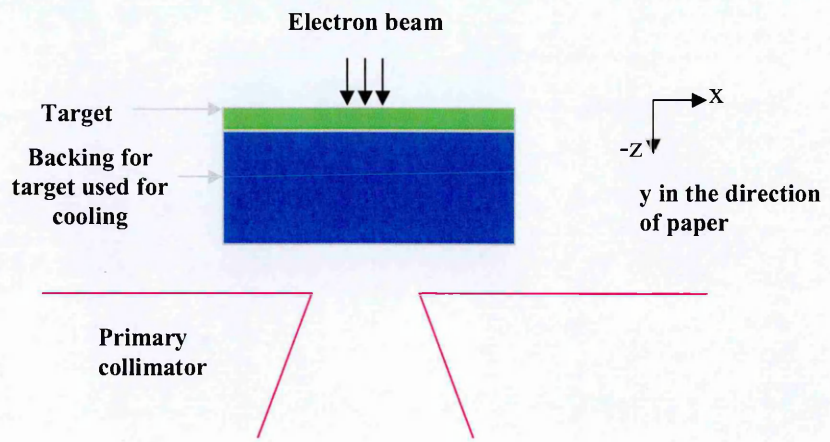

Fig. 7.6: Schematic diagram of the target of Varian Clinac 2100C.

7.6.2 Primary collimator

The primary collimator is the next structure after the target towards the isocentre and also in vacuum. It lies right beneath the target and is disc-shaped with a conical recess in the centre. It projects a circle of radius 24.38cm at the isocentre and defines the maximum angular opening of the treatment head. In effect the primary collimator makes an angle of approximately 27.4° at the apex of the cone, that is:

$$\tan^{-1}\left(\frac{24.38}{100}\right)x2 = 27.4^{o}$$

In this simulation, the primary collimator was considered as one entity, as shown in figure 7.7, using the surface card equations provided in the MCNP 4C2 manual [Bri01], in contrast to some simulations [Ong99, Ong00, Mar99] where it has been broken up into several discs or cylinders of varying diameter to account for the recess. By considering it as an entity the simulation runs faster since there are less number of cells for the particle to trace and therefore better sampling. Also the forced collision (fcl) card which ensures that a collision occurs in almost every particle in a cell has been used in this simulation to facilitate neutron production.

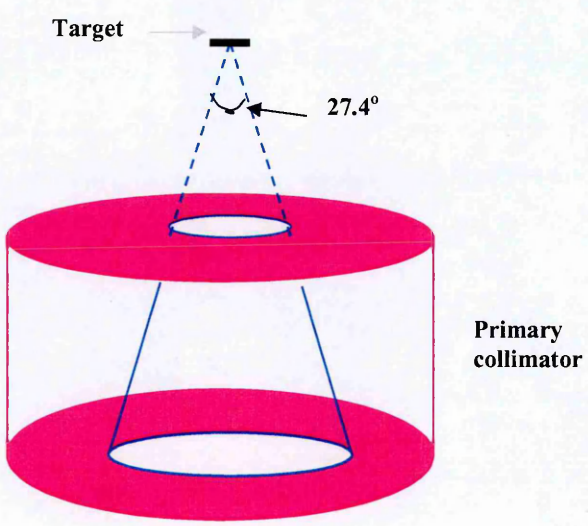

Fig. 7.7: Schematic diagram of the primary collimator.

7.6.3 Flattening filter

The flattening filter causes differential beam hardening and differential reduction in beam intensity so that a flat beam is obtained at the required depth for any field size ranging from less than 5x5 cm^2 to 40x40 cm^2. It is conical in shape with the axis in line with the central axis of the beam. The cone sits on a disc plate to form a composite body. In the simulation, the geometry of the composite body is given by a combination of the cone and a disc by employing the surface card equations provided in the MCNP4C2 manual [Bri01]. As discussed above, these were not sectioned into a series of cylinders or discs with varying radii. The flattening filter reduces the beam intensity in the central axis without affecting the beam energy at off-axis distances for any given field size [McC78, Mar99] and therefore will reduce the central axis dose rate with respect to edges.

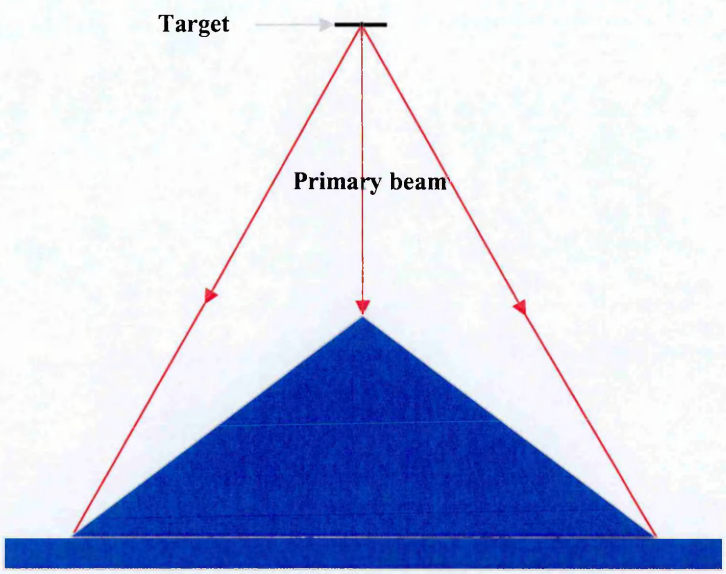

Fig. 7.8: Schematic diagram of the of flattening filter.

7.6.4 Monitor (Ionisation) chamber

The ionisation chamber monitors the position, intensity, symmetry and dose of both electron and photon beams. It consists of inner rings of pressurised plates held together on the outside by a ring of metallic material. The interest here is the metallic ring of material since the purpose of the project is to determine the neutron content The pressurised rings will produce a quantity of neutrons which can be considered negligible and has very little, if any, effect on the photon beam. Therefore in the design of the ionisation chamber the pressurised rings were ignored. The geometry of the ionisation chamber was taken to be a hollow metallic disc as shown below in figure 7.9.

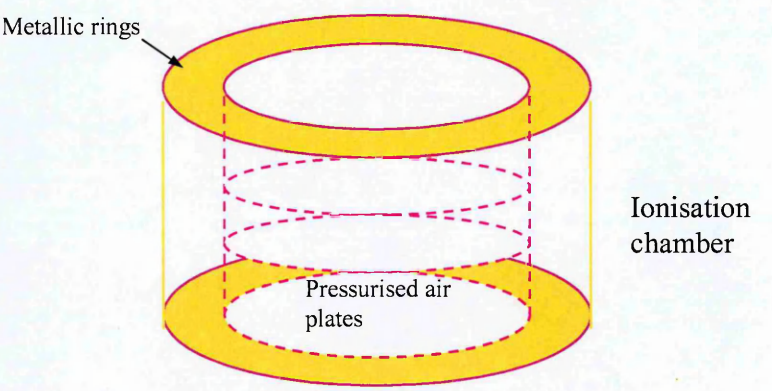

Fig. 7.9: Schematic diagram of the of the ionisation chamber.

7.6.5 Secondary collimator

The secondary collimator is much the same as the primary collimator except that it has a much wider conical recess. The angle at the apex on the cone coincides with that of the primary collimator and is the same, 27.4°. The secondary collimator further collimates the beam and projects a circle of radiation at the isocentre of the same maximum radius (24.28cm) as that of the primary collimator. The secondary collimator is not in a vacuum unlike the primary but both are made of the same material, tungsten.

7.6.6 Upper and lower jaws

There is a pair each of upper and lower jaws having planar front face and move in an arc described by a point at the target such that its centre coincides with the central axis of the beam. The front face of each jaw is parallel to the radiation field edge and is focused. In this model the movement of the jaws is achieved by angular displacement as is achieved in the real jaw movement. Due to the complexity of defining the displacement of the jaws, some researchers have used the linear displacement instead [Mar99, Ong99, Ong00]. In both models the penumbra is not affected since the jaws have their front face parallel to the field edge. However, this affects the beam flatness since the top surface of the real jaws changes its distance from the origin with field size, however, in the simplified model this distance is constant with field size. The two scenarios are demonstrated in figures 7.10a and 7.10b for angular and linear displacements respectively.

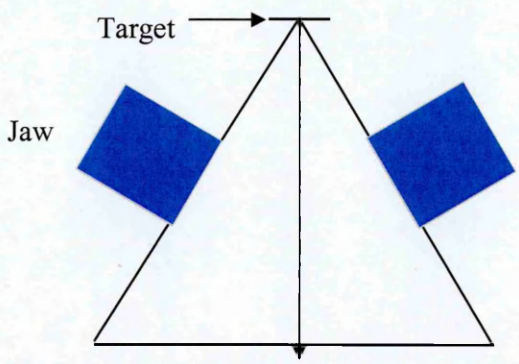

Fig. 7.10a: Angular displacement of jaws

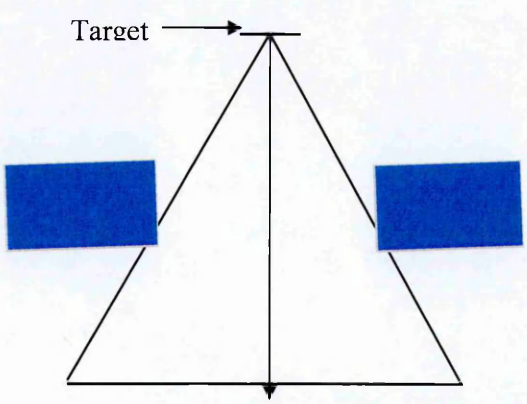

Fig.7.10b: Linear displacement of jaws

7.6.7 Multileaf collimators (mlcs)

The Varian multileaf collimators are divergent, on the y-axis and non-divergent on the x-axis. Divergent leaves have a smaller penumbra than non-divergent leaves. Most clinical treatments are prescribed at 90 to 95% isodose curve as this nullifies any significant difference between divergent and non-divergent leaves despite the former having the edge in terms of penumbra width. This is thought to occur at depth of maximum dose (d_{max}) for field sizes greater than 15x15 cm^2 when the penumbrae are compared [Mar99]. A major disadvantage of the non-divergent leaves is when opposite sides meet head on and their front faces are touching. There is some radiation transmission because of their curved cylindrical surface and which has been estimated to be as high as 38% [Mar99].

The Varian 2100C mlcs are mounted on the plate below the lower X-jaws as an add-on component. There are 52 leaves in total, with 26 leaves on each side mounted on two carriages, A and B. Each leaf and carriage has its own motor so that there are 52 independent motors for the leaves and two independent motors for the carriages. Since the maximum neutron production is the prime objective, interleaf radiation leakage was overcome by having a composite plate each for the X and Y carriages. That is, all the leaves on each carriage are not independent of each other as in reality. Also since the movement of the leaves individually is linear, this arrangement has no effect on the beam output. Also the arrangement is assumed to give the maximum neutron production. The setting of a field size is not affected in that the X and Y jaws effectively define the field size.

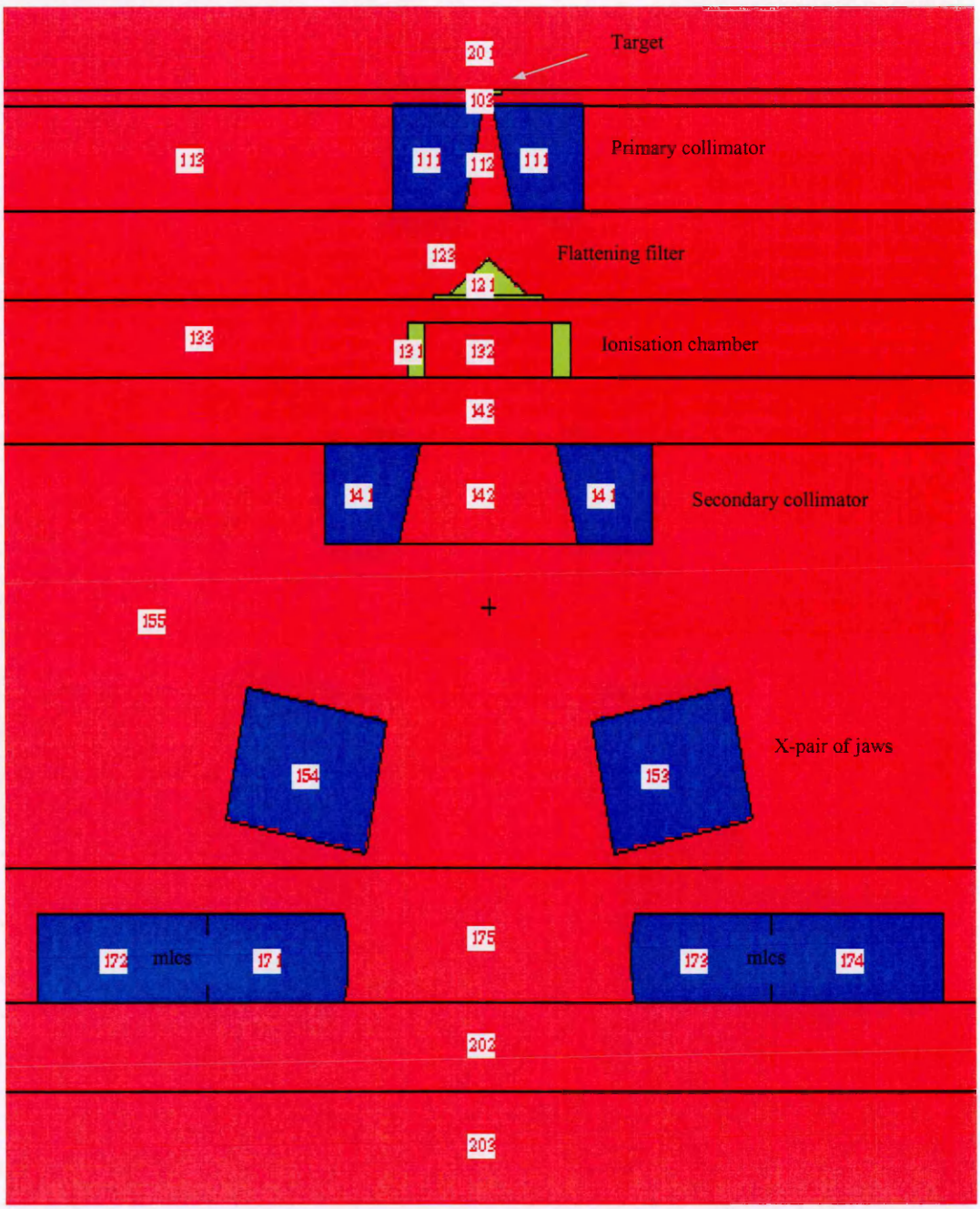

Fig. 7.11a: MCNP Geometry plot of the linac head simulation showing the various components and exactly the same as discussed in fig. 7.5. It should be noted here that only a pair of jaws appear in each plot due to the plot planes.

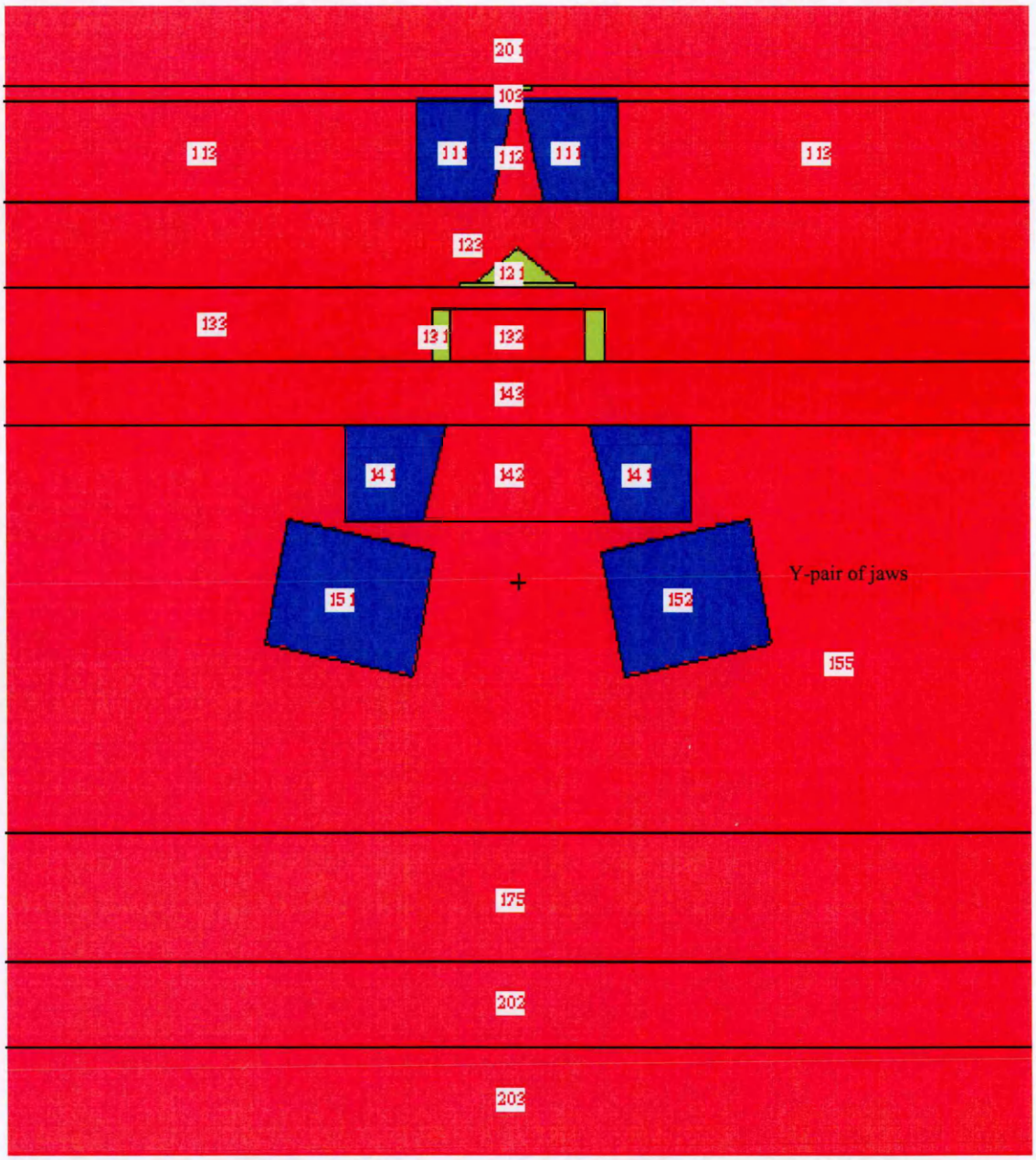

Fig. 7.11b: MCNP Geometry plot of the linac head simulation showing the various components and exactly the same as discussed in fig. 7.5. It should be noted here that only a pair of jaws appear in each plot due to the plot planes.

7.7 Tissue equivalent 'human' phantom, BOMAB

Three scenarios were considered in the calculation of the neutron dose. The in-air and in-phantom neutron dose determination were carried out in the exact replica of the experimental procedure and therefore will not be repeated in this section. As a further demonstration of the diversity of the simulation, a human phantom, BOMAB, [Sat89] was placed in the patient plane to determine the neutron dose to some parts (organs) of the patient undergoing photon dose treatment. The 15 MV photon beam is mostly used for pelvis treatment [Mac02], therefore in this simulation, $10x10cm^2$, $15x15cm^2$ and $20x20\ cm^2$ field sizes were set and investigated for pelvic treatment. The BOMAB phantom was modified to include the lungs, a radiation sensitive organ. Tallies were set at the lungs, abdomen and the thighs in addition to that of the pelvis, comprising the reproductive organs. Figure 7.12 shows the modified BOMAB phantom as viewed from lateral, transverse and in supine positions.

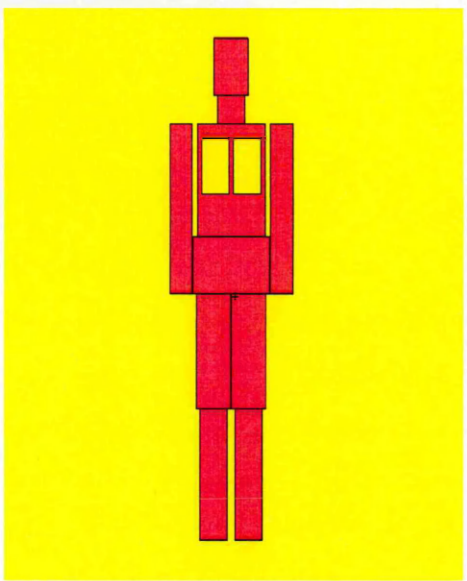

Fig. 7.12a: MCNP plot of tissue equivalent 'human' phantom (BOMAB) modified to include 'lungs'.

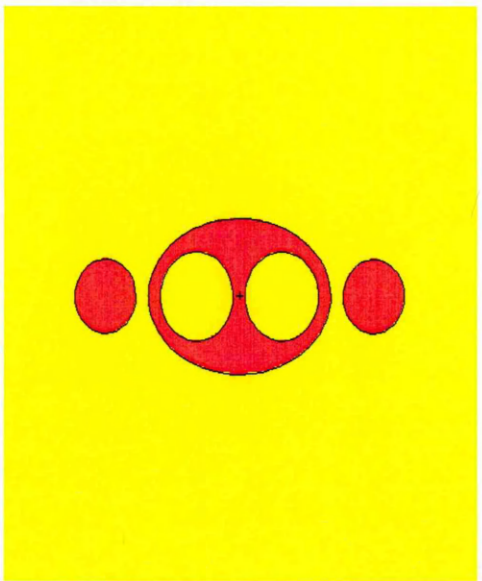

Fig. 7.12b: MCNP plot of the transverse section of the chest region of BOMAB. It includes sections of both arms.

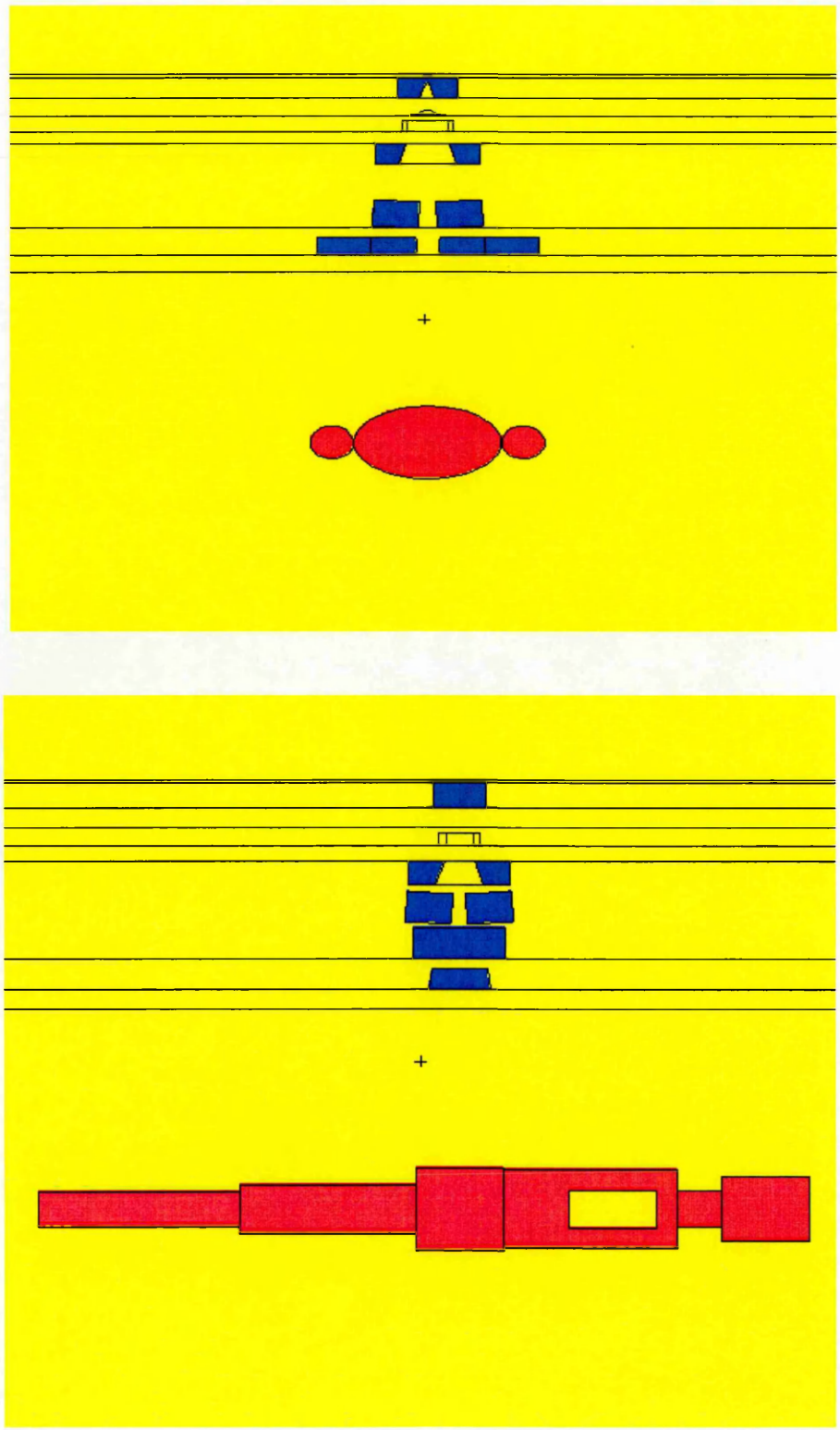

Fig. 7.12c: MCNP plots of the lateral and transverse sections of BOMAB in treatment position including components of the linac head.

7.8 Results and discussion

7.8.1 Photon output factors

The neutron dose equivalent per unit photon dose per incident electron are discussed below. In order to make the results more relevant and meaningful, they are compared with that experimentally determined. Some of the parameters that could not be determined experimentally were calculated and the results presented without any comparison. In all the simulations the gantry angle was maintained at 0° and source-to-surface distance, (SSD) at 100 cm to replicate experimental set up. In order to verify the accuracy of the simulation, the photon dose output factors in-air for the 5x5 cm^2, 10x10 cm^2, 20x20 cm^2 and 40x40 cm^2 field sizes were calculated and compared with measured values for the 15 MeV photons provided by the hospital. The photon output factor of a linac can be defined as the ratio of the photon dose at 100 source-to-surface distance (SSD) for a given field size to that of the 10x10 cm^2 field at the same SSD. Table 7.1 shows the comparison of output factors obtained by measurement and that calculated using MCNP.

Table 7.1: Comparison of calculated and measured output factors for 15 MV Varian Clinac 2100C.

Field size/ cm^2	Output Factor/MCNP	Output Factor/Measured
5x5	0.98 ± 1.8%	0.95
10x10	1.00 ± 1.8%	1.00
20x20	1.03 ± 2.2%	1.05
40x40	1.09 ± 1.8%	1.10

7.8.2 In-air simulation

Figure 7.13 shows the variation of neutron dose equivalent with field size on and off the central axis. The dose equivalent is almost independent of field size for distances greater than 20 cm outside the irradiated field and becomes more prominent at longer distance from the field edge. This effect was observed in the experimental determination of the neutron dose equivalent. On the central axis, there is a gradual

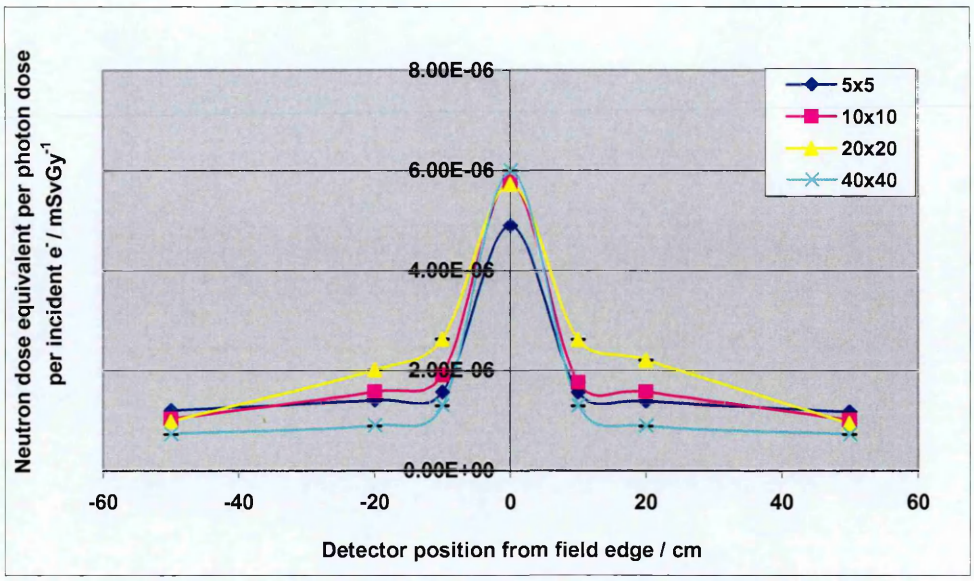

Fig. 7.13a: Variation of neutron dose equivalent per unit photon dose per incident electron with field size for 0^{o} gantry angle as a function of detector position from field edge for in-air calculations.

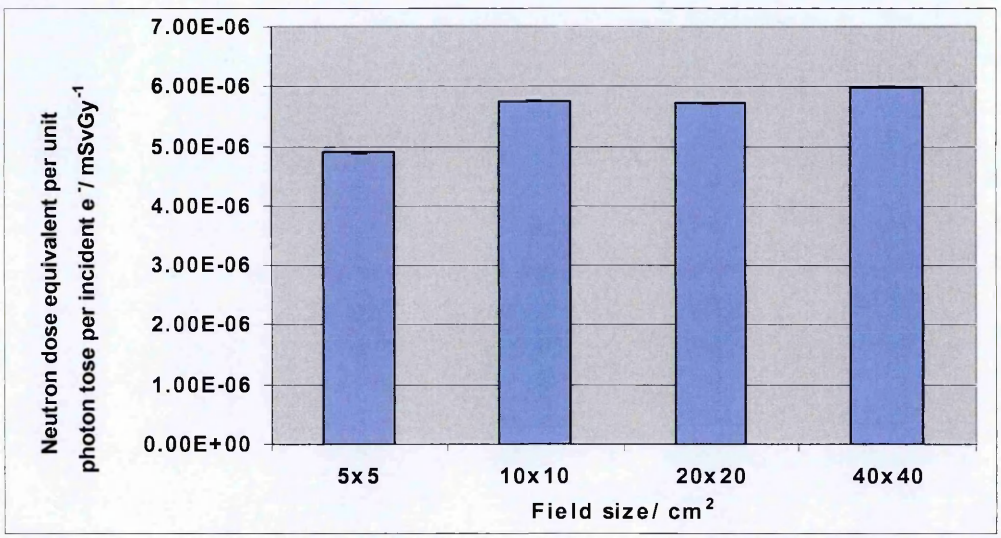

Fig. 7.13b: Variation of neutron dose equivalent per unit photon dose per incident electron with field size on the central beam axis for in-air calculations.

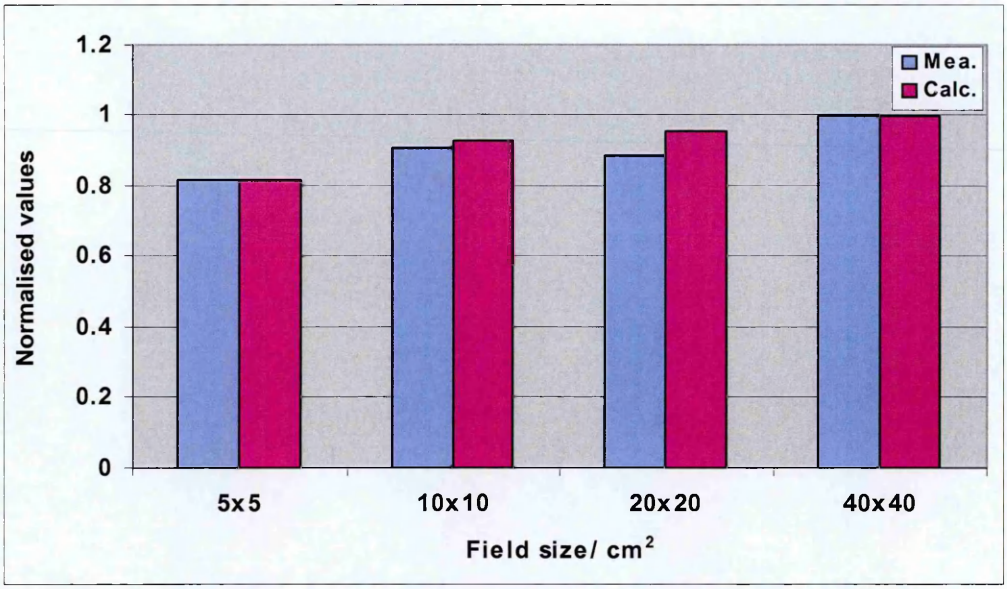

Fig. 7.14: Comparison of in-air neutron dose equivalent per unit photon dose on the central beam axis normalized to the neutron dose equivalent of the 40x40 cm^2 field.

increase in the neutron dose equivalent per unit photon dose with field size, however, values for 10x10 cm^2 and 20x20 cm^2 fields are virtually the same. In figure 7.14 the calculated and experimentally determined neutron dose equivalent along the central axis are compared for all the field sizes. The values are normalized to the dose equivalent of the 40x40 cm^2 field size, highest for both experiment and simulation and show a good agreement for all the field sizes. In figure 7.15 the calculated neutron dose equivalent is compared with measured values at detector position for each field size. The values are normalized to the central axis neutron dose equivalent and show a good agreement between experiment and simulation for all the field sizes and detector positions with the exception of the detector at position 50cm for 5x5 cm^2 and 10x10 cm^2 fields which shows a disparity of about 40-50%. Also observed in these figures is the greater agreement between experiment and calculation for field sizes 20x20 cm^2 and 40x40 cm^2.

From figure 7.15, it is quite clear there is good agreement between simulation and experiment for the in-air comparison, consequently, the in-air neutron spectrum at 100 cm SSD on the beam central axis was calculated for each field size as shown figure 7.16. From the spectra, the maximum neutron flux occurs at approximately 1 MeV in

agreement with the neutron spectrum of ^{252}Cf source as shown in figure 2.2a [NCR64] taking into account head shielding. The average energies of neutrons produced in the x-ray target and in the flattening filter are similar to those of fission neutrons, that is, in the 1-2 MeV range. Once transmitted through the massive shielding and collimation systems (usually of lead or tungsten) of the accelerator head, these neutrons present a strong spectral degradation. The average energy is typically below 1 MeV [NCRP 1984]. In addition, a cloud of lower energy neutrons is generated in the treatment room due to multiple scattering events in the walls, floor and ceiling and other large structures such as accelerator gantry, patients couch, shielding maze, etc. D'Errico et al [D'Er01a] measured the effective photoneutron energy of 1.8 – 2.1 MeV within the 10 – 18 MV x-ray beams, and 0.5 – 0.8 MeV for photoneutrons transmitted through the accelerator head. Rogers et al [Rog81] and McCall [McC79] observed that the unattenuated spectrum has over 85% of its fluence above 1 MeV, whereas a more realistic spectrum's shape takes cognizance of filtering by the shielding material in the head and scattering in the bunker and therefore only 15% of its fluence is above 1 MeV.

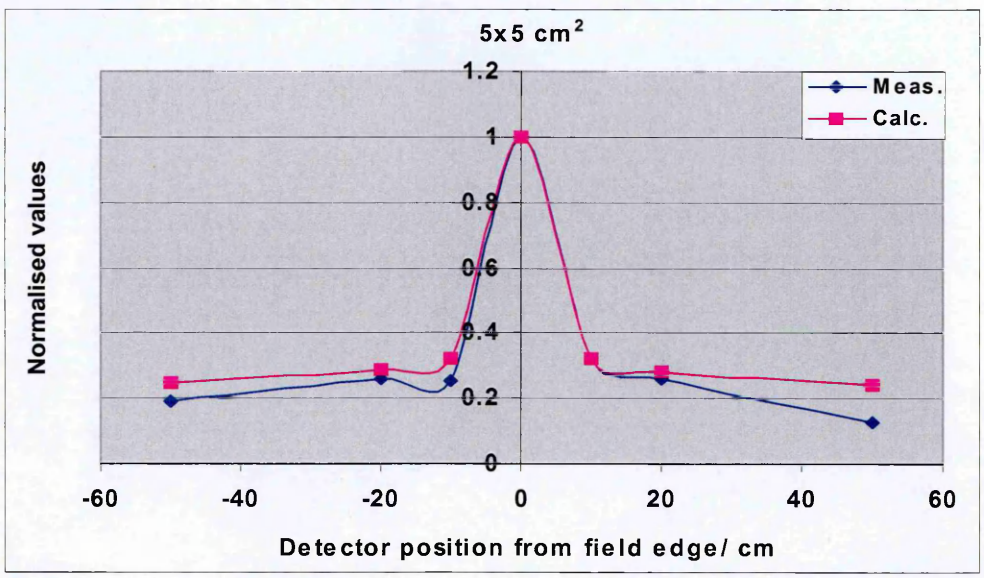

Fig. 7.15a: Comparison of in-air measurements and calculations for 5x5 cm^2 field. The neutron dose equivalent values have been normalised to that of the central axis

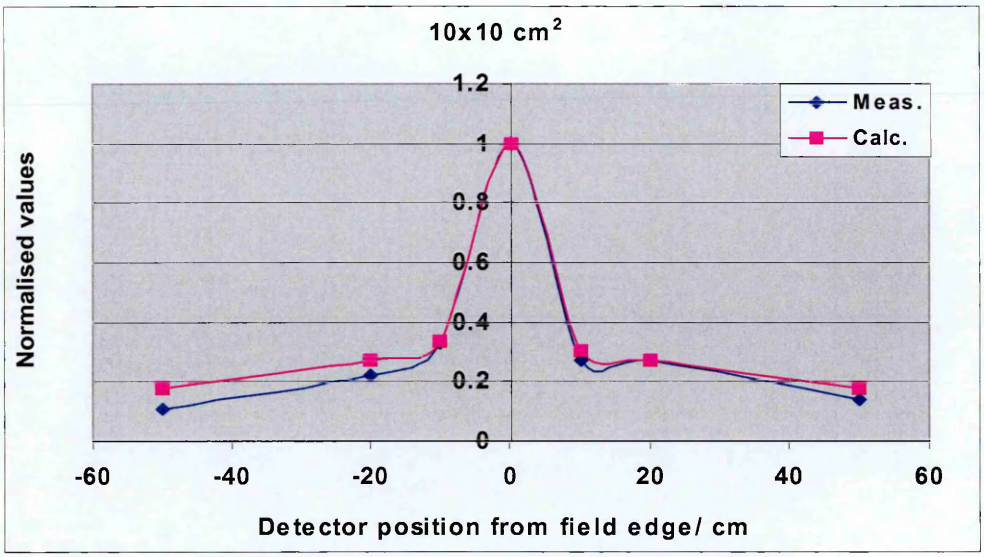

Fig. 7.15b: Comparison of in-air measurements and calculations for 10x10 cm^2 field. The neutron dose equivalent values have been normalised to that of the central axis.

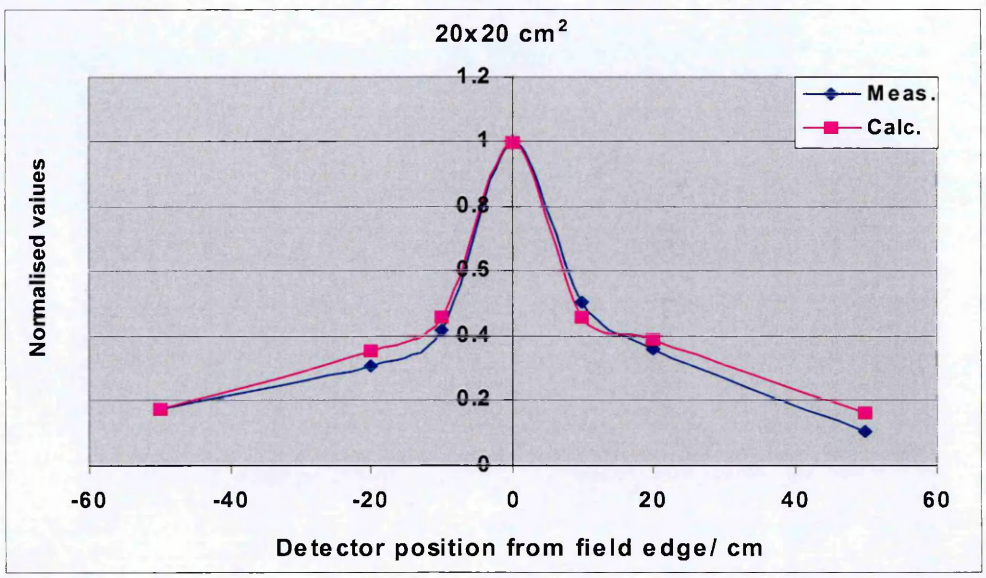

Fig. 7.15c: Comparison of in-air measurements and calculations for 20x20 cm^2 field. The neutron dose equivalent values have been normalised to that of the central axis.

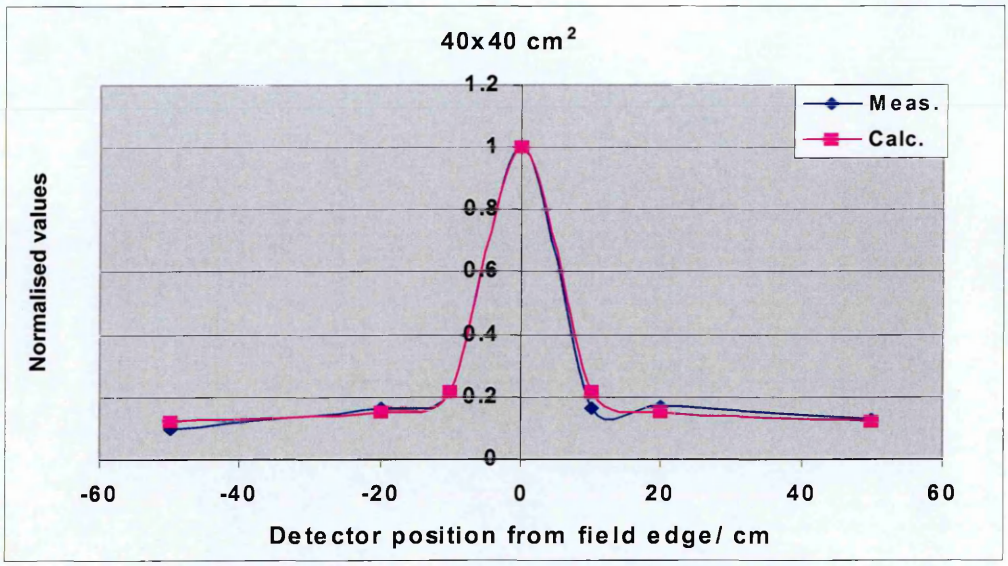

Fig. 7.15d: Comparison of in-air measurements and calculations for 40x40 cm^2 field. The neutron dose equivalent values have been normalised to that of the central axis.

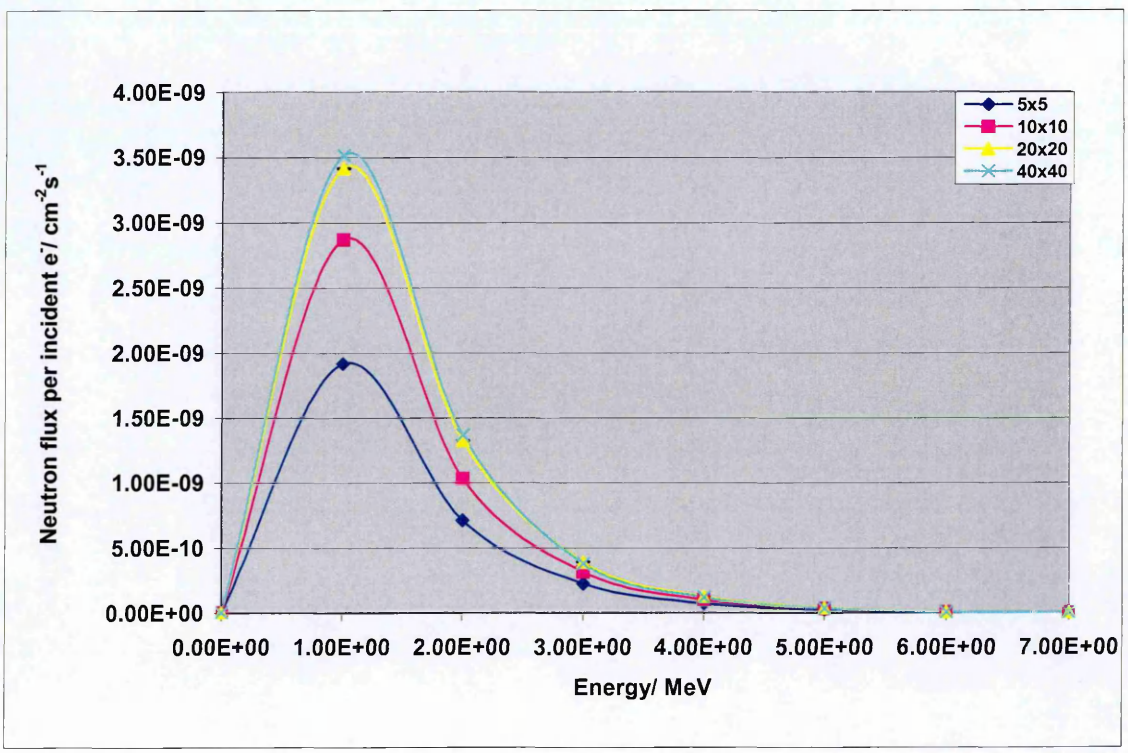

Fig. 7.16: Variation of neutron spectrum with field size at 100 cm SSD.

7.8.3 Water Phantom simulation

Table 7.2 shows the variation of neutron dose equivalent per unit photon dose per incident electron as a function of depth on the beam axis for the 5x5 cm^2, 10x10 cm^2 and the 20x20 cm^2 field size. A graphical representation is as shown in figure 7.17 which gives an indication that, irrespective of field size, the dose fall off along the central beam axis from a depth of 1 cm to 20 cm is exponential with a correlation coefficient of nearly 1. From a depth of 5 cm to 20 cm, the neutron dose equivalent is virtually independent of field size, however, it is apparent that the dose equivalent per photon dose is marginally highest for 5x5 cm^2 field at 1 cm depth in water. This trend is similar to that observed with measurements. The dose distribution off the central axis is virtually independent of field size even though some variations are observed at some depth and distances from the edge of each field. The results are available in the Appendix.

Figure 7.2 Variation of neutron dose equivalent per unit photon dose per incident electron as a function of depth in water on the central axis.

	Field size/ cm^2		
Detector depth in water/ cm	**5x5**	**10x10**	**20x20**
1	4.96E-5±8.88E-7	4.59E-5±4.73E-7	4.53E-5±3.33E-7
5	1.57E-5±4.77E-7	1.73E-5±3.35E-7	1.90E-5±3.39E-7
10	4.96E-6±2.37E-7	4.92E-6±1.59E-7	6.78E-6±1.87E-7
20	3.53E-7±5.20E-7	5.47E-7±3.05E-7	7.72E-7±3.52E-7

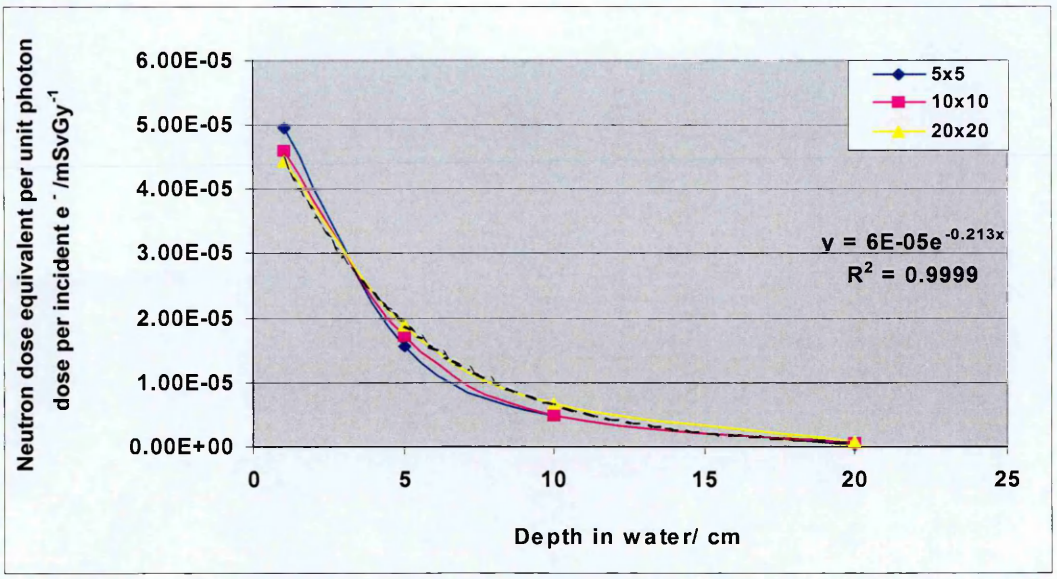

Fig. 7.17: Variation of neutron dose equivalent per unit photon dose along the central beam axis in phantom as a function of field size.

The comparison of simulation with experiment for the neutron dose equivalent per unit photon dose per incident electron along the central axis at a depth of 1 cm is as shown in figure 7.18. The neutron dose equivalent has been normalized to that of the 5x5 cm^2 field size, the highest in this case. It can be seen that simulation overestimates the neutron dose equivalent by approximately 10 to 15% and takes into consideration an error of about 20% generally associated with bubble detectors.

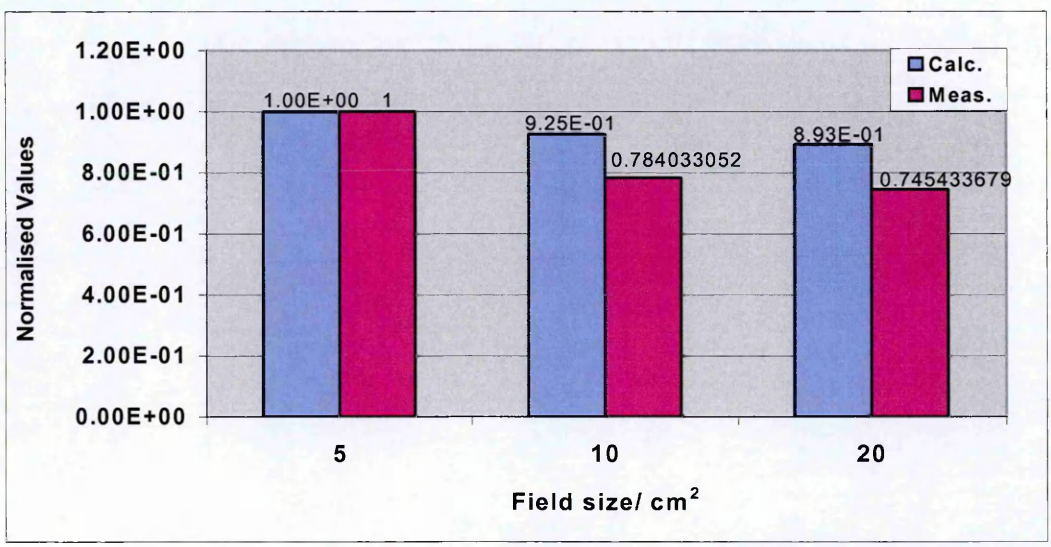

Fig. 7.18: Comparison of simulation with experiment for in phantom at 1cm depth water normalised to the 5x5 cm^2 field.

7.8.4 BOMAB phantom

The BOMAB phantom provided the opportunity to estimate the fractional neutron dose equivalent in some regions of the human body since it is difficult to determine by experimental methods. The photon treatment of the pelvis can result in neutron doses in some regions of the body notably the abdomen, lungs and thighs as shown in Table 7.3 since these are relatively much closer to the pelvis.

Table 7.3: The fractional neutron dose equivalent per unit volume of body part relative to the neutron dose equivalent in the pelvis.

Field size/ cm^2	Pelvis	Abdomen	Thigh	Lung
10x10	1.0	0.81	0.85	0.71
15x15	1.0	0.61	0.65	0.50
20x20	1.0	0.51	0.54	0.37

The neutron dose equivalent per unit photon dose and volume of body region decreases with increasing field size. There are more energetic neutrons in smaller field sizes than larger ones due to less neutron scattering or neutron spectrum 'hardening' in the former. These neutrons travel longer distances before attaining thermal equilibrium. On the other hand, larger field sizes have much less energetic neutrons and thus attain thermal equilibrium more quickly and undergo radiation capture with hydrogen, therefore, less neutron dose deposition. Irrespective of field size, the lungs receive the least neutron dose fraction per unit volume and the highest is found in the thigh just higher than the abdomen. Several radiosensitive organs are found in the abdomen and also the lungs and the reproductive organs are radiosensitive. The much higher radiobiological effectiveness of neutrons makes these organs susceptible to unaccountable for radiation and therefore the need for extra shielding to avoid secondary malignancies.

7.9 Conclusions

The joint use of simulation, Monte Carlo code MCNP4C2, and experimental methods constitute a suitable and effective system to evaluate the undesired neutron dose equivalent at the patient plane during a radiotherapy treatment with photon beams of energy greater than or equal to 10 MV. This tool provides a means of testing the efficacy of a method that can be used to investigate procedures that are not feasible with experimental methods. The Varian Clinac 2100C, operated at 15 MV photon energy, has been simulated to investigate the photoneutron contamination in its output.

Though the precise linac data were not made available due to manufacturer's proprietary rights, there is a good agreement between simulation and experiment for both in-air and phantom scenarios. The agreement for the in-air measurements and calculations is within 10 to 15% whilst that of in phantom is within 15 to 20% taking into consideration experimental errors. In the case of in-air, there is a greater agreement between the two methods for detector position from field edge within 20 cm but declines at much greater distance. This was generally observed for smaller field sizes as a discrepancy of between 40 and 50% was recorded for the 5x5 cm^2 and 10x10 cm^2 fields at 50 cm from the field edge.

The determination of the neutron dose equivalent in selected regions of the patient during high-energy photon treatment is a difficult one. Some researchers have used patients with extreme care and also anthropomorphic phantoms at much greater expense. The fractional dose to regions of the human body has been demonstrated using the BOMAB phantom developed for use in Monte Carlo codes. There are other phantoms such as the VIP-Man [Boz01] that can also be used for this purpose. Though this may not be precise, it provides some vital information as to the nature and distribution of neutron dose equivalent in the patient. Also the neutron spectrum in the patient plane at 100 cm source-to-surface distance has been calculated for 5x5 cm^2 10x10 cm^2 and 20x20 cm^2 and 40x40 cm^2 field sizes with a mean energy of approximately 1 MeV.

The discrepancies that have been observed with simulation and experiment may indicate the limitation in the MCNP calculations as well as the limitation of measurements in the high-energy photon beams. In any case there is a remarkable agreement between the two methods and can thus be complimentary.

8. Bunker design and modification for high-energy medical linear accelerators.

8.1 Introduction

Electromagnetic radiation and electrons produced by medical electron accelerators operating at energies above 8 MeV give rise, through mainly photonuclear disintegration reaction (γ,n) with the materials of the treatment head components, to a non-negligible neutron field inside the treatment room. This leakage radiation though small, provides whole body irradiation of the patient, which adds to the electron or photon dose delivered for therapeutic purposes because of the linear energy transfer (LET) of neutrons. In order to optimise treatment conditions it is important to quantify the contribution by the leakage radiation. On the other hand, radiation protection is not only about the patient, but also the personnel working in the treatment and adjacent rooms to the accelerator bunker as well as the general public in its vicinity. The leakage radiation is mainly composed of neutrons and the photons produced through neutron capture reactions with materials of the concrete room.

Much of the expense of shielding medical linear accelerators involves creating maze-like entrances to the treatment room in order to attenuate both the high-energy photons and the neutrons generated in the accelerator head. Neutrons scatter through large angles with little loss of energy and therefore can lead to unacceptable doses near the accelerator entrance, a high occupancy factor area in radiation therapy. Neutrons also generate capture gamma rays as they travel along the maze and this has been quantified to be as much as half the total dose at the entrance of the bunker [McG95]. Shielding for neutrons is often accomplished with the use of heavy treatment room doors, approximately one ton, incorporating lead shielding for scattered photons and capture gamma rays. Most centres use hydraulic or mechanical systems to open and close such doors which takes time and therefore prolongs patient treatment turn around times. They are unwieldy in case of an emergency, besides these shielding doors are expensive (ranging between $30,000 and $40,000 in 1995) [McG95].

Many hospitals are facing the task of replacing outdated linacs, most of which have energy less than 10 MeV, with new ones of much higher energy while still utilising the existing bunker or treatment room. The dilemma is the choice of treatment machine and the accompanying cost of shielding. Some centres have avoided the use of such expensive and heavy doors by choosing slightly lower energy linacs that have lower neutron generation such as 10 MV. Alternatively, some have used neutron moderating and absorbing materials in the walls of the accelerator maze [Ker79, Bai89, Mcg95, Lal97]. The merit of using high-energy linacs for treatment is enormous and outweighs that of low energy linacs in terms of effectiveness and efficiency therefore it is imperative to develop effective shielding in bunkers to increase the efficacy of radiation treatment.

Since the neutron dose usually constitutes about 80% of the total radiation dose measurable at the maze entrance [Ker79], much of the shielding design becomes the problem of reducing to an acceptable level the neutron dose quite considerably, by slowing down high energy neutrons to thermal ones through scattering. The thermal neutrons then undergo radiative capture reactions with the materials of the bunker (mainly concrete) resulting in the disappearance of the neutron. Much work has been done in this field in the use of neutron moderating and absorbing materials to reduce the neutron dose. The work presented here centres on the modification of a bunker by the introduction of baffles in the treatment room and the maze to aid scattering and absorption of neutrons and then the use of neutron absorbers to further reduce the neutron fluxes. The primary objective is to eliminate completely the shielding door while using high-energy linacs. The study has been carried out using Monte Carlo simulations.

8.2 Theoretical background

8.2.1 Neutron flux in maze

Neutrons constitute the most important radiation for which consideration must take into account not only radiation quantity but also radiation quality. X and gamma-rays of energy in common use produce substantially equal biological effects for equal doses. However, the relative biological effectiveness (RBE) of neutrons is not only higher but also depends on the neutron energy. The differences in biological effects of

radiation are related to differences in the linear energy transfer (LET) of charged particles produced in neutron interactions that deliver the absorbed dose.

The neutron fluence in a linac bunker maze comes from three notable sources; a direct component of high energy fast neutrons assumed to have travelled into the maze directly from the accelerator head which follows the inverse square law; a slowing down component whose lower energy neutrons (epithermal) enter the maze after fast neutrons have scattered a few times off the walls of the treatment room and, finally, thermal neutrons as a result of neutrons that have scattered several times and attained thermal equilibrium, creating a uniform flux of neutrons in the treatment room. McCall et al [McC87] and other workers [McG95, Lal97, McG00] give semi-empirical expressions for the flux of the direct, epithermal and thermal neutrons entering the maze from the treatment room as follows:

$$\phi_{direct} = \frac{aQ}{4\pi R^2} \tag{8.1}$$

$$\phi_{scattered} = 5.4\frac{aQ}{S} \tag{8.2}$$

$$\phi_{thermal} = 1.26\frac{aQ}{S} \tag{8.3}$$

The total neutron flux is the summation of the direct, scattered and thermal

$$\phi_{total} = \phi_{direct} + \phi_{epithermal} + \phi_{thermal} \tag{8.4}$$

Therefore the total neutron flux in the maze is given by

$$\phi_{total} = \frac{aQ}{4\pi R^2} + \frac{5.4aQ}{S} + \frac{1.26aQ}{S} \tag{8.5}$$

where Q is the neutron source strength from the treatment head, (neutrons/unit dose x-rays) and has a value of 2.25E12 and 1.91E12 for tungsten and lead respectively. The surface area of the treatment room is denoted by S while R is the distance from the accelerator target to the calculation point and **a** is a relative transmission factor for neutrons which penetrate the head shielding that takes a value of 1 for Pb and 0.85 for W.

8.3 Possible structural modification of bunker

NCRP Report Number 49 (NCR76) discusses in detail structural shielding designs for x-ray and gamma-ray energies up to 10 MeV. Above this energy the presence of neutrons necessitates extra shielding which researchers have used analytical and semi-empirical methods to formulate for the required shielding. Others have used Monte Carlo simulation to predict the most appropriate shielding that can be altered to suit a particular requirement. From equation 8.5, the total neutron flux can be reduced by an increase in the surface area (S) of the treatment room since R is a fixed parameter. This factor has been considered in this work by the introduction of baffles in the ceiling of the treatment room and at its entrance, and also in the maze. More bends in the maze aids scattering of neutrons and reduce the neutron content at the exit of the maze [McG95]. The maze length has a profound effect on the neutron dose, a tenth value dose at a length of 5m of the maze, has been reported by Kersey [Ker79]. MCNP simulation results showed that a maze length increased from 6.5 m to 9.5 m resulted in a neutron dose reduction of 80% [Car99]. Maze lengths greater than 5 m with more bends would be ideal to attenuate neutrons and therefore should reduce the neutron dose at the maze exit.

8.4 Neutron absorbers

The use of neutron moderating and absorbing materials enhances the reduction of neutron contribution to the total dose at the maze exit. However, substantial neutron capture gamma radiation is emitted which tend to overshadow the intended purpose. Good moderating and absorbing materials should provide effective shielding of neutrons and therefore contribute much less dose to the overall dose measured at the maze entrance. High hydrogen containing materials such as polyethylene have been used as moderating materials in combination with neutron absorbing materials. Some researchers have used wood [Bak01] which showed hardly any difference in the neutron fluence in comparison with the 'bare' maze concrete.

8.4.1 Traditional 1/v neutron absorbers

Boron-10 (^{10}B) and lithium-6 (^{6}Li) containing compounds have been materials of choice for this purpose as these are readily available and have been tested over the years. ^{10}B is by far the most effective due to the higher thermal neutron capture cross-section of 3840 barns for the $^{10}B(n,\alpha)$ reaction compared to 940 barns for the $^{6}Li(n,\alpha)$

reaction. These are 1/v neutron absorbers and therefore are ineffective as the energy of the neutron increases. On neutron capture ^{10}B emits a prompt γ-ray of energy 0.48 MeV which contributes to the dose due to photons. Reports of capture gamma ray levels at accelerator maze entrances vary widely in the literature, with estimates ranging from 20 to 50% of the total photon dose at the shielding door. Work done by McGinley et al [McG95b] suggests the presence of both low-energy photons scattered from the room and high-energy capture photons generated in the maze contribute to the photon dose at the maze door.

8.4.3 Other neutron absorbers

Rare-earth metals such as gadolinium, hafnium and samarium have large neutron absorption cross-sections that can be used to attenuate neutrons in the maze in place of the more favoured traditional neutron absorbers. These have metallic luster, are malleable and ductile and also stable in air. Table 8.1 shows the main characteristics of gadolinium isotopes [Gei00, Abd94] and clearly the most important isotopes, in terms of cross section and abundance, are ^{155}Gd and ^{157}Gd. In the process of thermal neutron capture by gadolinium nuclei, there are two main competing processes in the de-excitation of $^{158}Gd^*$: prompt gamma emission and conversion electrons. Auger electrons are emitted as vacant atomic orbitals are filled following the emission of conversion electrons of mean energy 91 keV and a range of about 0.01 cm [Gei00]. Table 8.2 shows some relevant characteristics of the main isotopes of gadolinium, hafnium and samarium including the resonance energies and neutron capture x-rays due to emission of conversion electrons [Jea78]. Due to their large neutron absorption

Table 8.1: The main characteristics of gadolinium isotopes [Gei00, Abd94].

Isotope	Abundance (%)	Cross section (barns)	Daughter isotope	Half-life
Nat Gd	100	48890	-	-
^{152}Gd	0.2	1100	^{153}Gd	241.6 d
^{154}Gd	2.2	90	^{155}Gd	stable
^{155}Gd	14.7	61000	^{156}Gd	stable
^{156}Gd	20.6	2.0	^{157}Gd	stable
^{157}Gd	15.68	255000	^{158}Gd	stable
^{158}Gd	24.9	2.4	^{159}Gd	18.6 h
^{160}Gd	21.9	0.8	^{161}Gd	3.66 min

cross-section gadolinium, hafnium and samarium have been used in reactor control rods. These metals and their compounds are available and can be incorporated in large matrices of neutron moderating materials, such as polyethylene, as neutron shielding in the maze. Though these metals are relatively expensive, the availability of compounds containing the isotopes makes them affordable for the purpose intended.

Table 8.2: Resonance energies and percentage K-shell neutron capture x-rays of isotopes of samarium, gadolinium and hafnium [Jea78, Abd94].

Nuclide	Resonance energy (eV)	Cross-section (barns)	K-shell x-rays (% n capture)
^{149}Sm	0.0976	132000	3.7
^{149}Sm	0.872	20600	3.7
^{177}Hf	1.098	34600	41
^{177}Hf	2.38	75000	41
^{155}Gd	0.0268	61000	25
^{157}Gd	0.0314	255000	25

8.5 Review of work done by others

Several researchers have worked on ways of reducing the neutron component in the maze by using either different design of mazes and or neutron absorbers in the maze by employing semi-empirical methods while others have used Monte Carlo calculations, and the MCNP code. Analytical methods have been employed by McCall [McC79] and the MCNP code and Kersey [Ker79] to evaluate the effectiveness of the maze length and number of bends of the maze to attenuate the neutron flux. A method proposed by Kersey assumes that neutrons are attenuated by a factor of ten for every 5m distance travelled through the maze. Although his method gives good agreement for several maze designs, other researchers have found it inadequate in describing the attenuation of mazes in which there is more than one bend before the maze exit. Analytical methods have been found inadequate in cases where there is deviation from a typical room-shielding configuration. The effect of neutron absorbing materials has been investigated experimentally by McGinley and Miner [MaG95] and Lalonde [Lal97] and both clad the maze walls with neutron moderating and absorbing materials. Monte Carlo calculations, MCNP, have been used by some workers to develop shielding configurations including work done by

Carinou and Kamenopoulou [Car99]. They found a good agreement between simulation and analytical calculations for maze lengths greater than 8.5m even though there were discrepancies with the methods developed by Kersey and McCall.

8.6 Materials and methods

8.6.1 MCNP simulation

The entire work was carried out employing the Monte Carlo Neutron Particle code MCNP4C2 [Bri01], to simulate all the cases considered in the calculation of the neutron dose and spectra at the maze exit. Tallies F6 and F4 have been used for this purpose in each input file to estimate per unit particle the neutron dose and neutron flux respectively. The tallies were in the form of a sphere at the maze exit in the same plane as the 100 cm SSD source position. Each input file run passed all the ten statistical tests the MCNP code normally undertakes to indicate the success or otherwise of the simulation. The success of a simulation is indicated by the relative error of less than 10% and a high and constant figure of merit (FOM) The overall standard deviation of each of these tallies in each output file was much less than 0.1% after running over 50 million particles (NPS). Each input file was run for approximately 24 hours using a personal computer (PC) running on a 1.9 GHz Intel Pentium 4 processor.

8.6.2 Linac bunker

Figure 8.1 shows the plan view of the schematic diagram of the linac bunker. The primary shielding is twice the length of the secondary and is 2m thick and shields the direct photon beam. The primary shielding is in the direct field of view of the beams from the treatment head and therefore extra shielding is required. The secondary shielding mainly attenuates scattered photon beams and need not be as thick as that of the primary. The physical dimensions of the bunker are 8 x 8 x 3.5 m^3 with a maze width of 2.5 m and 8 m long. The exit of the maze is on the side of the maze as recommended McGinley and Miner [McG95] since this gives a much lower neutron flux due to the extra bend which favours scattering of neutrons. The concrete used for this design was the Los Alamos heavy concrete formula [Boo85] though Barytes concrete has been used by some researchers for the same purpose [Car99]. As a

modern facility the bunker has no door in order to enhance the movement of patients and radiation workers to and from the treatment room. Besides avoiding the cost involved in providing a heavy shielded door, more patients can be treated in a given period due to much easier access to the treatment room as well as catering more satisfactorily in emergencies. The bunker is assumed to be in a basement therefore part of the soil structure has been incorporated in the simulation.

8.6.3 Modification of the bunker

The modification of the bunker involved the introduction of concrete baffles running along the ceiling of the treatment room and as part of the maze and exit. The baffles are as shown in figure 8.2 and their introduction in the treatment room increased the total surface area of the treatment room by approximately 20% of the original. The baffles in the maze together with that at the entrance of the treatment room created three bends in the maze. It was envisaged that this arrangement would enhance more scattering of fast neutrons to thermal and the subsequent neutron capture. Those in the ceiling were 1 m wide and 0.5m thick and run the length of the ceiling. Those in the maze were of the same size and run from the floor to the ceiling. The lip at the entrance of the maze from the treatment room is 0.75 m wide and 1.0 m thick and also runs from ceiling to floor.

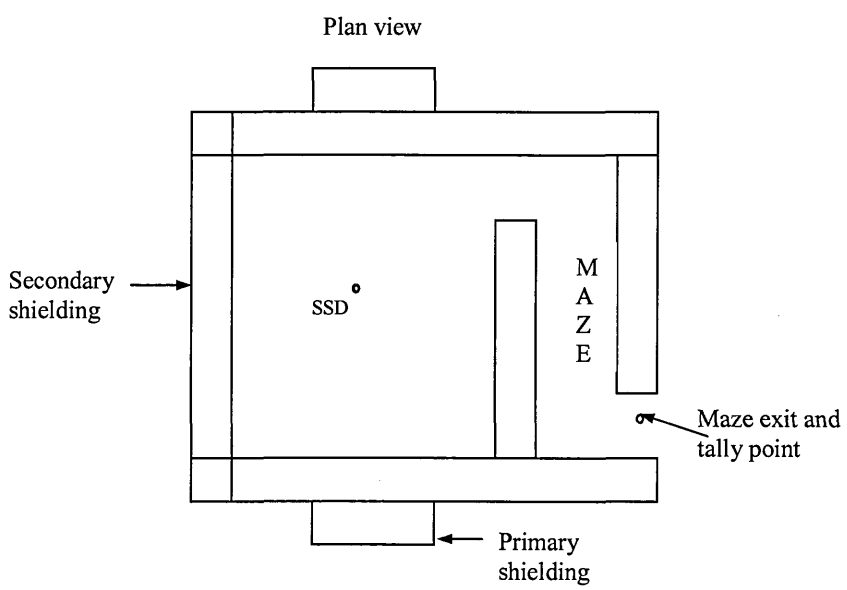

Fig. 8.1: Schematic diagram of the plan view of the linac bunker as used in the simulation. The actual dimensions of the bunker are 8x8x3.5 m^3

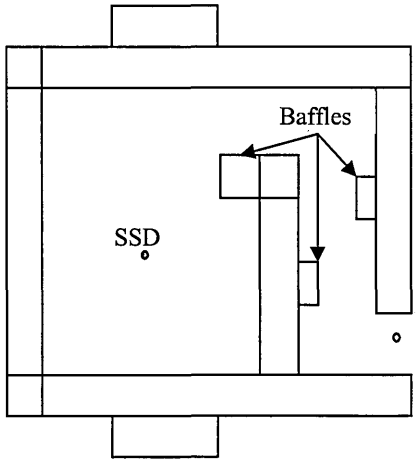

Fig. 8.2a: Plan view, through isocentre showing the baffles in the maze and treatment room.

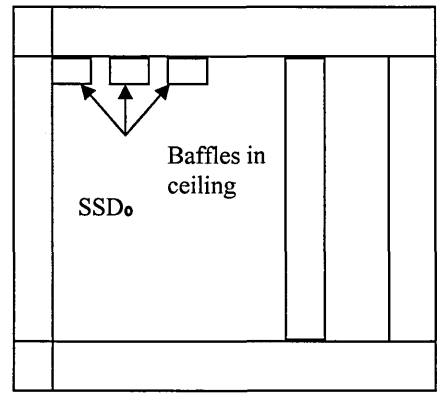

Fig. 8.2b: Transverse view, through SSD showing the baffles in the ceiling.

8.7 Neutron absorbers in maze

Neutron absorbers were introduced at the exit and entrance to the maze and in the ceiling and floor with the aim to attenuate further the neutrons in the maze thereby reducing the neutron flux and dose. Since most of the neutron absorbers are most effective in the lower end of the neutron spectrum, it was envisaged that the extra scattering provided by the introduction of baffles would result in lower energy neutrons. For the purpose of easy identification, the arrangement of neutron absorbers in the maze has been designated configurations in their description.

8.7.1 1/v neutron absorbers in maze

As traditional neutron absorbers lithium and boron, in the form of ^{6}Li and ^{10}B, in materials have been used to line portions of the maze in the simulation. The composition of the materials are as shown in Tables 8.3 and 8.4 as supplied by Premise Ltd and Reactor Experiments Inc. The percentage by weight of ^{10}B in the boron containing material was not stated by the manufacturer and so the natural abundance of ^{10}B (19.8%) was used in this simulation and the same with ^{6}Li (7.4%). Tables 8.3 and 8.4 give the percentage by weight of the materials containing boron and lithium, respectively, commonly used for neutron shielding.

Table 8.3: Boron containing material in the form of bricks and slabs of density 1.12 gcm^{-3} manufactured by Reactor Experiments Inc. Sunnyvale, California, U.S.A.

Element	% by Weight
Oxygen	**51.7**
Carbon	**27.17**
Boron (^{10}B)	**8.97 (1.78)**
Hydrogen	**6.88**
Nitrogen	**5.28**

Table 8.4: Slightly waxy solid lithium containing material of density 1.0 gcm^{-3} manufactured by Premadex Technical Data, Premise Ltd, Herts, UK.

Element	% by Weight
Oxygen	**39.9**
Carbon	**47.4**
Lithium (^{6}Li)	**1.3 (0.1)**
Hydrogen	**11.4**

In configuration A, Figure 8.3a, the maze entrance was clad with lithium and boron at the exit and lines from ceiling to floor in the portions shown. Lithium and boron are clad at the entrance and another portion of lithium at the exit of the maze in configuration B, Figure 8.3b. In configurations C, D, and E, Figures 8.3c, 8.3d and 8.3d respectively, lithium and boron clad the ceiling and/or the floor, as indicated.

8.7.2 Other neutron absorbing materials in maze

In order to investigate the use of other neutron absorbing materials, notably rare-earth metals namely: gadolinium, hafnium and samarium have also been used in the simulation. Some of their characteristic properties relating to neutron absorption have been discussed in the previous section and shown in Tables 8.1 and 8.2. In configurations C and E, Figures 8.3c and 8.3e, respectively, gadolinium and hafnium clad the entrance and exit of the maze in the form of thin metallic sheet while in configuration D, Figure 8.3d, samarium clad the entrance and gadolinium at the exit.

Natural gadolinium, ^{157}Gd, ^{177}Hf and ^{149}Sm isotopes have been investigated in this simulation as shown in Figures 8.3c, 8.3d and 8.3e given below. It is expected that the adoption of these materials in the future by others workers for neutron attenuation in the maze will vastly reduce neutrons and capture gamma content at the exit of the maze due to their relatively large neutron absorption cross sections and the release of conversion electrons as a competing process to capture gamma.

8.8 Neutron source

An isotropic ^{252}Cf fission source was used for the simulation and was positioned at the origin, SSD, at 150 m high above floor. The choice of the neutron fission spectrum from the isotopic ^{252}Cf source lies in the fact that its spectrum resembles that of the photoneutron produced from tungsten [NCR84] as shown in figure 2.3 (chapter 2). It can be argued that the spectrum represents the unfiltered spectrum from a linac and that utilising this for shielding calculations gives the best form of shielding required to effectively attenuate photoneutrons entering the maze. This source is one of the integrated sources available in the MCNP source bank and therefore with the appropriate commands one can incorporate it in the MCNP input file.

8.9 Bunker configurations

Figure 8.1 is designated configuration 'O' denoting the original bunker before modifications were made. This is a typical bunker in most hospitals or centres with the difference at the location of the exit and as discussed above this bunker has no shielding door. Figure 8.2 is designated configuration 'M' denoting the modifications made to the original bunker by the introduction of baffles in the treatment room and maze with the view of reducing the neutron content at the exit through scattering and capture of thermal neutrons. Configurations 'A' to 'E' show the addition of neutron absorbing materials in the maze to further attenuate the neutrons in the maze and also reduce capture gamma content as well. In configurations 'C', 'D' and 'E' neutron absorbing material boron and lithium clad the ceiling and floor. Figures 8.3a to 8.3e show the plan view of the bunker taken through the SSD.

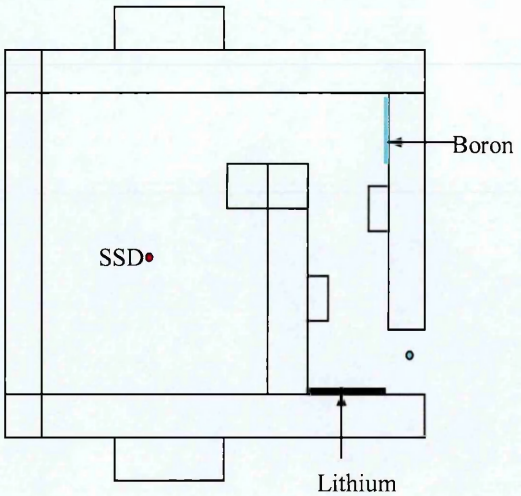

Fig. 8.3a: Configuration 'A', boron and lithium clad maze entrance and exit.

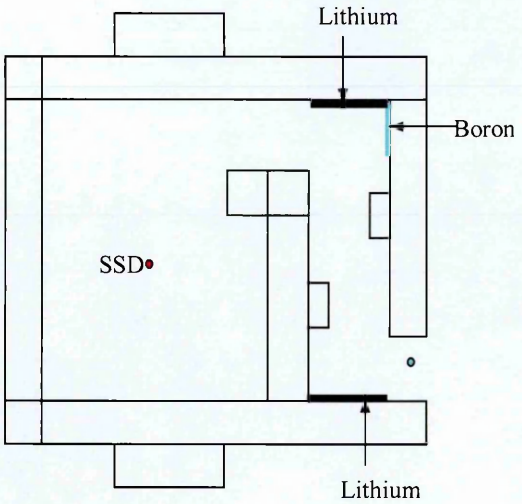

Fig. 8.3b: Configuration 'B', boron and lithium clad maze entrance and exit.

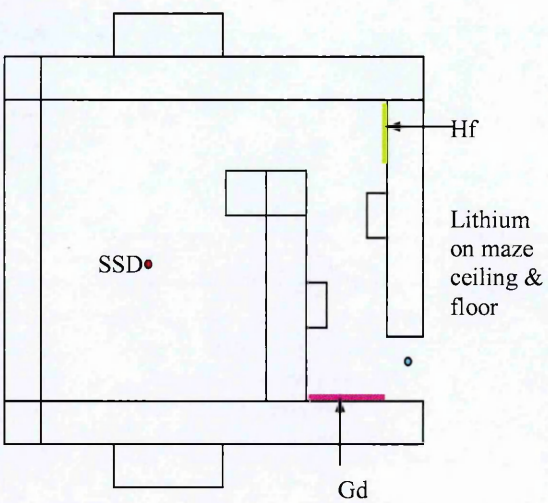

Fig. 8.3c: Configuration 'C', hafnium and gadolinium clad maze entrance and exit with lithium on ceiling and floor.

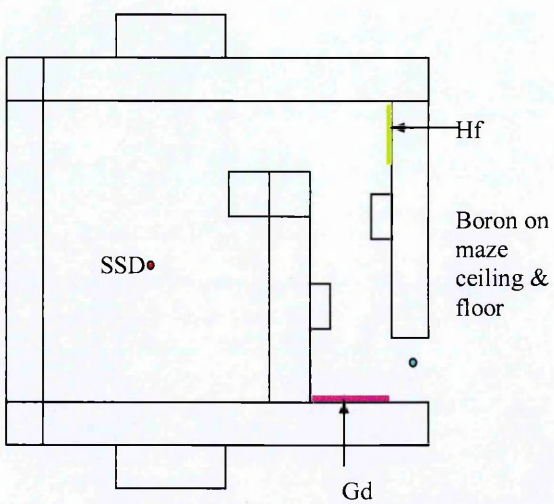

Fig. 8.3d: Configuration 'D', hafnium and gadolinium clad maze entrance and exit with lithium on ceiling and boron on floor.

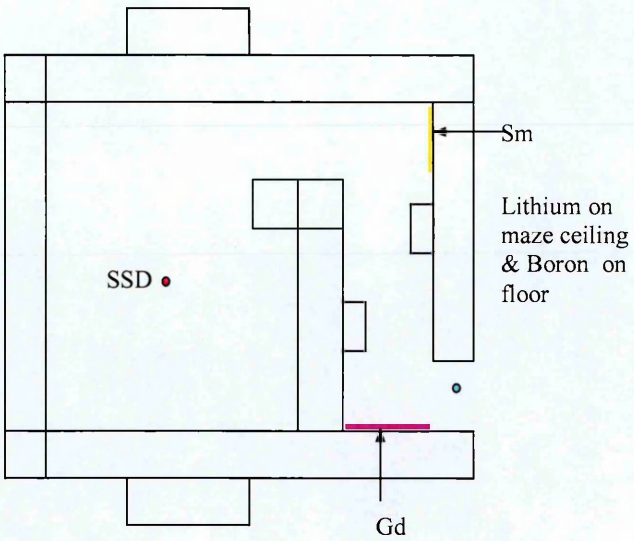

Fig. 8.3e: Configuration 'E', samarium and gadolinium clad maze entrance and exit and boron on ceiling and floor.

8.9.1 MCNP geometry

Figure 8.4 shows the geometry plots of the plan view (pz = 0, i.e x-y plane, through SSD) of the original and modified bunker designs. The cells and planes that make up the primary and secondary shielding are numbered and can be identified. The modified bunker shows in addition the baffles in the maze and treatment room. The cell numbered 70 is the source position and coincides with the SSD at 150 cm from the floor. Cell 72 is the tally point and at the maze exit from the treatment room. Figures 8.5a and 8.5b show the transverse sections of the bunker for plot planes py = 0 and px = 0 respectively, through SSD of the original and modified bunker. These show the baffles in the ceiling of the treatment room of the modified bunker and the soil underneath (green in colour) the building foundation of the bunker.

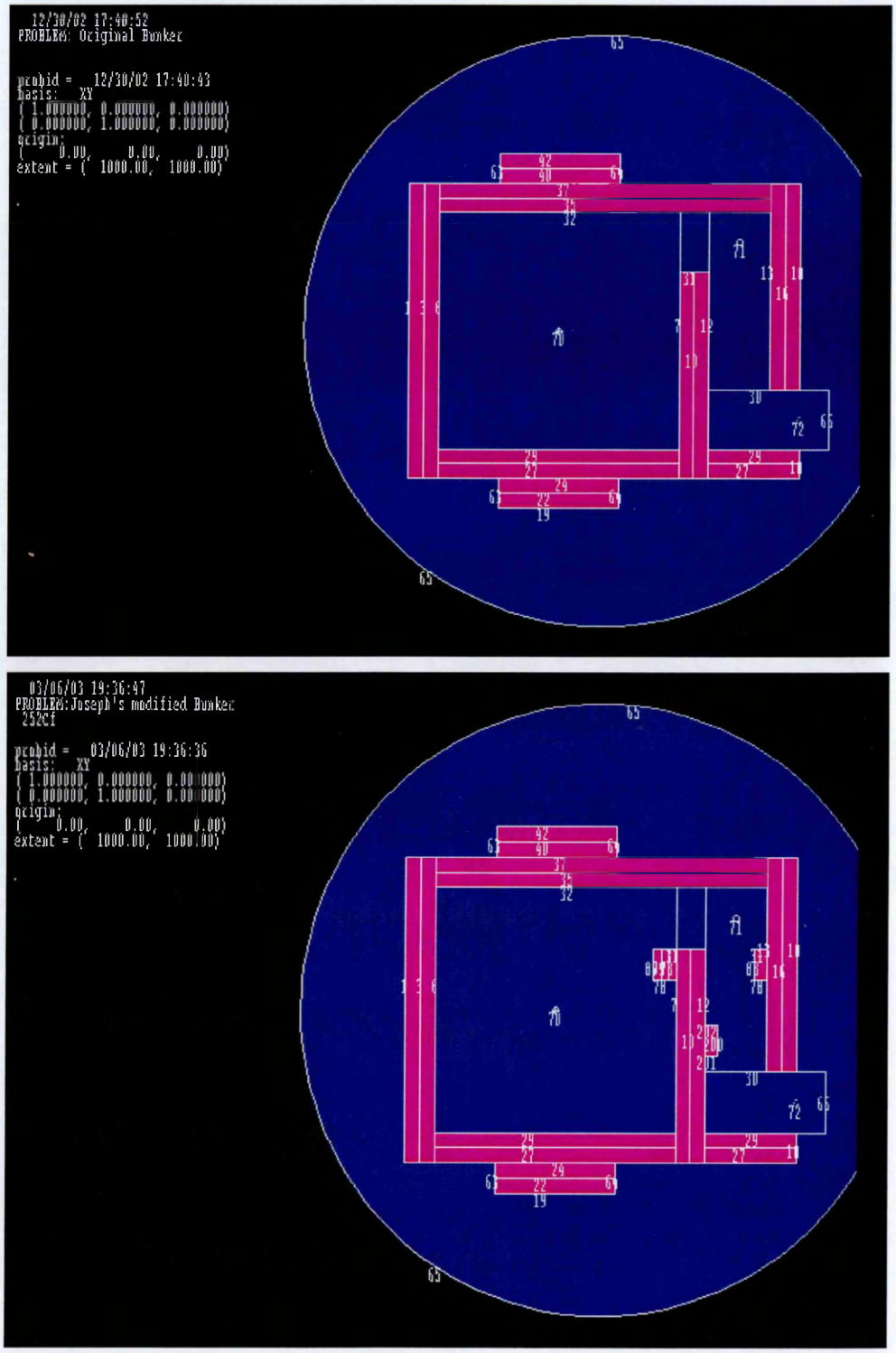

Fig. 8.4: MCNP geometry plot of the plan view of the original and modified bunker showing the primary and secondary shielding and the baffles in the maze and treatment room in the case of the modified bunker.

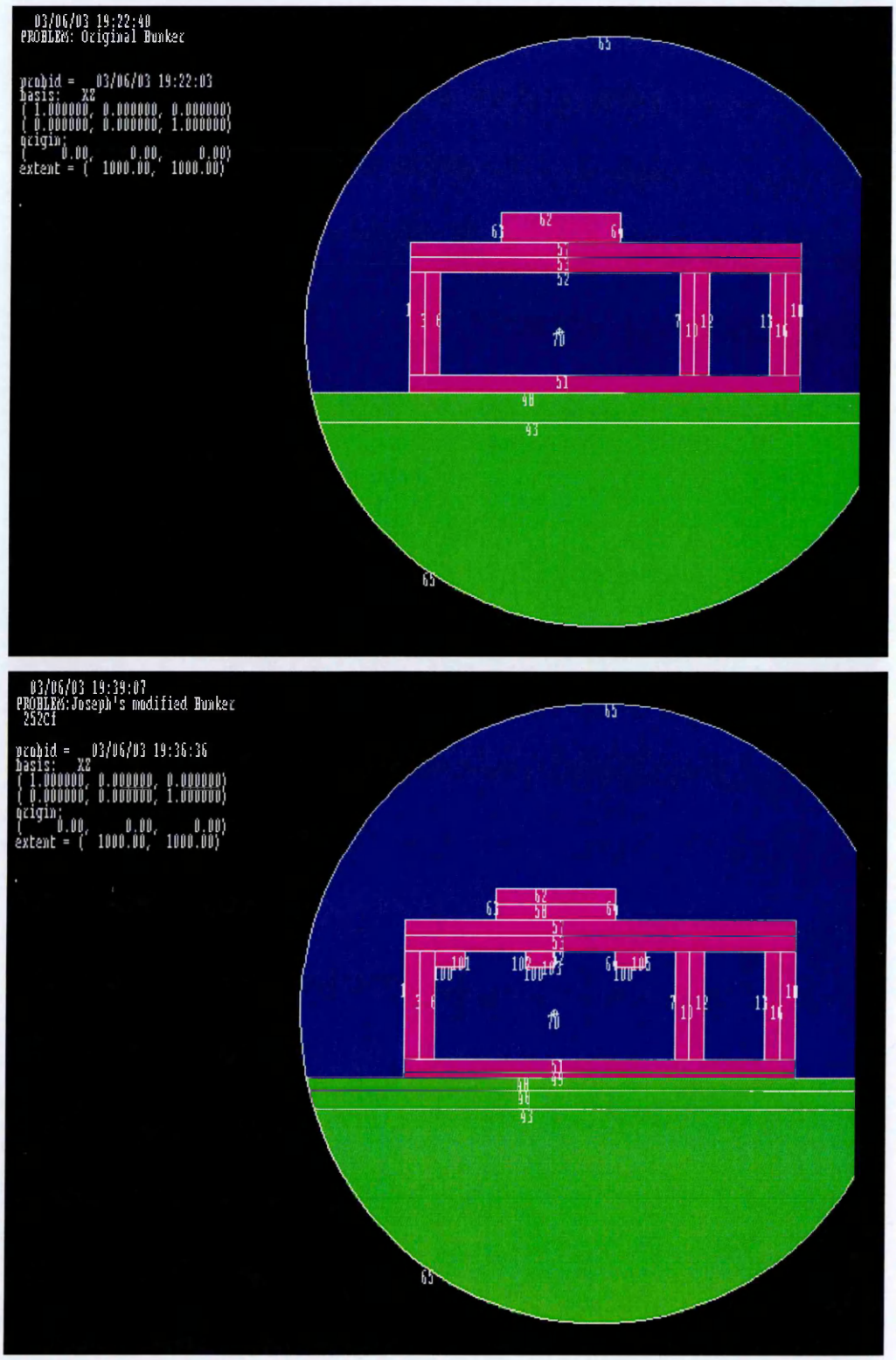

Fig. 8.5a: MCNP geometry plot of the transverse view of the original and modified bunker showing the primary and secondary shielding and the baffles in the ceiling of the treatment room in the case of the modified bunker.

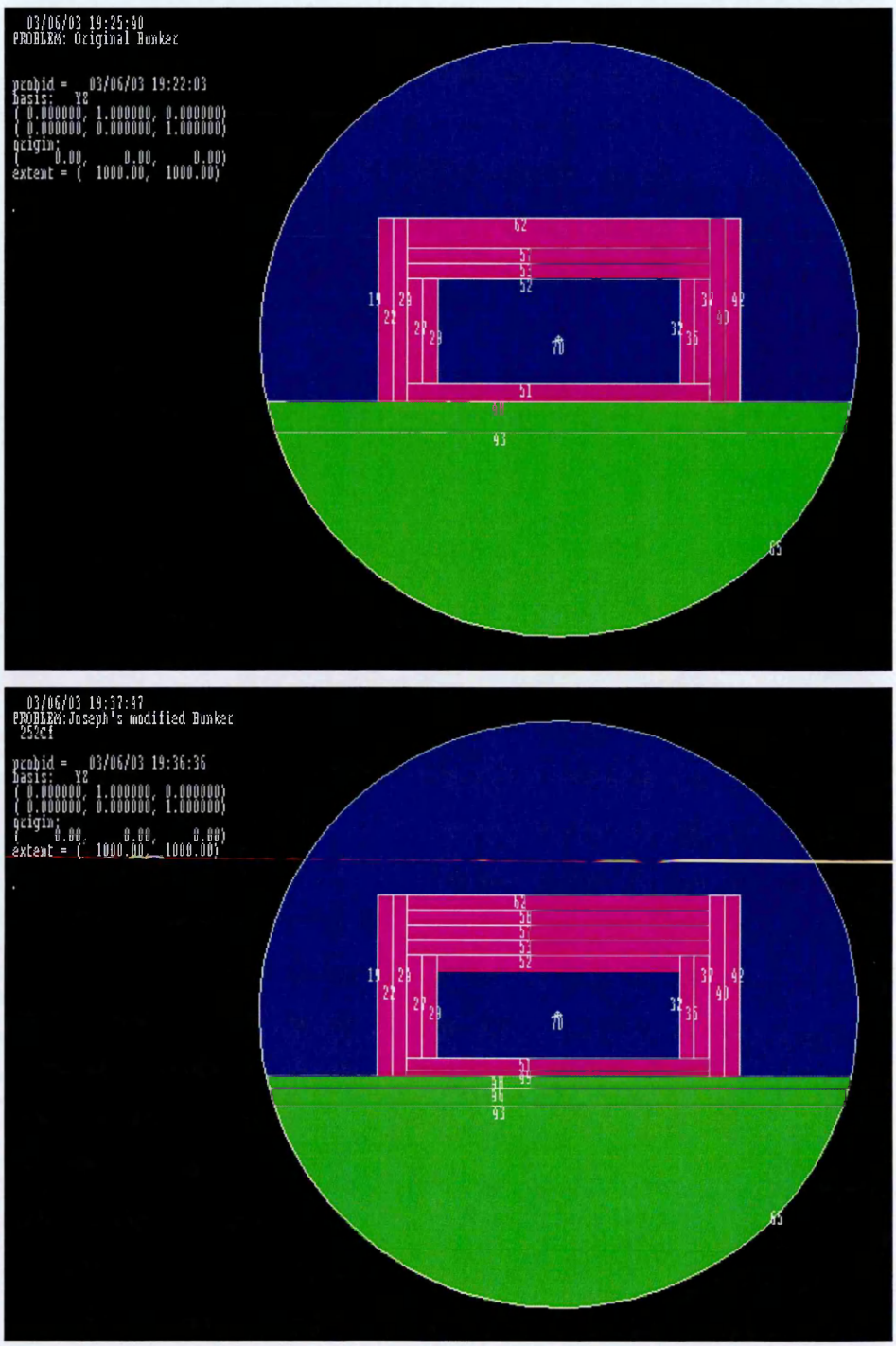

Fig. 8.5b: MCNP geometry plot of the transverse view of the original and modified bunker showing the primary and secondary shielding and the baffles in the ceiling of the treatment room in the case of the modified bunker.

8.10 Results and discussion

8.10.1 Effect of bunker modification

The effect of bunker modification is shown alongside that of the original bunker for the total neutron flux and dose as shown in figures 8.6 and 8.7, respectively. The neutron dose is the energy deposited by the neutrons in a unit mass of material while the neutron flux is the number of neutrons traversing a unit area per unit time. The reduction in the total neutron flux is approximately 45% while that of the neutron dose is marginally greater than 40% ($40<x<45\%$). The mean energy of direct neutrons from a linear accelerator is of the order of 1 – 2 MeV and that of scattered neutrons in the treatment room is about 25% that of the direct neutrons [McC78]. Considering the neutron spectrum in figure 8.13, the modal neutron energy occurs at 1 eV for both original and modified bunker and thus shows the extent of scattering undergone by high-energy neutrons to attain this energy level. The reduction of the total neutron flux and energy at the maze exit can be attributed to the following:

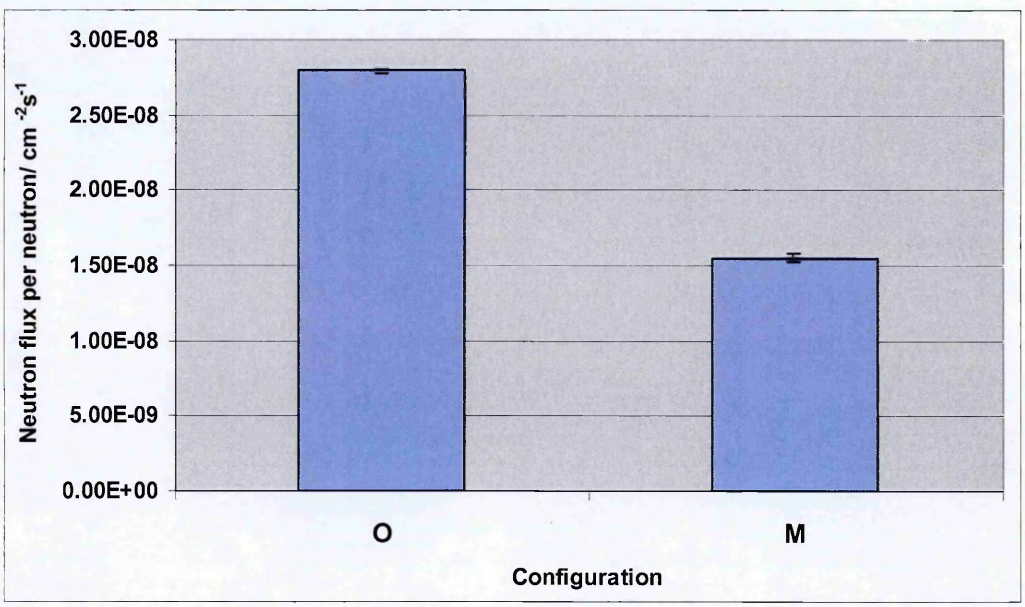

Fig. 8.6: The effect of bunker modification on the total neutron flux at the maze exit. O - original, M – modified.

i) Increase in the surface area of the treatment room in accordance to equation 8.5 maximises the denominator of the scattered and thermal parts. An increase in the surface area by 20% resulted in approximately 30% reduction in the total neutron flux. MCNP thus overestimates the total neutron flux by approximately 10% without considering the assumptions associated with equation 8.5. Epithermal and fast neutrons undergo further multiple scattering to lower energies in the ceiling and at the entrance to the maze from the treatment room. As more thermal neutrons are produced the probability for neutron capture reactions increases and thus account for the reduction, in part, of the neutron flux and consequently the neutron dose.

ii) The original maze had two bends, one at the entrance and the other at the exit of the maze. However introduction of the baffles increased these to four bends. This favours scattering of more energetic neutrons that enter the maze. The modified bunker has more concrete than that of the original and therefore more hydrogen content. This enhances transfer of energy from neutron to hydrogen due to their similar mass numbers. Thermal neutrons undergo radiative capture with the elements constituting the concrete notably hydrogen in the reaction $^{1}H(n,\gamma)^{2}H$ emitting a prompt gamma ray of energy 2.223 MeV. There is also reflection of neutrons in both configurations that causes a reduction in the neutron flux, however, the effect is more pronounced in the modified bunker since the selected positions of the baffles in the maze increase the probability of the occurrence of this effect.

The dimensions of these baffles are such that they do not interfere with access to the treatment room. About 30% reduction in the total neutron flux was observed in simulations using the baffles in the ceiling and at the entrance of the treatment. The position of the baffle at the entrance of the treatment room is strategic because from the field of view of the source, the solid angle the source makes with the entrance of the maze is reduced with the introduction of the baffle. Hence, more neutrons are attenuated before reaching the maze.

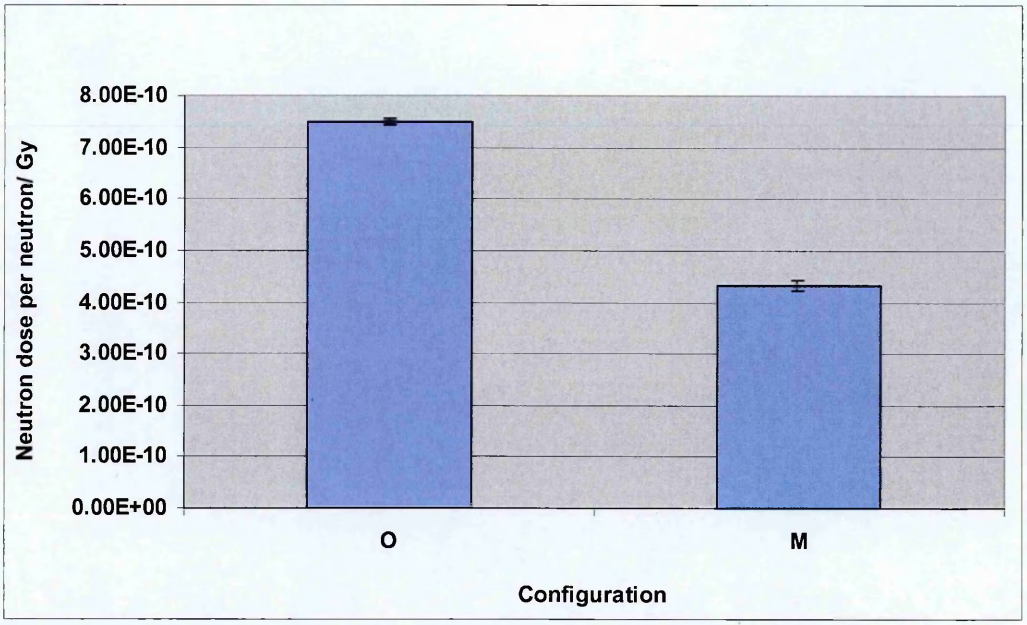

Fig. 8.7: The effect of bunker modification on the total neutron dose at the maze exit.

It is desirable that, since neutrons form approximately 80% [Ker79] of the radiation dose measurable at the maze entrance, the rationale behind any maze design should ultimately be focused at reducing the neutron dose to an acceptable level. The path often chosen to achieve this is first to slow the neutrons down to thermal energies using neutron moderating materials such as polyethylene and then absorbing them in wall-cladding neutron absorbing materials or at the shielding door. The applicability of equation 8.5 is a clear manifestation of the agreement between the semi-empirical formula and theory. Neutrons in general lose energy by scattering several times off the walls of the treatment room and the maze implying that a larger surface area favours scattering and the subsequent loss of energy by the neutrons. Some treatment room and maze designs have been considered in this respect [Ker79, Mul86, Mcg95] even though such methods are thought to over estimate the neutron dose [Car99].

Besides the bunker modification, special types of concrete including baritic and a mixture of standard concrete (70%) and colemanite (30%) [Ago95] and also barites [Car99] have been used either to construct or to simulate bunker designs. Some of these materials are not generally available except at localities where such materials

are naturally abundant. Even though such materials can be exported to other places the cost involved is a hindrance.

The length of the maze plays a very important role in reducing the total neutron component at the exit. The maze length in this design is 8m, that is 3m more than the length required to achieve a tenth value dose (TVD) analytically determined by Kersey [Ker79] at 5m. The length of the maze has also been a factor in realising the level of reduction in the total neutron flux and dose at the maze exit compared to other designs [Car99].

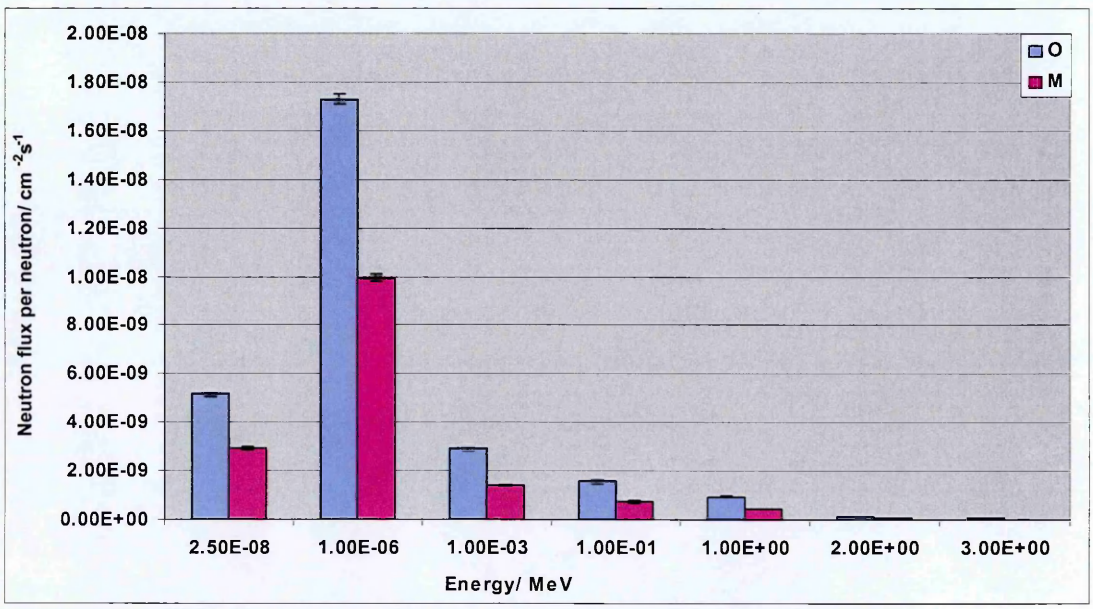

Fig. 8.8: Neutron spectrum for the original (O) and modified (M) bunkers.

8.10.2 Effect of neutron absorbers

Figures 8.9 and 8.10 show the effect of the addition of neutron absorbing materials in the configurations on the total neutron flux and dose. Considering the original bunker the neutron dose has been reduced by approximately 75%, 80%, 85%, 88%, 90% with respect to configurations A, B, C, D, and E. Also there is a reduction of approximately 55%, 65%, 75%, 78% and 80%, respectively, for configurations A, B, C, D, and E in comparison to the modified bunker configuration M. The neutron dose shows a much higher reduction from approximately 78% to 95% by comparing the original bunker with configuration A to E, respectively. Also by comparing the

modified bunker with the neutron absorbing configurations, the reduction in the neutron dose are 60%, 70%, 80%, 85% and 86% respectively for configurations A to E. The reduction in the neutron flux and dose at the exit of the maze is substantial demonstrating the effectiveness of the neutron absorbing materials notably the rare-earth elements. Measurements of the neutron dose equivalent in the maze using bubble detectors as discussed in chapter 6, revealed that the neutron dose is highest on the outer wall at the entrance of the maze from the treatment room as was observed by

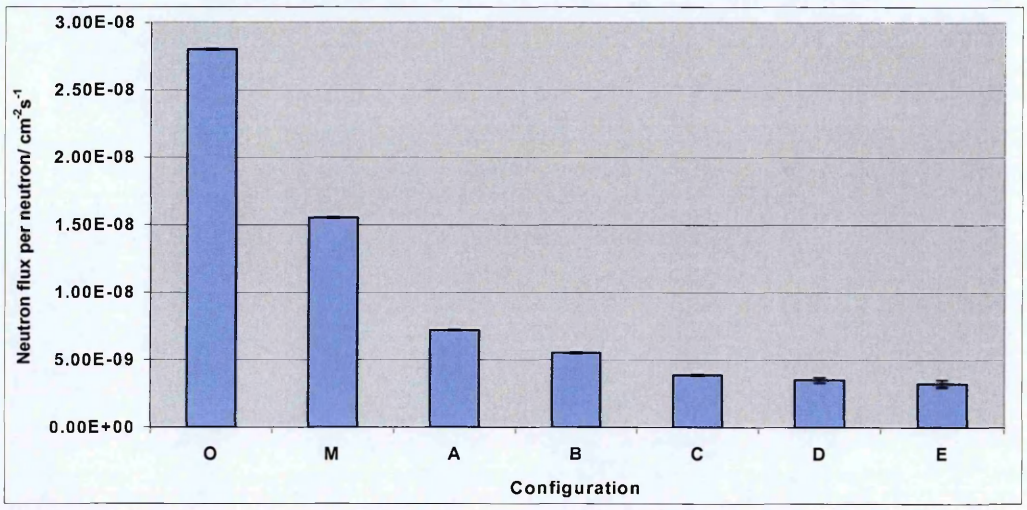

Fig. 8.9: Effect of neutron absorbing materials on the total neutron flux at the maze exit.

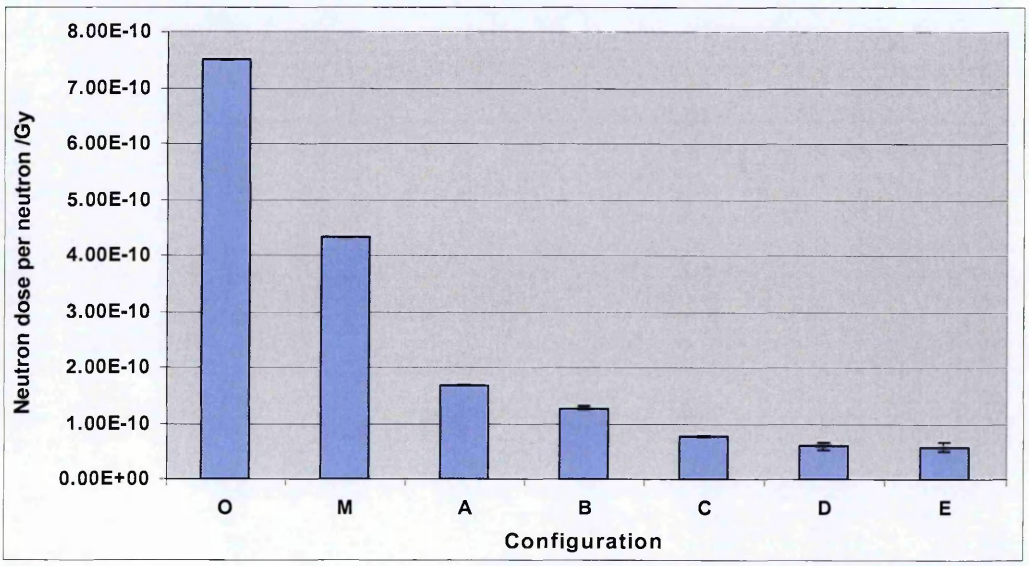

Fig. 8.10: Effect of neutron absorbing materials on the total neutron dose at the maze exit.

Lalonde [Lal97]. Consequently, the neutron absorbers were positioned strategically and appropriately to intercept the stream of neutrons that emerged from the treatment room along the outer wall. It was assumed that the fast neutrons which enter the maze from the treatment room, will undergo multiple scattering and may have lost a substantial amount of energy before reaching the maze exit. These are expected to bounce off the wall at the end of the maze before exiting the maze and on this assumption a neutron absorbing material was lined on this wall. The differences in the neutron flux and dose reductions calculated exist because of their neutron absorption cross-sections and the resonance peaks since only 5mm thick of each material was used. Comparing the neutron absorbers as shown in figures 8.11 and 8.12, there is a gradual fall in the neutron dose and flux from configuration A to E but virtually static from configuration D to E. The marginal difference in the neutron dose and flux can be attributed to the differences in the effective neutron absorption cross-sections and resonance energies of samarium and hafnium as shown in Table 8.2. Figures 8.13 and 8.14 show the neutron spectra of the neutron absorbing materials configurations, respectively. The effect of the extremely large neutron absorption cross-sections of the rare-earth elements is prominent in the thermal and 1 eV energies. These are also effective in the epithermal and high energies.

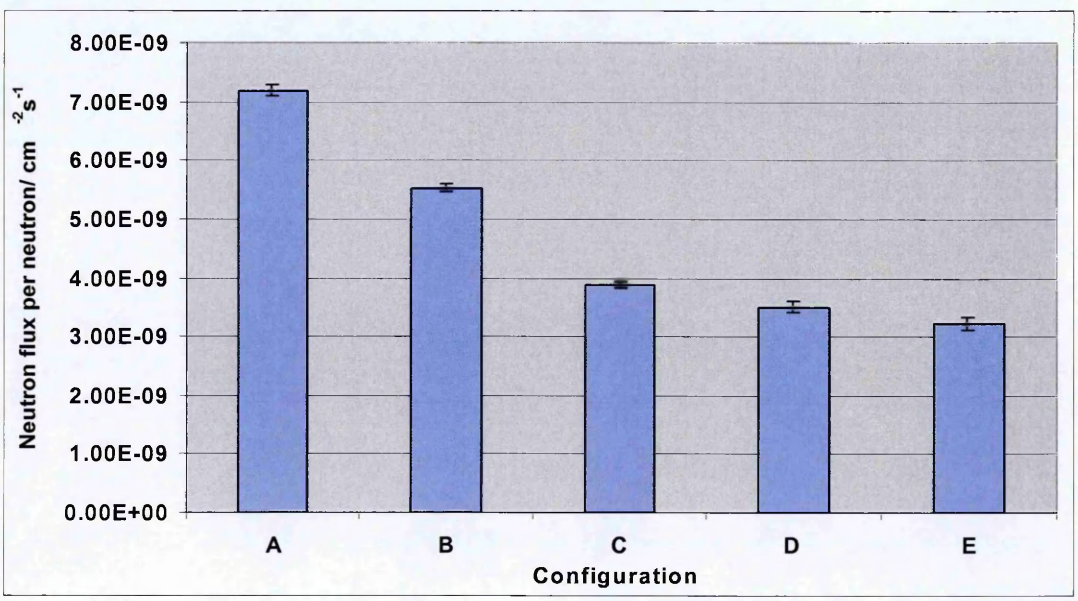

Fig. 8.11: Effect of neutron absorbing materials on the total neutron flux at the maze exit.

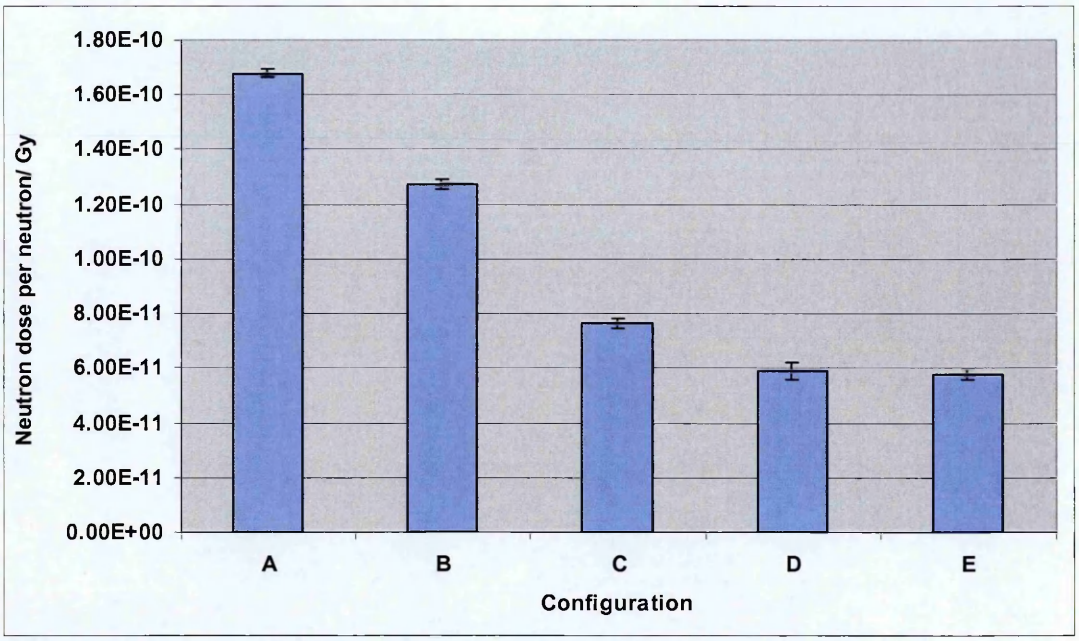

Fig. 8.12: Effect of neutron absorbing materials on the total neutron dose at the maze exit.

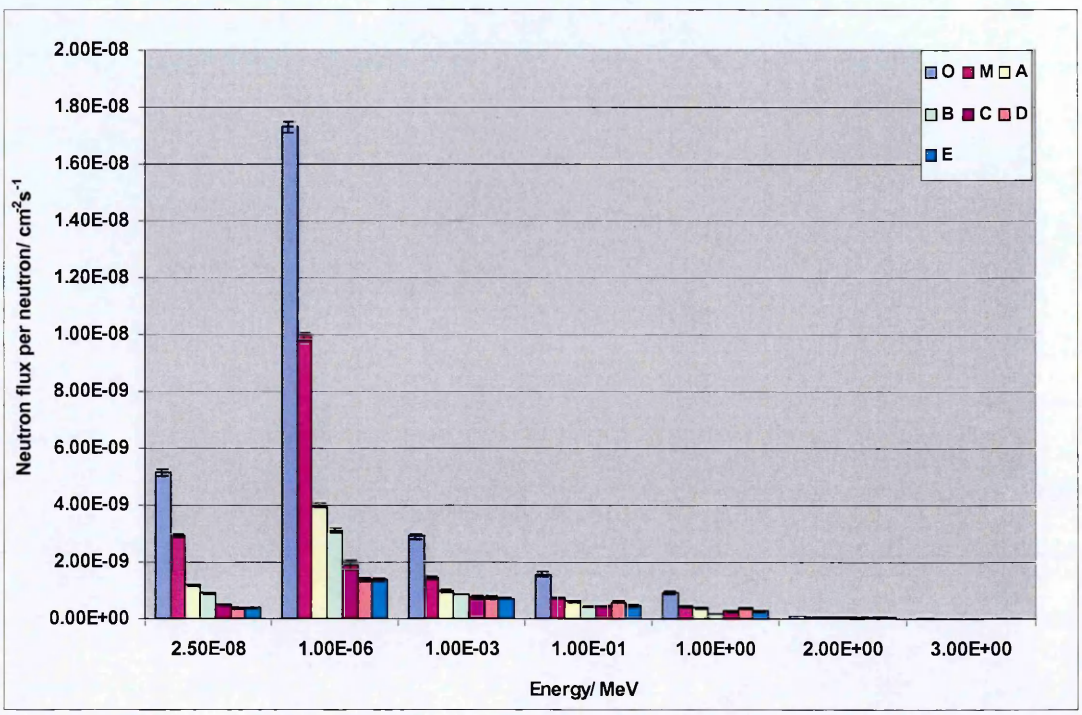

Fig. 8.13: Neutron energy spectrum for the configurations. The highest energy here is 3 MeV due to the relatively low flux recorded for much higher energies.

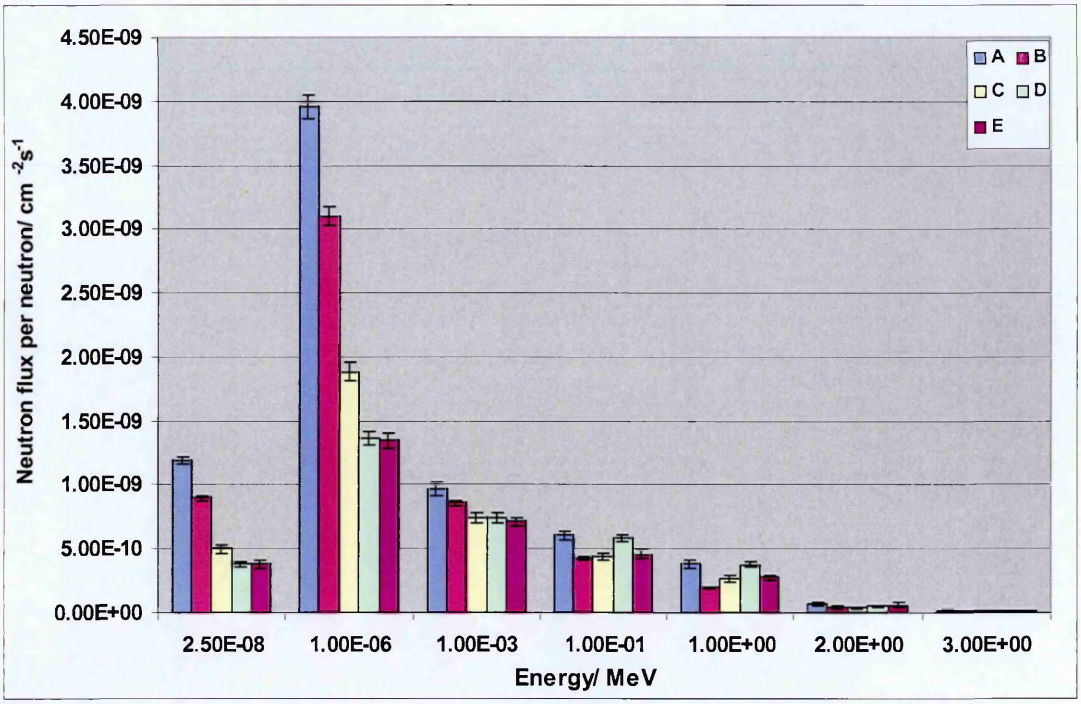

Fig. 8.14: Neutron spectrum at the maze exit due to the neutron absorbing materials.

Neutron moderating and absorbing materials have been used to shield neutrons in medical bunkers. The most common material used to moderate neutrons is polyethylene which is either used on its own or combined with a neutron absorbing material such as boron. The rationale behind this is that the neutron loses energy on interaction and is subsequently absorbed by boron. McGinley and Miner [McG95] used 5% boron in polyethylene to a greater effect. Traditionally, boron and lithium are preferred for such purposes. However, the neutron capture cross-section of boron and lithium falls rapidly with increasing neutron energy from 3840 and 940 barns/atom respectively at thermal energy to about 1 barn/atom at 100 keV. Therefore, these are generally ineffective at epithermal and higher energies.

The use of rare-earth metals as neutron absorbers has demonstrated the effectiveness of such materials for this purpose. Their relatively extreme neutron absorption cross section makes them suitable for neutron attenuation in the thermal and epithermal region. As observed in the comparison of the original and modified bunker, the modal neutron energy is 1 eV which is close to the resonance energy where their cross sections are very high. The introduction of neutron absorbers in the maze caused a further reduction in the total neutron dose and flux to approximately

90% of the original bunker configurations. The use of ^{177}Hf, ^{149}Sm and ^{157}Gd as neutron absorbers has enhanced the absorption of thermal and epi-thermal neutrons resulting from multiple scattering of fast neutrons in the treatment room and the maze. These undergo electron conversion processes on capture of the neutrons as a competing process to capture gammas and become stable on de-excitation. For example $^{158}Gd^*$ formed from the capture of a neutron by ^{157}Gd de-excites to the ground state of ^{158}Gd. These elements have metallic lustre, are malleable and form crystalline solids with the halides and therefore can be incorporated in the matrix of neutron moderating materials or similar material such as that for boron and lithium discussed above. There is no information in the literature suggesting the use of such materials as neutron absorbers apart from control rods in reactors. These are known to be relatively expensive but not when compared to having a shielding door. The effect of these neutron absorbers is such that the presence of a shielding door is not required as has been shown above. This will make the treatment room more accessible in times of emergency and also increase the number of patients treated in a day and consequently reduce waiting lists in the NHS as well as generating more income elsewhere.

8.11 Conclusions

It has been shown that the modification of linac bunkers by introduction of baffles in the treatment room and the maze can significantly reduce the neutron flux at the maze entrance. This confirms the theory that by increasing the surface area of the treatment room, that is maximising the denominator in equation 8.5, more neutrons are likely to attain thermal status and therefore a higher probability of undergoing neutron capture reactions. The increase of the number of bends in the maze from two to four by introduction of baffles also contributed to the lower neutron flux observed. This enhanced scattering and reflection of fast and epi-thermal neutrons in the maze and thus confirmed the fact that, as more bends are introduced in the maze, the neutron dose and flux at the maze exit falls. The reduction in the total neutron flux is approximately 45% while that of the neutron dose is marginally greater than 40% ($40<x<45\%$). The modification of the bunker should be done by taking into consideration patient and personnel mobility and convenience.

Conventional neutron absorbers have been efficient in reducing the neutron flux and dose, though modest. The use of large neutron absorption cross section materials namely; ^{157}Gd, ^{177}Hf and ^{149}Sm did not only cause a further reduction in the neutron flux but also eliminated the dose due to capture gamma rays associated with the use of the more generally preferred ^{10}B. The introduction of neutron absorbers in the maze caused a further reduction in the total neutron dose and flux to approximately 90% of the original bunker design. Although these isotopes are relatively expensive, the real cost of using them for shielding must take into consideration the health of the radiation workers and general public, the cost if a door has to be provided at the maze entrance in contrast to the number of patients that can be treated in a given period and the longer term benefits.

9.0 Conclusions and suggestions for further work

Photoneutron contamination in the photon output of a 15 MV Varian Clinac 2100C operated at 4 Gy/min has been investigated using experimental and MCNP calculations.

In order to ensure that the MCNP output was valid, an isotopic (^{241}Am-Be) irradiation facility was simulated to calculate the scattered and transmitted neutron fluxes from a bulk rectangular water phantom. Comparison of the simulation results with those obtained with the N-Probe and LGB neutron detectors revealed a reasonable agreement between the experiments and calculations for both transmitted and scattered neutron fluxes. The ratio of transmitted and scattered neutron flux for the 'long' width phantom orientation showed an agreement up to 84%. Both detectors respond to room scattered neutrons in addition to scattered and transmitted neutrons from the phantom unlike MCNP simulation. This accounts for the disparities between measurements and calculations. Other benefits derived from the simulation were the investigation of neutron flux variation with depth in the bulk sample and the development of appropriate shielding for the gamma-ray detector. A further development of the MCNP simulation to include the walls of the room is required.

Neutron flux measurements in the photon beam of linacs carried out by activation analysis requires the measurement of induced activity in the foils using gamma-ray detectors. The consistency and reproducibility of the measurement procedure is very important. The solid angle subtended by a bare and collimated detector to a point, disc and cylindrical sources can be calculated using a Monte Carlo based Fortran 90 program, COLDET, which makes use of variance reduction methods. The solid angles calculated compare well with that of theory and work done by Carrilla [Car96]. However, some differences arise when the actual dimensions of the source and detector are taken into account as was done in this work.

Superheated drop detectors (SDD) may be the most reliable detectors for determining the neutron dose equivalent (and neutron spectrum if threshold detector systems are used as reported elsewhere) in an intense photon beam due to their insensitivity to photons and the fact that neutrons are not produced by photon interactions with the detector material. SDDs have been used to measure the neutron dose equivalent per unit photon dose on the beam axis of a 15 MV Varian Clinac 2100C and at stipulated distances outside the irradiated field in the patient plane. Measurements were carried out at 100 cm source-to-detector distance (SSD) for in-air and in phantom scenarios and also at positions in the maze and control room. The measured neutron dose equivalent per unit photon dose in and outside the 10x10 cm^2 field size at 0^o gantry angle are comparable with values reported by other workers using similar detector technology [Ong00, D'Er01a, Lin01]. Our results were 1.57±0.10 $mSvGy^{-1}$ and 1.42±0.09 $mSvGy^{-1}$ for in-air and in phantom at 1 cm depth, respectively. For example neutron dose equivalent of 1.74 ± 0.09 $mSvGy^{-1}$ for a 40x40 cm^2 field size for in-air at 0^o gantry angle was less by 0.1 $mSvGy^{-1}$ than that measured by Lin et al [Lin01] and show good agreement between this work and that carried out by other workers. Even though the linacs are by different manufacturers the basic structure and materials used for the component parts are similar if not the same. The neutron dose equivalent on the beam axis increased gradually as field size was varied from 5x5 cm^2 to 40x40 cm^2 but a dip was observed for a field size of 20x20 cm^2. Further investigation is required to explain this observation. The dose equivalent was found to be independent of field size outside the irradiated field edge at distances greater than 20 cm.

There was no clear-cut relationship between the neutron dose equivalent with field size and gantry angle. However, the neutron dose equivalent in the maize was much higher for gantry angles 0^o and 180^o. This underscores the non-isotropic nature of photoneutrons due to multiple scattering in the treatment room. In all the in-air measurements a consistent lower neutron dose equivalent was recorded for the 20x20 cm^2 field size for repeated measurements.

A neutron dose equivalent of 1.81 ± 0.08 $mSvGy^{-1}$ was recorded at 1 cm depth on the beam axis for the 5x5 cm^2 field size for the water phantom measurements. The neutron dose equivalent was also found to be independent of field size at depths

greater than 5 cm. The depth of 50% (d_{H50}) maximum neutron dose equivalent was determined at less than 5 cm for a field size of 5x5 cm^2 but greater than 5 cm for 10x10 cm^2 and 20x20 cm^2 field sizes. The neutron dose equivalent on the beam axis at depth $\geq$5 cm was independent of field size.

In the maze, the neutron dose equivalent falls rapidly to a negligible value at the shielding door and control panel for both in-air and phantom measurements. This implies that the bunker is adequately shielded against neutrons. The highest neutron dose equivalent of 17.9 ± 3.96 $\mu SvGy^{-1}$ was recorded on the outer wall of the maze entrance for the 20x20 cm^2 field size when the water column in the phantom was 36 cm, the highest water level obtainable in the water phantom.

The neutron dose equivalent per unit photon dose obtained in this work in the patient plane form less than 0.1% of the photon dose and may be considered negligible. However, this can represent a risk to healthy tissues and contribute to secondary malignancy insurgence in a patient. From the measurements in the maze, the photoneutrons seem to be well and effectively attenuated but from the radiation protection perspective, the situation may be different because of the induced radionuclides created by the activation of the different materials in the treatment room and the maze through radiative capture reactions. This was not studied in this work. Dose rates due to captured gammas of ^{28}Al ($T_{1/2}$ of 2.25 min) and ^{22}Na ($T_{1/2}$ of 15hrs) have been measured by Spyrou and co-workers [Spy91], for example, a dose rate of $10\mu Svh^{-1}$ due to ^{22}Na induced in the wall material was measured in the bunker of 18 MV Varian linac operated at 4 Gy/min.

It is suggested that further investigations be conducted to ascertain why the neutron dose equivalent for 20x20 cm^2 field size was found to be lower for all the gantry angles in air. It is important to determine the neutron spectrum at 100 SSD using, for example, threshold superheated drop detectors in order to compare this with MCNP calculations. It would be useful to estimate the neutron dose equivalent in other planes in the bunker such as the ceiling and floor which may give more information about the neutron distribution in the bunker.

The Varian Clinac 2100C, discussed above was simulated to investigate the photoneutron contamination in its output using the MCNP4C2. This provided a means of evaluating a method that can be used to investigate parameters of the linac that cannot be achieved by experimental methods. Though the precise linac information about the treatment head was not made available due to manufacturer's rights and secrecy, there was good agreement between simulation and experiment for both in-air and phantom scenarios. The agreement for the in-air measurements and calculations was within 10 to 15% whilst that of the phantom was within 15 to 20% and within quoted experimental errors. With regards to in-air measurements and those outside the field of irradiation, there was good agreement between the two methods for detector position from field edge within 20cm. Due to the level of agreement between experiment and calculations the neutron spectrum at 100 cm source-to-surface distance was calculated for field sizes 5x5 cm^2 to 40x40 cm^2. Average neutron energy of approximately 1 MeV was found which compares well with literature. With regards to further work the neutron contributions produced by the various components of the linac head can be determined by partitioning the geometry into sections and also the total number of neutrons reaching the SSD. Clusters of computers and parallel/series connected computers will be required and this is now being set-up here in the Physics Department, University of Surrey.

The fractional neutron dose equivalent to radiosensitive organs of the patient during high-energy photon treatment has been demonstrated using a tissue equivalent phantom BOMAB compatible with MCNP. Though this may not be precise, it provides some vital information as to the nature and distribution of neutron dose equivalent in the patient. It is an uphill task to determine the neutron dose equivalent in a patient using SDDs, though some workers have used these with patients taking extreme precautions and some work has been done with anthropomorphic phantoms. Software packages such as the VIP-Man [Zu00] can be used for this purpose and in this case the organs can be set as tally sites. This is a recent project being undertaken in the Physics Department, University of Surrey.

The MCNP has been used to simulate a typical linear accelerator bunker to determine the effect of modification and neutron attenuating material on the neutron dose and flux at the exit of the maze. A ^{252}Cf neutron spectrum was used to represent

the spectrum of the medical linac. By increasing the surface area of the treatment room by approximately 20% with the introduction of baffles in the ceiling, at the entrance into the treatment room, and maze, the neutron dose and flux at the exit was reduced by almost 45%. The introduction of the baffles in the maze increased the number of bends in the maze and therefore enhanced the scattering and reflection of fast and epi-thermal neutrons causing them to thermalise. The bunker modification confirms the theory that an increase in the surface area of the treatment room results in a reduction in the neutron flux and therefore the neutron dose at the exit of the maze.

The use of non-traditional neutron absorbers has greatly enhanced the efficiency of neutron absorption since their cross sections are not energy dependent and are very large compared to more conventional neutron absorbers. ^{157}Gd, ^{177}Hf and ^{149}Sm did not only cause a further reduction in the neutron flux but also eliminated the dose due to capture gamma rays associated with the often used ^{10}B absorber, as the emission of conversion electrons is a competing process to prompt gamma ray emission. The introduction of neutron absorbers in the maze caused a further reduction in the total neutron dose and flux to approximately 90% of the original bunker. Although these nuclides are relatively expensive, the real cost of using them for shielding must take into consideration the risks radiation workers and the general public, the cost incurred if a door has to be provided at the maze entrance and contrasted to the number of patients that can be treated in a given period with associated longer term benefits.

This work has demonstrated the use of both experimental measurements and calculations using Monte Carlo code (MCNP4C2) in the determination of photoneutron contamination in the photon output of high-energy medical linear accelerators, linacs. Even though this can be done experimentally, the use of simulation codes offers a variety of options and trials at relatively little cost. The MCNP code was also used to design and modify the bunker housing such linacs to effectively reduce the number of neutrons in the maze and at the exit door. It can thus be concluded that the application of experiment and simulation is complimentary and effective, however, caution should be exercised to authenticate the MCNP output.

10. References

[AAP95] Stovall, M., Blackwell, C. R., Cundiff, J., Novack, D. H., et al. Fetal dose from radiotherapy with photon beams: Report of AAPM radiation therapy committee task group No. 36. Med. Phys. 22 (1) (1995).

[Abd94] Abdushulurov, D. A., Dzhuraev, A. A., Evteeva, S. S., Kovalenko, P. P., et al. Model calculation of efficiency of gadolinium-based converters of thermal neutrons. Nucl. Instrum. Meth., B 84 (1994) 400-404.

[Ade01] Adesanmi, C. A., Balogun, F. A., Fasasi, M. K., Tubosun, I. A., et al. A semi-empirical formula for HPGe detector efficiency calibration. J. Radioanal. and Nucl. Chem. 249 (3) (2001) 607-611.

[Ago92] Agosteo, S., Para, A. F., Silari, M., Torresin, A., et al. Monte Carlo simulation of neutron transport in a linac radiotherapy room. Nucl Instrum. and Meth., B72 (1992) 84-90.

[Ago93] Agosteo, S., Para, A. F., Maggioni, B. Neutron fluxes in radiotherapy rooms. Med. Phys. 20 (2) (1993) 407-414.

[Ago95] Agosteo, S., Para, A. F., Maggioni, B., Sangiust, V., et al. Radiation transport in a radiotherapy room. Health Phys. 68 (1) (1995) 27-34.

[All91] Allen, P.D., Chaudhi, M.A. Neutron yields from selected materials irradiated with high energy photons. Phys. Med. Biol. 36 (12) (1991) 1653-1664.

[And83] Anderson, D. W., Hwang, C. C. Accelerator room photoneutron and photon background measurements using thermoluminescent dosimeters. Health Phys. 44 (2) (1998) 115-125.

[Apf79] Apfel, R. E., The superheated drop detector. Nucl Instr and Meth, 162 (1979) 603-608.

[Apf84] Apfel, R. E., Roy, S. C. Investigation on the applicability of superheated drop detectors in neutron dosimetry. Nucl Instr and Meth, 219 (1984) 582-587.

[Apf85a] Apfel, R. E., Roy, S. C. Superheated drop detector: A possible alternative for neutron dosimetry. Radiat. Prot. Dosim, 10(1985) 327-330.

[Apf85b] Apfel, R. E., Roy, S. C., Lo, Y.-C. Prediction of the minimum neutron energy to nucleate vapour bubbles in superheated liquids. Phys. Rev. A31 (5) (1985) 3194-3198.

[Apf02] Apfel, R. E., D'Errico, F. A neutron spectrometer based on temperature variations in superheated drop compositions. Nucl Instr and Meth. A 476(2002) 298-303.

[Apf89] Apfel, R. E., Lo, Y.-C. Practical neutron dosimetry with superheated drops. Health Phys. 56 (1) (1989) 79-83.

[Ash90] Hosseini-Ashrafi, M. E. The quantitative measurement of neutron induced activity in biomedical applications. Ph.D. thesis, University Surrey (1990).

[Ash92] Hosseini-Ashrafi, M. E., Spyrou, N. M. Calculation of the average solidangle subtended by a photon-emitting source at a collimated detector and the contribution of collimator edge penetration. Appl. Radiat. Isot. Vol.43 (12) (1992) 1449-1460.

[Axt72] Axton, E.J., Bardell, A.G. Neutron production from electron accelerators used for medical purposes. Phys. Med. Biol. Vol.17 (2) (1972) 293-298.

[Bad82] Bading, J. R., Zeitz, L., Laughlin, J. S. Phosphorous activation neutron dosimetry and its application to an 18-MV radiotherapy accelerator. Med. Phys. 9 (6) (1982) 835-843.

[Bak01] Baker, C. R., Thomas S.J. Neutron transport in a clinical linear accelerator bunker: comparison of materials for reducing the photo-neutrons dose at the maze entrance. Radiat. Phys. and Chem. 61 (2001) 633-634.

[Blo02] Blomquist, M., Karlsson, M. G., Zackrisson, B., Karlsson, M. Multileaf collimation of electrons – clinical effects on electron energy modulation and mixed beam therapy depending on treatment head design. Phys. Med. Biol. 47 (2002) 1013-1024.

[Bou97] Bourgois, L., Delacroix, D., Ostrowsky, A. Use of bubble detectors to measure neutron contamination of a medical accelerator photon beam. Radiat. Prot. Dosim. Vol. 74 (4) (1997) 239-246.

[Boz01] Bozkurt, A., Chao, T.C., Xu, X. G. Fluence-to-dose conversion coefficients based on the VIP-MAN anatomical model and MCNPX code for monoenergetic neutrons above 20 MeV. Health Phys., Vol. 81 (2) (2001) 184 – 202.

[Bri01] Briesmeister, J. F. MCNP4C2 Manual, Los Alamos, (2001).

[Can02] CancerStats, Incident – UK, Cancer Research UK, 9 (2002).

[Car96] Carrillo, H. R. V. Geometrical efficiency for a parallel disc source and detector. Nucl. Instrum. Meth., A 371 (1996) 535-537.

[Car99] Carinou, E., Kamenopoulou, V., Stamatelatos, I. E. Evaluation of neutron dose in the maze of medical electron accelerators. Med. Phys. 26 (12) (1999) 2520-2525.

[Cha65] Chasman, C., Jones, k. W., Ristinen, R. A. Fast neutron bombardment of a lithium-drifted germanium gamma-ray detector. Nucl. Instrum. and Meth., 37 (1965) 1-8.

[Cha93] Chao, J.-H. Neutron –induced gamma-rays in germanium detectors. Appl. Radiat. Isot. Vol. 44 (3) (1993) 605-611.

[Chu91] Chung, C., Chen, Y. R. Application of a germanium detector as a low flux neutron monitor. Nucl. Instrum. Meth., A 301 (1991) 328-336.

[Chu99] Chung, C. U, G. Rapid radiation dose determined by bubble neutron dosemeters. Radiat. Prot. Dosim. Vol. 85 (1-4) (1999) 109-111.

[Cil87] Cilliers G.D., Cilliers C., Browde S. A study of the mantle technique for Hodgkin's disease using thermoluminescent dosimetry. Radiat. Therm. Oncol. 10 (1987) 321 – 326.

[Czi02] Czirr, J. B., Maerrill, D. B., Buehler, D., McKnight T. K., et al. Capture-gated neutron spectrometry. Nucl Instr and Meth, A 476 (2002) 309-312.

[D'Er90] D'Errico, F., Apfel, R.E. A new method for neutron depth dosimetry with the superheated drop detector. Radiat. Prot. Dosim. Vol. 30 (2) (1990) 101-106.

[D'Er94] D'Errico, F., Alberts, W. G. Superheated-drop (bubble) neutron detectors and their compliance with ICRP-60. Radiat. Prot. Dosim. Vol. 54 (3/4) (1994) 357-360.

[D'Er95] D'Errico, F., Alberts, W. G., Curzio, G., Guldbakke, S. et al. Active neutrons spectrometry with superheated drop (bubble) detectors. Radiat. Prot. Dosim. Vol. 70 (1-3) (1995) 159-162.

[D'Er96] D'Errico, F., Alberts, W. G., Dietz, E., Guldbakke, S. et al. Neutron ambient dosimetry with superheated drop detectors. Radiat. Prot. Dosim. 65 (1-4) (1996) 397-400.

[D'Er97a] D'Errico, F., Apfel, R. E., Curzio, G. Dietz, E. et al. Superheated emulsions: Neutronics and thermodynamics. Radiat. Prot. Dosim. Vol. 70 (1-4) (1997) 109-112.

[D'Er97b] D'Errico, F., Alberts, W. G., Matzke, M. Advances in superheated drop (bubble) detector techniques. Radiat. Prot. Dosim. Vol. 70 (1-4)(1997) 103-108.

[D'Er98a] D'Errico, F., Nath, R., Tana, L., Curzio, G. et al. In-phantom dosimetry and spectrometry of photoneutrons from an 18 MV linear accelerator. Med. Phys. 25 (9) (1998) 1717-1724.

[D'Er98b] D'Errico, F., Nath, R., Silvano, G., Tana, L. In-vivo neutron dosimetry during high-energy bremsstrahlung radiotherapy. Int. J. Radiat. Oncol. Biol. Phys. Vol. 41 (5) (1998) 1185-1192

[D'Er98c] D'Errico, F., Nath, R., Lamba, M., Holland, S. K. A position-sensitive superheated emulsion chamber for three-dimensional photon dosimetry. Phys. Med. Biol. 43 (1998) 1147-1158.

[D'Er99] D'Errico, F. Fundermental properties of superheated drop (bubble) detectors. Radiat. Prot. Dosim. Vol. 84 (1-4) (1999) 55-62.

[D'Er01a] D'Errico, F., Luszik-Bhadra, M., Nath, R., Siebert, B. R. L.,Wolf, U. Depth dose-equivalent and effective energies of photoneutrons generated by 6-18 MV X-ray beams for radiotherapy. Health Phys. 80 (1) (2001) 4-11.

[D'Er01b] D'Errico, F., Alberts, W. G., Curzio, G., Matzke, M. et al. A directional dose equivalent monitor for neutrons. Radiat. Prot. Dosim. Vol. 93 (4) (2001) 315-324.

[Dey77] Deye, J. A., Young, F. C. Neutron production from a 10 MV medical linac. Phys. Med. Biol., 22(1) (1977) 90-94.

[Din02] Ding, G. X., Duzenli, C., Kalach, N. I. Are neutrons responsible for the dose discrepancies between Monte Carlo calculations and measurements in the build-up region for a high-energy photon beam. Phys. Med. Biol. 47 (2002) 3251-3261.

[Gie00] Gierga, D. P., Yanch, J. C. An investigation of the feasibility of gadolinium for neutron capture synovectomy. Med. Phys. 27 (7) (2000)1685-1692.

[Gla54] Glaser, D. A. Progress report on the Development of Bubble Chambers. Nuovo Cimento Suppl. 9 (11) (1954) 361-368.

[Gla96] Glasgow, G. P., Kurup, R. G., Leybovich, L., Wang, S., et al. Dosimetry and use of cobalt-60, 100 cm source-axis-distance teletherapy units. Curr. Oncol. 3 (1996) 42-50.

[Gua97] Gauldrini, G. F., d'Errico, F., Noccioni, P. A Monte Carloevaluation of the neutron detection efficiency of a superheated drop detector. ENEA Report RT/AMB/97/1 (Roma: ENEA) (1997).

[Gur78] Gur, D., Rosen, J. C., Bukovitz, A. G., Gill, A. W. Fast and slow neutrons in an 18-MV photon beam from a Philips SL/75-20 linea accelerator. Med. Phys. 5 (3) (1978) 221-222.

[Hah63] Hahn, B., Peacock, R.N. Ultrasonic cavitation induced by neutrons. Nuovo Cimento. 28 (2) (1963) 335-340.

[Hof85] Höfert, M., Piesch, E. Neutron dosimetry with nuclear emulsions. Radiat. Prot. Dosim. 10 (1985) 189-195.

[Hol94] Hollnagel, R. A. Conversion functions of the dose equivalent Hsl(10) in the ICRU slab used for the calibration of personal neutron dosemeters. Radiat. Prot. Dosim. Vol. 54 (3/4) (1994) 227-230.

[Hor77] Horvath, C., Lin, H. J. A simple three-parameter equation of state with critical compressibility-factor correction. Can. J. Chem. Eng. 55 (1977) 450-456.

[ICR93] International Commission on Radiation Units and Measurements. Prescribing, recording, and reporting photon beam therapy Report 50 Bethesda, Maryland. (1993).

[ICR71] International Commission on Radiation Units and Measurements. Data for protection against ionising radiation from external sources. Oxford: Pergamon; Publication 21; (1971)

[Ing85] Ing, H., Piesch, E. Status of neutron dosimetry. Radiat. Prot. Dosim. 10 (1985) 5-15.

[Ing97] Ing, H., Noulty, R. A., Mclean, T. D. Bubble detectors – A maturing technology. Radiat. Meas. 27 (1) (1997) 1-11.

[Jea78] Jeavons, A. P., Ford, N. L., Lindberg, B., Sachot, R. A new position-sensitive detector for thermal and epithermal neutrons. Nucl Instr and Meth, 148 (1978) 29-33.

[Joh83] Johns, H. E., Cunningham, J. R. The physics of radiology, fourth edition. Charles C. Thomas, Springfield, Illinois (1983).

[Jor94] Jordan, T. J., Williams, P. C. The design and performance characteristics of a multileaf collimator. Phys. Med. Biol. 39 (1994) 231-251.

[Kar83] Karzmark, C.J. Advances in linear accelerator design for radiotherapy. Med. Phys. 11 (2) (1984) 105-128.

[Kas98] Kase, K R., Mao, X. S., Nelson, W. R., Liu, J. C., et al. Neutron fluence and energy spectra around the Varian Clinac 2100C/2300C medical accelerator. Health Phys. 78 (1) (1998) 38-47.

[Ker79] Kersey, R. W. Estimation of neutron and gamma radiation doses in the entrance mazes of SL 75-20 linear accelerator treatment rooms. Medicamundi 24(3) (1979) 151-155.

[Kha94] Khan, F. M. The Physics of Radiation Therapy, second edition, Williams & Wilkins, London (1994).

[Kno00] Knoll, G. F. Radiation detection and measurement, third edition. John Wiley & Sons, Chichester (2000).

[Lal97] J.B. Awotwi-Pratt effect of neutron-moderating materials in high-energy linear accelerator mazes. Phys. Med. Biol. 42 (1997) 335-344.

[Lar85] LaRiviere, P. D. Neutron sources in a 24-MV medical linear accelerator. Med. Phys. 12(6) (1985) 806-809.

[Lar86] LaRiviere, P. D., Tochilin, E. Photon transmission in lead at the entrance to the medical electron accelerator room. Radiat. Prot. Dosim. 14(3) (1986) 257-260.

[Leu92] Leuthold, G., Mares, V., Schruabe, H. Calculation of the neutron ambient dose equivalent on the basis of the ICRP revised quality factors. Radiat. Prot. Dosim. Vol. 40 (2) (1992) 77-84.

[Lim93] Lim, W., Wang, C. K. Computational studies of neutron response function for a neutron spectrometer which uses Freon-12, -22, and –115 superheated liquids. Nucl. Instrum. and Meth, A 335 (1993) 243-247.

[Lin95] Linborg, L., Bartlett, D., Drake, P., Klein, H., Schmitz, T. et al. Determination of neutron and photon dose equivalent at work places in nuclear facilities in Sweden. Radiat. Prot. Dosim. 61 (1995) 89-100.

[Lin01] Lin, J-P., Chu, T-C., Lin, S-Y., Liu, M-T. The measurement of photoneutrons in the vicinity of a Siemens Primus linear accelerator. Appl. Radiat. Isot. 55 (2001) 315-321.

[Lla72] Llacer, J., Kraner, H. W. Neutron damage and annealing in high purity germanium radiation detectors. Nucl. Instrum. and Meth., 98 (1972) 467- 475.

[Lo87] Lo, Y.-C. Characterization of a neutron detector based on superheated drops. Ph.D. thesis, Yale University (1987).

[Loy99] Loye, T. Sidhu, N. P. S., Sandison, G. A. Comparison of superheated drop detector with phosphorous pentaoxide powder for the detection of neutrons in 18 MV x-rays. Med. Phys. 26 (5) (1999) 845-847.

[Lus94] Luszil-Bhadra, M., Alberts, W. G., D'Errico, F., Dietz, E. et al. A CR-39 track dosemeter for routine individual neutron monitoring. Radiat. Prot. Dosim. Vol. 55 (4) (1994) 285-293.

[Mac02] Macaulay, E., private communication, (2002).

[Mao96] Mao, X., Kase, K R., Nelson, W. R. Giant dipole resonance neutron yields produced by electrons as a function of target material and thickness. Health Phys. 70 (2) (1996) 207-214.

[Mao97] Mao, X. S., Kase, K R., W. R., et al. Neutron sources in the Varian Clinac 2100C/2300C medical accelerator calculated by the EGS4 code. Health Phys. 72 (4) (1997) 524-529.

[Mar99] Marinos, N. L. Monte Carlo calculations and measurement of photon beams shaped by multileaf collimators in radiation therapy. Ph.D. thesis, University of London (1999).

[Mas57] Masket, A. V. Rev. Sci. Instrum. 28 (1957) 191.

[Mas83] Mascetti, J., Fouassier, C., Hagenmuller, P. J. Solid State Chem. 50 (1983) 204.

[McC79] McCall, R. C., Jenkins, T. M., Shore, R. A. Transport of accelerator produced neutrons in a concrete room. IEEE Trans. Nucl. Sci., Vol. NS 26 (1) (1979) 1592-1602.

[McC87] McCall, R. C. Neutron yield of medical electron accelerators. SLAC-Publication 4480, Nov (1987).

[McC97] McCall, R. C., Shielding for thermal neutrons. Med. Phys. 24 (1) (1997) 135-136.

[McC99] McCall, R. C., McGinley, P. H., Huffman, K. E. Room scattered neutrons. Med. Phys. 26(2) (1999) 206-207.

[McG83] McGinley, P. H., White, T. A. Air activation produced by high-energy medical accelerator. Med. Phys. 10 (1983) 796-800.

[McG84] McGinley, P. H., Wright, B. A., Meding, C. J. Dose to radiotherapy technologist from air activation. Med. Phys. 11 (1984) 855-858.

[McG92a] McGinley, P. H. Photoneutron production in the primary barriers of medical accelerator rooms. Health Phys. 62 (4) (1992) 359-362.

[McG92b] McGinley, P. H. Photoneutron fields in medical accelerator rooms with primary barriers constructed of concrete and metals. Health Phys. 63 (6) (1992) 698-701.

[McG93] McGinley, P. H., Ghavidel, S., Landry, J. A study of photoneutron dose levels produced by the Philips SL medical accelerators. Radiat. Prot. Manag.10 (1993) 45-50.

[McG95a] McGinley, P. H., Miner, M. S. A method of eliminating the maze door of medical accelerator rooms. Radiat. Prot. Man. 12(5) (1995) 29-37.

[McG95b] McGinley, P. H., Wood, M., Mills, M., Rodriguez, R. Dose levels due to neutrons in the vicinity of high-energy medical accelerator. Med. Phys. 3 (6) (1976) 397-402.

[McG00] MaGinley, P. H., Dhaba'an, A. H. Evaluation of the contribution of capture gamma rays, x-ray leakage, and scatter to the photon dose at the maze door for a high energy medical electron accelerator using a Monte Carlo transport code. Med. Physics 27 (1) (2000) 225-230.

[Met02] Metcalfe, P., Kron, T., Hoban, P. The physics of radiotherapy x-rays from linear accelerator, second edition. Medical Physics Publishing, Madison, Wisconsin (2002).

[Moe81] Moens, L., De Donder, J., Xi-lei, L., De Corte, F., et al. Calculations of the absolute peak efficiency of gamma-ray detectors for different counting geometries. Nucl. Instrum. Meth., 187 (1981) 451-472.

[Mul86] Muller-Runkel, R., Ovadia, J., Culbert, H., Cooke, R. H., et al. The neutron dose and energy spectrum outside a 20-MV accelerator treatment room. Med. Phys. 13 (5) (1986) 742-747.

[Nat84] Nath, R., Epp, E. R., Laughlin, J. S., Swanson, W. P., et al. Neutrons from high-energy x-rays medical accelerators: An estimate of risk to the radiotherapy patient. Med. Phys. 11(3) (1984) 231-241.

[Nat93] Nath, R., Meigooni, A. S., King, C. R., Smolen, S. et al. Superheated drop detector for determination of neutron dose equivalent to patients undergoing high-energy x-ray and electron radiotherapy. Med. Phys. 20 (3) (1993) 781-787.

[NCR71] NCRP. Protection against neutron radiation. Report 38 (Washington, DC: NCRP) (1971) 45-85.

[NCR84] Neutron contamination from medical electron accelerator. NCRP Report 9, Bethesda, Maryland, (1984).

[Nic86] Nicolaou, G. E., Khrbish, Y. S., Spyrou, N. M. The effect of solid angle on the reproducibility of an experimental set-up in prompt gamma-ray neutron activation analysis. Appl. Radiat. Isot. Vol. 37 (12) (1986) 1219-1224.

[Ong99] Ongaro, C., Zanini, A., Nastasi, U. Monte Carlo simulation of the photoneutron production in the high Z elements. Monte Carlo Methods Appl. (5) 69 – 79.

[Ong00] Ongaro, C., Zanini, A., Nastasi, U., Ottaviano, G., et al. Analysis of photoneutron spectra produced in medical accelerators. Phys. Med. Biol. 45 (2000) L55-L61.

[Pal84] Palta, R. J., Hogstrom, K. R., Tannanonta, C. Neutron leakage measurement from a medical linear accelerator. Med. Phys. 11 (4)(1984) 498-501.

[Por92] Portal, G., Dietz, G. Implications of new ICRP and ICRU recommendations for neutron dosimetry . Radiat. Prot. Dosim. 44 (1/4), (1992) 165-170.

[Pri78a] Price, K. W., Nath, R., Holeman, G. R. Fast and thermal neutron profiles for a 25-MV x-ray beam. Med. Phys. 5(4), (1978).

[Pri78b] Price, K. W., Holman, G. R., Nath, R. A technique for determining fast and thermal neutron flux densities in intense high-energy (8-30 MeV) photon yields. Health Phys. Vol. 35 (1978) 341-351.

[Rog81] Rogers, D. W., Van Dyk, G. Use of a neutron remmeter to measure leakage neutrons from medical electron accelerators. Med. Phys. 8 (2) (1981) 163-166.

[Roy87] Roy, S. C. Apfel, R. E., Lo, Y.-C. Superheated drop detector: a potential tool in neutron research. Nucl. Instrum. and Meth, A 255 (1987) 199-206.

[Roy00] Roy, S. C., Sandison, G. A. Shielding for neutron scattered dose to the fetus in patients treated with 18 MV x-ray beams. Med. Phys. 27 (8) (2000) 1800-1803.

[Roy01] Roy, S. C. Superheated liquid and its place in radiation physics. Radiat. Phys. and Chem. 61 (2001) 271-281.

[Rub94] Ruby, L. Further comments on the geometrical efficiency of a parallel-disk source and detector system. Nucl. Instrum. Meth., A 337 (1994) 531-533.

[Sán89] Sánchez, F., Madurga, G. Arráns, R. Neutron measurements around an 18 MV linac. Radioth. And Oncol. 15 (1989) 259-265.

[Sat89] Sartori, E. MCNP training course on anatomical structure. (1989)

[Sei58] Seitz, F. On the theory of the bubble chamber. 1 (1) (1958) 2-13.

[She88] Sherwin, A. G., Pearson, A. J., Richards, D. J., O'Hagan, J. B. Measurement of neutrons from high energy electron linear accelerator. Radiat. Prot. Dosim. Vol. 23 (1/4) (1988) 337-340.

[Sie82] Siebert, B. R. L., Caswell, R. S., Coyne, J. J. Calculation of quality factors for fast neutrons in materials composed of H, C, N, and O. Proc. 8th Symp. on Microdosimetry, EUR-8395 Luxembourg: Commission of the European Communities; (1982).

[Spy81] Spyrou, N. M., Matthews, I. P. A cyclic neutron activation system using an isotopic neutron source for the measurement of short-lived isotopes. J. Radioana. Chem., Vol. 61 (1-2) (1981) 195-209.

[Spy91] Spyrou, N.M. Calculation of dose levels in and around linac bunkers, private communications (1991).

[Sun92] Sun, Y. Y., Chu, B. T., Apfel, R. E. Radiation-induced cavitation process in a metastable superheated liquid. J. Comput. Phys. 103 (1) (1992) 116-140.

[Swa78] Swanson, W. P. Calculation of neutron yields released by electronsincident on selected materials. Health Phys. Vol. 35 (1978) 353-367.

[Swa79] Swanson, W. P. Improved calculation of photoneutron yields released by incident electrons. Health Phys. 37 (9) (1979) 347-358.

[Tho97] Thomas, D. J., Chartier, J. L., Klein, H., Naismith, O. F. et al. Results of a large scale neutron spectrometry and dosimetry comparison exercise at the Cadarache moderator assembly. Radiat. Prot. Dosim. 70 (1997) 313-322.

[Tho02] Thomas, D. J., Bardell, A. G., Macaulay, E. M. Nucl Instr and Meth, A 476 (2002) 31-35.

[Tos91] Tosi, G., Torresin, A., Agosteo, S., Para, A. F. et al. Neutro measurements around medical electron accelerators by active and passive detection techniques. Med. Phys. 18(1) (1991) 54-60.

[Tso95] Tsoulfanidis, N. Measurement and detection of radiation, second edition. Taylor & Francis, London (1995).

[Uwa86] Uwamino, Y., Nakamura, T., Ohkubo, T. Measurement and calculation of neutron leakage from a medical electron accelerator. Med. Phys. 13 (3) (1986) 374-384.

[Vai97] Vaijapurkar, S. G., Paturkar, R. T. A re-usable neutron measurement device based on superheated liquid. Radiat. Prot. Dosim. 74 (1997) 21-26.

[Van96] Van Dyk, J., Battista, J. J. Cobalt-60: An old modality, a renewed challenge. Curr. Oncol. (1996).

[Vei98] Veinot, K. G., Hertel, N. E., Brooks, K. W., Sweezy, J. E. Multisphere neutron spectra measurements near a high energy medical accelerator. Health Phys. 75(3) (1998) 285-290.

[Ver72] Verghese, K., Gardner, R. P., Felder, R. M. Solid angle subtended by a circular cylinder. Nucl. Instrum. and Meth., 101 (1972) 391-393.

[Wie77] Wielopolski, L. The Monte Carlo calculation of the average solid angle suspended by a right circular cylinder from distributed sources. Nucl Instr and Meth, 143 (1977) 577-581.

[Wie92] Wielopolski, L., Ren, X. High-energy x-ray beam chacterisation using photonuclear reaction. Med. Phys. 19 (6) (1992) 1435- 1439.

[Xu00] Xu, X. G., Chao, T. C., Bozkurt, A. VIP-MAN: An image-based wholebody adult male model constructed from color photographs of the visible human project for multi-particle Monte-Carlo calculations. Health Phys. 78 (5) (2000) 476-486.

[Zhu95] Zhu, T. C., Bjarngard, B. E. The fraction of photons undergoing head scatter in x-ray beams. Phys. Med. Biol. 40 (1995) 1127-1134.

Appendix.

In-air measurements

Table of results showing the neutron dose equivalent on the beam axis and outside the irradiation field for different field sizes at 0^{o} gantry angle.

	Detector position /cm						
Field size/ cm^2	-50	-20	-10	0	10	20	50
5x5	0.27±0.09	0.37±0.10	0.36±0.10	1.41±0.11	0.45±0.10	0.36±0.10	0.17±0.09
10x10	0.17±0.09	0.35±0.09	0.51±0.09	1.57±0.10	0.43±0.10	0.42±0.10	0.22±0.09
20x20	0.26±0.08	0.47±0.09	0.64±0.09	1.54±0.10	0.78±0.09	0.55±0.09	0.16±0.08
40x40	0.17±0.08	0.28±0.08	0.38±0.09	1.74±0.09	0.28±0.08	0.29±0.08	0.22±0.08

Table of results showing the neutron dose equivalent on the beam axis and outside the irradiation field for different field sizes at 90^{o} gantry angle.

	Detector position /cm						
Field size/ cm^2	-50	-20	-10	0	10	20	50
5x5	0.37±0.10	0.38±0.10	0.36±0.10	1.55±0.11	0.56±0.10	0.37±0.10	0.18±0.09
10x10	0.52±0.09	0.92±0.10	1.07±0.10	1.82±0.10	0.98±0.10	0.98±0.10	0.45±0.09
20x20	0.36±0.08	0.49±0.09	0.48±0.09	1.27±0.10	0.61±0.10	0.38±0.09	0.09±0.08
40x40	0.18±0.08	0.29±0.09	0.39±0.08	1.88±0.09	0.28±0.08	0.15±0.08	0.11±0.08

Table of results showing the neutron dose equivalent on the beam axis and outside the irradiation field for different field sizes at 180^{o} gantry angle.

	Detector position /cm						
Field size/ cm^2	-50	-20	-10	0	10	20	50
5x5	0.19±0.09	0.38±0.10	0.37±0.10	1.61±0.11	0.38±0.11	0.19±0.09	0.09±0.08
10x10	0.36±0.09	0.58±0.10	0.57±0.09	1.79±0.10	0.47±0.10	0.37±0.09	0.35±0.09
20x20	0.18±0.10	0.30±0.08	0.39±0.09	1.04±0.10	0.42±0.09	0.29±0.09	0.16±0.08
40x40	0.18±0.08	0.20±0.08	0.20±0.09	1.84±0.09	0.19±0.08	0.15±0.09	0.11±0.08

Table of results showing the neutron dose equivalent on the beam axis and outside the irradiation field for different field sizes at 270° gantry angle.

	Detector position /cm						
Field size/ cm^2	-50	-20	-10	0	10	20	50
5x5	0.38±0.10	0.39±0.10	0.57±0.10	1.52±0.11	0.60±0.10	0.48±0.10	0.18±0.09
10x10	0.37±0.09	0.40±0.09	0.39±0.09	1.43±0.10	0.48±0.10	0.57±0.10	0.36±0.09
20x20	0.19±0.09	0.41±0.08	0.41±0.09	1.37±0.10	0.66±0.09	0.40±0.09	0.18±0.08
40x40	0.18±0.08	0.20±0.09	0.30±0.08	1.98±0.09	0.20±0.08	0.31±0.08	0.28±0.08

Phantom measurement

Table of results showing the variation of neutron dose equivalent per photon dose ($mSvGy^{-1}$) on the beam axis and outside the irradiation field with depth for 5x5 cm^2 field.

	Distance from field edge/ cm			
Depth in water/ cm	0	10	20	30
1	1.805±0.087	0.397±0.088	0.305±0.085	0.276±0.084
5	0.796±0.086	0.305±0.083	0.211±0.085	0
10	0.702±0.085	0.103±0.085	0.107±0.085	0
20	0.439±0.083	0.104±0.086	0	0

Table of results showing the variation of neutron dose equivalent per photon dose ($mSvGy^{-1}$) on the beam axis and outside the irradiation field with depth for 10x10 cm^2 field.

	Distance from field edge/ cm			
Depth in water/ cm	0	10	20	30
1	1.415±0.091	0.329±0.086	0.340±0.088	0.307±0.089
5	0.825±0.085	0.168±0.076	0.170±0.078	0.086±0.087
10	0.668±0.087	0.173±0.077	0.087±0.076	0.088±0.088
20	0.466±0.084	0.078±0.074	0.078±0.072	0.079±0.075

Table of results showing the variation of neutron dose equivalent per photon dose ($mSvGy^{-1}$) on the beam axis and outside the irradiation field with depth for 20x20 cm^2 field.

	Distance from field edge/ cm			
Depth in water/ cm	0	10	20	30
1	1.348±0.088	0.585±0.084	0.517±0.086	0.470±0.088
5	0.695±0.088	0.259±0.075	0.177±0.079	0.120±0.075
10	0.557±0.086	0.088±0.074	0.089±0.075	0
20	0.386±0.087	0.088±0.078	0.090±0.075	0

Neutron dose in maze

In air

Table of results showing the variation of neutron dose equivalent per photon dose ($\mu SvGy^{-1}$) in the maze and control panel area (Figure 6.6) with field size at 0^o gantry angle.

	Detector position			
Field size/ cm^2	A	B	C	D
5x5	10.10±3.22	1.83±1.37	0	0
10x10	13.77±3.5	2.58±1.53	0	0.86±0.80
20x20	8.19±2.66	5.74±2.23	0	0
40x40	8.60±1.97	4.30±1.8	0	0

Table of results showing the variation of neutron dose equivalent per photon dose ($\mu SvGy^{-1}$) in the maze and control panel area (Figure 6.6) with field size at 90^o gantry angle.

	Detector position			
Field size/ cm^2	A	B	C	D
5x5	8.25±2.90	2.75±1.68	0	0
10x10	10.33±3.10	4.30±1.98	0	0
20x20	3.28±1.68	2.46±1.46	0	0
40x40	3.91±1.80	1.57±1.14	0	0

Table of results showing the variation of neutron dose equivalent per photon dose ($\mu SvGy^{-1}$) in the maze and control panel area (Figure 6.6) with field size at 180° gantry angle.

	Detector position			
Field size/ cm²	A	B	C	D
5x5	10.08±3.22	3.67±1.94	0	0
10x10	16.35±3.86	2.58±1.53	0	0
20x20	3.29±1.68	2.47±1.46	0	0
40x40	6.26±2.27	3.91±1.80	0	0

Table of results showing the variation of neutron dose equivalent per photon dose ($\mu SvGy^{-1}$) in the maze and control panel area (Figure 6.6) with field size at 270° gantry angle.

	Detector position			
Field size/ cm²	A	B	C	D
5x5	9.16±3.10	0.92±0.90	0	0
10x10	15.49±3.75	3.44±1.77	0	0
20x20	3.28±1.68	1.64±1.20	0	0
40x40	0.78±0.70	0	0	0

Water phantom on couch

Table of results showing the variation of neutron dose equivalent per photon dose ($\mu SvGy^{-1}$) in the maze and control panel area (Figure 6.6) with water level at 17 cm in phantom.

	Detector position			
Field size/ cm²	A	B	C	D
5x5	3.60±1.94	0	0	0
10x10	8.45±2.80	3.38±1.77	0	0
20x20	6.44±2.38	0	0	0

Table of results showing the variation of neutron dose equivalent per photon dose ($\mu SvGy^{-1}$) in the maze and control panel area (Figure 6.6) with water level at 21cm in phantom.

	Detector position			
Field size/ cm^2	A	B	C	D
5x5	6.30±2.46	1.80±1.37	0	0
10x10	6.76±2.50	3.38±1.77	0	0
20x20	8.04±2.66	2.41±1.46	0	0

Table of results showing the variation of neutron dose equivalent per photon dose ($\mu SvGy^{-1}$) in the maze and control panel area (Figure 6.6) with water level 26 cm in phantom

	Detector position			
Field size/ cm^2	A	B	C	D
5x5	10.80±3.35	1.80±1.37	0	0
10x10	5.07±2.17	2.53±1.53	0	0
20x20	12.10±3.26	0.80±0.74	0	0

Table of results showing the variation of neutron dose equivalent per photon dose ($\mu SvGy^{-1}$) in the maze and control panel area (Figure 6.6) with water level at 36 cm in phantom.

	Detector position			
Field size/ cm^2	A	B	C	D
5x5	7.20±2.74	2.70±1.68	0	0
10x10	2.53±1.53	2.53±1.53	0	0
20x20	17.7±3.96	0	0	0

MCNP Linac simulation results.

Variation of the neutron dose equivalent per photon dose per unit incident electron with depth of detector in the water phantom.

5x5 cm^2 field

	Distance from field edge/ cm			
Depth in water / cm	0	10	20	30
1	4.96E-5±8.88E-7	1.63E-5±3.2E-7	1.50E-5±2.84E-7	1.38E-5±2.41E-7
5	1.57E-5±2.80E-7	4.18E-6±1.63E-7	4.01E-6±1.69E-7	3.63E-6±1.99E-7
10	4.96E-6±2.37E-7	1.07E-6±6.39E-8	1.01E-6±7.65E-8	9.03E-7±6.33E-8
20	3.53E-7±5.20E-8	1.42E-7±1.27E-8	1.38E-7±2.11E-8	9.30E-8±1.14E-8

10x10 cm^2 field

	Distance from field edge/ cm			
Depth in water / cm	0	10	20	30
1	4.59E-5±4.33E-7	1.83E-5±3.46E-7	1.54E-5±2.05E-7	1.45E-5±2.81E-7
5	1.73E-5±3.35E-7	5.79E-6±1.25E-7	5.30E-6±1.39E-7	4.55E-6±1.62E-7
10	4.92E-6±1.59E-7	1.78E-6±9.77E-8	1.43E-6±8.39E-8	1.23E-6±8.87E-8
20	5.47E-7±3.05E-8	2.41E-7±2.38E-8	1.80E-7±1.46E-8	1.33E-7±1.44E-8

20x20cm^2 field

	Distance from field edge/ cm			
Depth in water / cm	0	10	20	30
1	4.53E-5±3.33E-7	2.09E-5±2.76E-7	1.75E-5±3.24E-7	1.49E-5±2.62E-7
5	1.90E-5±3.39E-7	7.64E-6±2.18E-7	5.57E-6±1.59E-7	4.65E-6±1.47E-7
10	6.78E-6±1.87E-7	2.30E-6±1.04E-7	1.76E-6±9.49E-8	1.26E-6±4.59E-8
20	7.72E-7±3.52E-8	3.35E-7±2.59E-8	1.69E-7±1.09E-8	1.62E-7±1.17E-8

Publications.

Awotwi-Pratt, J. B., Hosseini-Ashrafi, M. E., Spyrou, N. M.
The effect of bunker modification and neutron absorbing materials on neutron flux in high-energy medical linear accelerators mazes.
Published in: Proceedings of the 7th international conference on applications of nuclear techniques, "Nuclear and atomic industrial & analytical applications", Crete, Greece, June 17 – 23, 2001.

Spyrou, N. M., Awotwi-Pratt, J. B., Williams, A. M.
Monte Carlo calculations and neutron spectrometry in quantitative prompt gamma neutron activation analysis (PGNAA) of bulk samples using an isotopic neutron source.
Accepted for publication in: Journal of Radioanalytical and Nuclear Chemistry.

Presentations.

Awotwi-Pratt, J. B., Hosseini-Ashrafi, M. E., Spyrou, N. M.
The effect of bunker modification and neutron absorbing materials on neutron flux in high-energy medical linear accelerators mazes.
Presented at: Universities Nuclear Technology Forum, University of Glasgow, Glasgow, UK. April 3rd – 5th, 2001. (Oral).

Awotwi-Pratt, J. B., Hosseini-Ashrafi, M. E., Spyrou, N. M.
The effect of bunker modification and neutron absorbing materials on neutron flux in high-energy medical linear accelerators mazes.(Revised).
Presented at: 7th International conference on applications of nuclear techniques, "Nuclear and Atomic Industrial and Analytical Applications". Crete, Greece. June 17th – 23rd, 2001. (Oral).

Spyrou, N. M., Awotwi-Pratt, J. B., Williams, A. M.
Monte Carlo calculations and neutron spectrometry in quantitative prompt gamma neutron activation analysis (PGNAA) of bulk samples using an isotopic neutron source.
Presented at: 7th International conference on Nuclear Analytical Methodes in the Life Sciences. Antalya, Turkey. June 16th – 21st, 2002. (Oral).

" Never walk into an environment and assume that you understand it better than the people who live there"

Kofi Annan
UN Secretary General

" In this great future you cannot forget your past"

Bob Marley